CHAPTER 2(A)

SYMMETRICAL LIQUID CRYSTALLINE DIMERS OF AZO/AZOMETHINE NAPHTHALENE

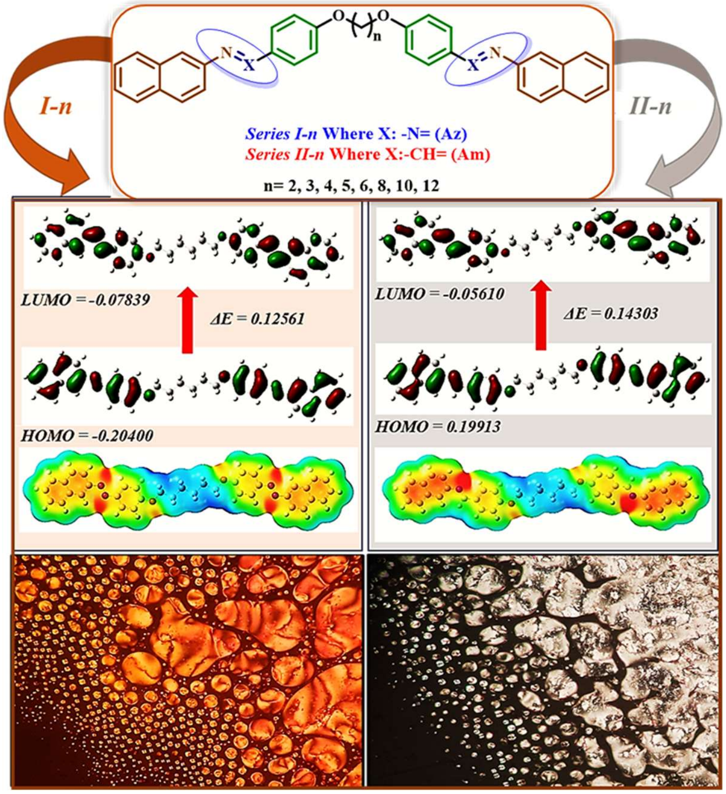

2A.1 Introduction

The introduction of a bulky naphthalene moiety in the molecule of liquid crystalline (LC) material can change its transition temperatures[1–3]. Two rigid mesogenic units are joined by a flexible spacer in the LC dimers[4,5]. Calamitic liquid crystal (LC) dimers, characterized by their rod-shaped structure, have garnered the most attention among various types of LC dimers. These dimers involve linking two units, which can be either identical (symmetric) or non-identical (non-symmetric), using a flexible spacer. The flexible spacer allows for a degree of molecular motion and the mesogenic units, on the other hand, provide the necessary rigidity for maintaining the ordered orientation of molecules, which is important for the formation of liquid crystal phases. The dimeric architecture of liquid crystals can be modified by introducing different linking groups such as ether[6–9], ester[10], methylene[11], carbonyl[12], thioether[13], thioester[14], etc. between the hydrocarbon spacer and mesogenic units, resulting in variations in molecular shape and mesogenic properties. Additionally, the azo and azomethine groups can be functionalized with different substituents to tune the mesomorphic properties of the LC. A new geometry of LCs that could produce molecules with variable mesomorphic properties and other technological applications is being developed, and the azo (-N=N-) and azomethine (-CH=N-) groups are thought to be worthy linking groups. The mesomorphic properties of LCs are stabilized by Schiff base and azo linkages, which uphold the rigidity and linearity of the molecular geometry. LC dimers with imine linkages are advantageous for many applications like thermo-stable mechanisms and corrosion inhibitor systems[15].

Yang et al. synthesized two new series of symmetrical azobenzene-dimers, integrating the structural specificity of dimers with the optical properties of azobenzene.[16] Hegde et al. revealed that the optical properties of bent-shaped dimeric azo dyes are significantly altered by the spacer effect, leading to notable changes in photoisomerization.[17] Gorecka et al. reported a series of azobenzene dimers capable of forming a banana (B_4) phase, suggesting their potential as photoactive matrices for material confinement due to their photosensitivity.[18] Yeap et al. synthesized and characterized a new series of symmetrical dimeric molecules with photoreactive azo groups linked by a chiral unit and a flexible spacer employing a terminal decyloxy group throughout, describing their synthesis and thermotropic properties.[19] Arakawa et al. synthesized and characterized thioether-linked 4-cyanoazobenzene-based LC dimers, wherein symmetric dimers with varying chain lengths (n = 3,5,7,9,11) exhibited elusive monotropic twist-bend nematic (N_{TB}) phases.[20] Prasad et al. synthesized a new homologous series of compounds to study how different lateral substituents and ester linkage directions affect mesogenic properties in dimerized calamitic, and non-mesogenic azo moieties connected by alkylene spacers.[21] Svoboda et al. synthesized and analyzed physical properties of novel core-to-core dimers with top-to-bottom linkages between bent molecule cores, observing preservation of mesomorphic behaviour and formation of SmC_{APA} phases, albeit in narrower temperature ranges, by modifying spacer length, linkage groups, and terminal chain polarity.[22] Prajapati et al. have reported symmetrical H-shaped mesogenic twin liquid crystalline compounds.[23–26] The azo group can undergo reversible isomerization upon exposure to light, leading to changes in the mesomorphic properties of the LCs. This photo-responsive behaviour has potential applications in areas such as optical data storage, optical switching, and photo-responsive coatings.[27–29] **Fig. 2A.1** displays several examples of symmetrical LC dimers featuring azo linkages.

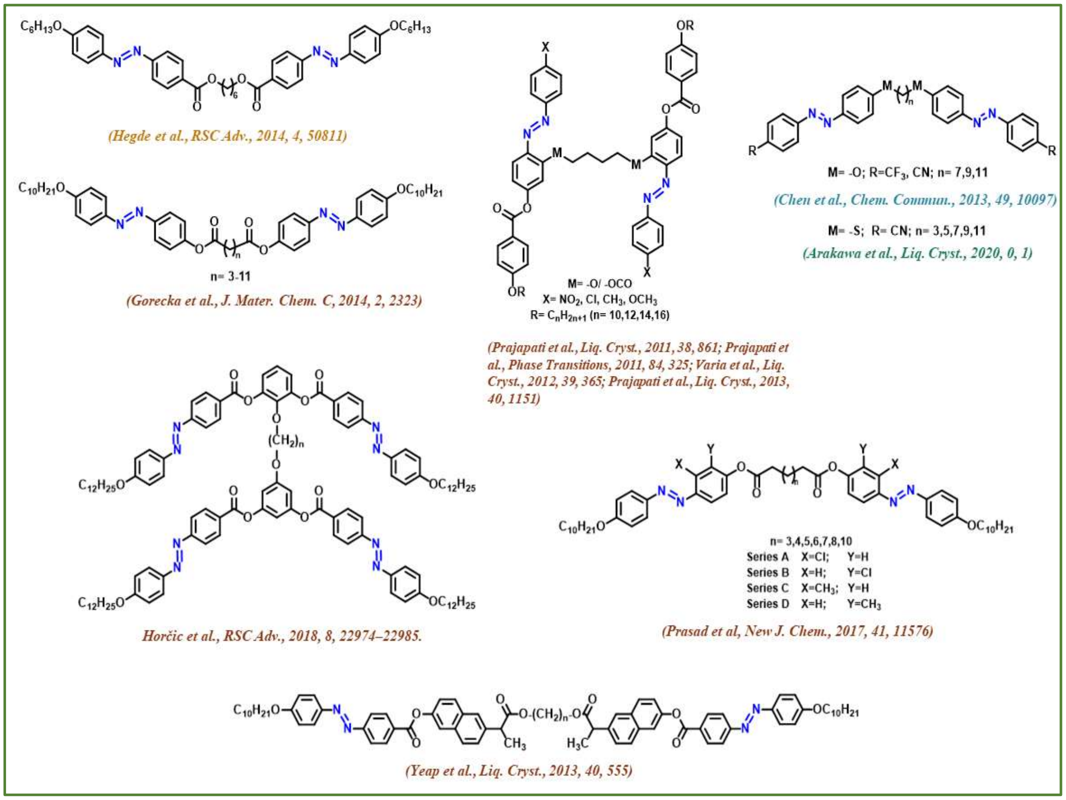

Fig. 2A.1: Some examples of Symmetrical LC dimers containing azo linkages

Various research groups have contributed to the synthesis and characterization of liquid crystalline dimers with azomethine linkages. **Fig. 2A.2** presents various examples of Symmetrical LC dimers incorporating azomethine linkages. Yelamaggad et al. devised a series of symmetrical dimers composed of salicylaldimine moieties linked by flexible alkylene central spacers through ether connections.[30] Meanwhile, Iwan et al. achieved a milestone by synthesizing the poly(1,4-butanediol)bis(4-aminobenzoate)-based LC imines, extensively exploring their phase behaviour and optoelectronic attributes.[31]

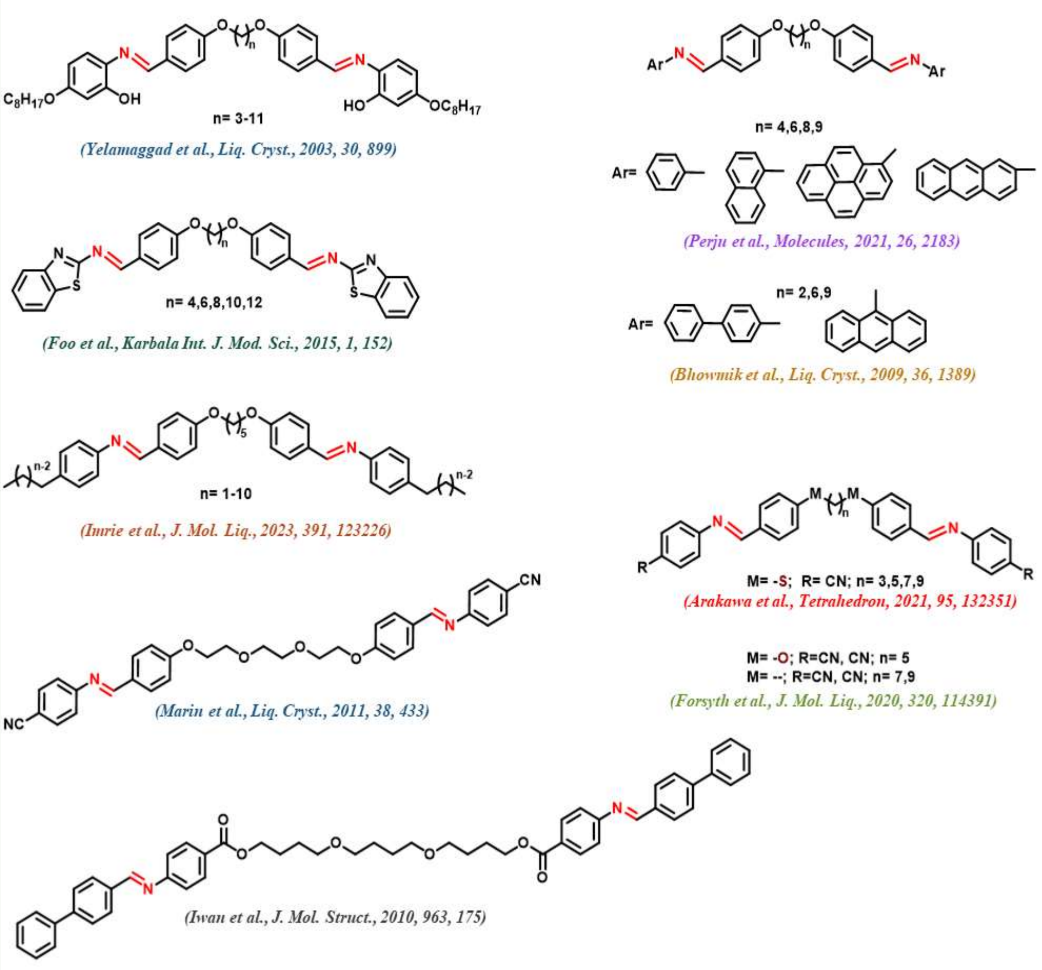

(Yelamaggad et al., Liq. Cryst., 2003, 30, 899)

(Perju et al., Molecules, 2021, 26, 2183)

(Foo et al., Karbala Int. J. Mod. Sci., 2015, 1, 152)

(Bhowmik et al., Liq. Cryst., 2009, 36, 1389)

(Imrie et al., J. Mol. Liq., 2023, 391, 123226)

(Arakawa et al., Tetrahedron, 2021, 95, 132351)

(Marin et al., Liq. Cryst., 2011, 38, 433)

(Forsyth et al., J. Mol. Liq., 2020, 320, 114391)

(Iwan et al., J. Mol. Struct., 2010, 963, 175)

Fig. 2A.2: Reports of Symmetrical LC dimers containing azomethine linkage

Bowmik et al. conducted condensation reactions of benzaldehyde, biphenyl carboxaldehyde, and 9-anthraldehyde with various aromatic diamines using tosic acid as a catalyst, yielding a series of azomethine dimers.[32] Additionally, Marin et al. introduced a novel azomethine dimer, delving into its thermotropic properties, unveiling a monotropic nematic mesophase and crystalline polymorphism.[33] Perju et al.

synthesized another set of azomethine dimers through condensation reactions of flexible bis-benzaldehydes with aromatic amines containing diverse aromatic groups.[34] Imrie et al. contributed to the field by reporting the symmetric LC dimers, specifically 1,5-bis(4'-oxyanilinebenzylidene-4-alkane)pentanes.[35] Furthermore, they investigated four series of LC dimers based on benzylideneaniline mesogenic units, varying the lengths of terminal alkyloxy chains.[36] Arakawa et al. established two homologous series of thioether-linked cyanobenzylideneaniline-based liquid crystal dimers.[37] S-T. Ha et al. expanded the scope by reporting a series of homologous symmetrical dimers, α,ω-bis[4-(6'-methoxybenzothiazol-2'-yl)iminomethylphenoxy]alkane, featuring alkyl spacer groups with different lengths.[38]

2A.2 Objectives

Based on the aforementioned factors, we extended our investigation by synthesizing a homologous series comprising two distinct sets of liquid crystalline dimers. Synthesis, characterization and study of mesomorphic properties of series ***I-n***; 1,N-bis(4-((E)-naphthalen-2-yldiazenyl)phenoxy)alkane and series ***II-n***; (N,N'E,N,N'E)-N,N'-(((butane-1,4-diylbis(oxy))bis(4,1-phenylene))bis(methanylylidene))bis(naphthalen-2-amine) containing naphthalene moiety at both ends possessing chains of varying central methylene spacer lengths (n = 2,3,4,5,6,8,10,12). The objective of the current work is to synthesize and examine their mesomorphism, as well as their photophysical properties and thermal properties. The effect of the number of flexible methylene spacers (n = 2,3,4,5,6,8,10,12) on transition temperatures was studied. Density functional theory (DFT) calculations were used to study various theoretical parameters for the series we have synthesized, and theoretical findings were then compared to experimental results.

2A.3 Results and Discussion

2A.3.1 Synthesis

The synthesis of (E)-4-(naphthalen-2-yldiazenyl)phenol (NpAzOH) involves a two-step process: diazotization of naphthalen-2-amine to form a diazonium salt intermediate, followed by its coupling with phenol under basic conditions. This process is widely used in the synthesis of azo dyes and plays a crucial role in the field of organic chemistry and colour chemistry.

The synthesis of (E)-4-((naphthalen-2-ylimino)methyl)phenol (NpAmOH) involved a condensation reaction between naphthalen-2-amine and 4-hydroxybenzaldehyde, resulting in the formation of a Schiff base derivative. The reaction was conducted under reflux conditions with an acid catalyst, and the product was isolated.

The Williamson etherification reaction is then conducted by reacting NpAzOH/NpAmOH with the appropriate α,ω-dibromoalkane, facilitated by a base in an anhydrous solvent to yield the corresponding dimers.

The synthetic route for the dimers ***I-n*** (**Scheme 2A.1**) and ***II-n*** (**Scheme 2A.2**) having methylene spacer length n = 2,3,4,5,6,8,10,12 is shown here in Scheme 2A.1 and 2A.2, respectively.

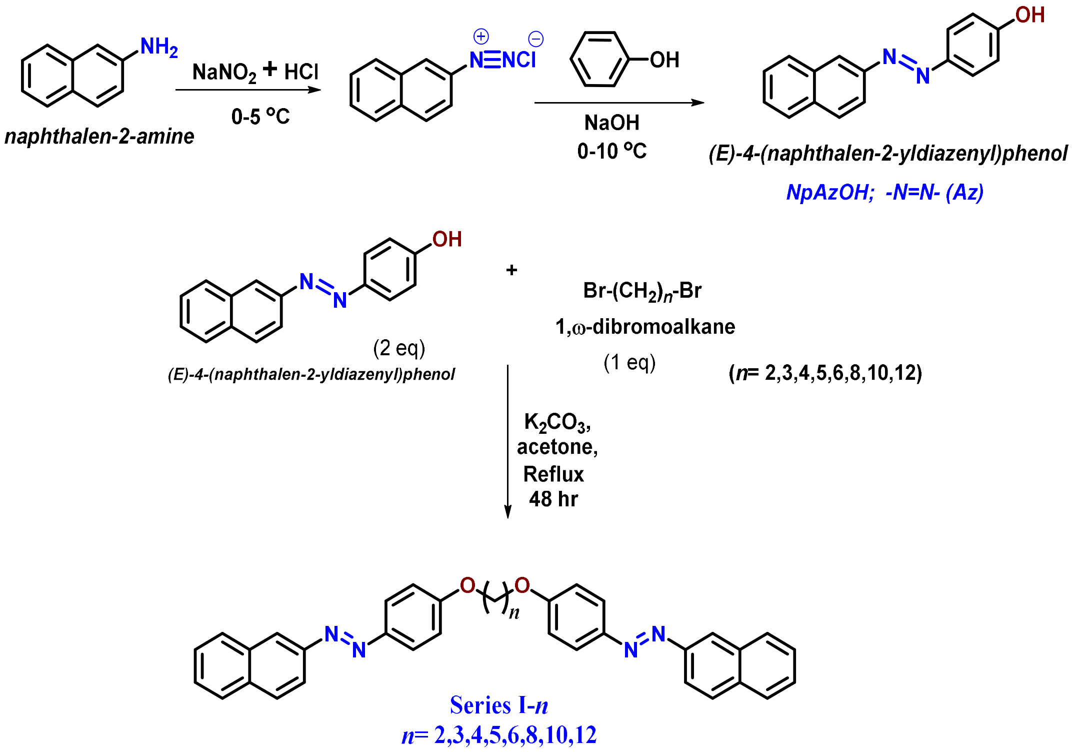

Scheme 2A.1: Synthetic route for the dimers of Series *I-n*

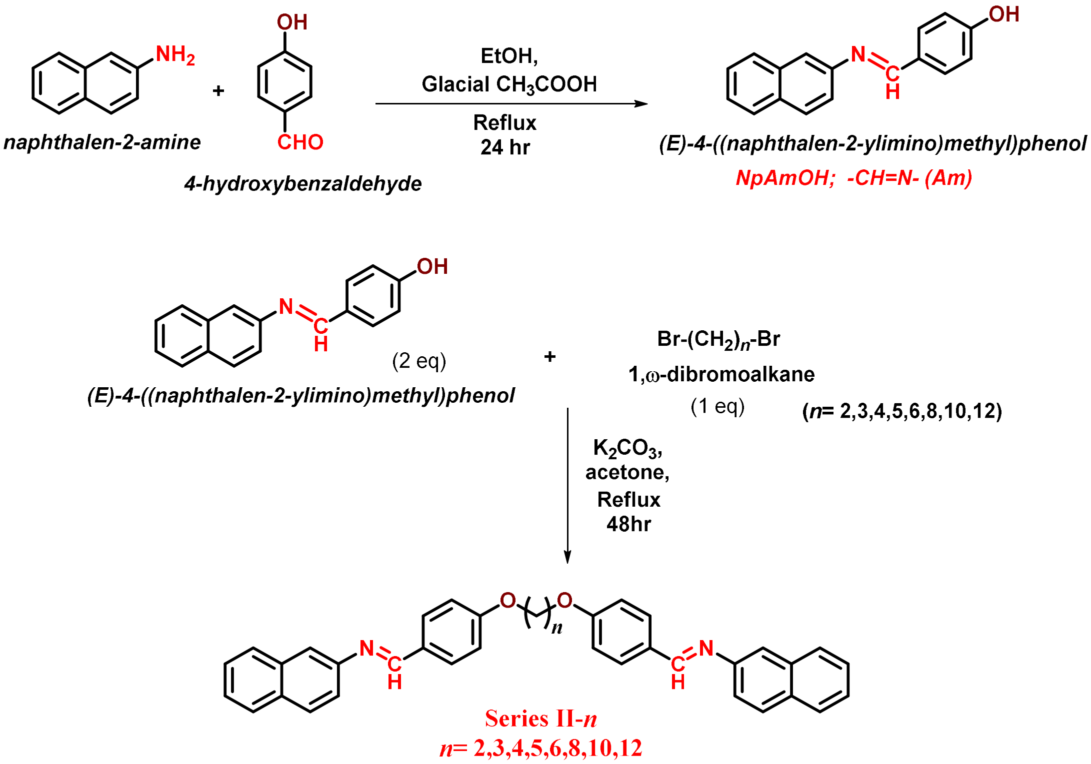

Scheme 2A.2: Synthetic route for the dimers of Series *II-n*

2A.3.2 Chemistry

Different spectroscopic methods, including FT-IR, ^{1}H-NMR and ^{13}C-NMR, to determine the structures of dimers.

In the **FT-IR** spectra of the dimers, bands were observed in the frequency range of 2995-2868 cm^{-1}, which were attributed to the stretching vibrations of aliphatic C-H bonds. Additionally, in dimers of series ***I-n***, the -N=N- stretching frequency appeared in the range of 1600-1590 cm^{-1}. On the other hand, the band appearing at the frequency range of 1610-1580 cm^{-1} was attributed to the stretching vibrations of -C=N- in dimers of series ***II-n***. Furthermore, strong absorptions were observed at 1260-1240 cm^{-1}, which were attributed to the ether groups present in the spacer chain.

In the **^{1}H-NMR** spectra obtained, a consistent trend in ^{1}H-^{1}H splitting and chemical shifts was observed across all members of the homologous series. The diagnostic peaks were discussed based on the representative compounds of series ***I-n*** and series ***II-n***. Specifically, the presence of the azomethine protons (-CH=N-) appeared as a singlet around δ 8.50-8.60 ppm in the ^{1}H-NMR spectra. The absorption of aromatic protons from two distinguishable positions in the aromatic rings resulted in a multiplet appearing between δ 7.00-8.00 ppm. Additionally, triplets were detected at δ 4.01-4.30 ppm, which were assigned to the methylene protons adjacent to the oxygen in the spacer chain. Moreover, a multiplet was observed at an up-field around δ 0.80-2.35 ppm, and this was attributed to the methylene protons of the flexible spacer in dimers.

In the **^{13}C NMR** spectrum of dimers, multiple peaks appeared around δ 0-50 ppm for aliphatic carbons in the flexible spacer, δ 110-165 ppm for aromatic carbons in the naphthalene and phenyl rings, and δ 60-70 ppm for carbons in the ether linkages (phenoxy groups). Additionally, carbons directly bonded to the azo groups may exhibit peaks in the range of δ 150-165 ppm. Dimers of series ***II-n*** give an extra peak for the carbon of the azomethine (-CH=N-) group around δ 160-170 ppm. The elemental analysis was carried out for all the reported dimers.

The mass spectrum was recorded using a Time-of-Flight Mass Spectrometer (TOF-MS) in positive ion mode. The spectrum showcases various peaks, each corresponding to different ionized fragments. The presence of a peak at a particular value of m/z as a molecular ion peak $[M+H]^+$ confirms the molecular weight of the compounds.

The calculated theoretical percentages of elements derived from the molecular formula are matching with the experimental elemental analysis results.

2A.3.3 Mesomorphic Behaviour

Differential Scanning Calorimetry (DSC) and Polarizing Optical Microscopy (POM) were employed to analyze phase transition temperatures and optical textures.

2A.3.3.1 Differential scanning calorimetry study (DSC)

The thermograms were calculated utilising DSC During both heating and cooling cycles, all phase transitions of the compounds were monitored at a rate of 10 ºC min^{-1}. The transition temperatures (ºC) and corresponding enthalpies (kJ mol^{-1}) extracted from the DSC thermograms are presented in **Table 2A.1** for ***I*-n** and **Table 2A.2** for ***II*-n**.

Table 2A.1: Transition temperatures (in °C) and associated enthalpy of transition (ΔH) in (kJ mol−1) of I-n

Dimer *I*-n	n	Transition temperatures (°C) and ΔH (kJ mol-1)	
		Heating	Cooling
***I*-2**	2	Cr 235.56 (51.15) N 241.59 (0.89) Iso	Iso 237.24 (-1.98) N 208.65 (-59.20) Cr
***I*-3**	3	Cr 217.08 (89.67) Iso	Iso 203.87 (-80.93) Cr
***I*-4**	4	Cr 219.30 (49.19) N 227.04 (1.83) Iso	Iso 225.38 (-2.26) N 199.01 (-45.03) Cr
***I*-5**	5	Cr 203.54 (91.34) Iso	Iso 199.02 (-83.21) Cr
***I*-6**	6	Cr 189.28 (99.31) N 198.57 (2.19) Iso	Iso 197.78 (-2.23) N 186.28 (-49.04) Cr
***I*-8**	8	Cr 193.09 (217.77) Iso	Iso 175.64 (-3.61) N 168.28 (-196.65) Cr
***I*-10**	10	Cr 177.86 (65.06) Iso	Iso 168.64 (-2.57) N 158.37 (-57.33) Cr
***I*-12**	12	Cr 168.26 (164.25) Iso	Iso 161.56 (-2.85) N 150.13 (-99.20) Cr

N, Nematic; Iso, Isotropic liquid; Cr, Crystalline solid

Table 2A.2: Transition temperatures (in °C) and associated enthalpy of transition (ΔH) in (kJ mol^{-1}) of *II*-n

Dimer II-n	n	Transition temperatures (°C) and ΔH (kJ mol^{-1})	
		Heating	Cooling
II-2	2	Cr 259.22 (111.69) Iso	Iso 232.81 (-2.73) N 190.49 (-86.49) Cr
II-3	3	Cr 201.61 (99.17) Iso	Iso 228.12 (-89.91) Cr
II-4	4	Cr 207.63 (54.13) N 234.60 (2.48) Iso	Iso 232.06 (-2.19) N 201.49 (-52.61) Cr
II-5	5	Cr 166.34 (61.25) Iso	Iso 129.19 (-59.97) Cr
II-6	6	Cr 196.99 (59.63) Iso	Iso 194.34 (-3.22) N 163.98 (-56.14) Cr
II-8	8	Cr 190.61 (52.99) Iso	Iso 189.12 (-2.40) N 178.90 (-51.72) Cr
II-10	10	Cr 179.09 (57.13) Iso	Iso 172.64 (-1.98) N 145.48 (-57.66) Cr
II-12	12	Cr 177.52 (65.71) Iso	Iso 159.74 (-2.67) N 150.78 (-63.82) Cr

N, Nematic; Iso, Isotropic liquid; Cr, Crystalline solid

The representative DSC scans of ***I*-4** as shown in **Fig. 2A.3(a)**. Dimer ***I*-4** show two exotherms corresponding to the transitions at 219.30 °C and 227.04 °C on the heating scan which corresponds to the Cr-to-N-to-Iso phase sequence with enthalpy change of 49.19 and 1.83 kJ mol^{-1} respectively. In the cooling scan reverse transitions were observed as two endotherms at 225.38 °C with an enthalpy change of 2.26 kJ mol^{-1} and 199.01 °C with an enthalpy change of 45.03 kJ mol^{-1} which corresponds to Iso-to N-to-Cr state. The representative DSC scans of ***II*-4** as shown in **Fig. 2A.3(b)**, also show the same enantiotropic mesophase. ***II*-4** shows endothermic transitions Cr-to-N and N-to-Iso at 207.63 °C (ΔH= 54.13 kJ mol^{-1}) and 234.60 °C (ΔH=2.48 kJ mol^{-1}) on heating. On cooling, it shows two exothermic peaks at 232.06 °C (ΔH=2.19 kJ mol^{-1}) and 201.49 °C (ΔH=52.61 kJ mol^{-1}) for Iso-to-N and N-to-Cr transitions respectively (**Fig. 2A.3b**).

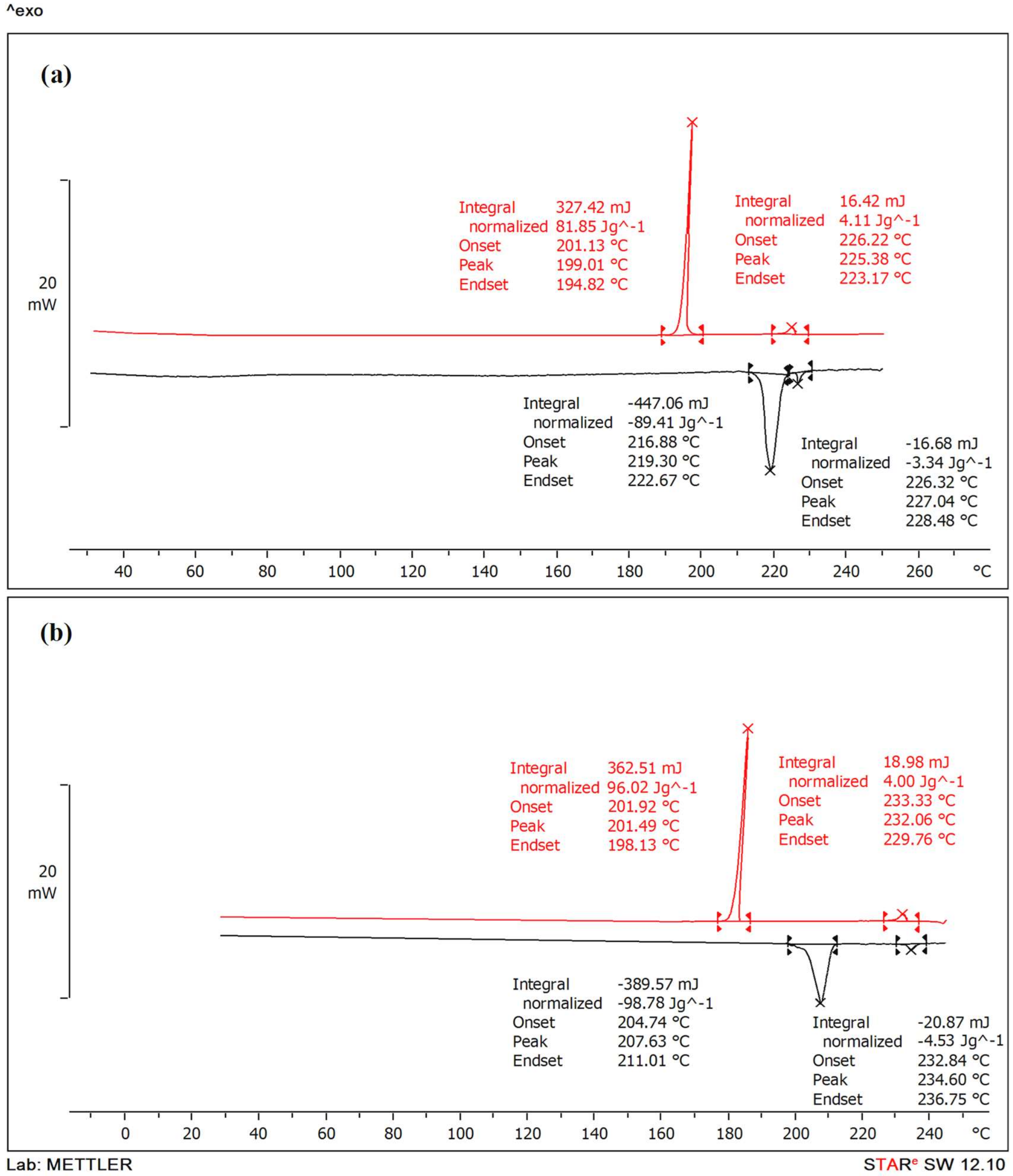

Fig. 2A.3: DSC thermogram of (a) *I*-4 and (b) *II*-4 during heating and cooling cycles

2A.3.3.2 Polarising optical microscopy (POM)

The solid samples were sandwiched between the untreated glass plate and a cover slip and subjected to heating followed by cooling scans at the rate of 10 °C min^{-1} for textural observations through POM. In the first series of compounds ***I*-n**, the nematic phase was observed in compounds ***I*-2,4,6,8,10,12** whereas compounds ***I*-3,5** are non-mesogenic. **Fig. 2A.4** shows the optical microphotographs of ***I*-4.**

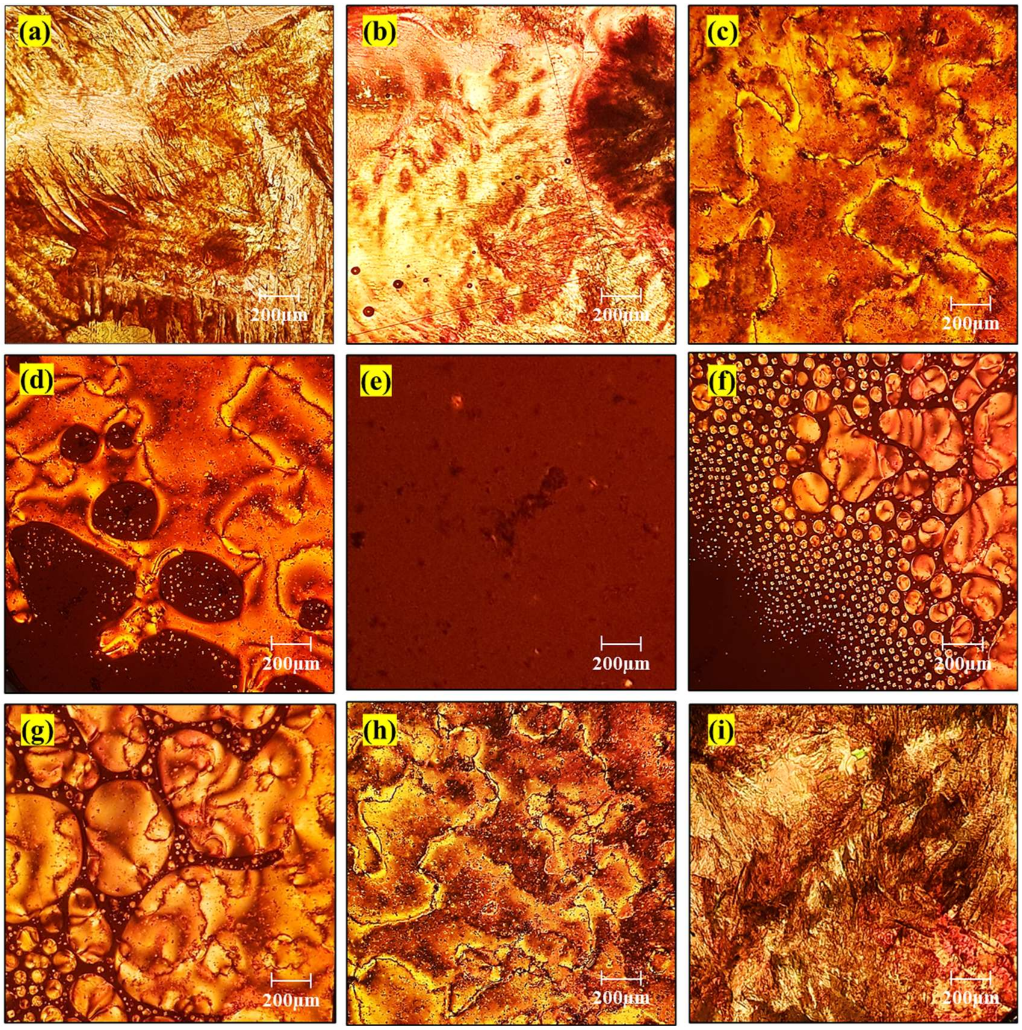

Fig. 2A.4: Optical microphotograph of *I*-4 (a) Crystalline solid (b) Cr-N transition at 218 °C on heating (c) Schlieren texture of nematic phase at 220 °C (d) N-Iso transition (e) Isotropic liquid at 228 °C (f) On cooling, Nematic droplets at 226 °C (g) coalescence of nematic droplets (h) Schlieren Texture at 224 °C (i) N-Cr transition at 199 °C

The optical microphotographs of ***I*-4** reveal its intriguing mesogenic properties through a series of distinct transitions and phases. Initially, at lower temperatures, it appears as a well-defined crystalline solid (**Fig. 2A.4a**), marked by its ordered molecular arrangement. As the temperature rises, a significant transition occurs at 218 °C (**Fig. 2A.4b**), characterized by a change from the crystalline structure to a nematic phase (Cr-N), indicative of the liquid crystalline nature of the compound. On further heating at 220 °C, the microphotograph captures the emergence of a schlieren texture (**Fig. 2A.4c**), signifying the presence of a well-defined nematic phase. Subsequently, a transition to the isotropic liquid (N-Iso) is observed (**Fig. 2A.4d**), showcasing a disordered molecular arrangement at 228 °C (**Fig. 2A.4e**). Intriguingly, upon cooling, the nematic droplets begin to form at 226 °C (**Fig. 2A.4f**), indicative of the persistence of liquid crystalline behaviour even during cooling processes. These nematic droplets subsequently coalesce (**Fig. 2A.4g**), and at 224 °C, the schlieren texture reappears (**Fig. 2A.4h**) as the temperature decrease continues. Finally, at 199 °C, a N-Cr transition occurred (**Fig. 2A.4i**), completing the cycle of transitions.

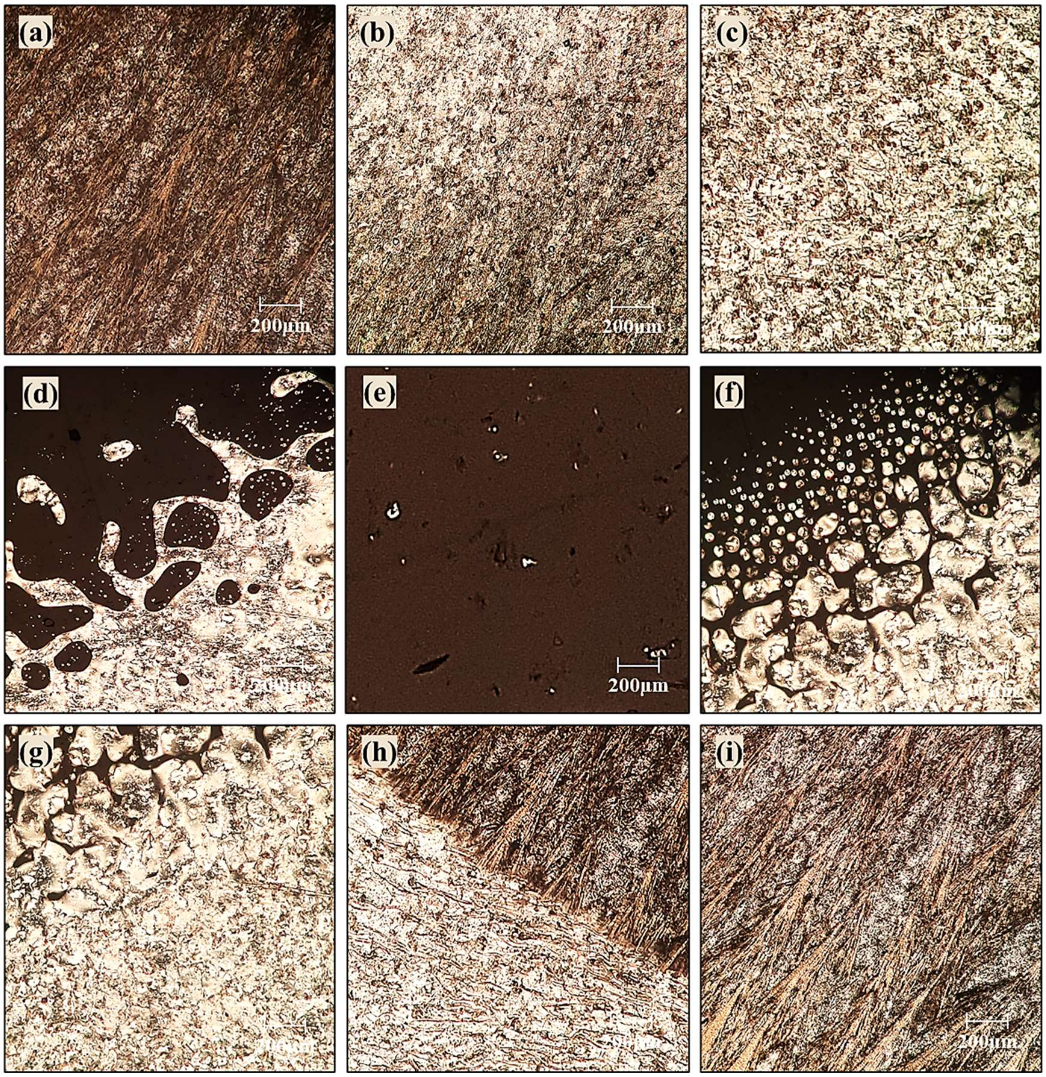

Fig. 2A.5: Optical microphotograph of *II*-4 (a) Crystalline solid (b) Cr-N transition at 205 °C on heating (c) Schlieren texture of nematic phase at 207 °C (d) N-Iso transition 234 °C (e) Isotropic liquid at 236 °C (f) On cooling, Nematic droplets at 233 °C (g) Schlieren Texture at 232 °C (h) N-Cr transition at 202 °C (i) Crystalline state at 200 °C

The optical microphotographs of ***II*-4** show same mesogenic behaviour as of ***I*-4** Initially observed as a crystalline solid (**Fig. 2A.5a**), upon heating, it exhibits a Cr-N transition at 205 °C (**Fig. 2A.5b**). This transition becomes evident through the emergence of a schlieren texture at 207 °C (**Fig. 2A.5c**), indicative of the formation of the nematic phase characterized by aligned yet disordered molecular arrangement. Further heating leads to the N-Iso transition, transforming the material into an isotropic liquid state at 234 °C (**Fig. 2A.5d, e**). Upon cooling, the formation of nematic droplets at 233 °C (**Fig. 2A.5f**), which subsequently coalesce to restore the schlieren texture at 232 °C (**Fig. 2A.5g**). Eventually, the ***II*-4** undergoes an N-Cr transition at 202 °C (**Fig. 2A.5h, i**).

2A.3.3.3 Structure-property relationship

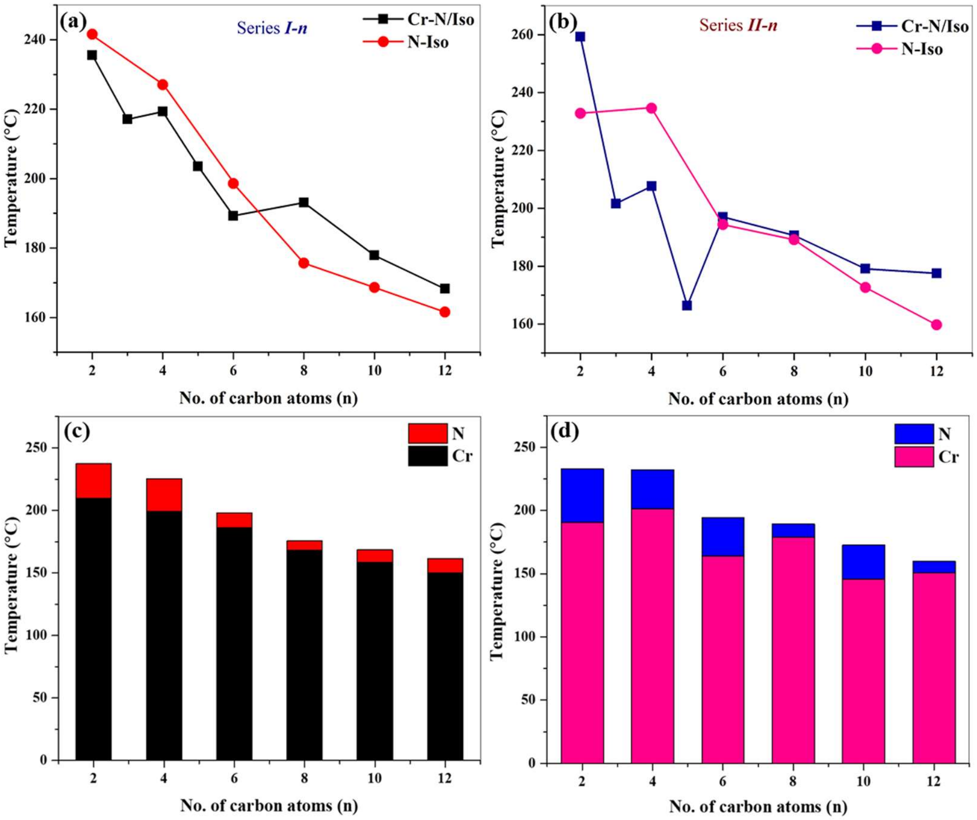

Fig. 2A.6: Line graph of (a) *I*-n and (b) *II*-n showing the relationship between the flexible spacer and transition temperatures. Bar graph of (c) *I*-n and (d) *II*-n showing nematic mesophase stability of the prepared dimers in the cooling cycle

The azo dimers, ***I*-n** and azomethine dimers, ***II*-n**, with varying carbon atom counts (n=2,4,6,8,10,12), exhibit distinct mesophases characterized by their nematic behaviour. This unique property is accompanied by a substantial mesophase range and the presence of both monotropic and enantiotropic mesophases. Interestingly, ***I*-n** and ***II*-n** dimers with odd carbon atoms (n=3 and 5) do not display mesogenic properties.

Fig. 2A.6 illustrates the correlation between the flexible spacer and transition temperature, along with the nematic mesophase length. The graphical representation includes both a line graph and a bar graph depicting the relationships for ***I*-n** and ***II*-n**. The mesogenic nature of the even-membered dimers (n=2,4,6,8,10,12) can be attributed to their planar geometry, while the odd-membered dimers (n=3,5) possess a somewhat bent structure. This structural distinction likely contributes to the mesophase disparity. Furthermore, enhanced thermal stability characterizes the even-membered dimers, in contrast to the odd-membered dimers. The occurrence of enantiotropic mesophase is limited to ***II*-4** among the dimers of series ***II***, which is may be due to weaker intermolecular forces in the molecules. Notably, the higher members (n=8, 10, 12) of both series display a monotropic nematic mesophase. With increasing chain length, two opposing factors come into play: a reduction in terminal attractions and increased molecular polarizability, which resists interlayer sliding. Dimers with flexible spacer chains with octyl, decyl, and dodecyl lack the structural resilience to endure thermal vibrations, leading to sharp melting at their melting points without transitioning to the liquid crystal state in both the series ***I*** and ***II***. The symmetrical dimer containing an azomethine group (***II*-n**) with a naphthalene moiety demonstrates an exclusive monotropic nematic mesophase, characterized by a significantly greater mesophase length when compared to azo dimers (***I*-n**).

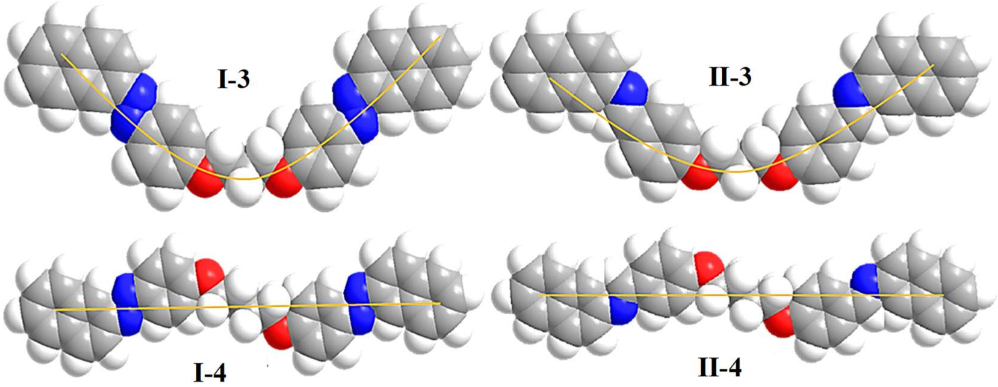

Fig. 2A.7: Energy-minimized Space-filling model (MM2 models derived from ChemBio 3D Ultra 14.0 software) structures of dimers showing the effect of flexible spacer

It was observed from the molecular shape of dimers in the all-trans conformation presented by energy minimized space-filling model (**Fig. 2A.7**) (MM2 models derived from ChemBio 3D Ultra 14.0 software) that the odd membered dimers (n=3,5) are somewhat bent, whereas the even membered dimers (n=2,4,6,8,10,12) are linear. The mesogenic nature of the even-membered dimers (n=2,4,6,8,10,12) can be attributed to their linear geometry. This structural distinction likely contributes to the mesophase disparity.

Table 2A.3 presents an outline of transition temperatures (in °C) and comparative geometry data, contrasting the ***II*-n** series with a closely related series with comparable structures[34].

Table 2A.3: Comparison of transition temperatures (°C) of present series II-n and structurally related series A[34,39]

No. of C in chain (n)	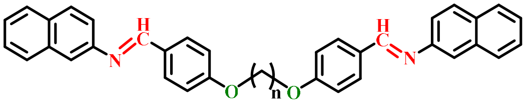 **Series *II-n***		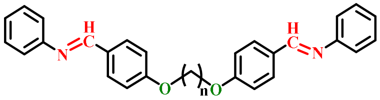 **Series A (0.O*n*O.0)** [39]	
	Transition Temperatures (°C)			
	$T_{Cr\text{-}I}$	$T_{N\text{-}I}$	$T_{Cr\text{-}I}$	$T_{N\text{-}I}$
2	259.22	232.81	189	-
3	201.61	-	133	-
4	234.60	232.06	189	(116)
5	166.34	-	115	-
6	196.99	(194.34)	166	-
8	190.61	(189.12)	160	-
10	179.09	(172.64)	154	-
12	177.52	(159.74)	150	-

N, Nematic; Iso, Isotropic liquid; Cr, Crystalline solid; (_) denotes a monotropic transition; (-) *Transition not exist.*

Dimers within Series A[39] have been reported predominantly as non-mesogenic, with the exception of the dimer featuring a tetramethylene spacer (n=4), which exhibits monotropic behaviour. In contrast, the dimers in our present ***II-n*** series display both enantiotropic (n=2,4) and monotropic (n=6,8,10,12) mesogenic behaviour. Specifically, within our present series, ***II-4*** demonstrates enantiotropic mesophase behaviour whereas the 0.O4O.0 of series A shows monotropic behaviour. From Table 2A.3, it is evident that the dimers in our current series exhibit higher thermal as well as mesophase stability compared to those in series A. The key distinguishing factor between ***II-n*** series and series A lies in their aromatic core composition. While ***II-n*** incorporates a naphthalene moiety, series A includes just a single phenyl ring at the terminal end. This variance results in an elongation of the molecular structure and an increase in polarizability. This elongation and increased polarizability collectively contribute to increased thermal stability and mesophase stability within our present series. In summary, the incorporation of a naphthalene moiety into our dimeric structures imparts mesogenic properties, characterized by an extended mesophase range and improved thermal stability.

For both series of dimers in our present work, the nematic-isotropic enthalpies are small for even-membered dimers. Similar and indeed lower values of enthalpies were found for the corresponding pyrene-based dimers.[40–42] The low values presumably reflect the biaxiality of the mesogenic units that is enhanced by the naphthalene units in these dimers as described by Donaldson et al.[43]

2A.3.4. TGA studies

The thermal stability investigation of the homologous series ***I*-n** and ***II*-n** was carried out using thermogravimetric analysis (TGA). Illustrated in **Fig. 2A.8** are the representative TG curves for ***I*-6,12** and ***II*-6,12** dimers as an example. As depicted in **Fig. 2A.8**, the thermal decomposition took place within the temperature range of 420–460 °C, with onset temperatures of 336 °C and 321 °C for ***I*-6** and ***I*-12**, respectively. The points of maximum degradation rate (T_{max}) were observed at 449.8 °C and 450.2 °C for ***I*-6** and ***I*-12**, correspondingly. Furthermore, even at temperatures as high as 600 °C, the degradation process remained incomplete, yielding residual quantities ranging from 26.9% to 4.45%. This outcome aligns with existing research suggesting that the degradation of azo-based materials predominantly involves azo bond cleavage through reductive mechanisms. These findings collectively underscore the remarkable thermal stability of the dimers under study, particularly up to 450 °C. For the ***II***-n series, thermal decomposition manifested in the temperature span of 300-320 °C, commencing at 304°C and 319°C for ***II*-6** and ***II*-12**, respectively.

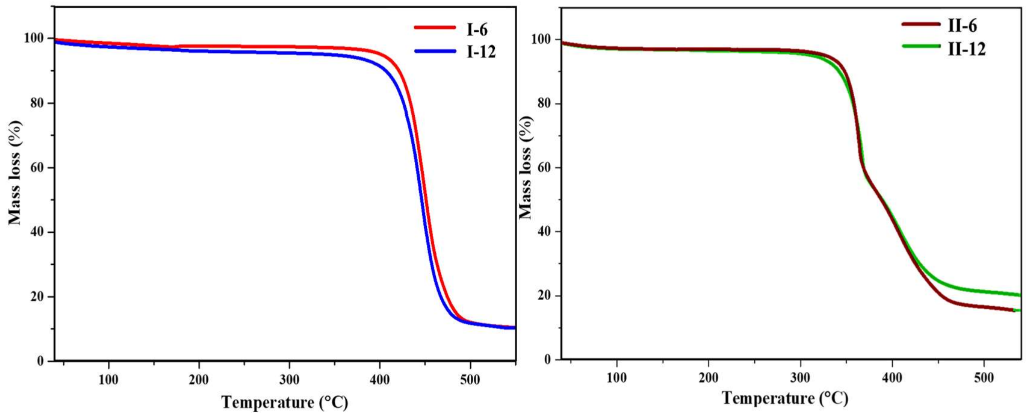

Fig. 2A.8: TG curve for prepared dimers (a) *I*-6,12 and (b) *II*-6,12

The temperatures of maximum degradation rate (Tmax) were noted as 366.8°C and 369.5°C for ***II*-6** and ***II*-12**, respectively. Similar to the ***I*-n** series, incomplete degradation was evident up to 600°C for ***II***-n compounds, resulting in residual levels spanning from 6.9% to 6.45%.

2A.3.5. Computational Studies

DFT theoretical calculations are required to comprehend the molecular approaches, predicted optimized structures, and vibrational frequencies The theoretical calculations for the proposed compounds were carried out by Gaussian 09 software and performed using the DFT/B3LYP method with 6–31 G (d,p) basis set[45] was selected for the calculations. We optimized the energy of conformations until they found a minimum-energy geometrical structure and then used that structure to calculate frequencies and thermodynamic properties. **Fig. 2A.9** shows the optimized molecular structures of the compounds.

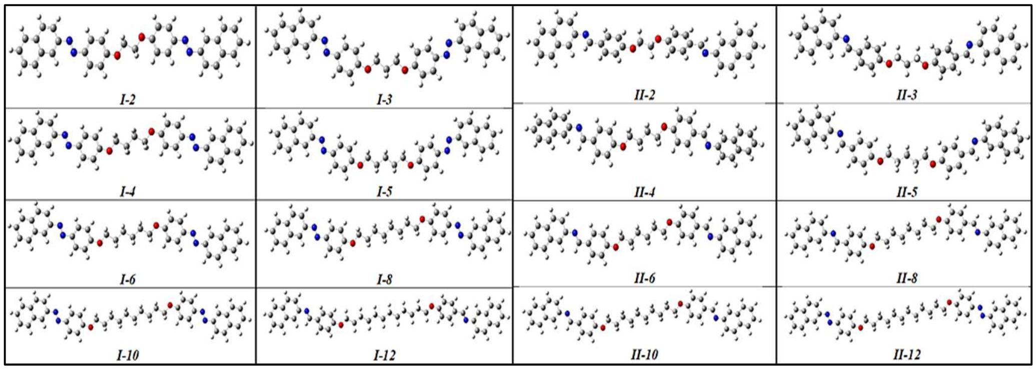

Fig. 2A.9: Optimized molecular structures of all the prepared dimers of both Series *I-n* and *II-n*

2A.3.5.1 Vibrational studies

Fig. 2A.10 displays the experimental FT-IR spectrum of ***I*-4** and ***II*-4** respectively, in the solid state, along with a comparison to the corresponding theoretical spectrum predicted in the gas phase using the B3LYP/6-31G method. The spectra exhibit a reasonable correlation, although some notable differences can be attributed to the absence of crystalline packing interactions in the gas phase calculations.

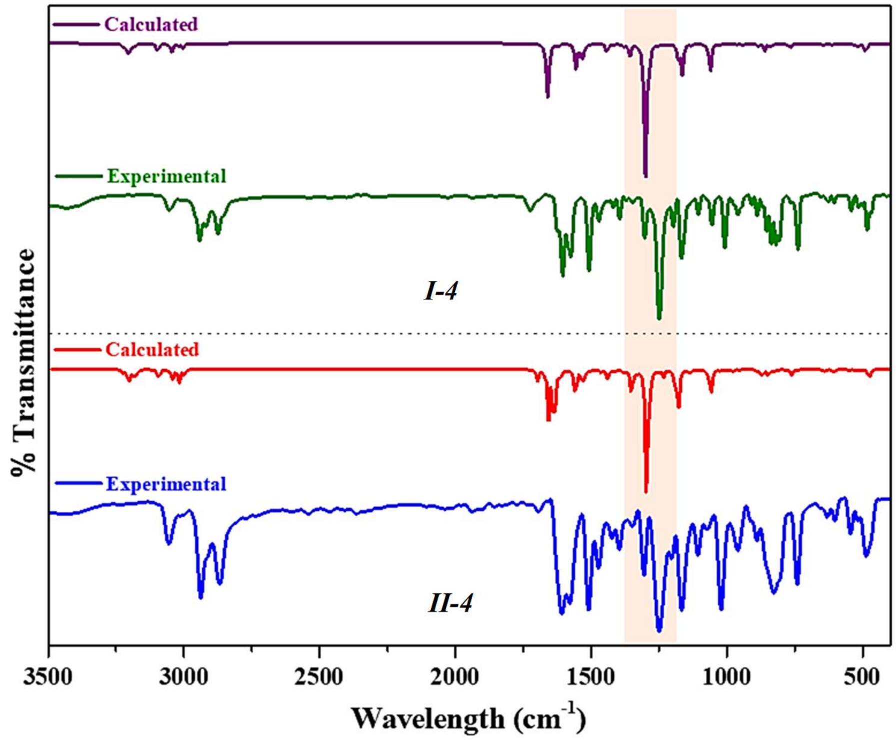

Fig. 2A.10: Theoretical and Experimental infrared spectrum of dimers *I*-4 and *II*-4 predicted by using B3LYP/6-31G level of theory

Assignments of Bands:

4000-2000 cm^{-1} Region: This spectral region typically corresponds to stretching modes of C-H and CH_3 groups present in ***I*-4**. C-H stretching vibrations of aromatic rings were found in the region of 3000–2800 cm^{-1}. In ***I*-4**, the calculated CH stretching modes are predicted between 3111 and 3027 cm^{-1}. Hence, the group of bands between 3188 and 3025 cm^{-1} and the weak IR band at 2897 cm^{-1} can be assigned to these vibration modes. The absorption bands between 3025 and 2897 cm^{-1} are attributed to the antisymmetric and symmetric stretching modes of CH_2 groups belonging to the flexible spacer. All of these bands are common for ***II*-n**.

2000-1000 cm^{-1} Region: This region is characterized by the presence of N=N, C-O, C=C, C-C, and C-N stretching modes, as well as deformation and rocking modes of CH and CH_3 groups, and certain deformations of aromatic rings in ***I*-4**. Here, the C-O stretching mode is predicted to be a strong band at 1290 cm^{-1}, which corresponds to the strong IR band at 1250 cm^{-1}. The N=N stretching mode, attributed to the azo group, is predicted at 1650 cm^{-1}, it is assigned to the medium-intensity IR bands at 1620 cm^{-1}. The series of IR bands observed at 1568, 1532, 1405, 1365, 1285, and 1210 cm^{-1} can be confidently assigned to the C=C and C-C stretching modes of phenyl and naphthyl rings. Some bands in the 1300–1000 cm^{-1} range correspond to C–H in-plane bending vibrations. All of these bands are common for ***II*-n**, except N=N. Instead of azo linkages they possess azomethine linkages, which are expected to give a strong band at 1690 cm^{-1}. Experimental spectra showed the band around 1655 cm^{-1}.

1000-400 cm^{-1} Region: In this region, various vibrations are expected, including C-C and C-N stretching modes, C-H out-of-plane deformations, deformations, wagging, and twisting modes of the C-O group, as well as twisting CH_3 and deformations and torsion modes of both phenyl and naphthyl rings in ***I*-4**. The out-of-plane CH deformations are predicted and assigned between 1100 and 600 cm^{-1}.

2A.3.5.2. Frontier molecular orbitals (FMOs) and Molecular electrostatic potential (MEP)

DFT studies on Both the series involve computational analysis of its electronic structure, molecular properties, vibrational modes, and reactivity. These studies complement experimental data, providing valuable insights into the compound's behaviour and potential applications.

Alterations in electron density are most effectively depicted using contours of electrostatic potential[46]. This graphical representation portrays the distribution of charges through a gradient of colours, elucidating the areas accountable for attractive and repulsive forces arising from interactions. The elongation of wavelength results from an inversely proportional shift in electrostatic potential (ESP), encompassing isodensity values ranging from -2.662e-2 to 2.662e-2 eV, as depicted in **Fig. 2A.11**. Blue segments indicate regions of reactivity, characterized by high polarization due to electron deficiency, while red segments signify less reactivity, marked by elevated electron densities and reduced polarization due to intramolecular bond formation. Notably, the augmentation of atomic sites corresponds to extensive changes in the blue regions, whereas green regions represent neutrally charged areas. **Fig. 2A.11** displays the electrostatic potential (ESP) contours of the dimers ***I*-n** and ***II*-n**, as predicted using the B3LYP/6-31G level of theory.

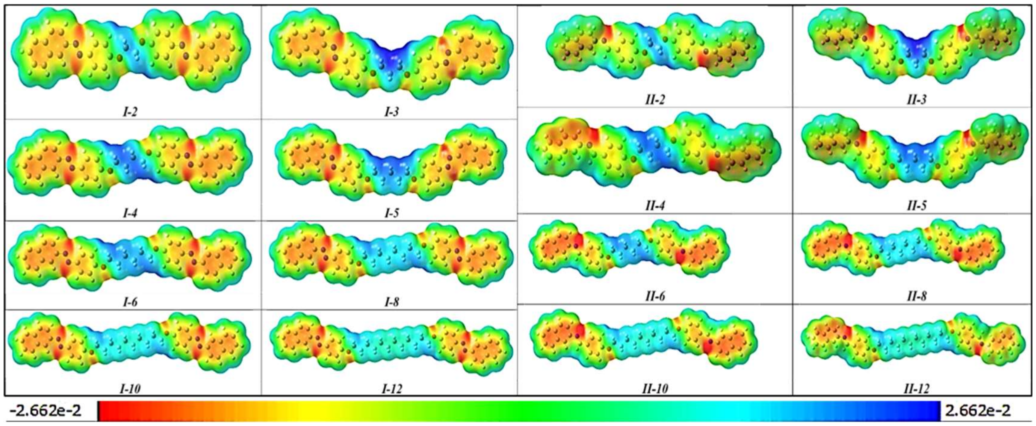

Fig. 2A.11: ESP contours of the dimers *I*-n and *II*-n predicted by using B3LYP/6-31G level of theory

The electronic properties such as HOMO (Highest Occupied Molecular Orbital) and LUMO (Lowest Unoccupied Molecular Orbital) energy levels, dipole moment, and thermodynamic properties such as enthalpy and entropy were calculated for the optimised geometries. The frontier molecular orbitals (FMOs) were analysed to predict the chemical reactivity and stability of the compounds.

In liquid crystals, the electronic structure, characterized by HOMO and LUMO energy levels, influences molecular stability and interactions. Ionization Potential (I) reflects the ease of electron removal, while Electron Affinity (A) measures the tendency to gain an electron, affecting charge distribution and intermolecular interactions. The Energy Gap (ΔE) determines electronic transitions' ease, impacting optical and electrical properties. Global Hardness (δ) and Softness (χ) relate to stability and reactivity, shaping responses to external stimuli. Chemical Reactivity (ω) and Electrophilicity Index influence compound reactivity and transformation under different conditions in liquid crystals.

Table 2A.4: Quantum mechanical descriptors of the dimers calculated using B3LYP/6-31G level of theory

Dimer	*HOMO*	*LUMO*	*I* (eV)	*A* (eV)	*ΔE* (eV)	*η*	*δ*	*χ*	*ω*
***I*-2**	-0.207	-0.081	5.622	2.214	3.408	1.704	0.587	3.918	4.505
***I*-3**	-0.206	-0.080	5.606	2.187	3.419	1.710	0.585	3.896	4.440
***I*-4**	-0.205	-0.079	5.581	2.161	3.420	1.710	0.585	3.871	4.382
***I*-5**	-0.205	-0.079	5.566	2.147	3.418	1.709	0.585	3.856	4.351
***I*-6**	-0.204	-0.078	5.551	2.133	3.418	1.709	0.585	3.842	4.319
***I*-8**	-0.203	-0.078	5.534	2.117	3.417	1.708	0.585	3.825	4.283
***I*-10**	-0.203	-0.077	5.523	2.107	3.416	1.708	0.585	3.815	4.261
***I*-12**	-0.203	-0.077	5.516	2.101	3.415	1.708	0.586	3.808	4.247
***II*-2**	-0.203	-0.057	5.517	1.546	3.971	1.985	0.504	3.531	3.140
***II*-3**	-0.202	-0.056	5.501	1.535	3.966	1.983	0.504	3.518	3.120
***II*-4**	-0.201	-0.056	5.48	1.533	3.948	1.974	0.507	3.506	3.114
***II*-5**	-0.201	-0.056	5.468	1.522	3.945	1.973	0.507	3.495	3.096
***II*-6**	-0.199	-0.056	5.419	1.527	3.892	1.946	0.514	3.473	3.098
***II*-8**	-0.199	-0.061	5.403	1.666	3.736	1.868	0.535	3.534	3.344
***II*-10**	-0.198	-0.061	5.392	1.657	3.736	1.868	0.535	3.525	3.325
***II*-12**	-0.199	-0.063	5.426	1.716	3.711	1.855	0.539	3.571	3.437

I, Ionization Potential; *A*, Electron Affinity; *ΔE*, Energy gap; *η*, Global hardness; *δ*, Global softness; *χ*, Chemical reactivity; *ω*, Electrophilicity index

The quantum mechanical descriptors presented in **Table 2A.4** offer a visual representation of alterations in electron density through Frontier Molecular Orbital (FMO) Contours, as depicted in **Fig. 2A.12.** The energy values provided in **Fig. 2A.12** correspond to the Highest Occupied Molecular Orbital energy (E_{HOMO}), Lowest Unoccupied Molecular Orbital energy (E_{LUMO}), and the energy difference (ΔE), all expressed in atomic units (a.u.), where 1 atomic unit equals 27.2114 electronvolts (eV). For instance, a change of (ΔE = 0.12 a.u.) equates to (0.12 * 27.2114 eV = 3.40 eV).

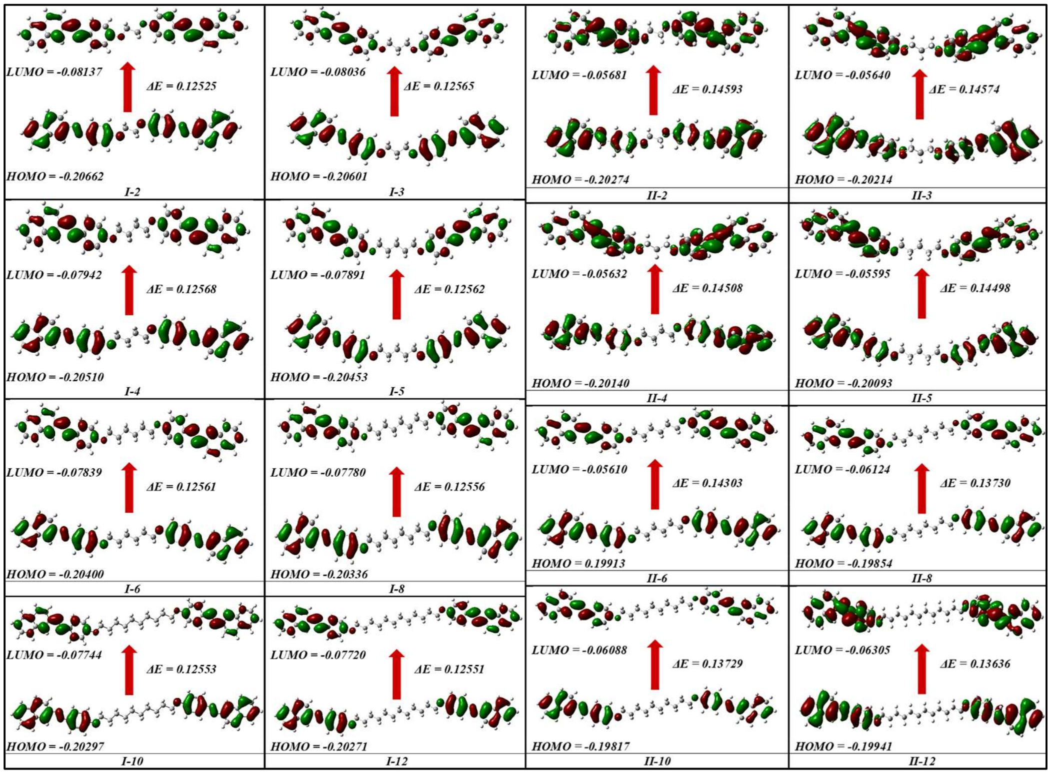

Fig. 2A.12: FMOs of the dimers *I*-n and *II*-n calculated by using B3LYP/6-31G level of theory

Table 2A.5 outlines the optical properties and dimensional parameters of two series of dimers (Series ***I*** and Series ***II***). Key characteristics include dipole moment, polarizability, length (L), width (D), aspect ratio (L/D), and mesophase range (ΔT) in degrees Celsius. As we can see from table, the dipole moment is cancelled out due to the symmetric distribution of charges, resulting in a net dipole moment of zero. The polarizability of a molecule tends to increase as the number of carbons in a flexible spacer increases. This is often attributed to the larger size and increased electron cloud of longer carbon chains. Dimers of both series show the same trend which is expected. The aspect ratio is a valuable parameter in understanding the shape of the molecule. A higher aspect ratio indicates a more elongated or rod-like structure, while a lower aspect ratio suggests a more compact or bent structure. Molecules with a higher aspect ratio, indicating a more rod-like shape, are associated with nematic mesophases, where the molecules are aligned in a common direction but with no specific positional order. Generally, higher aspect ratios might lead to a more temperature-sensitive mesophase transition. The elongated shape of molecules can make them more responsive to temperature changes.

Table 2A.5 Optical properties and dimensional parameters of the dimers

Dimer	*Dipole Moment μ (debye)*	*Polarizability α (a.u.)*	*Length (L) Å*	*Width (D) Å*	*Aspect ratio (L/D)*	*Mesophase range (ΔT) °C*
			Series *I*			
***I*-2**	0.000	529.101	30.353	5.559	5.460	27.59
***I*-3**	0.000	538.056	30.858	7.779	3.966	-
***I*-4**	0.000	550.466	31.984	5.560	5.752	26.37
***I*-5**	0.000	560.158	33.399	7.781	4.292	-
***I*-6**	0.000	572.139	35.364	5.560	6.360	11.50
***I*-8**	0.000	594.252	37.883	5.561	6.812	7.36
***I*-10**	0.000	616.602	40.408	5.560	7.267	10.27
***I*-12**	0.000	639.098	42.936	5.561	7.720	11.43
			Series *II*			
***II*-2**	0.000	495.894	30.607	5.565	5.350	42.32
***II*-3**	0.000	505.302	30.858	7.603	3.941	-
***II*-4**	0.000	517.683	31.984	6.007	5.367	30.57
***II*-5**	0.000	527.730	33.399	7.712	4.356	-
***II*-6**	0.000	560.649	35.364	6.321	5.498	30.36
***II*-8**	0.000	582.866	37.883	6.547	5.686	10.22
***II*-10**	0.000	605.293	40.408	6.708	5.919	27.16
***II*-12**	0.000	607.185	42.936	6.823	6.186	8.96

2A.3.6. Photochromic behaviour

Photoisomerization is commonly initiated by the π-π* transition, leading to the inter-conversion between cis *(Z)* and trans *(E)* isomers, a characteristic that renders azobenzene a dynamic substance. For applications in optical data storage, it is preferable to have a prolonged thermal back relaxation time, allowing for extended processing and storage of information. In this study, photoisomerization was investigated using a dual-beam spectrophotometer with a 1 cm quartz cuvette equipped with a 365 nm filter. The experiments demonstrated a clear correlation between the UV-Visible spectra of trans *(E)* and cis *(Z)* isomers of ***I*-4**.

In **Fig. 2A.13(a)**, the UV-Visible spectra for ***I*-4** with varying UV exposure times are presented. UV illumination times are indicated, with 0 seconds representing no UV exposure and an intensity of 5 mW cm^{-2}. The absorption maxima at 360 nm decreases, followed by a slight increase in absorbance at longer (450 nm) wavelength.

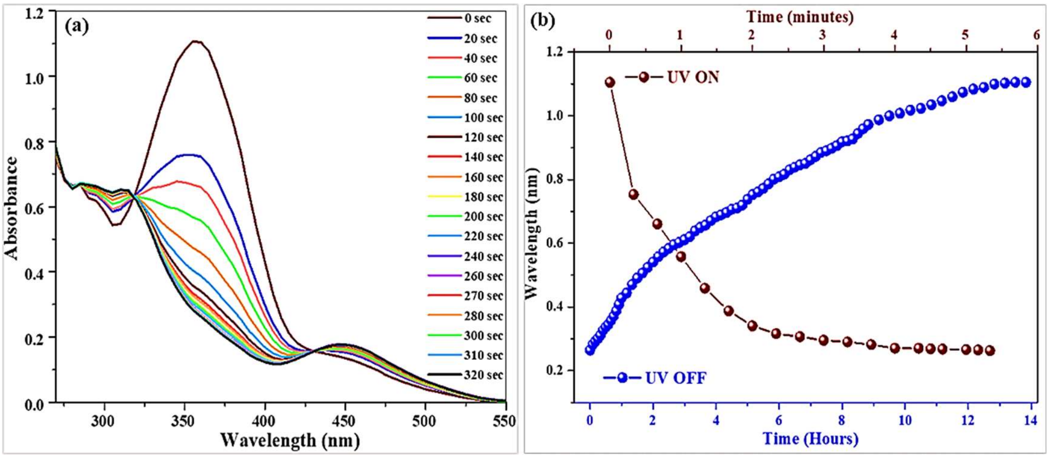

Fig. 2A.13: Absorption spectra for *I*-4 (a) with various UV exposure times and a 365 nm filter (b) Plot as a function of time during UV illumination (*E*-*Z*) and thermal back relaxation from photo stationary state (*Z*-*E*)

The photo conversion efficiency (CE) of the E-Z photoisomerization process was determined using the equation [$\boldsymbol{CE}$= ($A_{t_0} - A_{t_\infty}/A_{t_0}$)*100%]. Approximately 4.5 minutes were required to reach a photo saturation state due to the photoisomeric equilibrium of the E-Z form of the compound, where A_{t_∞} represents absorbance after UV exposure (0.26266) and A_{t_0} represents absorbance before UV exposure (1.10509). The calculated photo conversion efficiency (CE) of ***I*-4** was found to be 76.23%, indicating a relatively high efficiency. The thermodynamic instability of the Z isomer was observed, attributed to steric crowding and susceptibility to thermal back relaxation to its E isomer after reaching a photo saturation state. The Photoisomerization process of ***I*-4** as a function of recovery time is as shown in **Fig. 2A.13(b),** it took about 12.1 hours to convert back to a stable *E* configuration. Once the compound reaches a photo saturation state, it is kept in the dark without external energy, and absorbance is measured until complete conversion to the E form. Two isosbestic points indicate the absence of any side reactions. In the photo saturation state, a dynamic equilibrium is established between the *E* and *Z* isomers, influenced by factors such as light wavelength and intensity, temperature, and the specific molecular structure of the azo compound.

2A.4 Conclusion

Two new series of symmetric liquid crystal dimers of general formula ***I*-n** and ***II*-n** (n = 2–6,8,10,12) possessing azobenzene and azomethine moieties have been synthesised. The effect of the length and structure of the mesogenic units and the nature of the spacer have been studied in sixteen symmetrical dimers. All the naphthalene-based symmetrical dimers with an even number of flexible spacers (-methylene unit) are nematogenic. All the naphthalene-based symmetrical dimers with an odd number of atoms in the linking group joining two azobenzene and azomethine moieties are non-mesogenic due to the bent shape of the molecular structure. The dimers with azo-central linkages exhibited enantiotropic nematic mesophase while the dimers with azomethine central linkage exhibited monotropic nematic mesophase. The symmetrical azomethine (***II*-n**) dimer having naphthalene moiety exhibits purely nematic mesophase with greater nematic mesophase length compared to azo dimers. The photoisomerization study of ***I*-4** revealed a high photo conversion efficiency (CE) of 76.23%, with a notable thermodynamic instability observed in the *Z* isomer, leading to a prolonged recovery time of approximately 12.1 hours for its conversion back to a stable E configuration.

2A.5 Experimental Section

2A.5.1 Materials

All the starting materials and reagents were purchased from (S.R.L. Chemicals, Mumbai) and used without further purification. Solvents like acetone, ethyl acetate and petroleum ether (60-80) were de-moisturized and purified before use.

2A.5.2. Measurements

Thin-layer chromatography (TLC) was performed on aluminium sheets pre-coated with Kiesel 60F254 silica gel. A Bruker Alpha II spectrometer was used to acquire Fourier Transform Infrared Spectroscopy (FT-IR) spectra of compounds as potassium bromide (KBr) pellets. Using deuterated chloroform ($CDCl_3$) solvent and internal standard tetramethyl silane (TMS), proton and carbon nuclear magnetic resonance (^{1}H-NMR and ^{13}C-NMR) spectrum data were obtained on an Advance Bruker 400 spectrometer (400 MHz). Chemical shift is reported in parts per million (ppm) downfield from TMS and coupling constants (*J*) is reported in Hertz (Hz). Proton count multiplicities are reported as singlet (s), doublet (d), triplet (t), multiplet (m). Elemetar Analysensysteme, Unicube, was used for elemental analysis. The optical textures of various substances were examined using the Leica DM 2500P POM (Polarizing Optical Microscope). Thermograms were recorded on DSC-822, Mettler Toledo with Stare software. DSC measurements were investigated using aluminium pans and sample quantities of 2–3 mg. All measurements were taken in a nitrogen atmosphere at 30 mL min^{-1} with a heating rate of 10 °C min^{-1}. SYNAPT-XSHDBA064 TOF-MS in positive ion mode were used for Mass spectrometry. The SII EXSTAR6000 TG-DTA instrument was used to perform TG-DTA analyses. Using an aluminium pan and a heating rate of 10 °C min^{-1}, the experiments were conducted in a N_2 atmosphere between 30 °C and 550 °C. UV–Visible spectra were recorded on Agilent UV Cary 60 and Perkin Elmer Lambda-35 dual-beam spectrophotometer. The molecular properties in the current work are calculated with the help of the Gaussian 09 software using the DFT with method B3LYP, basis set 6-31 G (d, p), polarised, and diffuse functions. The geometrical optimization was carried out to minimize the energy of the system, and all calculations were done in their respective equilibrium geometry. Visualization of electronic properties with Gauss View in software is the gradient of colours of respective molecules.

2A.5.3 Synthesis and Characterization

2A.5.3.1 Synthesis of the (E)-4-(naphthalen-2-yldiazenyl)phenol (NpAzOH)

5.0 gm of Naphthalen-2-amine (0.0349 mol) was placed in a three-necked flask, immersed in an ice–water bath at 0 °C, followed by addition of concentrated hydrochloric acid (15 mL) in water (15 mL). 2.6 gm Sodium nitrite (0.038 mol) dissolved in minimum amount of water was added dropwise to the aqueous naphthalen-2-amine solution with dil. HCl. The mixture was kept stirring at 0 °C for 30 min, and a clear solution of the diazonium salt was obtained. Then a solution of phenol 3.28 gm (0.0349 mol) in 55 ml 10% NaOH was slowly added to the above mixture, an aqueous NaOH solution was used to adjust the pH value to 8–9. After the reaction, and the solution was let to stand for 2 h and then excessive hydrochloric acid was added to change the pH to 5. The precipitate was filtered and washed to neutral pH with water. Then it was recrystallised with 50 mL of anhydrous ethanol, and finally dried to obtain a reddish-brown solid. The final orange powder was used for the next reaction.

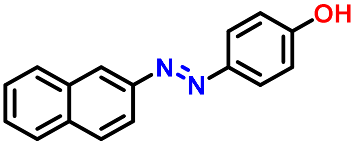

(*E*)-4-(naphthalen-2-yldiazenyl)phenol

Orange crystals, Yield: 83%; m.p.: 149 °C (reported 148 °C)^2; **IR** ν_{max}/cm^{-1}: 3052.41, 2926.93, 2853.42 (C_{sp3}**-H**), 1594.88 (-N=N-), 1496.89 ($C_{sp2\text{-aromatic}}$), 1246.79 (-C-O-), 1148.56 (-C-N-), 743.77; ***^{1}H NMR (400MHz, $CDCl_3$): δ (In ppm):*** 9.60 (s, 1 H, -OH), 8.43 (d, *J*=2Hz, 1H, Naph**-H**), 8.03 (d, *J*=9.2Hz, 1H, Naph**-H**), 7.97 (s, 1H, Naph**-H**), 7.94 (d, *J*=2.4Hz, 2H, Naph**-H**), 7.91 (d, *J*=8Hz, 2H, Ar**-H**), 7.57 (d, *J*=9.2Hz, 2H, Naph**-H**), 6.99 (d, *J*=8.8Hz, 2H, Ar**-H**)

2A.5.3.2 Synthesis of the (E)-4-((naphthalen-2-ylimino)methyl)phenol (NpAmOH)

The condensation reaction between naphthalen-2-amine and 4- hydroxybenzaldehyde results in Schiff base derivative. 5.0 gm Naphthalen-2-amine (0.0349 mol) and 4.29 gm 4-hydroxybenzaldehyde (0.0349 mol) were dissolved in 30 mL of absolute ethanol. A few drops of glacial acetic acid were added as a catalyst. The reaction mixture was refluxed for 5 h. After completion of reaction, the reaction mixture cooled at room temperature and precipitated red solid was filtered off and washed with ethanol and dried under vacuum. The final white powder was used for the next reaction.

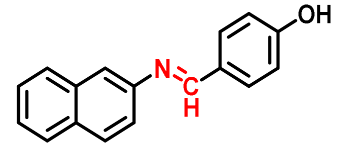

(*E*)-4-((naphthalen-2-ylimino)methyl)phenol

Off white crystals, Yield: 81%; m.p.: 160 °C (reported 159 °C); **IR** ν_{max}/cm^{-1}: 3052.41, 2926.93, 2853.42 (C_{sp3}-**H**), 1594.88 (-N=N-), 1496.89 ($C_{sp2-aromatic}$), 1246.79 (-C-O-), 1148.56 (-C-N-), 743.77; ***^{1}H NMR (400MHz, DMSO-d6): δ (In ppm):*** 10.02 (s, 1 H, -OH), 8.60 (s, 1H, -**CH**=N), 7.92 (d, *J*=9.2Hz, 1H, Naph-**H**), 7.89 (d, *J*=8.8Hz, 2H, Naph-**H**), 7.83 (d, *J*=8.4Hz, 2H, Naph-**H**), 7.65 (s, 1H, Naph-**H**), 7.50 (d, *J*=7.2Hz, 2H, Ar-**H**), 7.44 (d, *J*=6.8Hz, 1H, Naph-**H**), 6.91 (d, *J*=8.4Hz, 2H, Ar-**H**)

2A.5.3.3 Synthesis of the 1,ω-bis(4-((E)-naphthalen-2-yldiazenyl)phenoxy)alkane (I-n)

In a round bottom flask, *(E)*-4-(naphthalen-2-yldiazenyl)phenol (1.6 mmol), α,ω-dibromoalkane (0.69 mmol) and dry K_2CO_3 (1.9 mmol) in dry acetone (50 ml) was added, and the resulting solution was refluxed for 48 hours. After the completion of the reaction, the reaction mixture was filtered, and washed with acetone. The solvent was evaporated in the rotary evaporator and crude product was collected. The product was purified by column chromatography (petroleum ether 60–80 °C: ethyl acetate, 98: 2; v/v) over silica gel and the purity of the compound was performed by the TLC.

2A.5.3.4. Characterization of dimers I-n

1,2-bis(4-((E)-naphthalen-2-yldiazenyl)phenoxy)ethane (I-2):

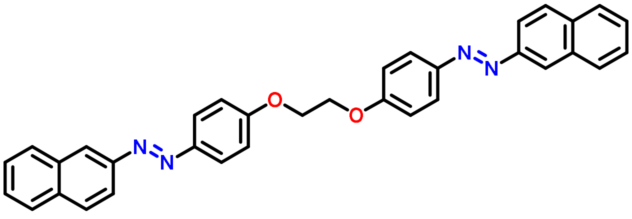

1,2-bis(4-((*E*)-naphthalen-2-yldiazenyl)phenoxy)ethane

Orange crystals, Yield: 59%; **IR** ν_{max}/cm^{-1}: 3052.41, 2926.93, 2853.42 (C_{sp3}-**H**), 1594.88 (-N=N-), 1496.89 ($C_{sp2-aromatic}$), 1246.79 (-C-O-), 1148.56 (-C-N-), 743.77; ***^{1}H NMR (400MHz, $CDCl_3$): δ (In ppm):*** 8.43 (s, 2H, Naph-**H** X 2), 8.09 (d, *J*=6Hz, 2H, Naph-**H** X 2) 8.07 (d, *J*=8.6Hz, 4H, Naph-**H** X 2), 8.03 (d, *J*=9.6Hz, 2H, Naph-**H** X 2), 7.93 (d, *J*=8.4Hz, 4H, Ar-**H** X 2), 7.57 (d, *J*=6.8Hz, 4H, Naph-**H** X 2), 7.10 (d, *J*=6.4Hz, 4H, Ar-**H** X 2), 4.32 (t, *J*=6 Hz, 4H, -O**CH**$_2$- X 2); ***^{13}C NMR (400MHz, CDCl$_3$): δ (In ppm):*** 160.94, 150.02, 146.56, 135.62, 133.11, 129.29, 128.24, 127.22, 126.90, 124.85, 117.25, 114.95, 68.73; **Elemental Analysis:** $C_{34}H_{26}N_4O_2$: (cal): C, 78.14; H, 5.01; N, 10.72; O, 6.12; found C, 78.10; H, 4.98; N, 10.70; O, 6.11; %;

1,3-bis(4-((E)-naphthalen-2-yldiazenyl)phenoxy)propane (I-3):

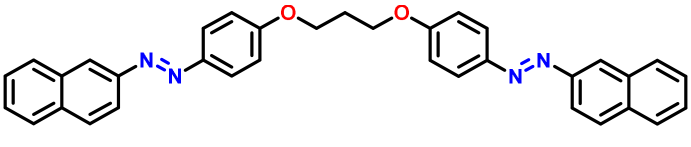

1,3-bis(4-((*E*)-naphthalen-2-yldiazenyl)phenoxy)propane

Orange crystals, Yield: 56%; **IR** ν_{max}/cm^{-1}: 3052.19, 2932.02, 2853.59 (C$_{sp3}$-**H**), 1596.77 (-N=N-), 1495.05 (C$_{sp2\text{-}aromatic}$), 1255.46 (-C-O-), 1140.96 (-C-N-), 741.96; ***^{1}H NMR (400MHz, CDCl$_3$): δ (In ppm):*** 8.43 (s, 2H, Naph-**H** X 2), 8.09 (d, *J*=6Hz, 2H, Naph-**H** X 2) 8.07 (d, *J*=8.6Hz, 4H, Naph-**H** X 2), 8.03 (d, *J*=9.6Hz, 2H, Naph-**H** X 2), 7.92 (d, *J*=8.4Hz, 4H, Ar-**H** X 2), 7.57 (d, *J*=6.8Hz, 4H, Naph-**H** X 2), 7.09 (d, *J*=6.4Hz, 4H, Ar-**H** X 2), 4.32 (t, *J*=6Hz, 4H, -O**CH**$_2$- X 2), 2.41-2.35 (m, 2H, -O-C-**CH**$_2$); ***^{13}C NMR (400MHz, CDCl$_3$): δ (In ppm):*** 160.66, 150.20, 146.52, 135.64, 133.61, 129.59, 127.95, 127.29, 126.52, 124.82, 117.22, 114.98, 68.07, 29.04; **Elemental Analysis:** $C_{35}H_{28}N_4O_2$: (cal): C, 78.34; H, 5.26; N, 10.44; O, 5.96; found C, 78.31; H, 5.23; N, 10.41; O, 5.94; %;

1,4-bis(4-((E)-naphthalen-2-yldiazenyl)phenoxy)butane (I-4):

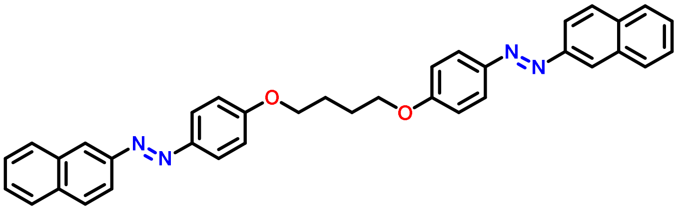

1,4-bis(4-((*E*)-naphthalen-2-yldiazenyl)phenoxy)butane

Orange crystals, Yield: 61%; **IR** ν_{max}/cm^{-1}: 3052.29, 2932.07, 2857.07 (C$_{sp3}$-**H**), 1596.78 (-N=N-), 1495.29 (C$_{sp2\text{-}aromatic}$), 1255.48 (-C-O-), 1140.94 (-C-N-), 742.00; ***^{1}H NMR (400MHz, CDCl$_3$): δ (In ppm):*** 8.43 (s, 2H, Naph-**H** X 2), 8.09 (d, *J*=6Hz, 2H, Naph-**H** X 2) 8.07 (d, *J*=8.6Hz, 4H, Naph-**H** X 2), 8.03 (d, *J*=9.6Hz, 2H, Naph-**H** X 2), 7.92 (d, *J*=8.4Hz, 4H, Ar-**H** X 2), 7.57 (d, *J*=6.8Hz, 4H, Naph-**H** X 2), 7.05 (d, *J*=6.4Hz, 4H, Ar-**H** X 2), 4.08 (t, *J*=6Hz, 4H, -O**CH**$_2$- X 2), 1.97-1.89 (m, 4H, -O-C-**CH**$_2$- X 2); ***^{13}C NMR (400MHz, CDCl$_3$): δ (In ppm):*** 161.08, 150.30, 147.27, 134.65, 133.57, 129.26, 128.04, 127.29, 126.68, 124.87, 117.29, 114.78, 68.32, 29.26; **Elemental Analysis:** $C_{36}H_{30}N_4O_2$: (cal): C, 78.52; H, 5.49; N, 10.17; O, 5.81; found C, 78.50; H, 5.46; N, 10.14; O, 5.78; %;

1,5-bis(4-((E)-naphthalen-2-yldiazenyl)phenoxy)pentane (I-5):

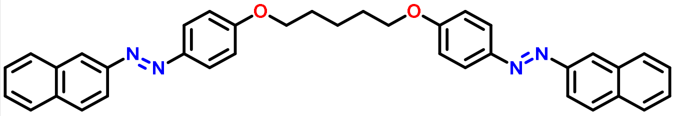

1,5-bis(4-((*E*)-naphthalen-2-yldiazenyl)phenoxy)pentane

Orange crystals, Yield: 59%; **IR** ν_{max}/cm^{-1}: 3054.05, 2940.66, 2859.12 (C_{sp3}-**H**), 1600.69 (-N=N-), 1497.59 ($C_{sp2\text{-}aromatic}$), 1250.21 (-C-O-), 1138.34 (-C-N-), 744.83; ^{1}***H NMR (400MHz, CDCl$_3$): δ (In ppm):*** 8.42 (s, 2H, Naph-**H** X 2), 8.08 (d, *J*=6Hz, 2H, Naph-**H** X 2) 8.06 (d, *J*=8.6Hz, 4H, Naph-**H** X 2), 8.02 (d, *J*=9.6Hz, 2H, Naph-**H** X 2), 7.92 (d, *J*=8.4Hz, 4H, Ar-**H** X 2), 7.57 (d, *J*=6.8Hz, 4H, Naph-**H** X 2), 7.06 (d, *J*=6.4Hz, 4H, Ar-**H** X 2), 4.13 (t, *J*=6Hz, 4H, -O**CH$_2$**- X 2), 1.98-1.91 (m, 4H, -O-C-**CH$_2$**- X 2), 1.69-1.65 (m, , 2H, -O-C-C -**CH$_2$**); ^{13}***C NMR (400MHz, CDCl$_3$): δ (In ppm):*** 161.01, 150.36, 147.32, 134.54, 133.60, 129.28, 127.95, 127.22, 126.67, 124.80, 117.57, 114.60, 68.78, 31.91, 29.27; **Elemental Analysis:** $C_{37}H_{32}N_4O_2$: (cal): C, 78.70; H, 5.71; N, 9.92; O, 5.67; found C, 78.69; H, 5.68; N, 9.90; O, 5.65; %;

1,6-bis(4-((E)-naphthalen-2-yldiazenyl)phenoxy)hexane (I-6):

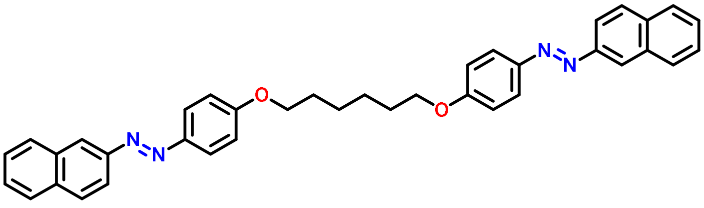

1,6-bis(4-((*E*)-naphthalen-2-yldiazenyl)phenoxy)hexane

Orange crystals, Yield: 55%; **IR** ν_{max}/cm^{-1}: 3050.12, 2940.10, 2854.21 (C_{sp3}-**H**), 1600.62 (-N=N-), 1497.22 ($C_{sp2\text{-}aromatic}$), 1251.30 (-C-O-), 1141.60 (-C-N-), 741.30; ^{1}***H NMR (400MHz, CDCl$_3$): δ (In ppm):*** 8.41 (s, 2H, Naph-**H** X 2), 8.08 (d, *J*=6Hz, 2H, Naph-**H** X 2) 8.06 (d, *J*=8.6Hz, 4H, Naph-**H** X 2), 8.02 (d, *J*=9.6Hz, 2H, Naph-**H** X 2), 7.93 (d, *J*=8.4Hz, 4H, Ar-**H** X 2), 7.57 (d, *J*=6.8Hz, 4H, Naph-**H** X 2), 7.06 (d, *J*=6.4Hz, 4H, Ar-**H** X 2), 4.13 (t, *J*=6Hz, 4H, -O**CH$_2$**- X 2), 2.00-1.93 (m, 4H, -O-C-**CH$_2$**- X 2), 1.77-1.69 (m, , 4H, -O-C-C -**CH$_2$**- X 2); ^{13}***C NMR (400MHz, CDCl$_3$): δ (In ppm):*** 161.17, 150.33, 147.08, 134.42, 133.65, 129.27, 127.99, 127.28, 126.67, 124.85, 117.21, 114.72, 68.11, 31.02, 29.48; **Elemental Analysis:** $C_{38}H_{34}N_4O_2$: (cal): C, 78.87; H, 5.92; N, 9.68; O, 5.53; found C, 78.84; H, 5.90; N, 9.65; O, 5.51; %;

1,8-bis(4-((E)-naphthalen-2-yldiazenyl)phenoxy)octane (I-8):

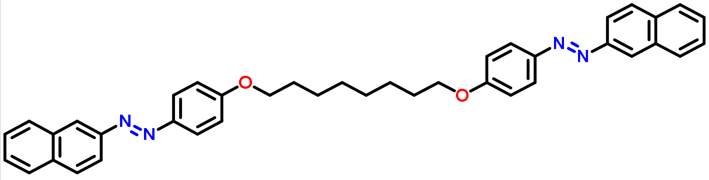

1,8-bis(4-((*E*)-naphthalen-2-yldiazenyl)phenoxy)octane

Orange crystals, Yield: 58%; **IR** ν_{max}/cm^{-1}: 3050.41, 2936.43, 2857.69 (C_{sp3}-**H**), 1599.93 (-N=N-), 1497.63 ($C_{sp2\text{-}aromatic}$), 1254.42 (-C-O-), 1141.77 (-C-N-), 741.45; ***^{1}H NMR (400MHz, CDCl$_3$): δ (In ppm):*** 8.42 (s, 2H, Naph-**H** X 2), 8.08 (d, *J*=6Hz, 2H, Naph-**H** X 2) 8.06 (d, *J*=8.6Hz, 4H, Naph-**H** X 2), 8.02 (d, *J*=9.6Hz, 2H, Naph-**H** X 2), 7.92 (d, *J*=8.4Hz, 4H, Ar-**H** X 2), 7.57 (d, *J*=6.8Hz, 4H, Naph-**H** X 2), 7.06 (d, *J*=6.4Hz, 4H, Ar-**H** X 2), 4.13 (t, *J*=6Hz, 4H, -O**CH$_2$**- X 2), 1.74 (m, 4H, -O-C-**CH$_2$**- X 2), 1.43 (m, , 4H, -O-C-C-**CH$_2$**- X 2), 1.30 (m, , 4H, -O-C-C-C-**CH$_2$**- X 2); ***^{13}C NMR (400MHz, CDCl$_3$): δ (In ppm):*** 161.29, 150.30, 147.04, 134.48, 133.65, 129.25, 127.90, 127.31, 126.61, 124.72, 117.30, 114.74, 68.93, 32.46, 31.04, 28.41; **Elemental Analysis:** $C_{40}H_{38}N_4O_2$: (cal): C, 79.18; H, 6.31; N, 9.23; O, 5.27; found C, 79.15; H, 6.29; N, 9.20; O, 5.23; %;

1,10-bis(4-((E)-naphthalen-2-yldiazenyl)phenoxy)decane (I-10):

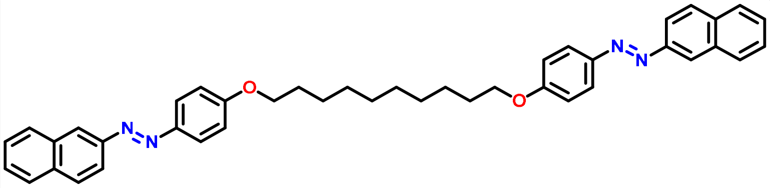

1,10-bis(4-((*E*)-naphthalen-2-yldiazenyl)phenoxy)decane

Orange crystals, Yield: 56%; **IR** ν_{max}/cm^{-1}: 3054.18, 2920.83, 2850.62 (C_{sp3}-**H**), 1605.63 (-N=N-), 1502.23 ($C_{sp2\text{-}aromatic}$), 1266.84 (-C-O-), 1141.69 (-C-N-), 747.24; ***^{1}H NMR (400MHz, CDCl$_3$): δ (In ppm):*** 8.93 (d, *J*=8.9Hz, 2H, Naph-**H** X 2), 8.74 (s, 2H, Naph-**H** X 2), 8.01 (d, *J*=8.6Hz, 4H, Naph-**H** X 2), 7.78 (d, *J*=8.8Hz, 4H, Ar-**H** X 2), 7.59 (d, *J*=7.6Hz, 4H, Naph-**H** X 2), 7.58 (d, *J*=6Hz, 2H, Naph-**H** X 2), 7.09 (d, *J*=8.8Hz, 4H, Ar-**H** X 2), 4.5 (t, *J*=7.2Hz, 4H, -O**CH$_2$**- X 2), 1.74 (m, 4H, -O-C-**CH$_2$**- X 2), 1.43 (m, , 4H, -O-C-C-**CH$_2$**- X 2), 1.30 (m, , 8H, -O-C-C-C-(**CH$_2$**)$_2$- X 2); ***^{13}C NMR (400MHz, CDCl$_3$): δ (In ppm):*** 161.34, 150.12, 147.15, 134.56, 133.71, 129.70, 127.94, 127.21, 126.60, 124.82, 117.23, 114.72, 68.19, 33.48, 31.07, 29.43, 27.86; **Elemental Analysis:** $C_{42}H_{42}N_4O_2$: (cal): C, 79.46; H, 6.67; N, 8.83; O, 5.04; found C, 79.42; H, 6.65; N, 8.80; O, 5.03; %;

1,12-bis(4-((E)-naphthalen-2-yldiazenyl)phenoxy)dodecane (I-12):

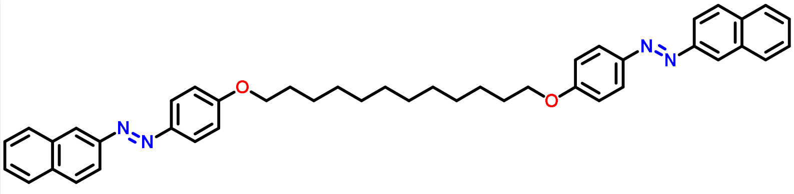

1,12-bis(4-((*E*)-naphthalen-2-yldiazenyl)phenoxy)dodecane

Orange crystals, Yield: 57%; **IR** ν_{max}/cm^{-1}: 3054.26, 2922.12, 2850.25 (C_{sp3}-**H**), 1604.95 (-N=N-), 1502.09 ($C_{sp2\text{-}aromatic}$), 1263.58 (-C-O-), 1141.19 (-C-N-), 746.87; ***^{1}H NMR (400MHz, $CDCl_3$): δ (In ppm):*** 8.93 (d, *J*=8.9Hz, 2H, Naph-**H** X 2), 8.74 (s, 2H, Naph-**H** X 2), 8.01 (d, *J*=8.6Hz, 4H, Naph-**H** X 2), 7.78 (d, *J*=8.8Hz, 4H, Ar-**H** X 2), 7.59 (d, *J*=7.6Hz, 4H, Naph-**H** X 2), 7.58 (d, *J*=6Hz, 2H, Naph-**H** X 2), 7.09 (d, *J*=8.8Hz, 4H, Ar-**H** X 2), 4.5 (t, *J*=7.2Hz, 4H, -O**CH_2**- X 2), 1.74 (m, 4H, -O-C-**CH_2**- X 2), 1.43 (m, , 4H, -O-C-C-**CH_2**- X 2), 1.30 (m, , 12H, -O-C-C-C-(**CH_2**)$_3$- X 2); ***^{13}C NMR (400MHz, $CDCl_3$): δ (In ppm):*** 161.70, 150.39, 146.95, 134.52, 133.61, 129.24, 127.93, 127.25, 126.66, 124.77, 117.33, 114.78, 68.38, 34.15, 32.87, 29.56, 29.23, 28.21; **Elemental Analysis:** $C_{44}H_{46}N_4O_2$: (cal): C, 79.73; H, 6.99; N, 8.45; O, 4.83; found C, 79.71; H, 6.95; N, 8.41; O, 4.82; %;

2A.5.3.5 Synthesis of the (1E,1'E)-1,1'-((alkane-1,ω-diylbis(oxy))bis(4,1-phenylene))bis(N-(naphthalen-2-yl)methanimine)(II-n)

In a round bottom flask (E)-4-((naphthalen-2-ylimino)methyl)phenol (1.6 mmol), α,ω-dibromoalkane (0.69 mmol) and dry K_2CO_3 (1.9 mmol) in dry acetone (50 ml) was added, and the resulting solution was refluxed for 48 hours. After the completion of reaction, the reaction mixture was filtered, washed with acetone and dried. The product was purified by repeated recrystallization from ethanol.

2A.5.3.6 Characterization of dimers II-n

(1E,1'E)-1,1'-((ethane-1,2-diylbis(oxy))bis(4,1-phenylene))bis(N-(naphthalen-2-yl)methanimine) (II-2):

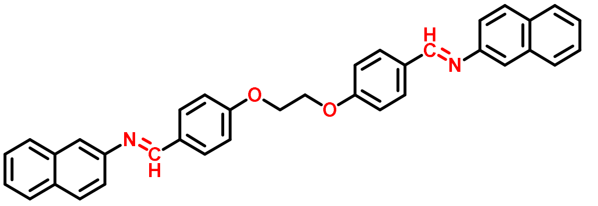

(1*E*,1'*E*)-1,1'-((ethane-1,2-diylbis(oxy))bis
(4,1-phenylene))bis(*N*-(naphthalen-2-yl)methanimine)

White solid, Yield: 59%; **IR** ν_{max}/cm^{-1}: 3053.88, 2942.87, 2852.61 (C_{sp3}-**H**), 1604.03 (-CH=N-), 1503.50 ($C_{sp2\text{-}aromatic}$), 1248.40 (-C-O-), 1161.29 (-C-N-), 745.28; ***^{1}H NMR (400MHz, CDCl$_3$): δ (In ppm):*** 8.54 (s, 1H, -**CH**=N- X 2), 7.92 (d, *J*=6Hz, 2H, Naph-**H** X 2), 7.90 (d, *J*=8.6Hz, 4H, Naph-**H** X 2), 7.87 (d, *J*=9.6Hz, 2H, Naph-**H** X 2), 7.60 (s, 2H, Naph-**H** X 2), 7.48 (d, *J*=8.4Hz, 4H, Ar-**H** X 2), 7.46 (d, *J*=6.8Hz, 4H, Naph-**H** X 2), 7.06 (d, *J*=6.4Hz, 4H, Ar-**H** X 2), 4.28 (t, *J*=6 Hz, 4H, -O**CH$_2$**- X 2); ***^{13}C NMR (400MHz, CDCl$_3$): δ (In ppm):*** 165.76, 161.64, 150.32, 147.00, 134.53, 133.47, 129.26, 127.92, 127.24, 126.65, 124.83, 117.32, 114.40, 67.93; **Elemental Analysis:** $C_{36}H_{28}N_2O_2$: (cal): C, 83.05; H, 5.42; N, 5.38; O, 6.15; found C, 83.02; H, 5.40; N, 5.35; O, 6.11; %;

(1E,1'E)-1,1'-((propane-1,3-diylbis(oxy))bis(4,1-phenylene))bis(N-(naphthalen-2-yl)methanimine) (II-3):

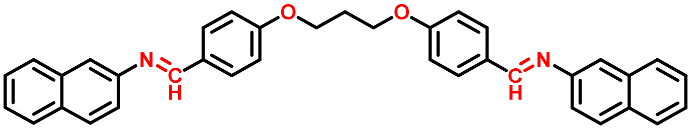

(1*E*,1'*E*)-1,1'-((propane-1,3-diylbis(oxy))bis
(4,1-phenylene))bis(*N*-(naphthalen-2-yl)methanimine)

White solid, Yield: 62%; **IR** ν_{max}/cm^{-1}: 3054.44, 2949.69, 2854.90 (C_{sp3}-**H**), 1609.24 (-CH=N-), 1510.36 ($C_{sp2\text{-}aromatic}$), 1251.41 (-C-O-), 1166.04 (-C-N-), 740.10; ***^{1}H NMR (400MHz, CDCl$_3$): δ (In ppm):*** 8.54 (s, 1H, -**CH**=N- X 2), 7.93 (d, *J*=6Hz, 2H, Naph-**H** X 2), 7.90 (d, *J*=8.6Hz, 4H, Naph-**H** X 2), 7.87 (d, *J*=9.6Hz, 2H, Naph-**H** X 2), 7.61 (s, 2H, Naph-**H** X 2), 7.48 (d, *J*=8.4Hz, 4H, Ar-**H** X 2), 7.46 (d, *J*=6.8Hz, 4H, Naph-**H** X 2), 7.05 (d, *J*=6.4Hz, 4H, Ar-**H** X 2), 4.28 (t, *J*=6 Hz, 4H, -O**CH$_2$**- X 2), 2.39-2.33 (m, 2H, -O-C-**CH$_2$**); ***^{13}C NMR (400MHz, CDCl$_3$): δ (In ppm):*** 165.76, 161.36, 150.31, 147.10, 134.41, 133.41, 129.33, 127.93, 127.29, 126.66, 124.79, 117.27, 114.84, 68.19, 29.49; **Elemental Analysis:** $C_{37}H_{30}N_2O_2$: (cal): C, 83.12; H, 5.66; N, 5.24; O, 5.98; found C, 83.10; H, 5.61; N, 5.22; O, 5.93; %;

(1E,1'E)-1,1'-((butane-1,4-diylbis(oxy))bis(4,1-phenylene))bis(N-(naphthalen-2-yl)methanimine) (II-4):

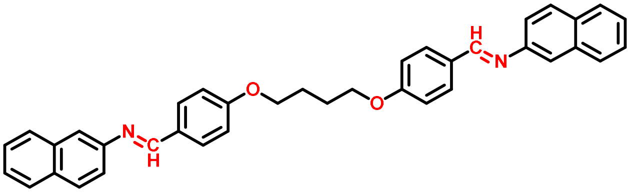

White solid, Yield: 60%; **IR** ν_{max}/cm^{-1}: 3055.77, 2945.05, 2857.35 (C_{sp3}-**H**), 1607.42 (-CH=N-), 1510.72 ($C_{sp2-aromatic}$), 1252.09 (-C-O-), 1170.75 (-C-N-), 740.95; ***^{1}H NMR (400MHz, CDCl$_3$): δ (In ppm):*** 8.53 (s, 1H, -**CH**=N- X 2), 7.92 (d, *J*=6Hz, 2H, Naph-**H** X 2), 7.90 (d, *J*=8.6Hz, 4H, Naph-**H** X 2), 7.87 (d, *J*=9.6Hz, 2H, Naph-**H** X 2), 7.59 (s, 2H, Naph-**H** X 2), 7.51 (d, *J*=8.4Hz, 4H, Ar-**H** X 2), 7.47 (d, *J*=6.8Hz, 4H, Naph-**H** X 2), 7.02 (d, *J*=6.4Hz, 4H, Ar-**H** X 2), 4.07 (t, *J*=6.4Hz, 4H, -O**CH$_2$**- X 2), 1.89-1.82 (m, 4H, -O-C-**CH$_2$**- X 2); ***^{13}C NMR (400MHz, CDCl$_3$): δ (In ppm):*** 165.73, 161.77, 150.31, 146.83, 134.46, 133.62, 129.24, 127.92, 127.15, 126.96, 124.77, 117.20, 114.75, 68.35, 29.39; **Elemental Analysis:** $C_{38}H_{32}N_2O_2$: (cal): C, 83.18; H, 5.88; N, 5.11; O, 5.83; found C, 83.23; H, 5.92; N, 5.15; O, 5.86; %;

(1E,1'E)-1,1'-((pentane-1,5-diylbis(oxy))bis(4,1-phenylene))bis(N-(naphthalen-2-yl)methanimine) (II-5):

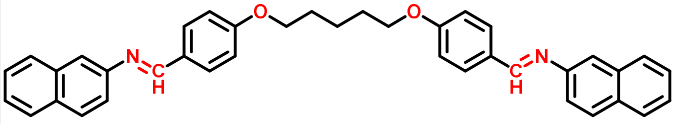

White solid, Yield: 61%; **IR** ν_{max}/cm^{-1}: 3052.17, 2932.16, 2854.30 (C_{sp3}-**H**), 1605.92 (-CH=N-), 1509.23 ($C_{sp2-aromatic}$), 1252.50 (-C-O-), 1159.02 (-C-N-), 743.45; ***^{1}H NMR (400MHz, CDCl$_3$): δ (In ppm):*** 8.53 (s, 1H, -**CH**=N- X 2), 7.91 (d, *J*=6Hz, 2H, Naph-**H** X 2), 7.89 (d, *J*=8.6Hz, 4H, Naph-**H** X 2), 7.86 (d, *J*=9.6Hz, 2H, Naph-**H** X 2), 7.59 (s, 2H, Naph-**H** X 2), 7.47 (d, *J*=8.4Hz, 4H, Ar-**H** X 2), 7.44 (d, *J*=6.8Hz, 4H, Naph-**H** X 2), 7.01 (d, *J*=6.4Hz, 4H, Ar-**H** X 2), 4.05 (t, *J*=6.4Hz, 4H, -O**CH$_2$**- X 2), 1.85-1.78 (m, 4H, -O-C-**CH$_2$**- X 2), 1.69-1.65 (m, 2H, -O-C-C -**CH$_2$**-); ***^{13}C NMR (400MHz, CDCl$_3$): δ (In ppm):*** 165.73, 161.77, 150.31, 146.83, 134.46, 133.62, 129.24, 127.92, 127.15, 126.96, 124.77, 117.20, 114.75, 68.35, 29.39; **Elemental Analysis:**

$C_{39}H_{34}N_2O_2$: (cal): C, 83.24; H, 6.09; N, 4.98; O, 5.69; found C, 83.21; H, 6.02; N, 4.94; O, 5.63; %;

(1E,1'E)-1,1'-((hexane-1,6-diylbis(oxy))bis(4,1-phenylene))bis(N-(naphthalen-2-yl)methanimine) (II-6):

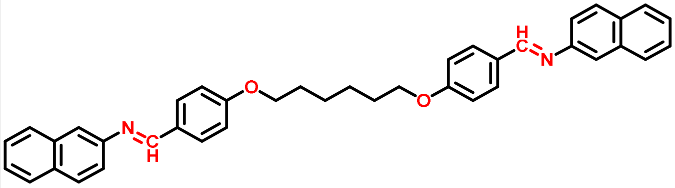

(1*E*,1'*E*)-1,1'-((hexane-1,6-diylbis(oxy))bis
(4,1-phenylene))bis(*N*-(naphthalen-2-yl)methanimine)

White solid, Yield: 63%; **IR** ν_{max}/cm^{-1}: 3057.58, 2937.55, 2854.07 (C$_{sp3}$-**H**), 1607.76 (-CH=N-), 1507.36 (C$_{sp2\text{-aromatic}}$), 1250.27 (-C-O-), 1167.82 (-C-N-), 744.23; ***^{1}H NMR (400MHz, CDCl$_3$): δ (In ppm):*** 8.54 (s, 1H, -**CH**=N- X 2), 7.92 (d, *J*=6Hz, 2H, Naph-**H** X 2), 7.89 (d, *J*=8.6Hz, 4H, Naph-**H** X 2), 7.86 (d, *J*=9.6Hz, 2H, Naph-**H** X 2), 7.60 (s, 2H, Naph-**H** X 2), 7.47 (d, *J*=8.4Hz, 4H, Ar-**H** X 2), 7.44 (d, *J*=6.8Hz, 4H, Naph-**H** X 2), 7.02 (d, *J*=6.4Hz, 4H, Ar-**H** X 2), 4.09 (t, *J*=6.4Hz, 4H, -O**CH$_2$**- X 2), 1.92-1.87 (m, 4H, -O-C-**CH$_2$**- X 2), 1.35-1.21 (m, 4H, -O-C-C -**CH$_2$**- X 2); ***^{13}C NMR (400MHz, CDCl$_3$): δ (In ppm):*** 165.81, 161.34, 150.37, 147.11, 134.50, 133.61, 129.24, 127.93, 127.20, 126.65, 124.79, 117.26, 114.71, 68.13, 32.14, 29.46; **Elemental Analysis:** $C_{40}H_{36}N_2O_2$: (cal): C, 83.30; H, 6.29; N, 4.86; O, 5.55; found C, 83.26; H, 6.25; N, 4.82; O, 5.54; %;

(1E,1'E)-1,1'-((octane-1,8-diylbis(oxy))bis(4,1-phenylene))bis(N-(naphthalen-2-yl)methanimine) (II-8):

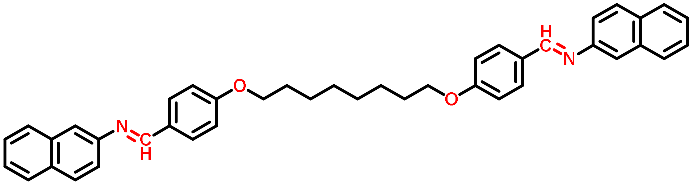

(1*E*,1'*E*)-1,1'-((octane-1,8-diylbis(oxy))bis
(4,1-phenylene))bis(*N*-(naphthalen-2-yl)methanimine)

White solid, Yield: 59%; **IR** ν_{max}/cm^{-1}: 3055.50, 2938.19, 2858.74 (C$_{sp3}$-**H**), 1607.88 (-CH=N-), 1509.28 (C$_{sp2\text{-aromatic}}$), 1249.39 (-C-O-), 1166.77 (-C-N-), 740.87; ***^{1}H NMR (400MHz, CDCl$_3$): δ (In ppm):*** 8.55 (s, 1H, -**CH**=N- X 2), 7.93 (d, *J*=6Hz, 2H, Naph-**H** X 2), 7.89 (d, *J*=8.6Hz, 4H, Naph-**H** X 2), 7.87 (d, *J*=9.6Hz, 2H, Naph-**H** X 2), 7.60 (s, 2H, Naph-**H** X 2), 7.47 (d, *J*=8.4Hz, 4H, Ar-**H** X 2), 7.43 (d, *J*=6.8Hz, 4H, Naph-**H**

X 2), 7.02 (d, J=6.4Hz, 4H, Ar-**H** X 2), 4.05 (t, J=6Hz, 4H, -O**CH$_2$**- X 2), 2.19-2.05 (m, 4H, -O-C-**CH$_2$**- X 2), 0.93-0.84 (m, , 8H, -O-C-C-(**CH$_2$)$_2$**- X 2); ***^{13}C NMR (400MHz, CDCl$_3$): δ (In ppm):*** 165.84, 161.72, 150.31, 146.97, 134.62, 133.79, 129.28, 127.93, 127.18, 126.64, 124.72, 117.31, 114.84, 68.25, 32.85, 31.03, 29.11; **Elemental Analysis:** C$_{42}$H$_{40}$N$_2$O$_2$: (cal): C, 83.41; H, 6.67; N, 4.63; O, 5.29; found C, 83.38; H, 6.63; N, 4.61; O, 5.26; %;

1E,1'E)-1,1'-((decane-1,10-diylbis(oxy))bis(4,1-phenylene))bis(N-(naphthalen-2-yl)methanimine) (II-10):

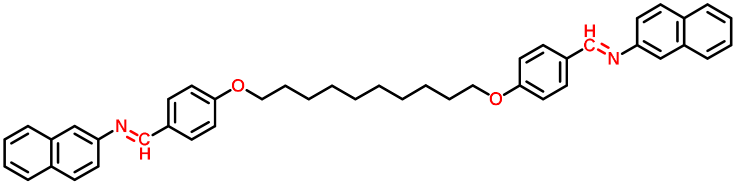

(1*E*,1'*E*)-1,1'-((decane-1,10-diylbis(oxy))bis (4,1-phenylene))bis(*N*-(naphthalen-2-yl)methanimine)

White solid, Yield: 59%; **IR** ν_{max}/cm^{-1}: 3051.46, 2917.93, 2851.51 (C$_{sp3}$-**H**), 1608.04 (-CH=N-), 1514.03 (C$_{sp2\text{-}aromatic}$), 1251.55 (-C-O-), 1167.04 (-C-N-), 740.35; ***^{1}H NMR (400MHz, CDCl$_3$): δ (In ppm):):*** 8.55 (s, 1H, -**CH**=N- X 2), 7.93 (d, J=6Hz, 2H, Naph-**H** X 2), 7.89 (d, J=8.6Hz, 4H, Naph-**H** X 2), 7.86 (d, J=9.6Hz, 2H, Naph-**H** X 2), 7.60 (s, 2H, Naph-**H** X 2), 7.50 (d, J=8.4Hz, 4H, Ar-**H** X 2), 7.45 (d, J=6.8Hz, 4H, Naph-**H** X 2), 7.02 (d, J=6.4Hz, 4H, Ar-**H** X 2), 4.15 (t, J=6Hz, 4H, -O**CH$_2$**- X 2), 2.19-2.07 (m, 8H, -O-C-(**CH$_2$)$_2$**- X 2), 0.93-0.82 (m, 8H, -O-C-**C**-C-(**CH$_2$)$_2$**- X 2); ***^{13}C NMR (400MHz, CDCl$_3$): δ (In ppm):*** 165.95, 161.96, 150.33, 146.96, 134.54, 133.65, 129.19, 127.91, 127.23, 126.64, 124.79, 117.32, 114.73, 68.31, 32.87, 31.02, 29.31, 26.00; **Elemental Analysis:** C$_{44}$H$_{44}$N$_2$O$_2$: (cal): C, 83.51; H, 7.01; N, 4.43; O, 5.06; found C, 83.48; H, 6.97; N, 4.41; O, 5.03; %;

(1E,1'E)-1,1'-((dodecane-1,12-diylbis(oxy))bis(4,1-phenylene))bis(N-(naphthalen-2-yl)methanimine) (II-12):

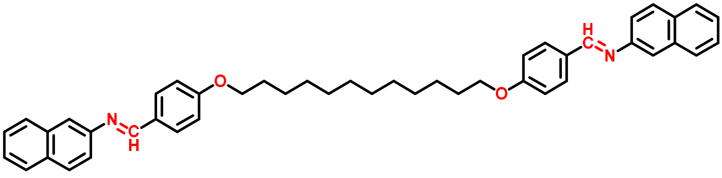

(1*E*,1'*E*)-1,1'-((dodecane-1,12-diylbis(oxy))bis (4,1-phenylene))bis(*N*-(naphthalen-2-yl)methanimine)

White solid, Yield: 62%; **IR** ν_{max}/cm^{-1}: 3052.07, 2924.90, 2852.42 (C$_{sp3}$-**H**), 1607.60 (-CH=N-), 1508.65 (C$_{sp2\text{-}aromatic}$), 1247.84 (-C-O-), 1164.70 (-C-N-), 746.45; ***^{1}H NMR***

(400MHz, $CDCl_3$): δ (In ppm): 8.53 (s, 1H, -**CH**=N- X 2), 7.90 (d, *J*=6Hz, 2H, Naph**-H** X 2), 7.88 (d, *J*=8.6Hz, 4H, Naph**-H** X 2), 7.86 (d, *J*=9.6Hz, 2H, Naph**-H** X 2), 7.59 (s, 2H, Naph**-H** X 2), 7.48 (d, *J*=8.4Hz, 4H, Ar**-H** X 2), 7.44 (d, *J*=6.8Hz, 4H, Naph**-H** X 2), 7.02 (d, *J*=6.4Hz, 4H, Ar**-H** X 2), 4.05 (t, *J*=6Hz, 4H, -O**CH$_2$**- X 2), 1.87-1.81 (m, 4H, -O-C-**CH$_2$**- X 2), 1.51-1.47 (m, 4H, -O-C-C-**CH$_2$**- X 2), 1.33-1.23 (m, 12H, -O-C-C-C-(**CH$_2$**)$_3$- X 2); ***^{13}C NMR (400MHz, $CDCl_3$): δ (In ppm):*** 165.76, 161.36, 150.35, 146.94, 134.62, 133.62, 129.24, 127.92, 127.22, 126.64, 124.77, 117.33, 114.75, 68.38, 34.17, 32.85, 29.40, 28.12, 26.04; **Elemental Analysis:** $C_{46}H_{48}N_2O_2$: (cal): C, 83.60; H, 7.32; N, 4.24; O, 4.84; found C, 83.57; H, 7.30; N, 4.21; O, 4.82; %;

2A.6 Spectras

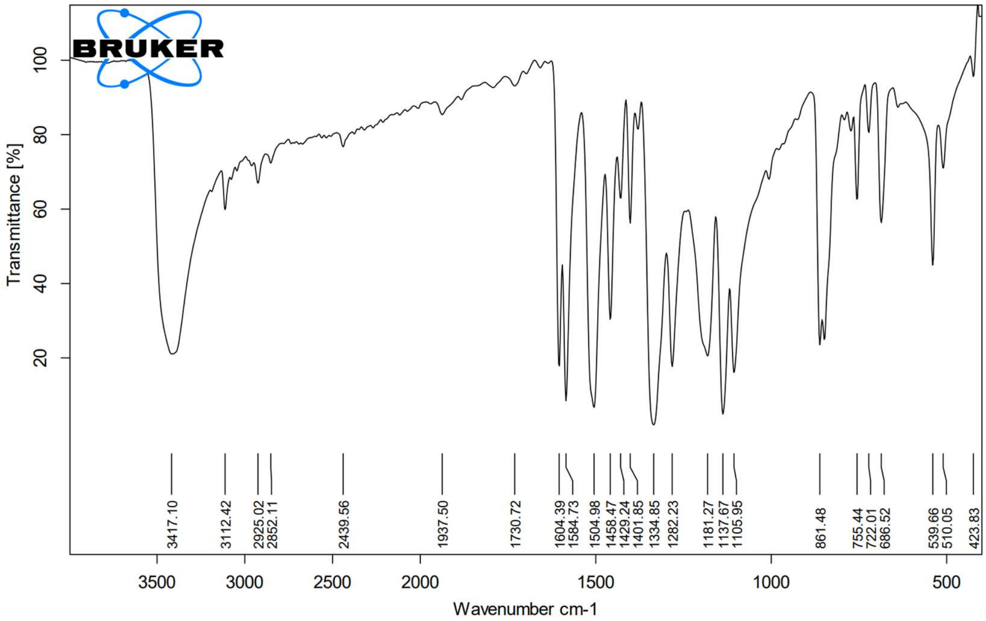

Fig. S2A.1: FT-IR spectra of NpAzOH

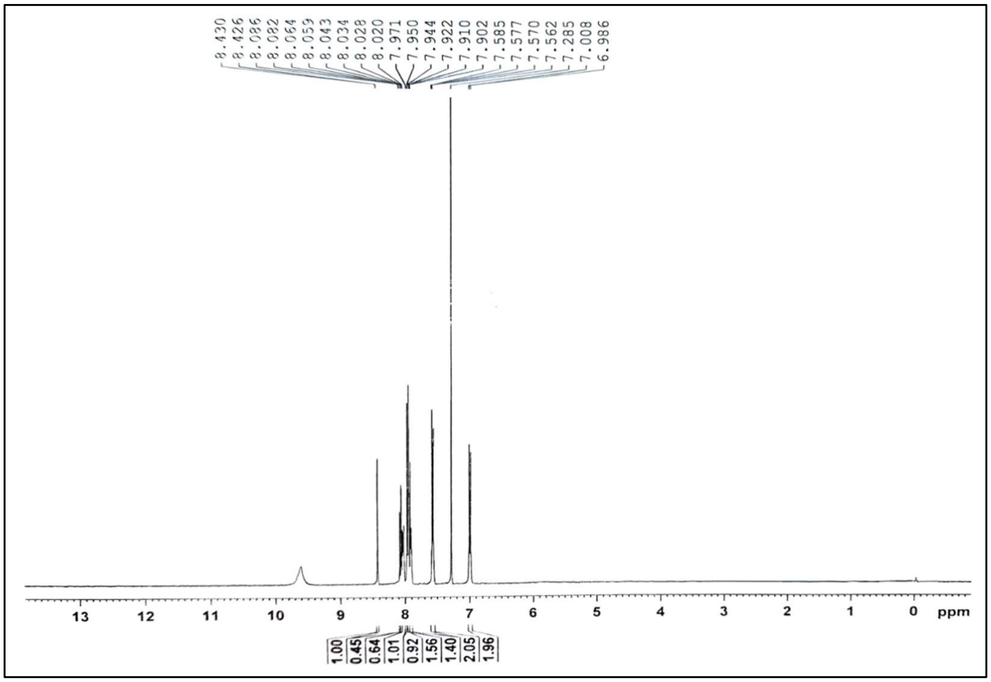

Fig. S2A.2: ^{1}H NMR of NpAzOH

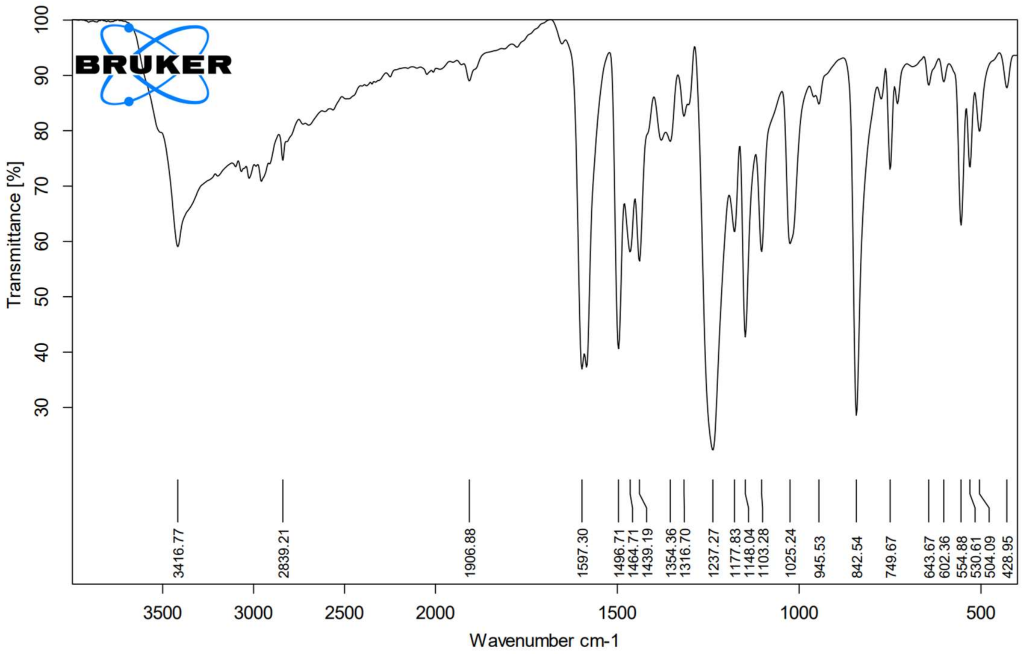

Fig. S2A.3: FT-IR spectra of NpAmOH

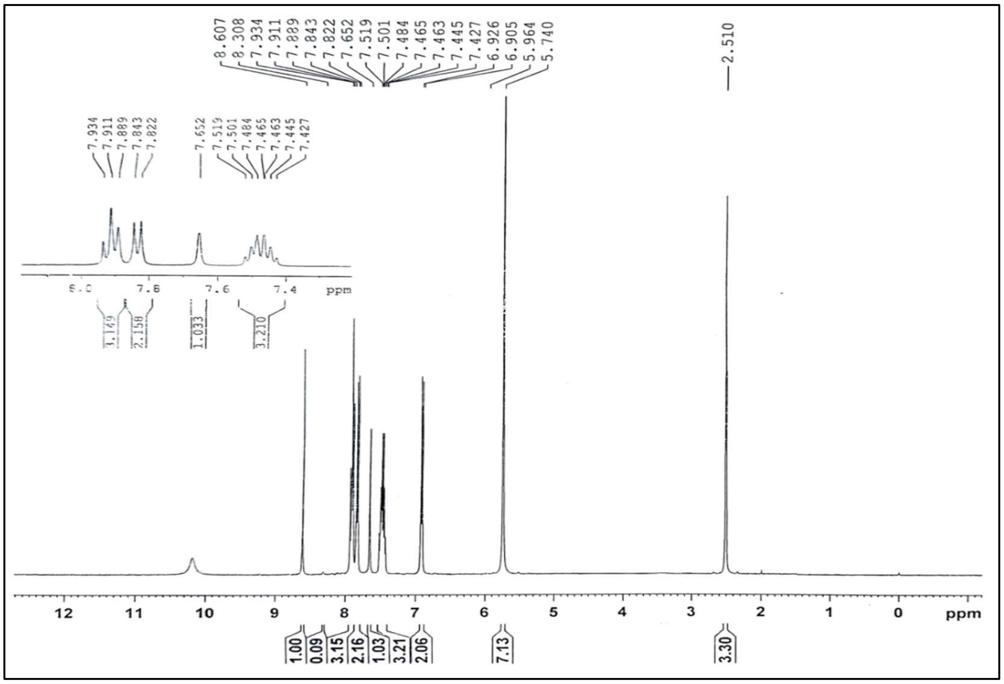

Fig. S2A.4: ^{1}H NMR of NpAmOH (DMSO-d6)

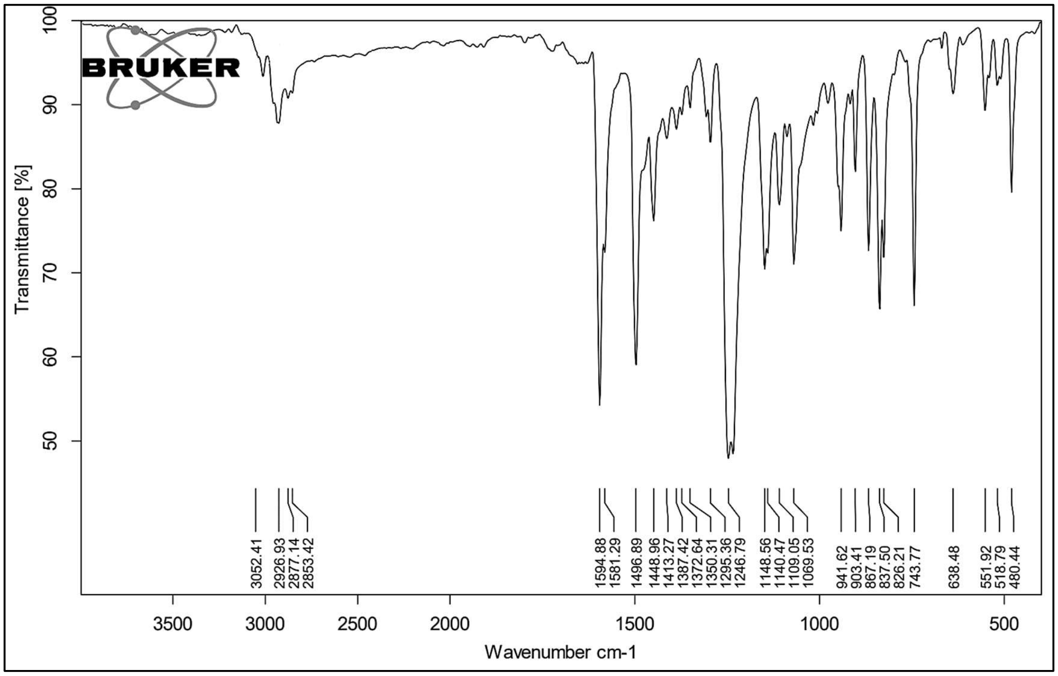

Fig. S2A.5: FT-IR spectra of *I-2*

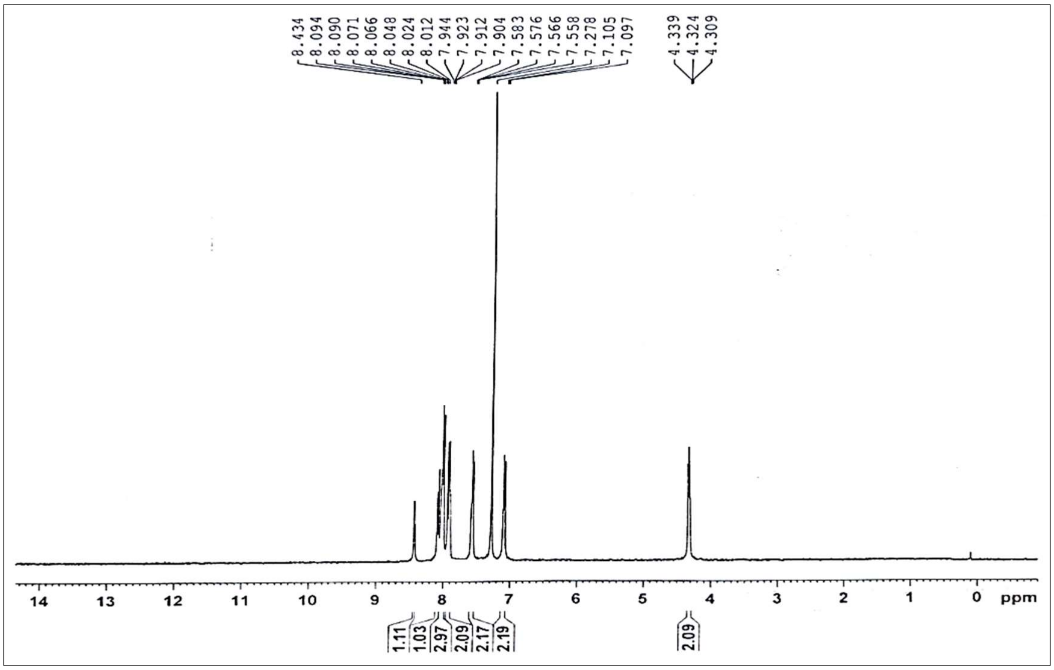

Fig. S2A.6: ^{1}H NMR of *I-2*

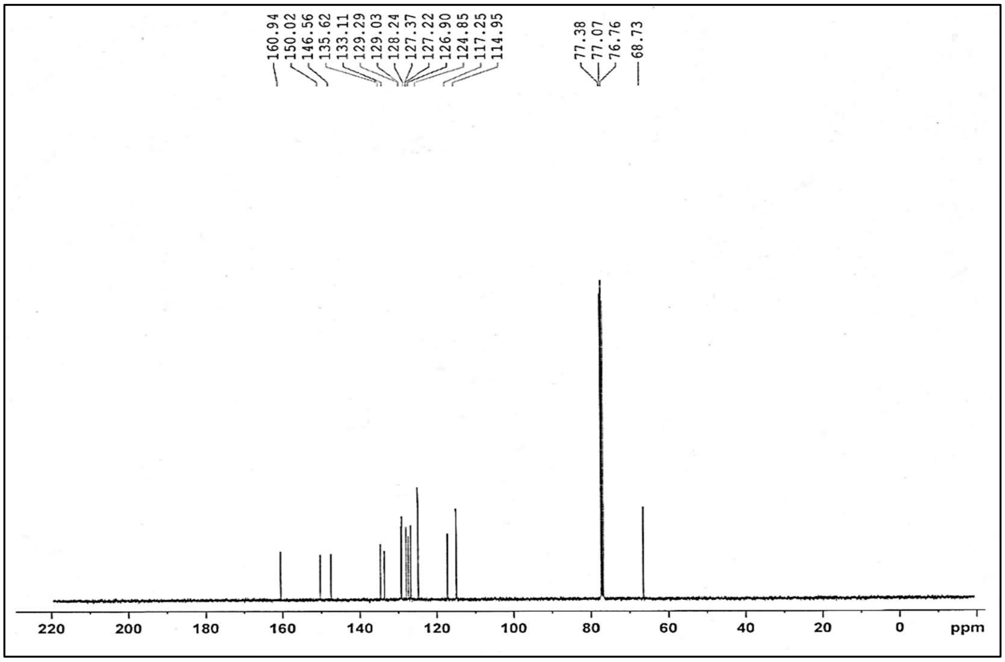

Fig. S2A.7: ^{13}C NMR of *I-2*

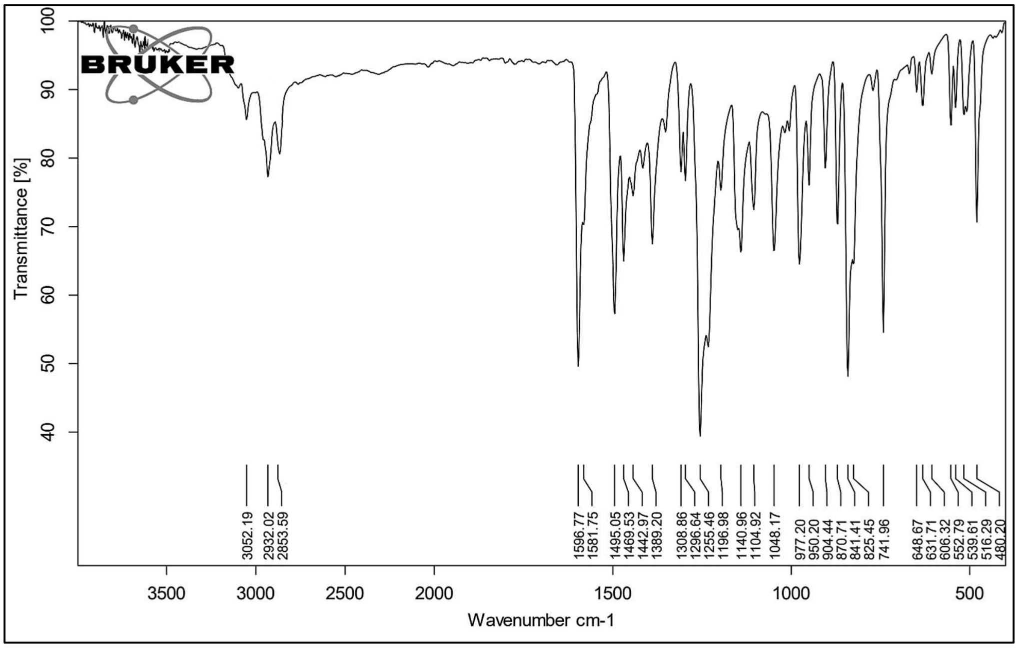

Fig. S2A.8: FT-IR spectra of *I-3*

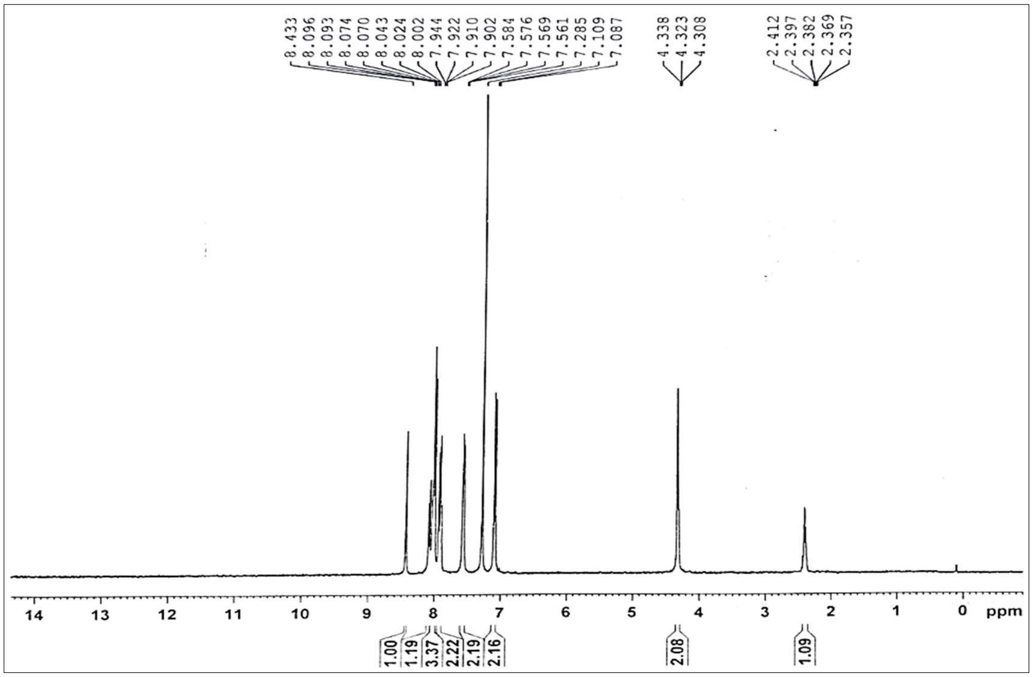

Fig. S2A.9: ^{1}H NMR of *I-3*

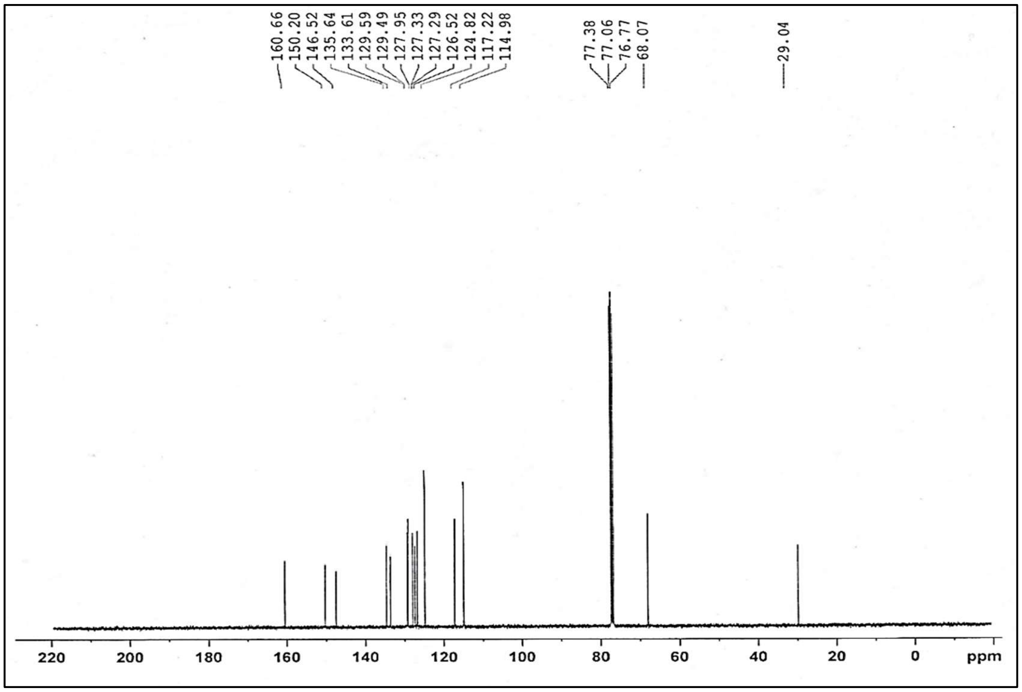

Fig. S2A.10: ^{13}C NMR of *I-3*

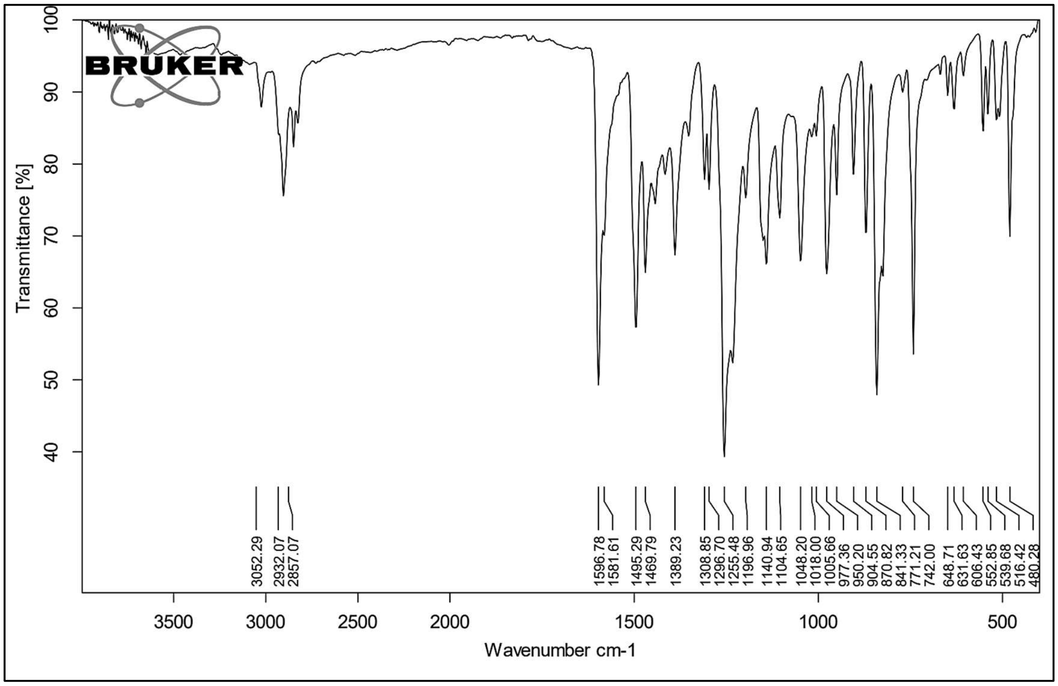

Fig. S2A.11: FT-IR spectra of *I-4*

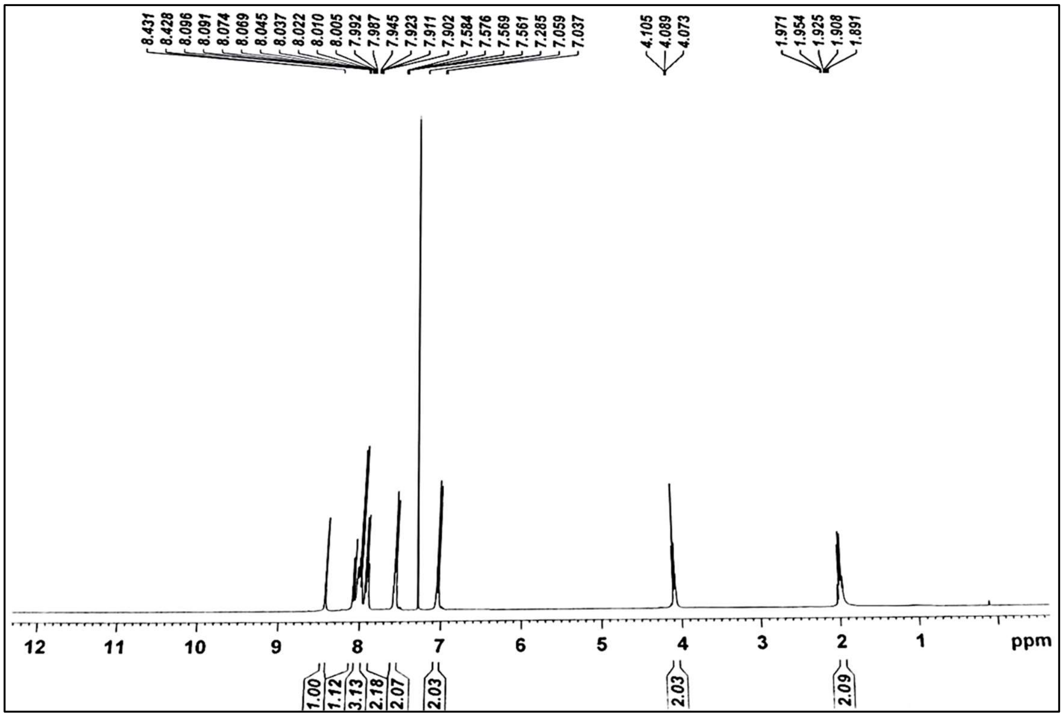

Fig. S2A.12: ^{1}H NMR of *I-4*

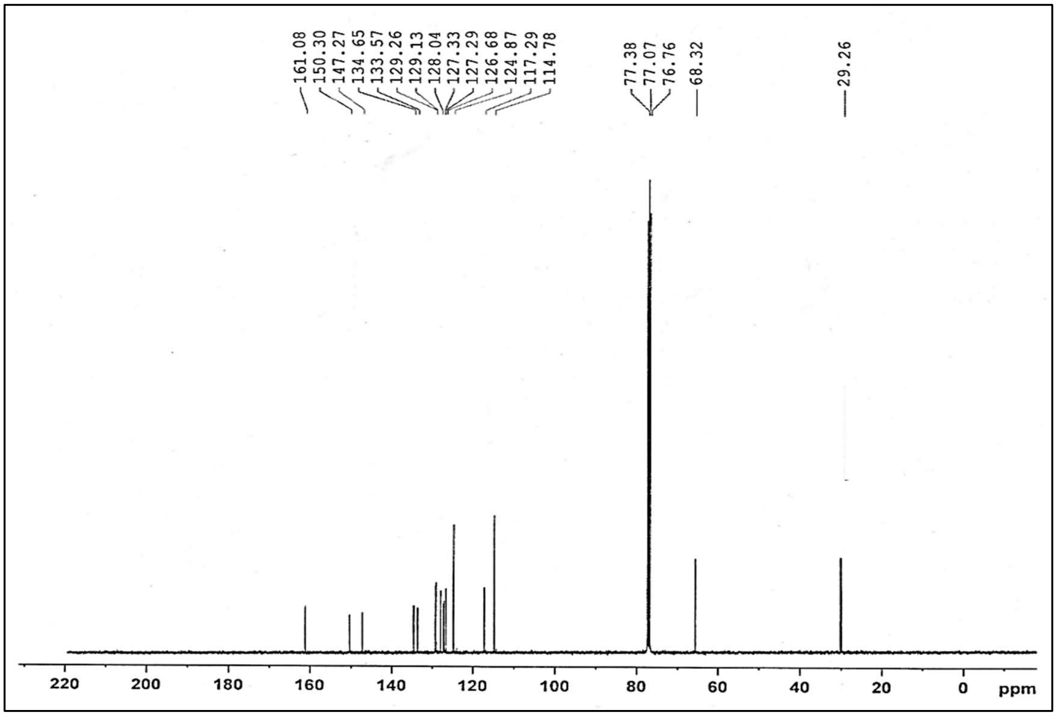

Fig. S2A.13: ^{13}C NMR of *I-4*

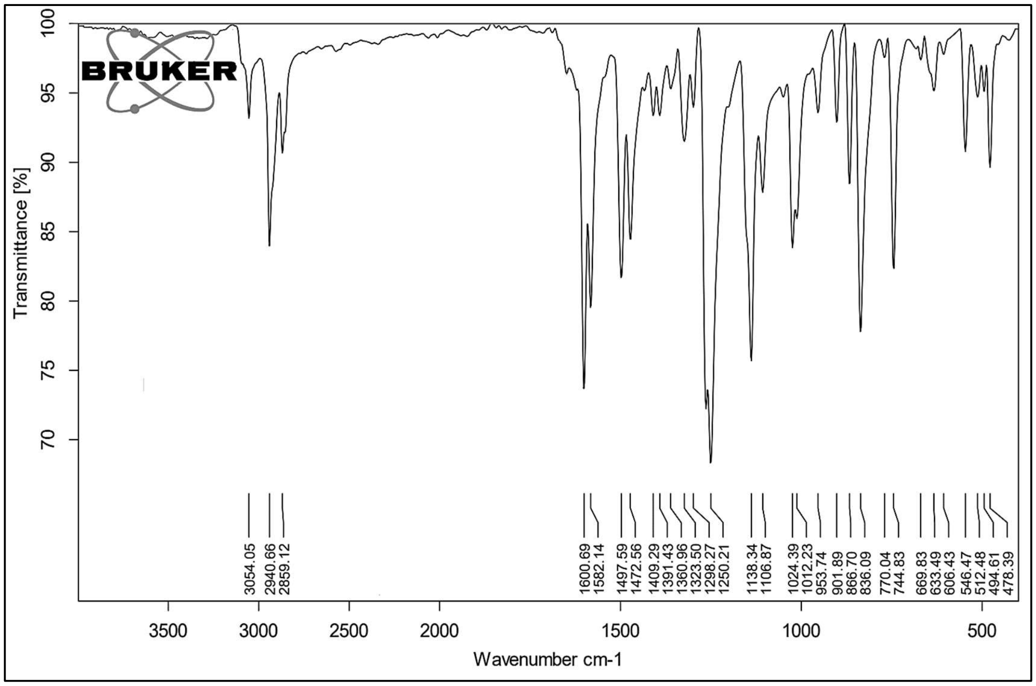

Fig. S2A.14: FT-IR spectra of *I-5*

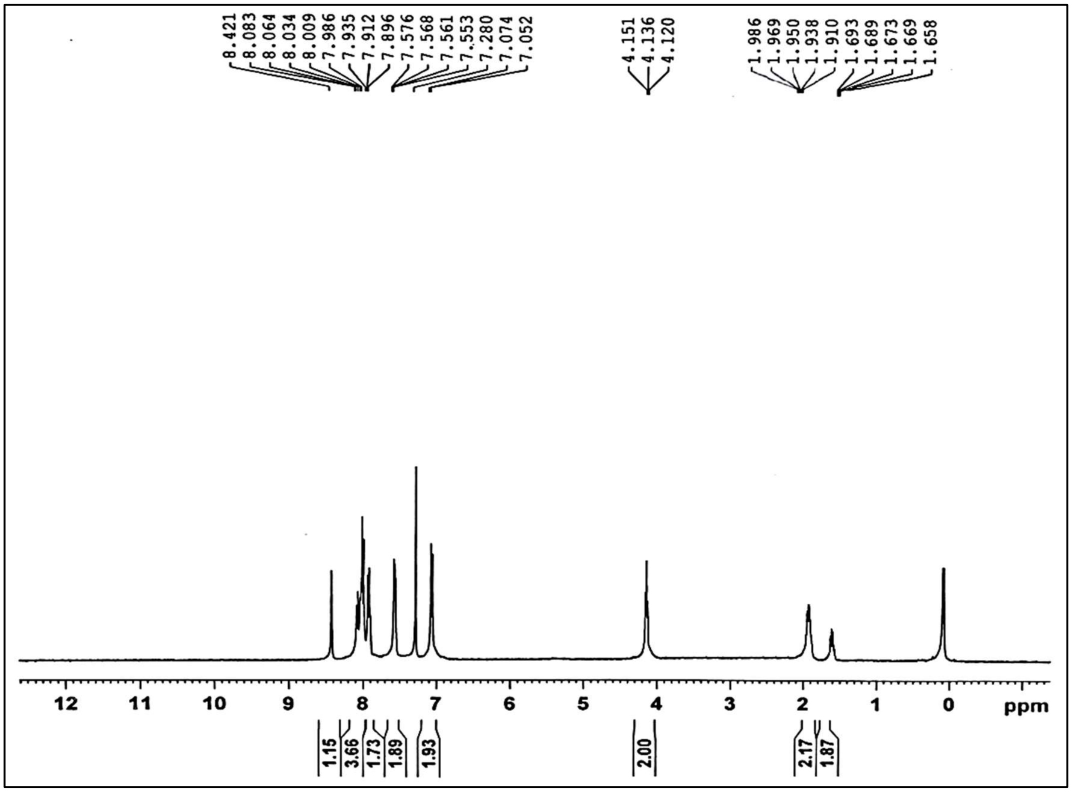

Fig. S2A.15: ^{1}H NMR of *I-5*

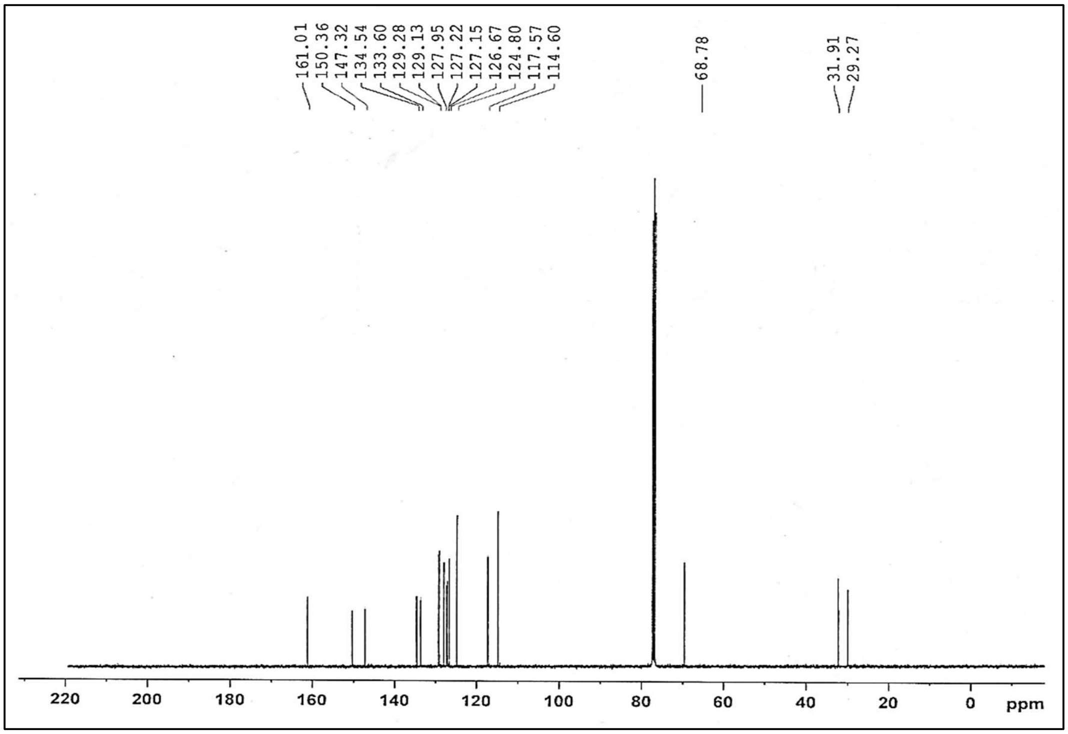

Fig. S2A.16: ^{13}C NMR of *I-5*

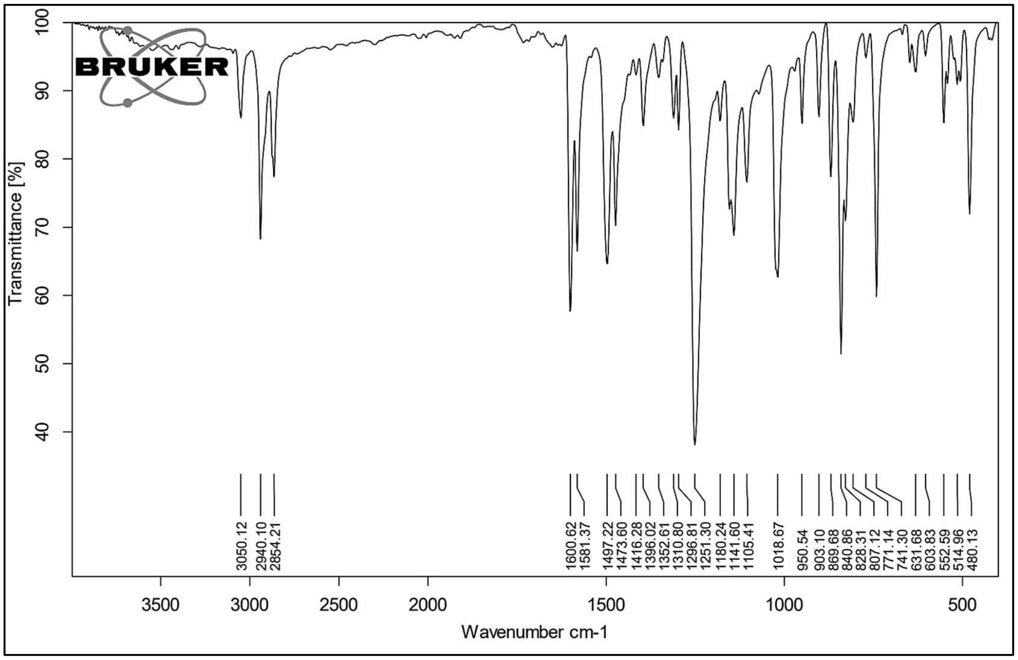

Fig. S2A.17: FT-IR spectra of *I-6*

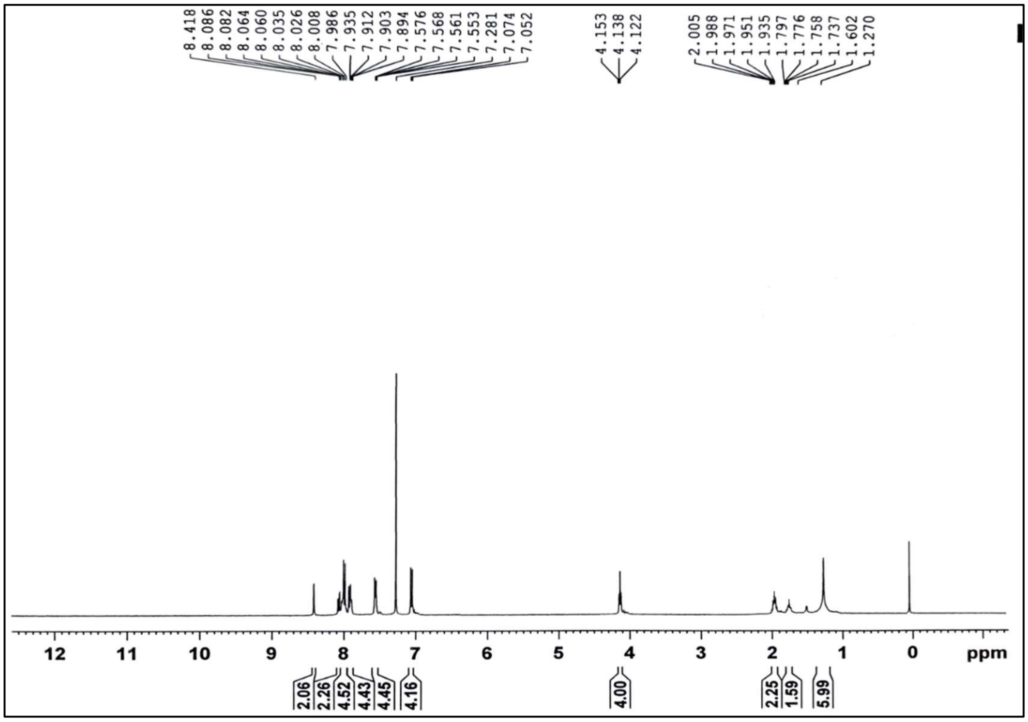

Fig. S2A.18: ^{1}H NMR of *I-6*

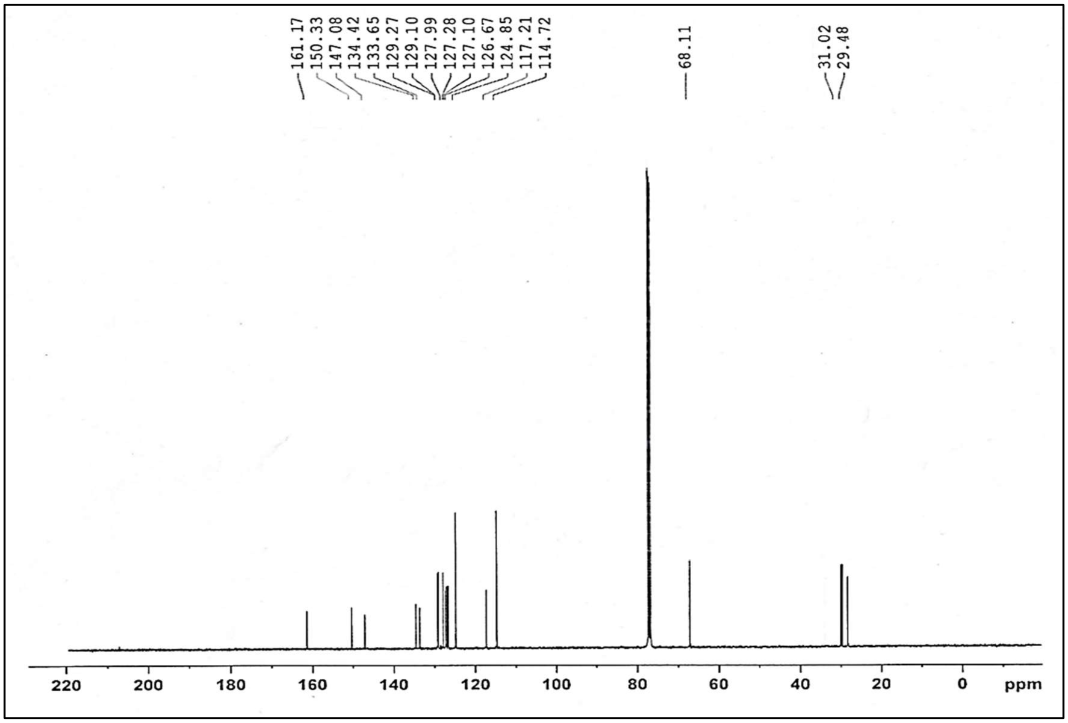

Fig. S2A.19: ^{13}C NMR of *I-6*

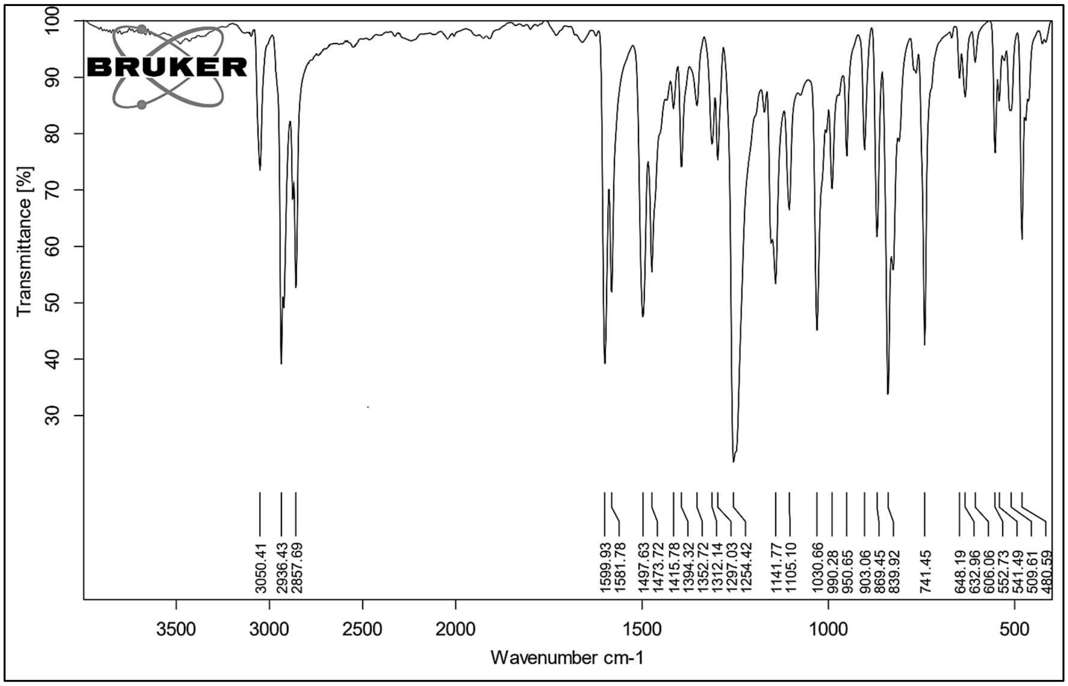

Fig. S2A.20: FT-IR spectra of *I-8*

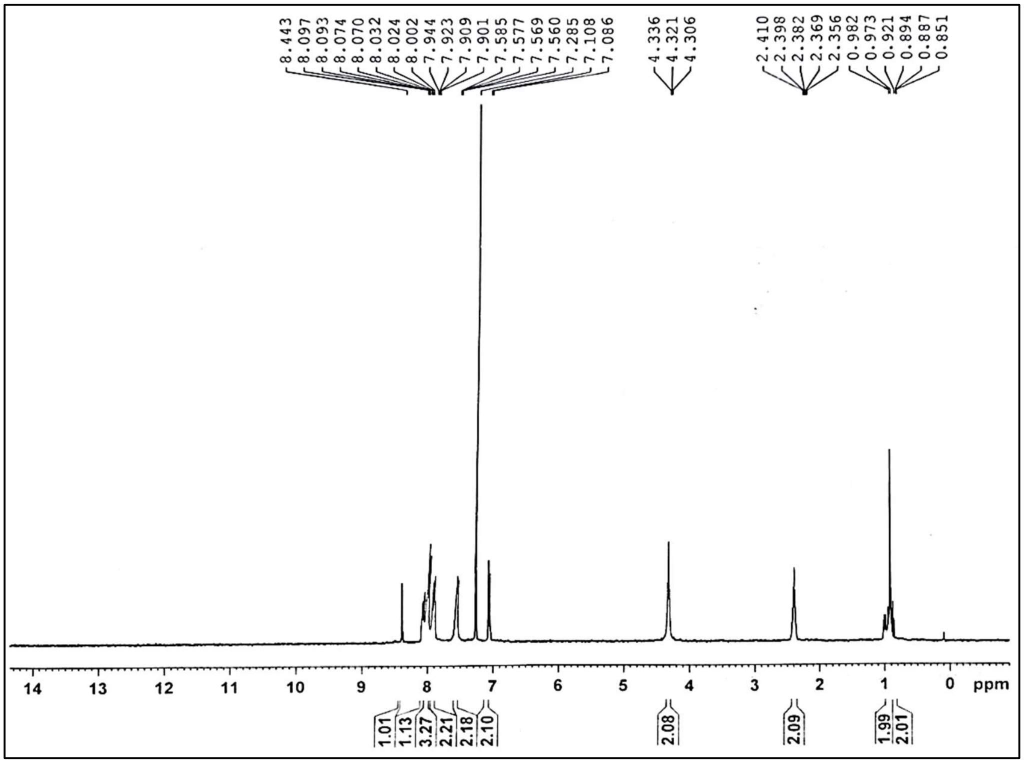

Fig. S2A.21: ^{1}H NMR of *I-8*

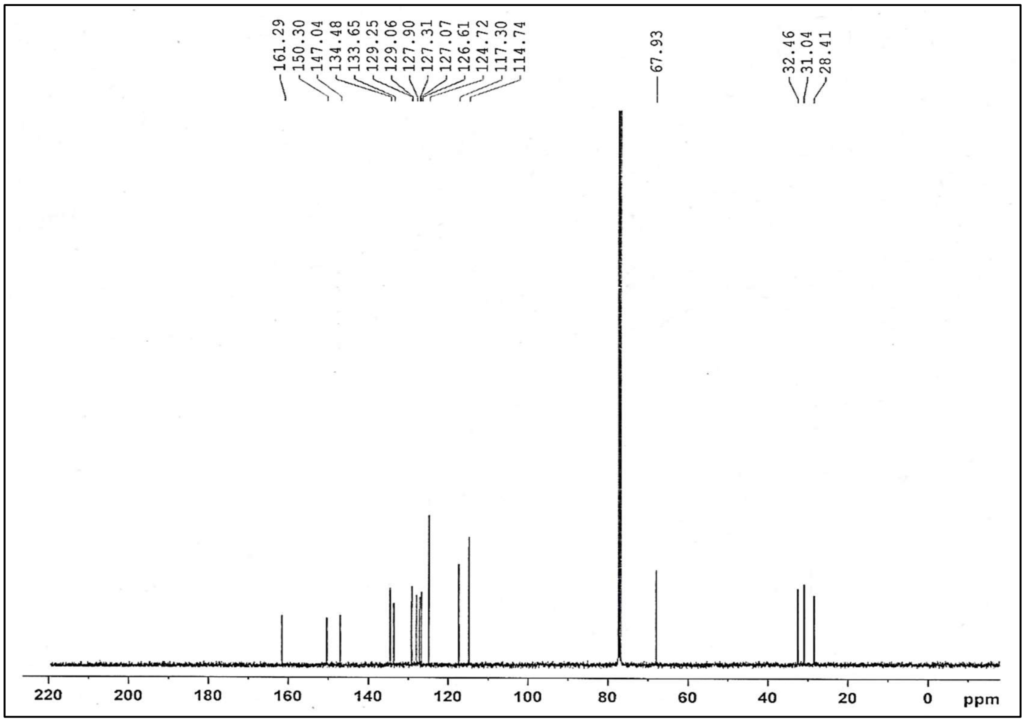

Fig. S2A.22: ^{13}C NMR of *I-8*

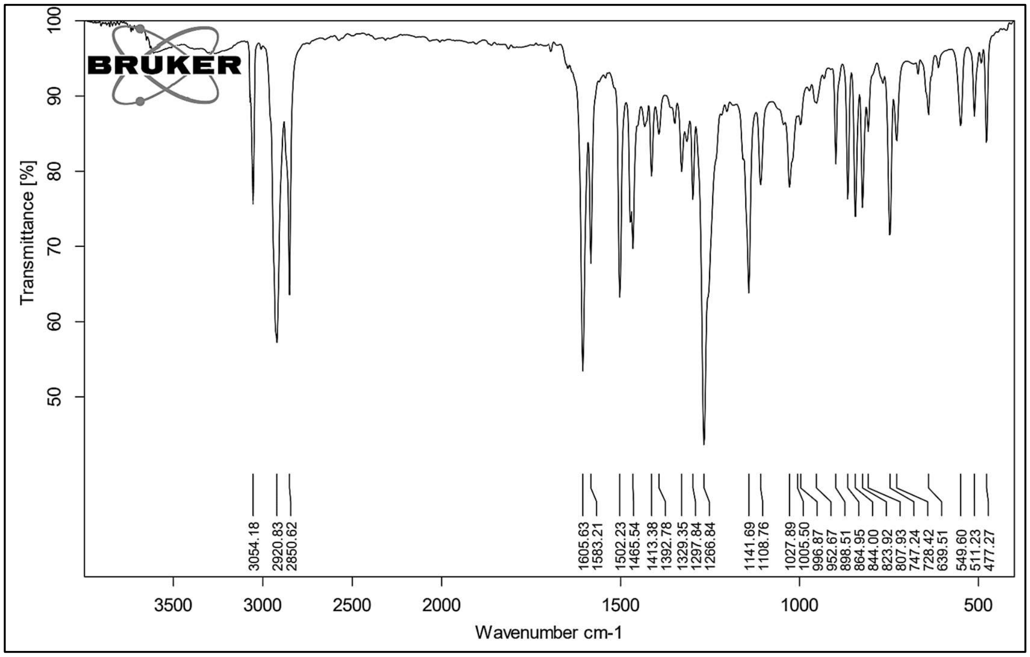

Fig. S2A.23: FT-IR spectra of *I-10*

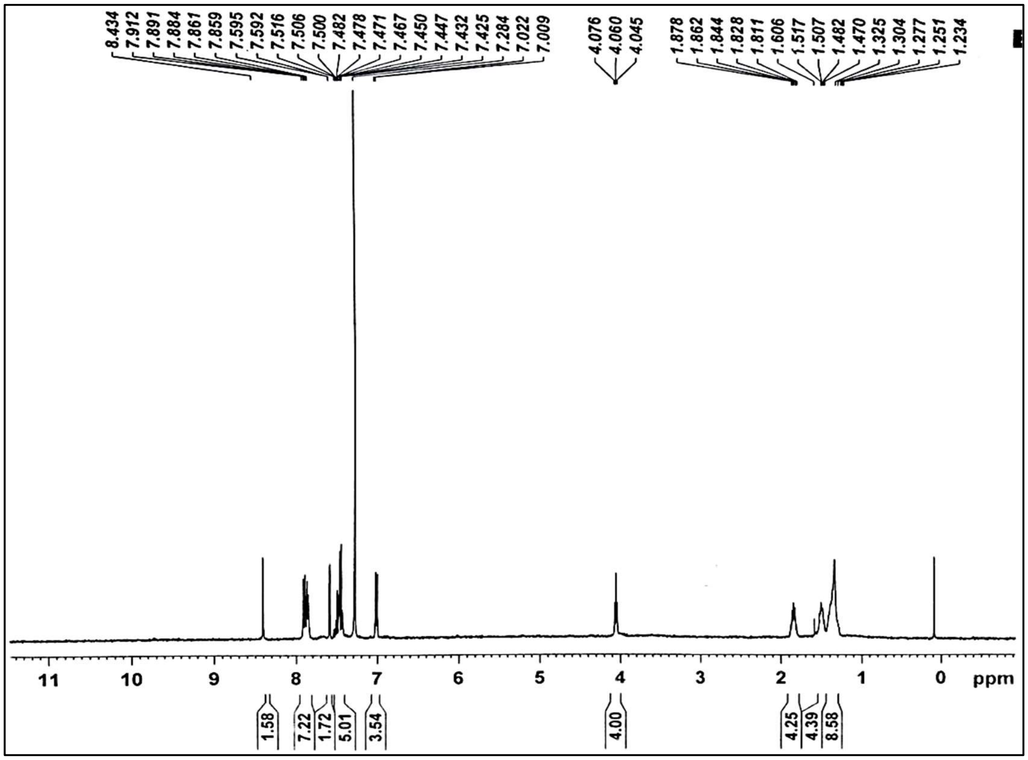

Fig. S2A.24: ^{1}H NMR of *I-10*

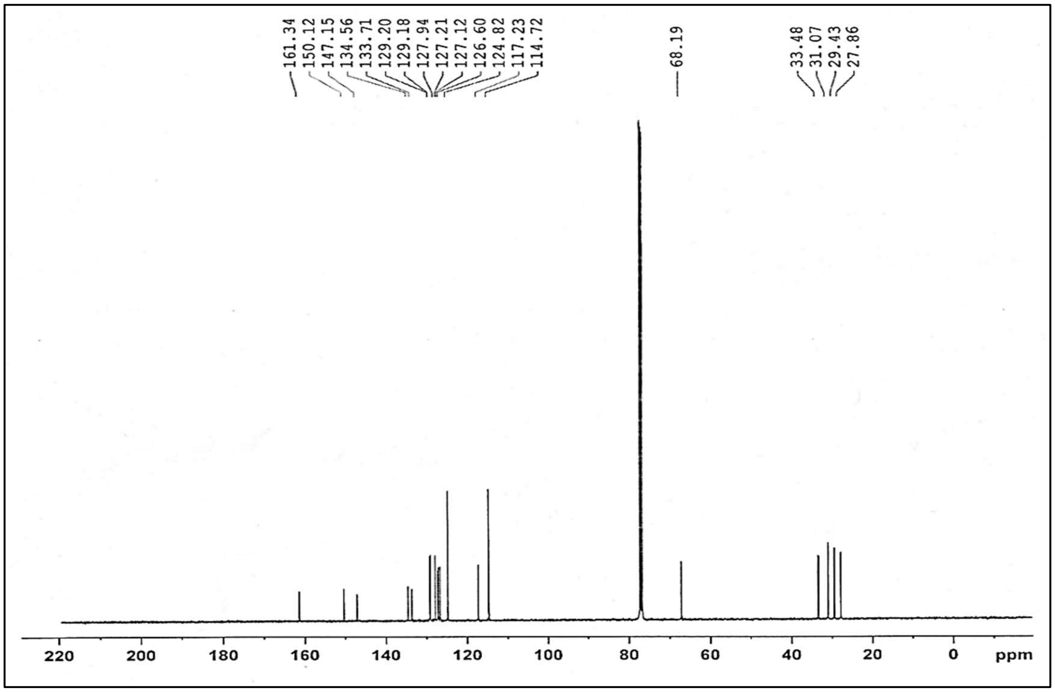

Fig. S2A.25: ^{13}C NMR of *I-10*

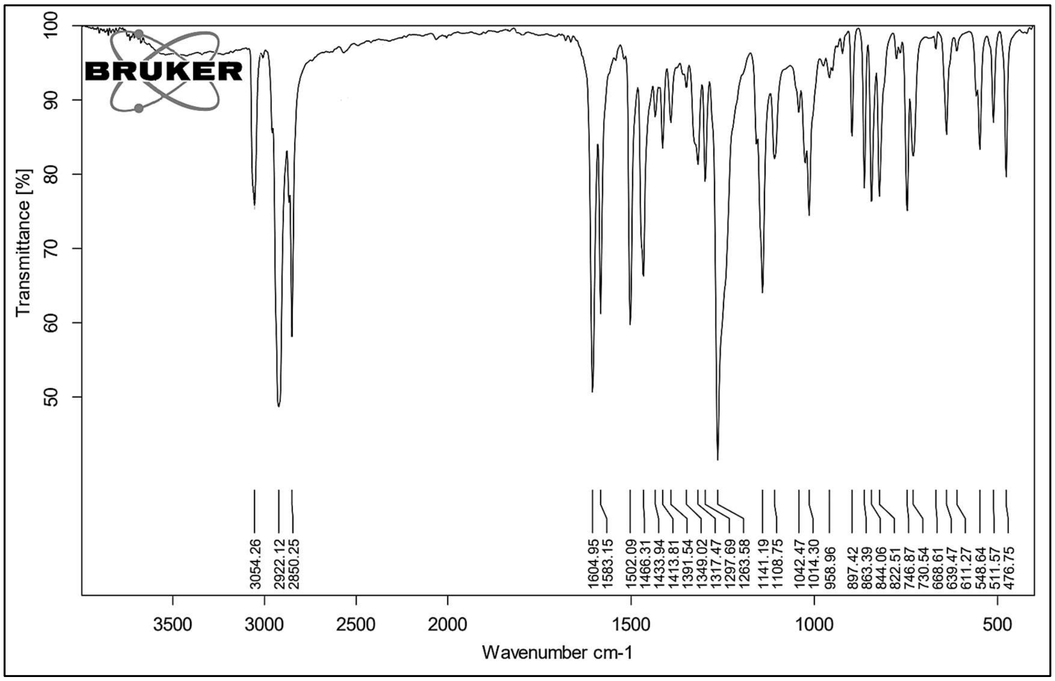

Fig. S2A.26: FT-IR spectra of *I-12*

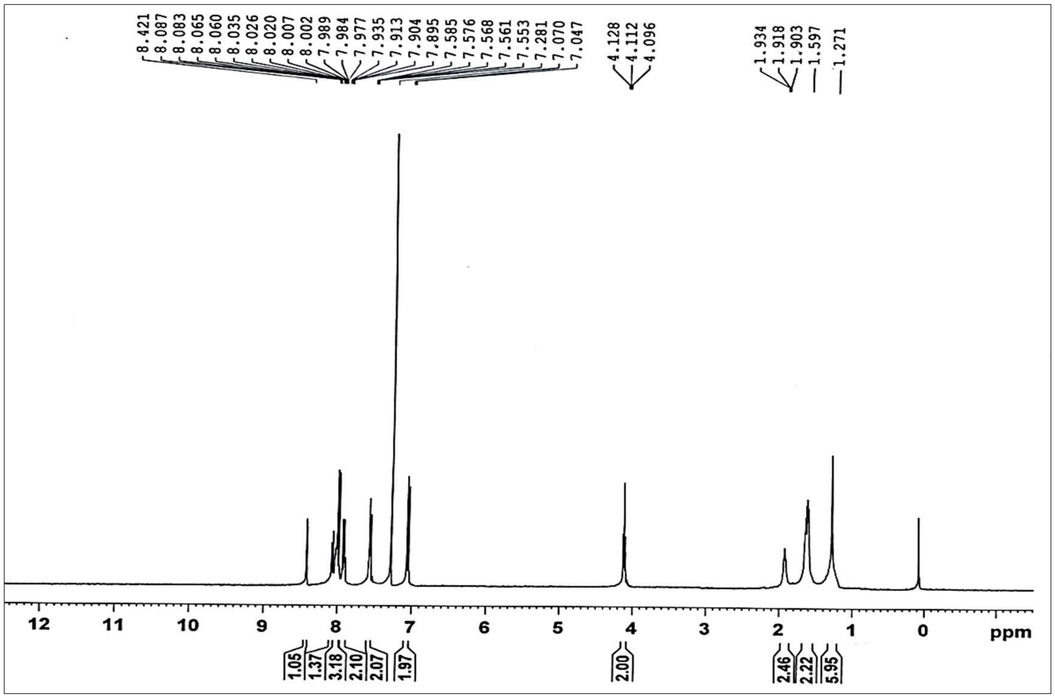

Fig. S2A.27: ^{1}H NMR of *I-12*

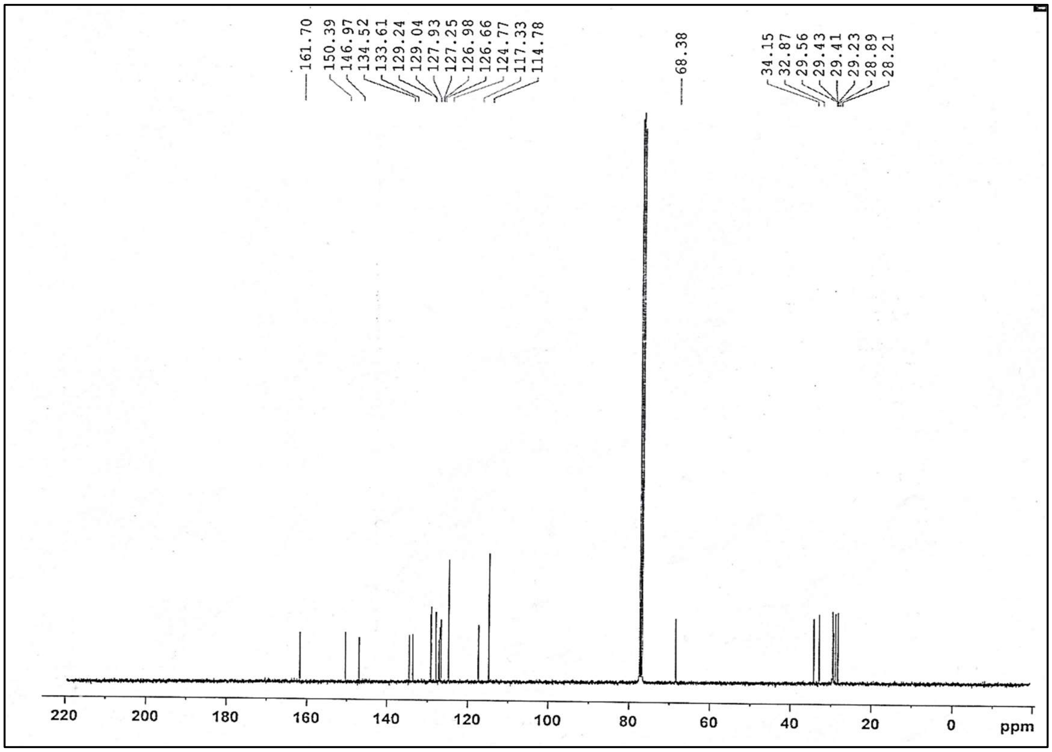

Fig. S2A.28: ^{13}C NMR of *I-12*

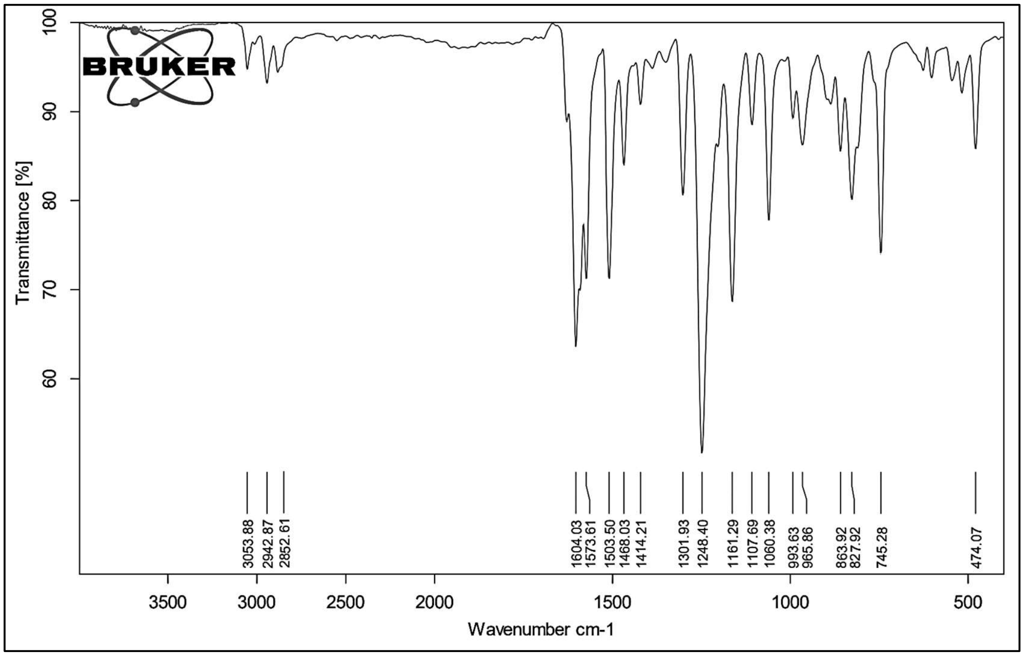

Fig. S2A.29: FT-IR spectra of *II-2*

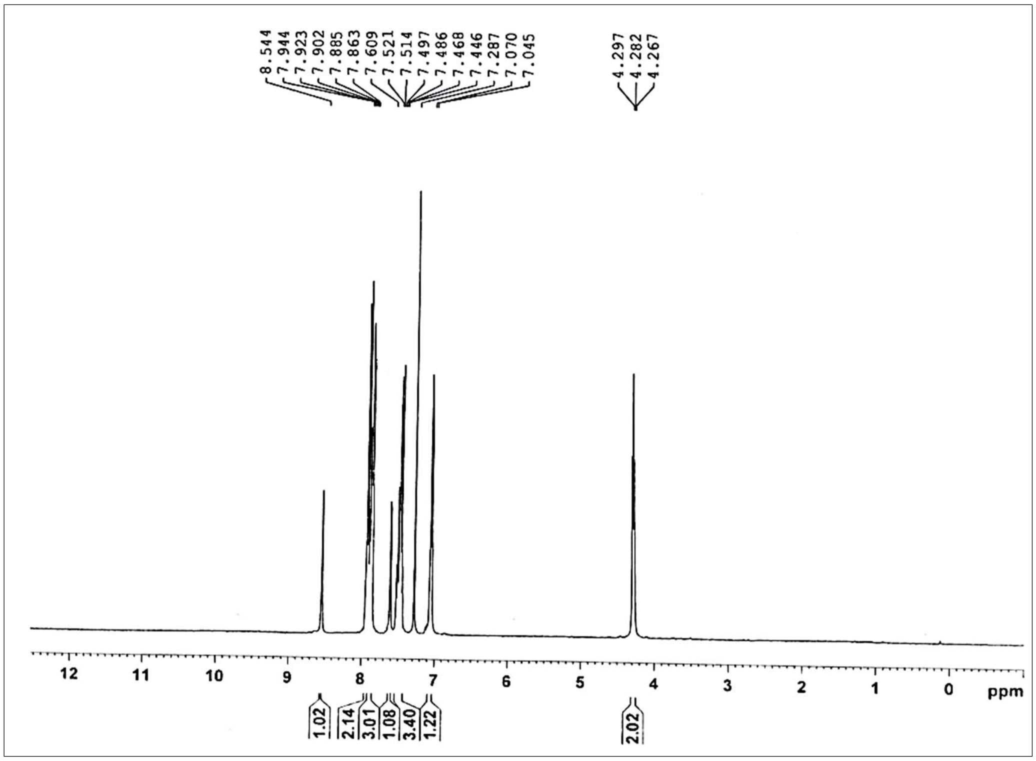

Fig. S2A.30: ^{1}H NMR of *II-2*

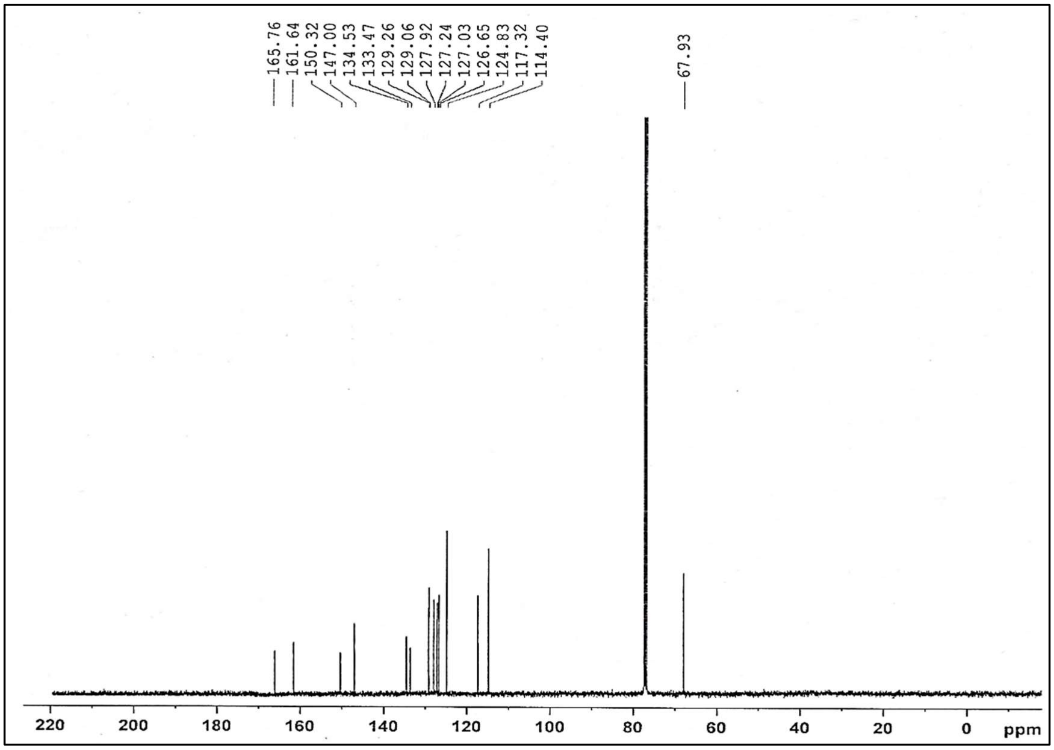

Fig. S2A.31: ^{13}C NMR of *II-2*

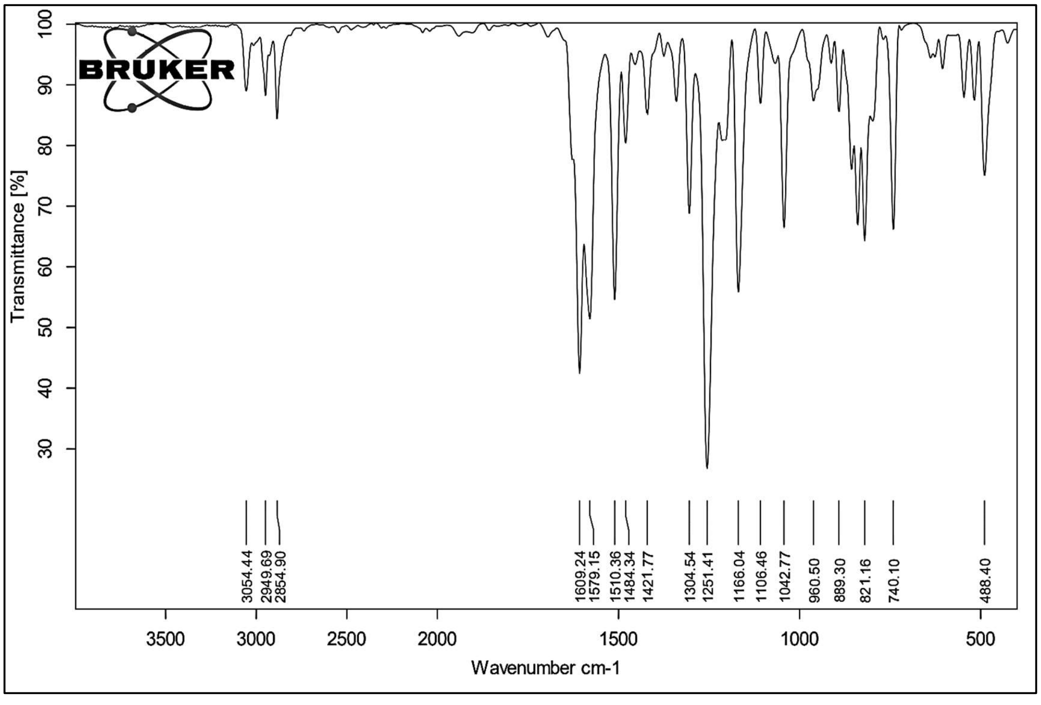

Fig. S2A.32: FT-IR spectra of *II-3*

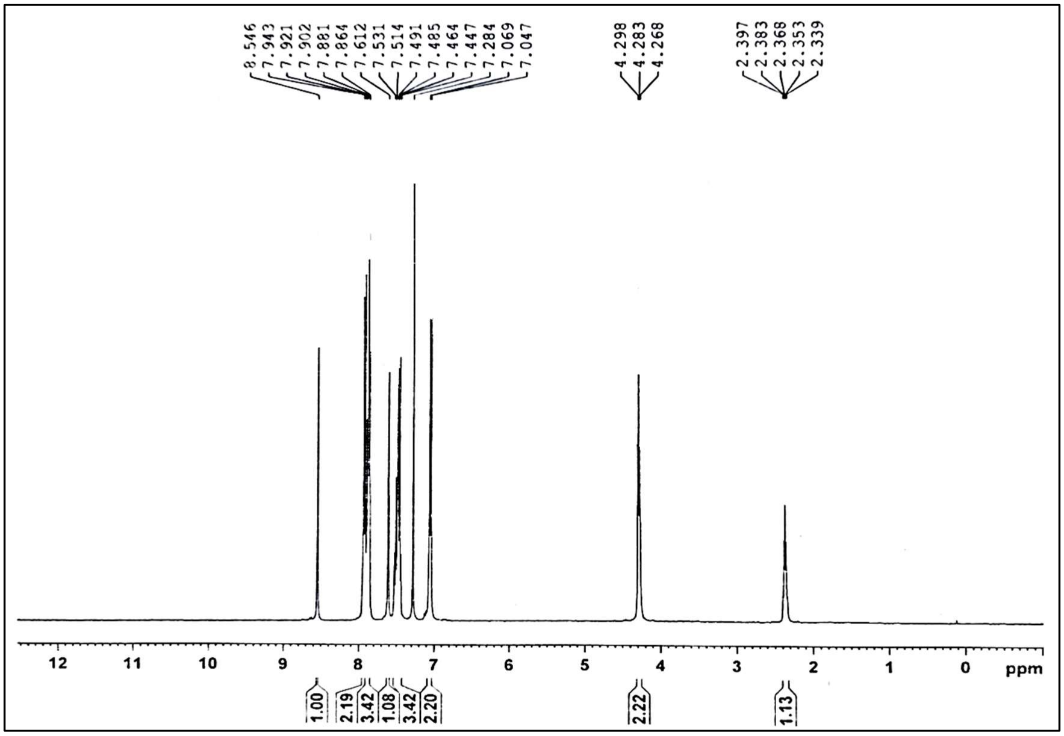

Fig. S2A.33: ^{1}H NMR of *II-3*

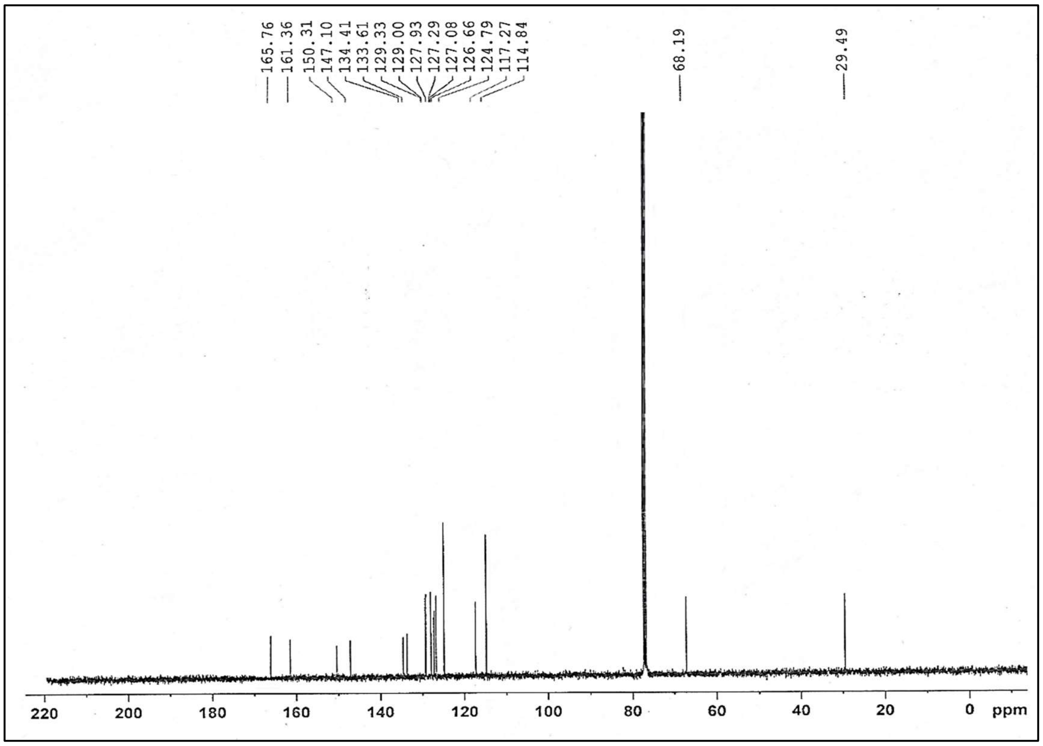

Fig. S2A.34: ^{13}C NMR of *II-3*

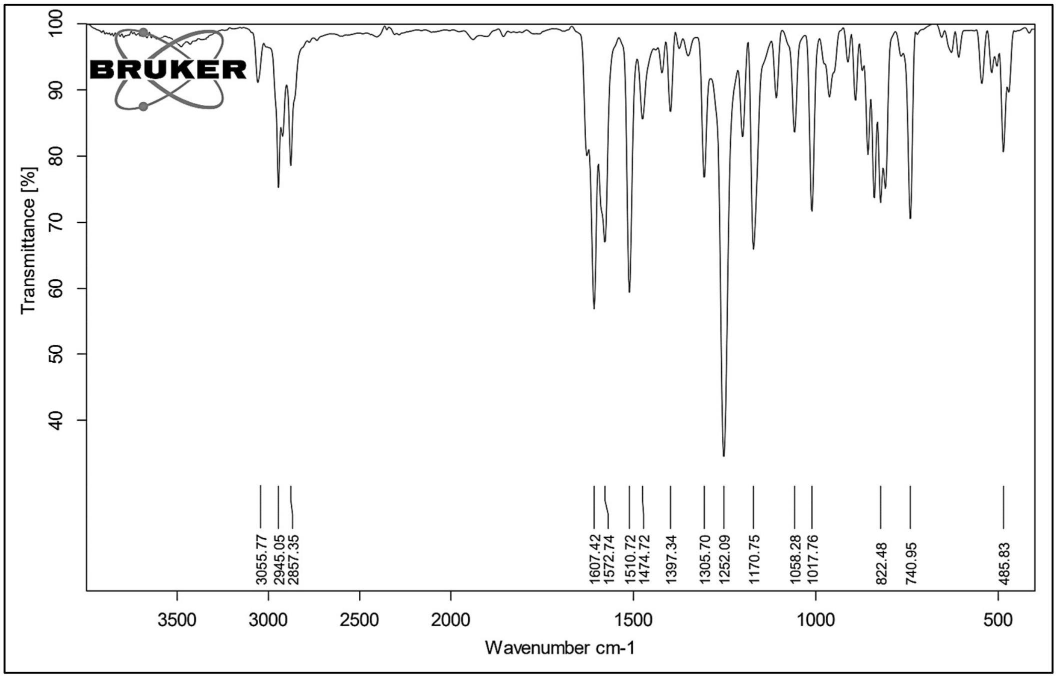

Fig. S2A.35 FT-IR spectra of *II-4*

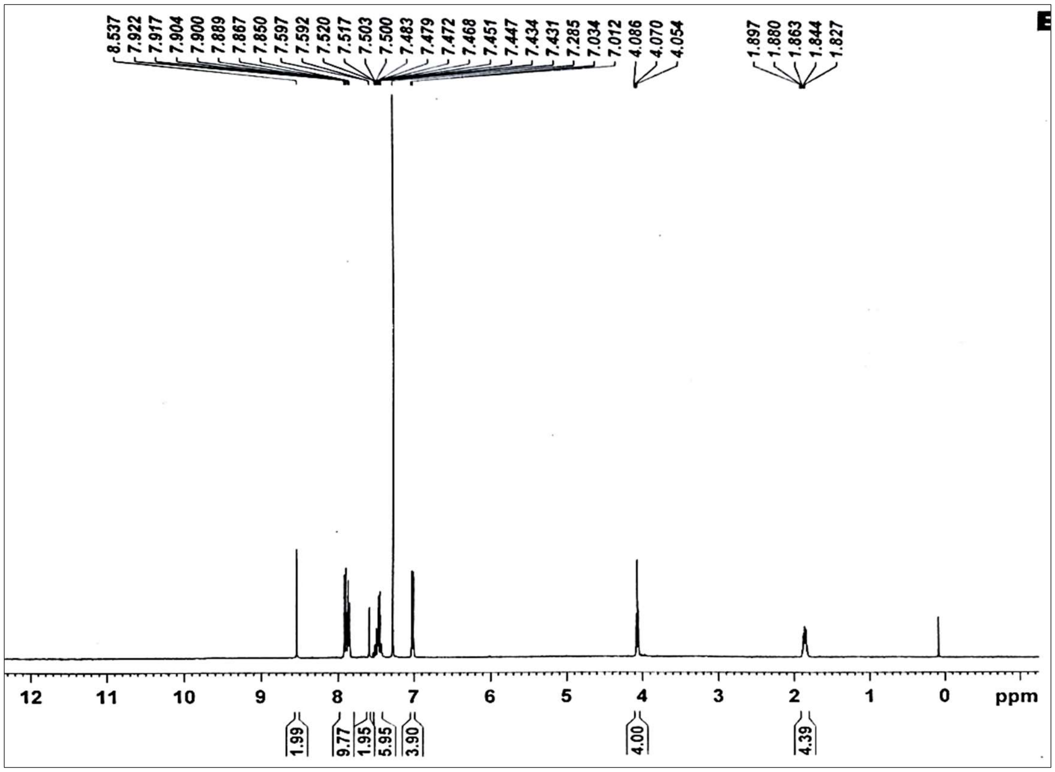

Fig. S2A.36: ^{1}H NMR of *II-4*

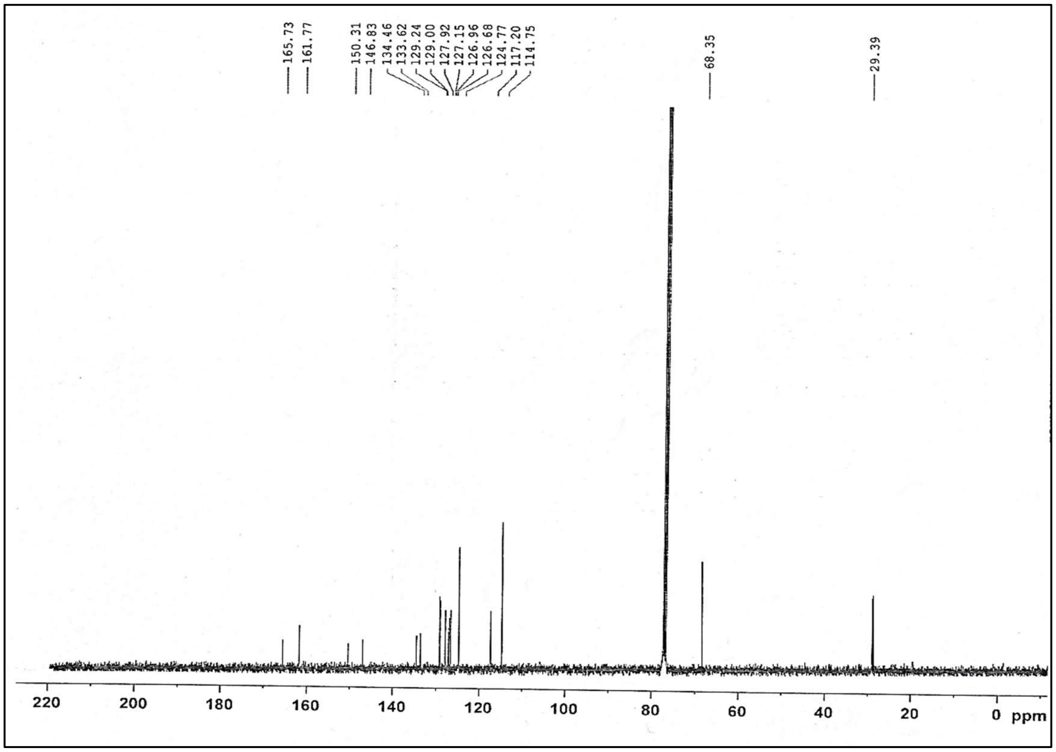

Fig. S2A.37: ^{13}C NMR of *II-4*

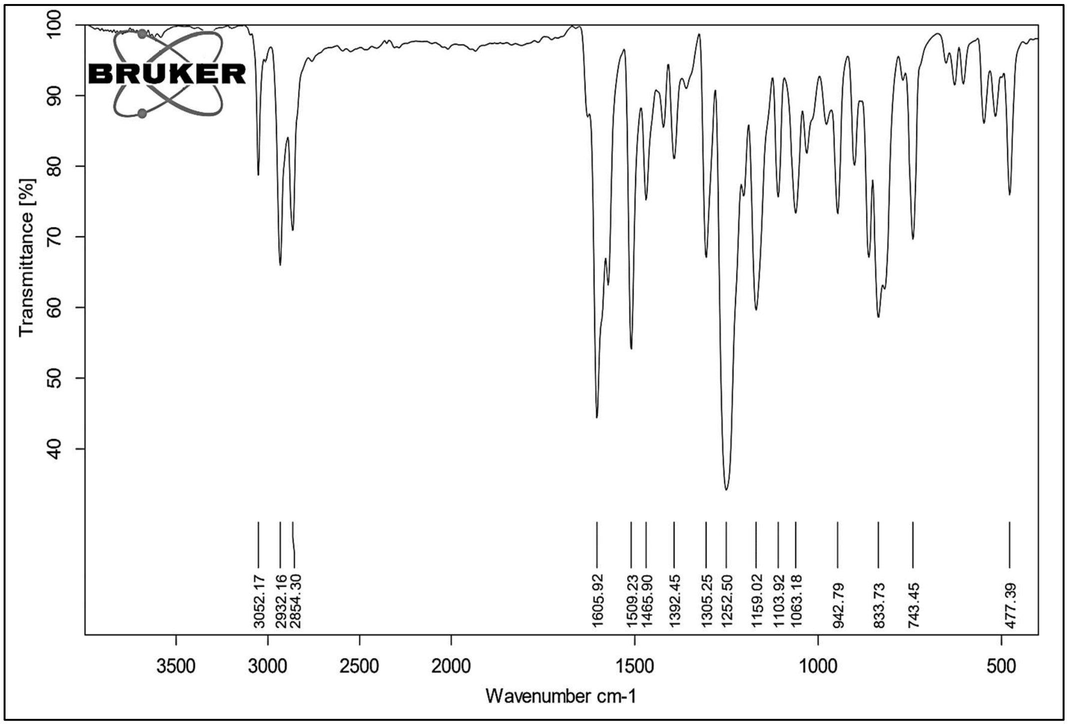

Fig. S2A.38: FT-IR spectra of *II-5*

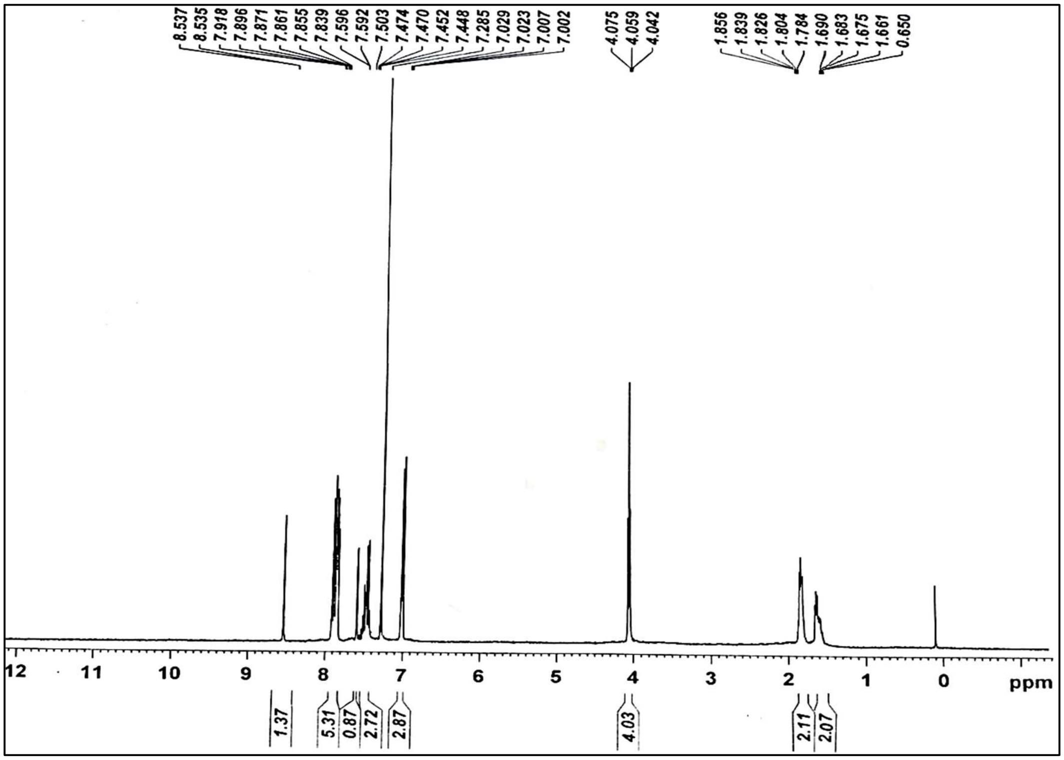

Fig. S2A.39: ^{1}H NMR of *II-5*

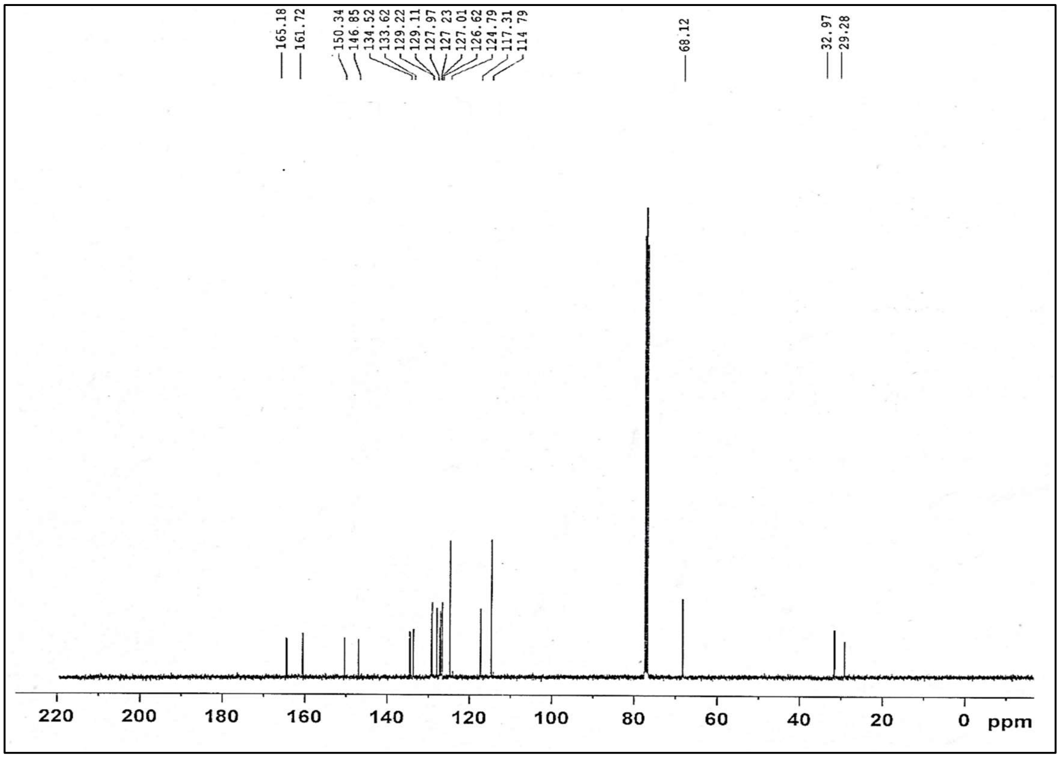

Fig. S2A.40: ^{13}C NMR of *II-5*

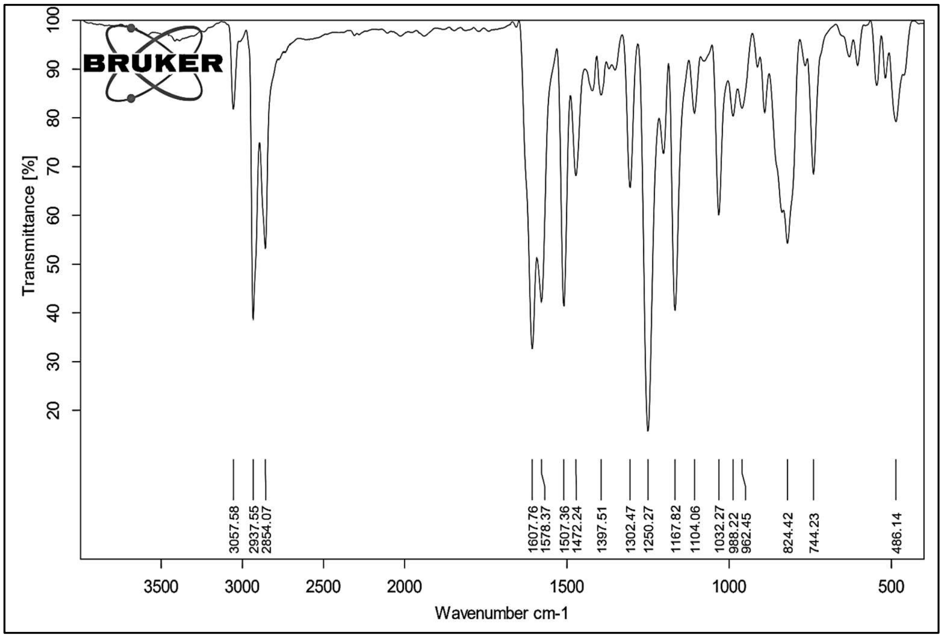

Fig. S2A.41: FT-IR spectra of *II-6*

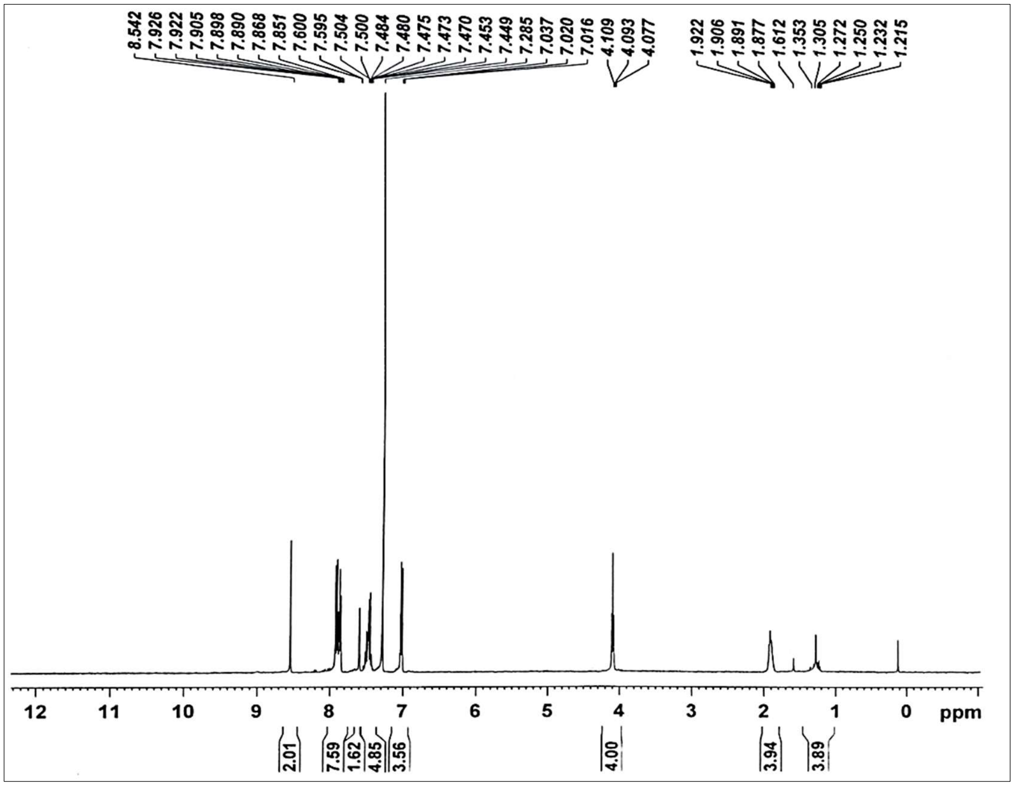

Fig. S2A.42: ^{1}H NMR of *II-6*

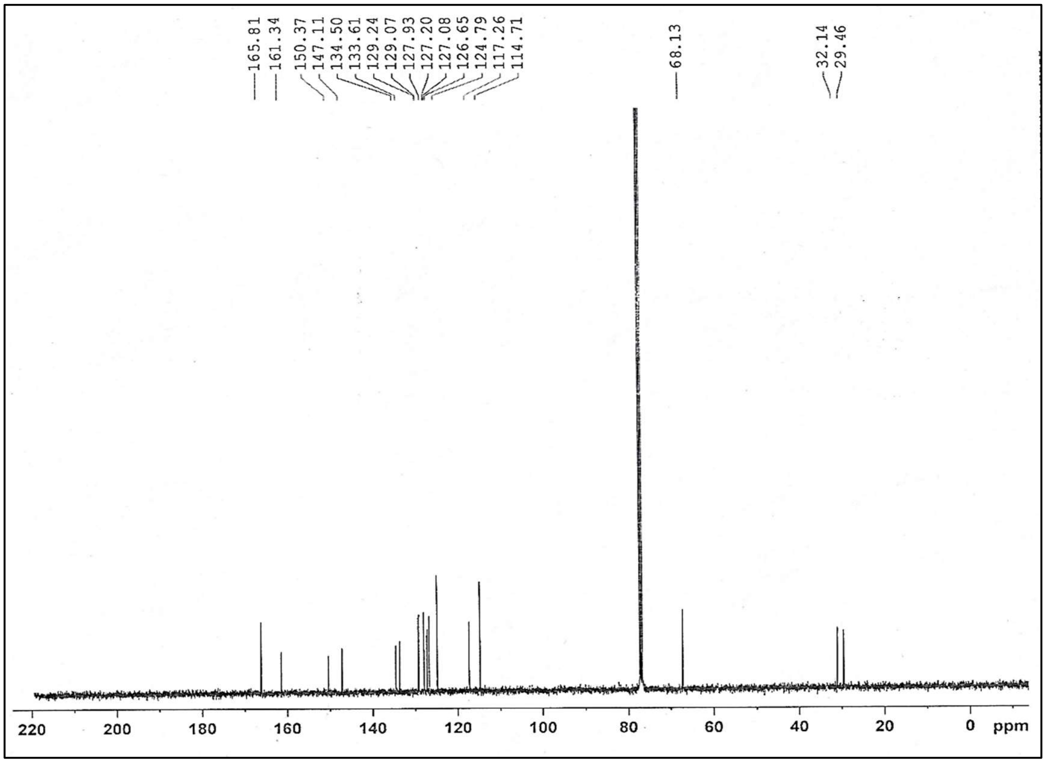

Fig. S2A.43: ^{13}C NMR of *II-6*

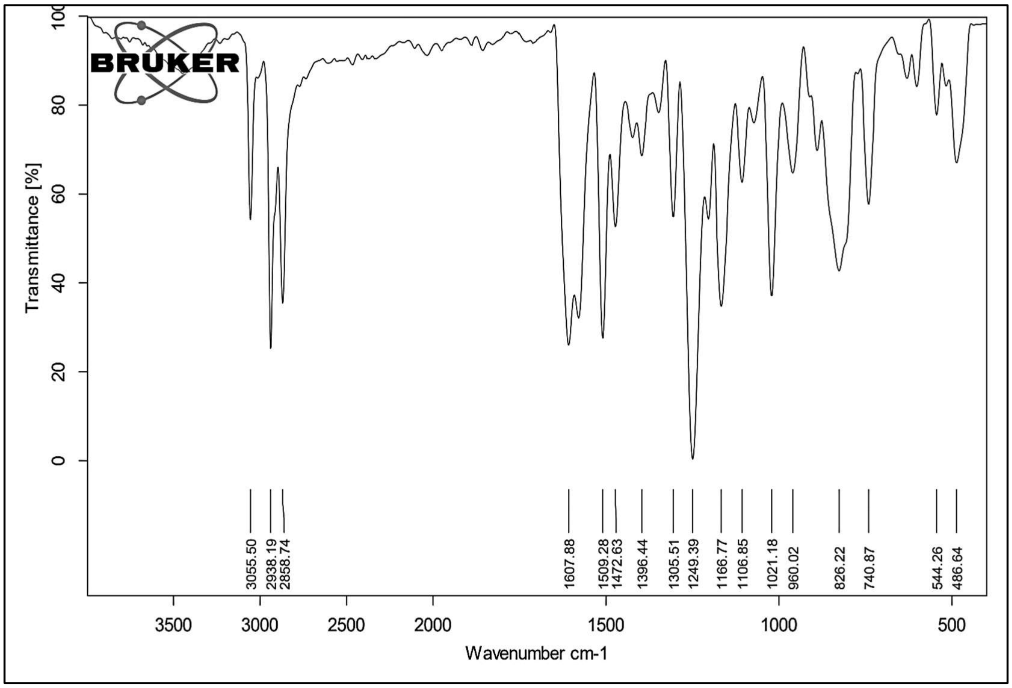

Fig. S2A.44: FT-IR spectra of *II-8*

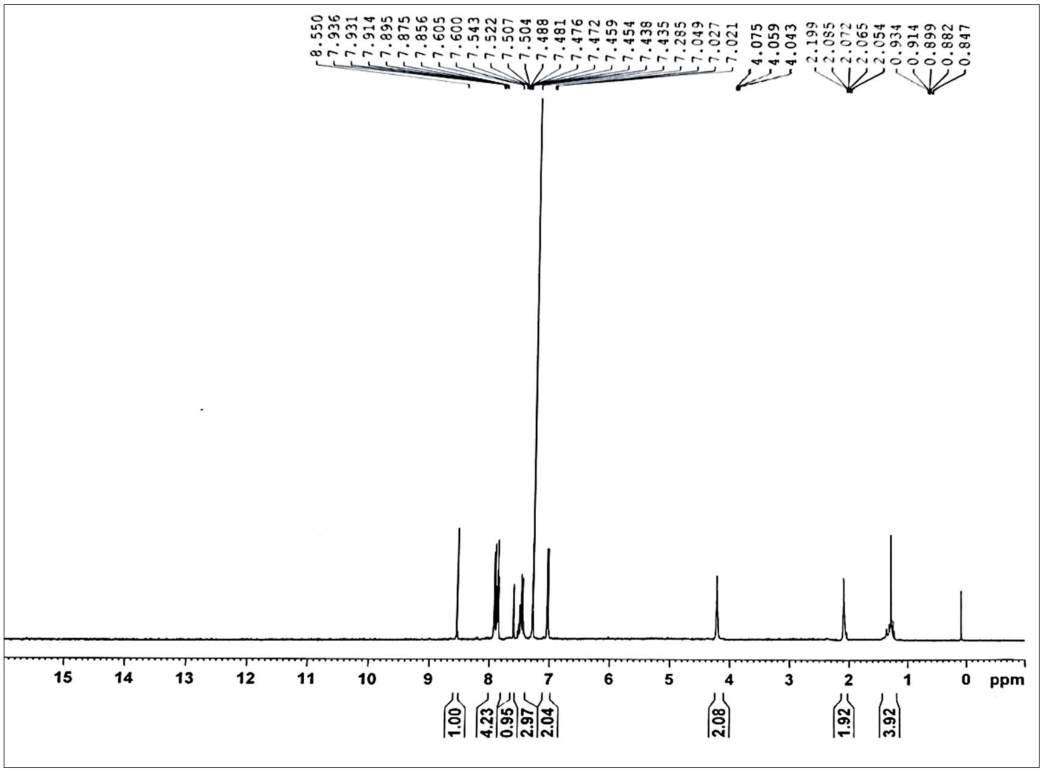

Fig. S2A.45: ^{1}H NMR of *II-8*

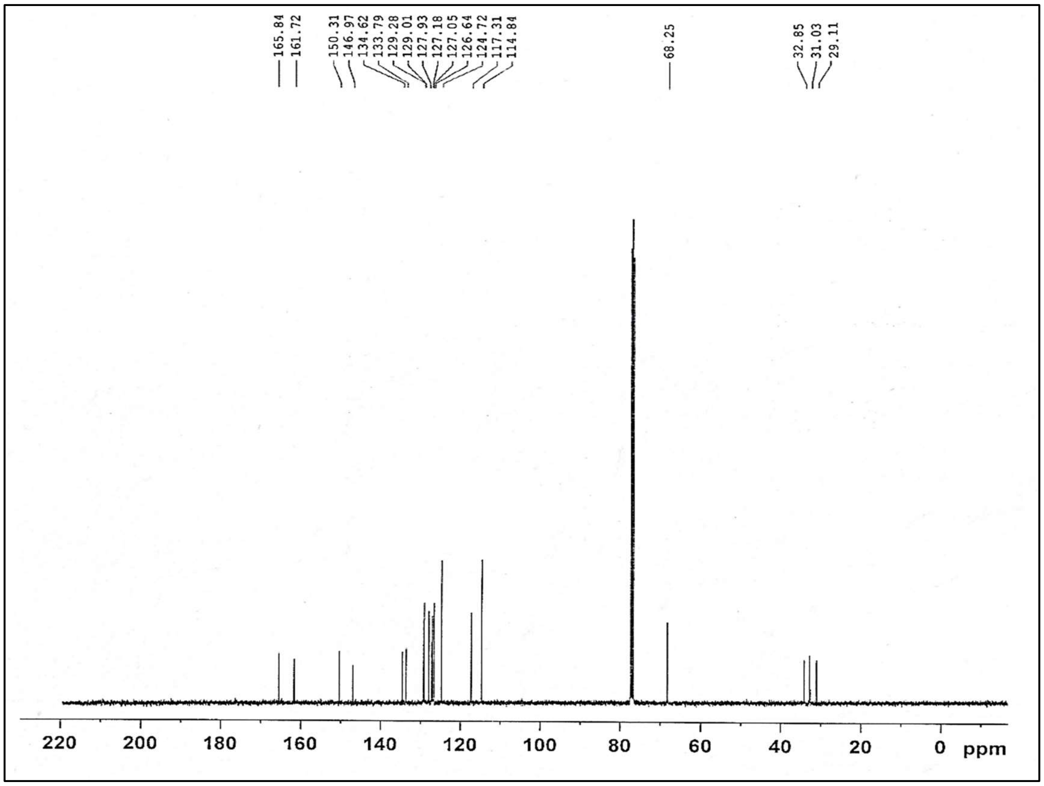

Fig. S2A.46: ^{13}C NMR of *II-8*

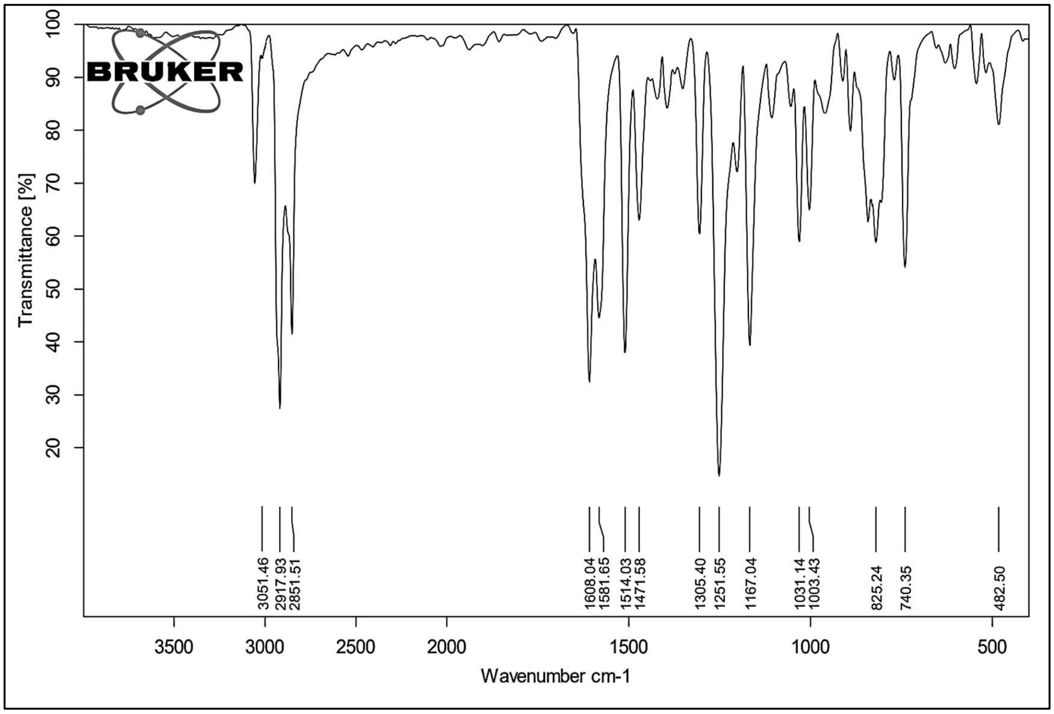

Fig. S2A.47: FT-IR spectra of *II-10*

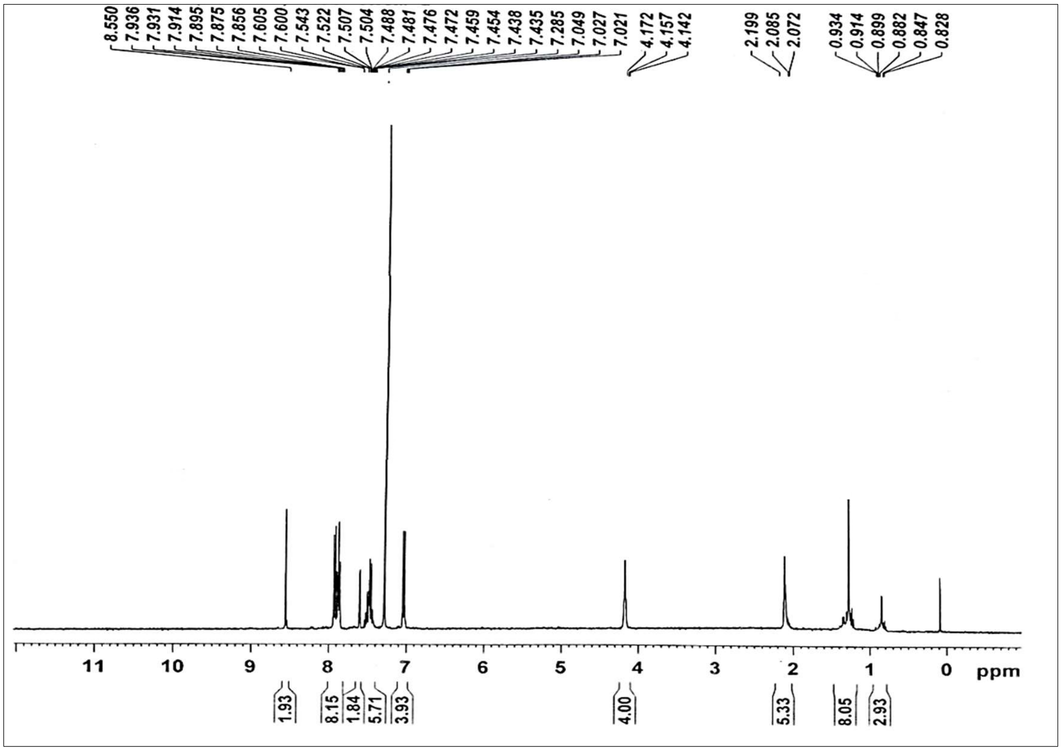

Fig. S2A.48: ^{1}H NMR of *II-10*

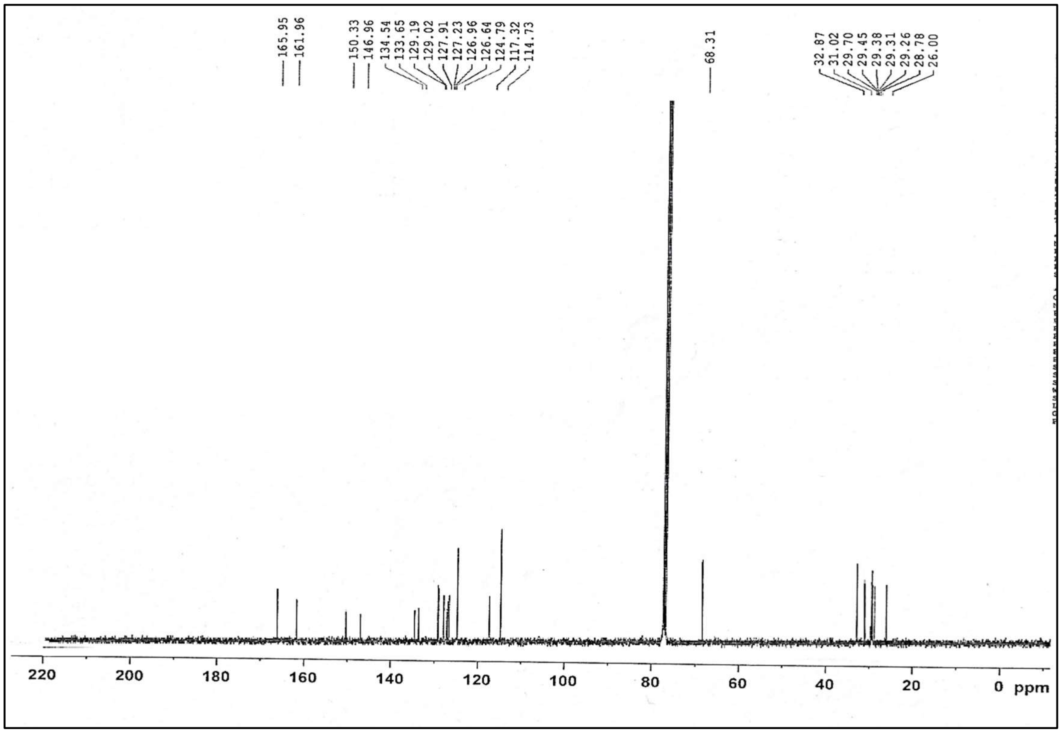

Fig. S2A.49: ^{13}C NMR of *II-10*

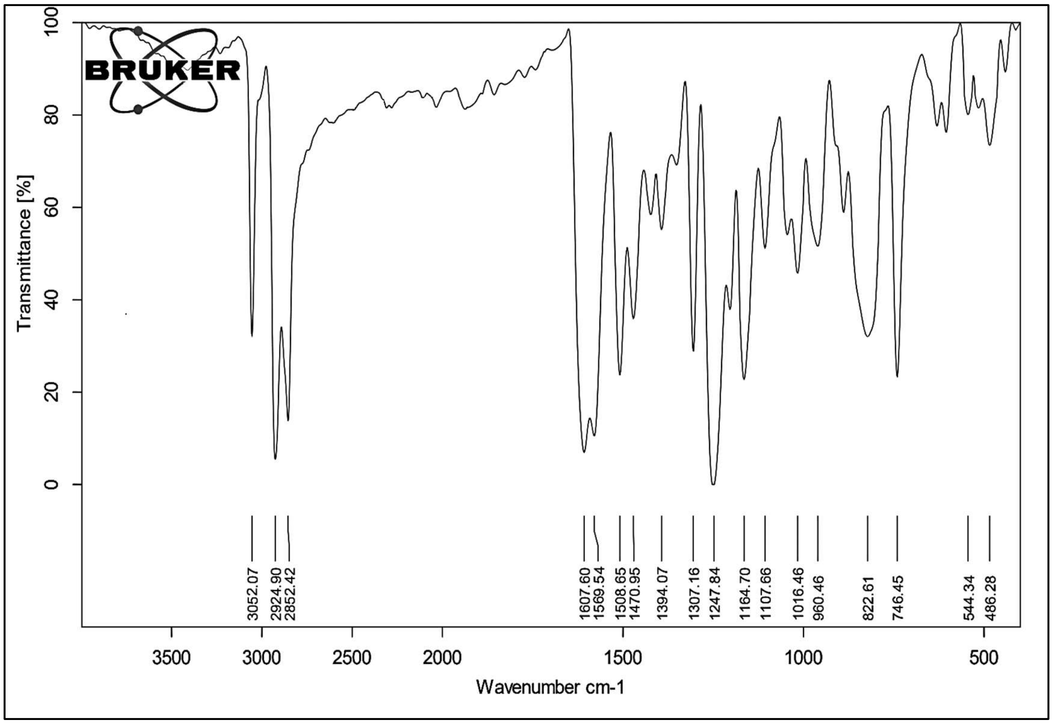

Fig. S2A.50: FT-IR spectra of *II-12*

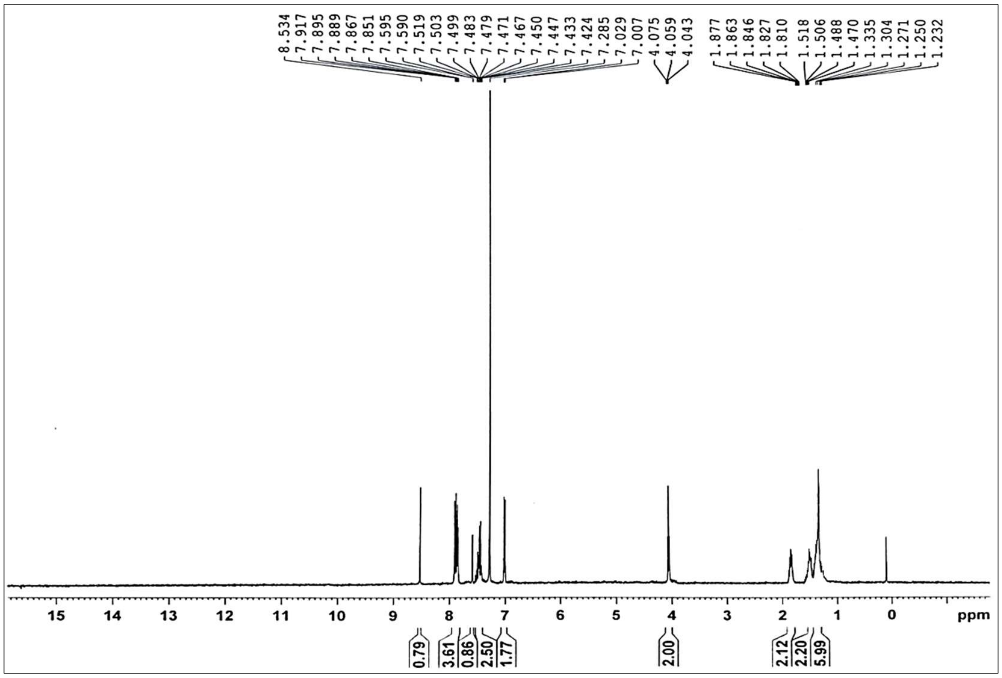

Fig. S2A.51: ^{1}H NMR of *II-12*

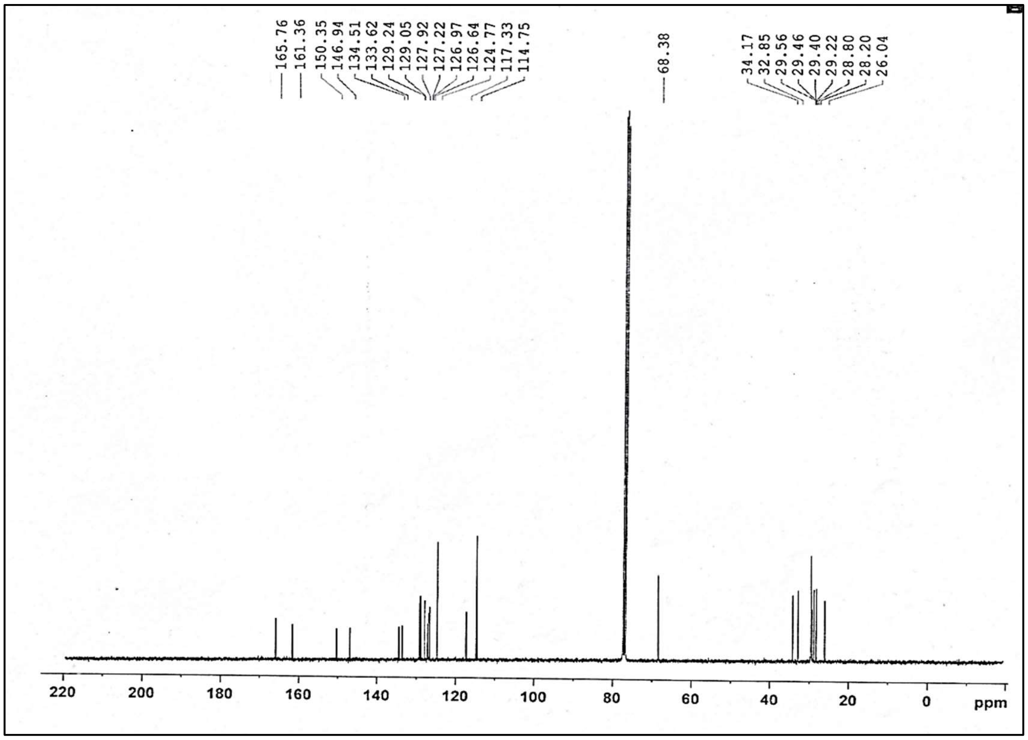

Fig. S2A.52: ^{13}C NMR of *II-12*

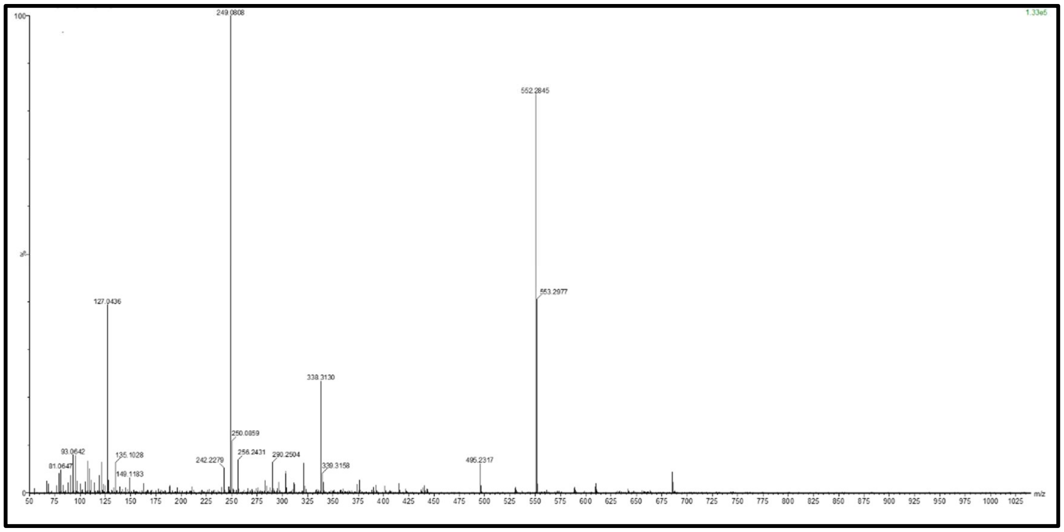

Fig. S2A.53: Mass spectra of *I-4*

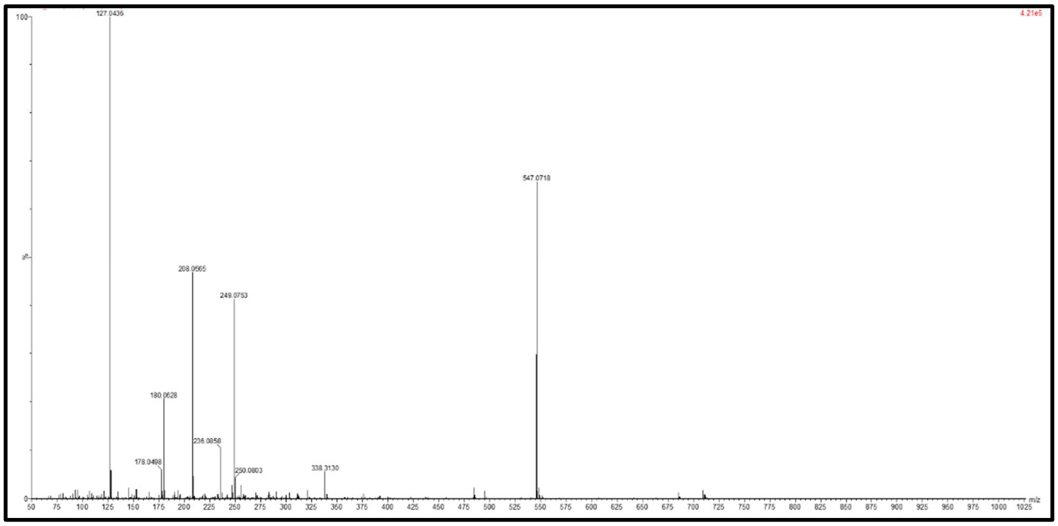

Fig. S2A.54: Mass spectra of *II-4*

2A.7 DSC thermogram of prepared dimers

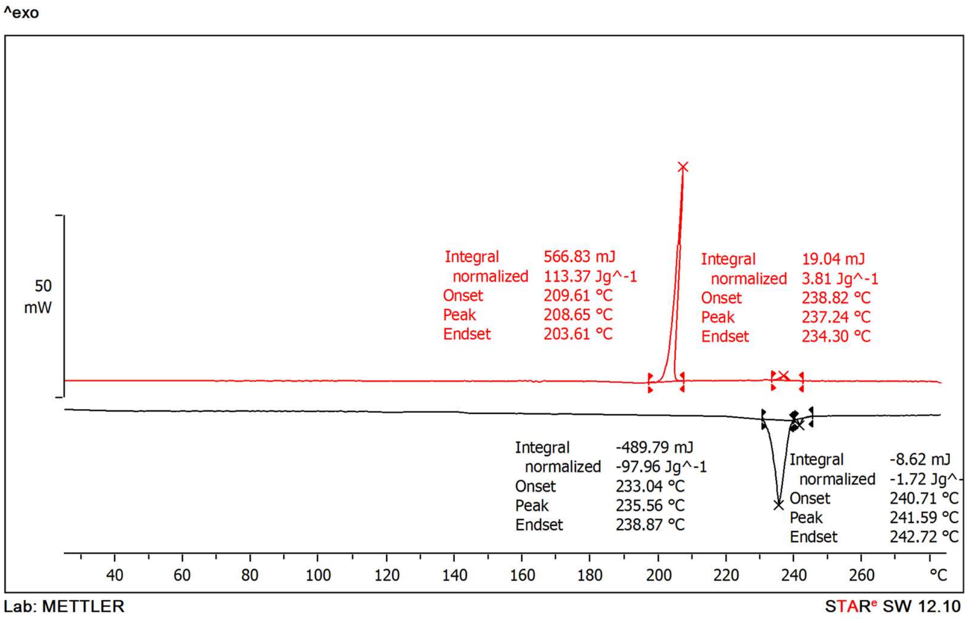

Fig. S2A.55: DSC Thermogram of *I-2*

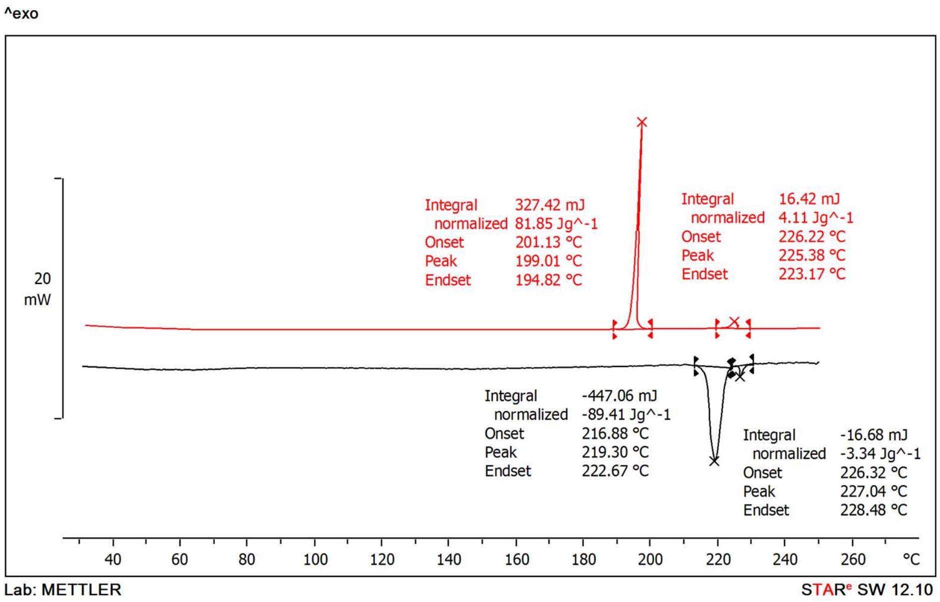

Fig. S2A.56: DSC Thermogram of *I-4*

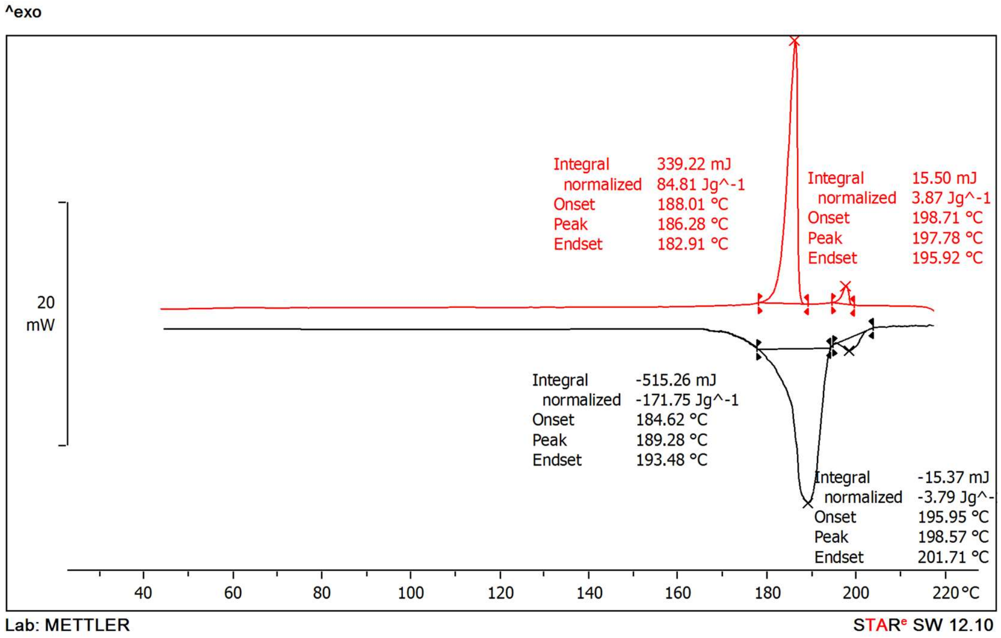

Fig. S2A.57: DSC Thermogram of *I-6*

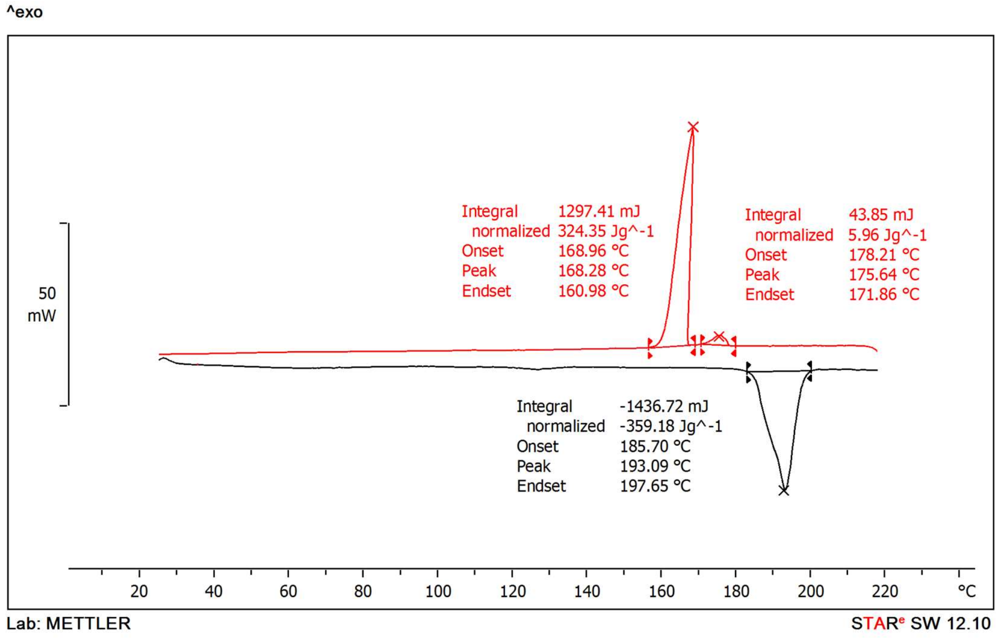

Fig. S2A.58: DSC Thermogram of *I-8*

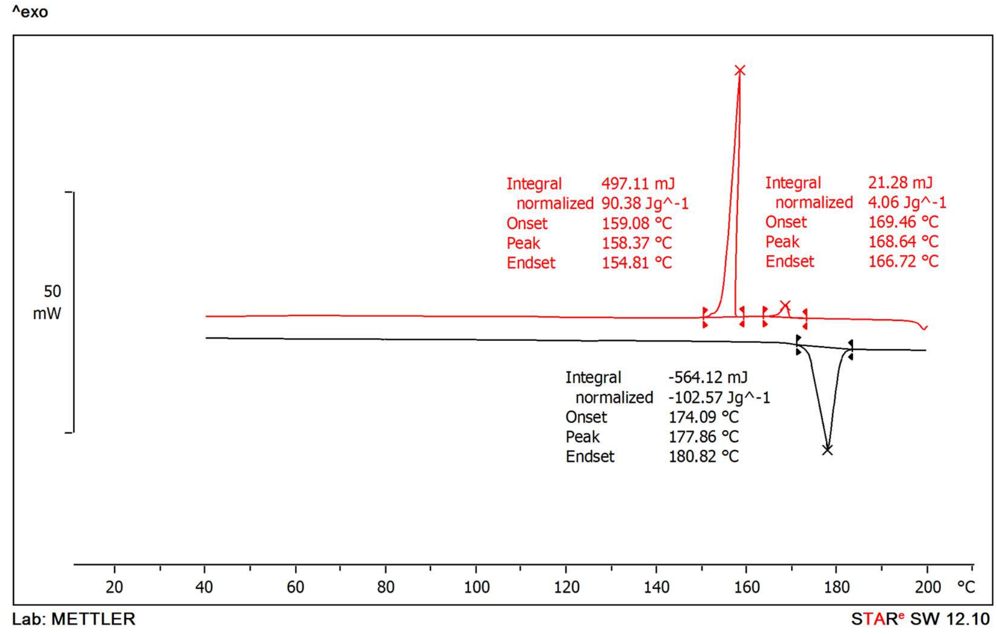

Fig. S2A.59: DSC Thermogram of *I-10*

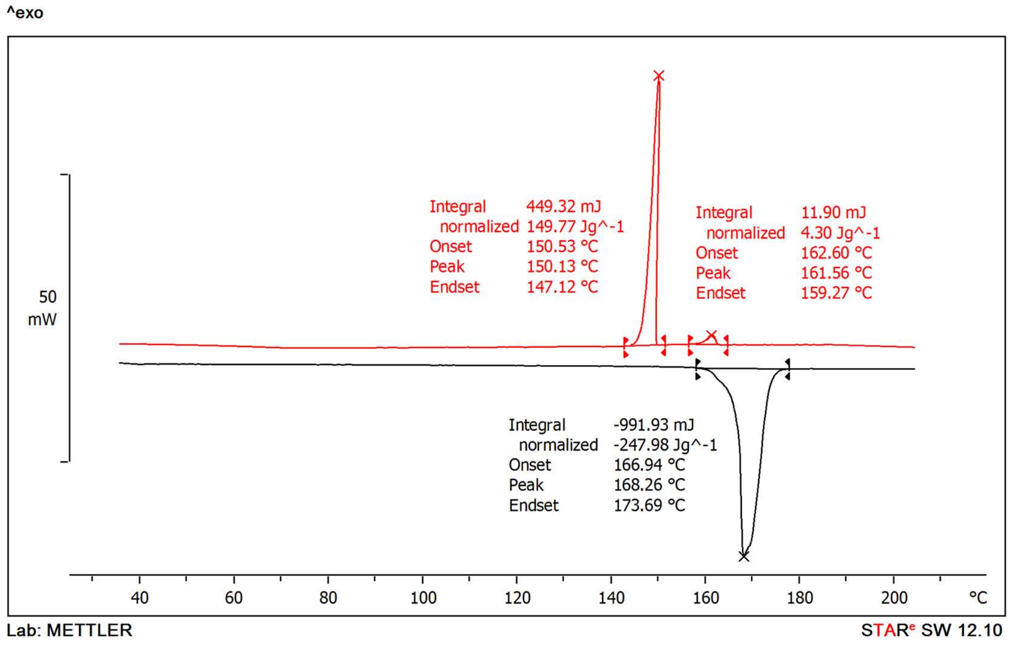

Fig. S2A.60: DSC Thermogram of *I-12*

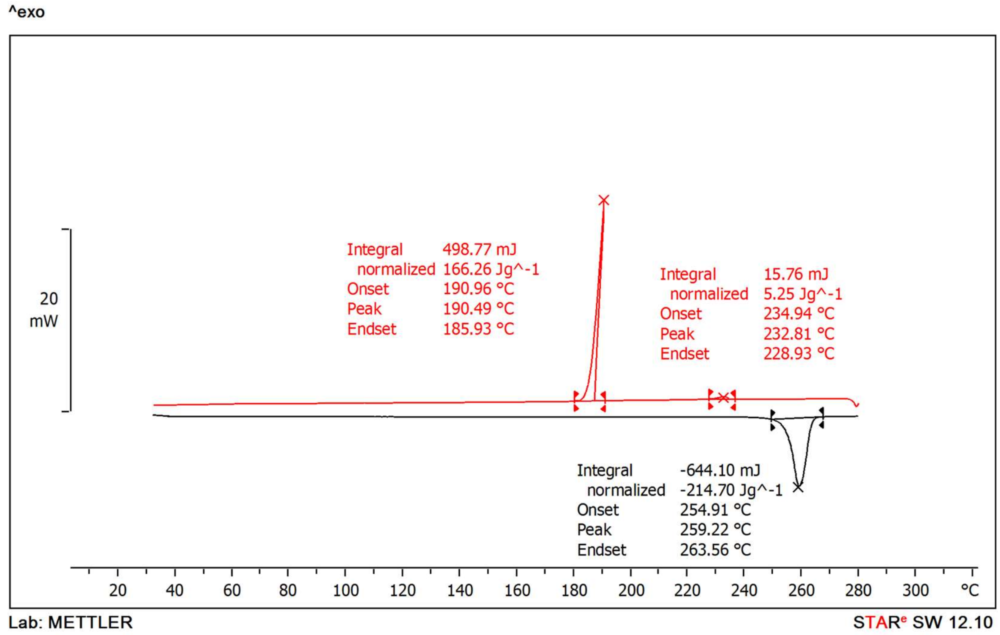

Fig. S2A.61: DSC Thermogram of *II-2*

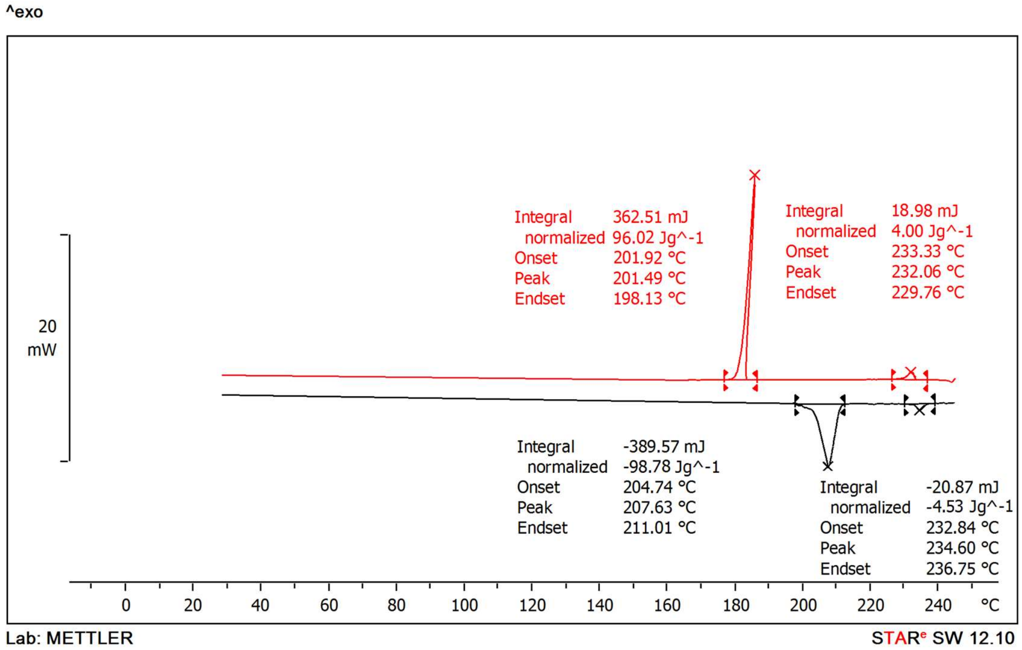

Fig. S2A.62: DSC Thermogram of *II-4*

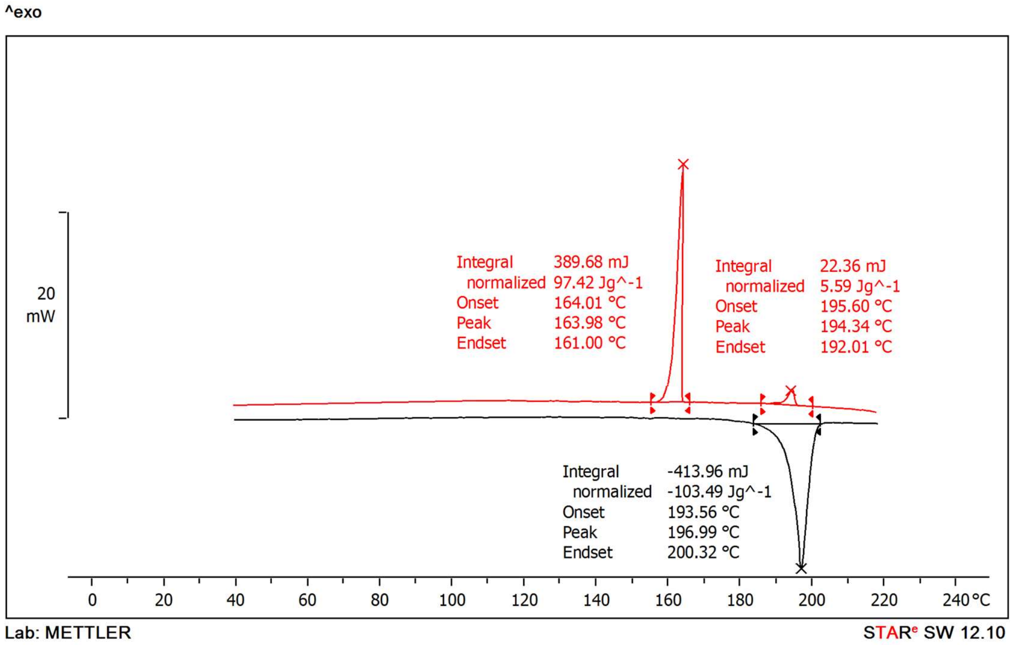

Fig. S2A.63: DSC Thermogram of *II-6*

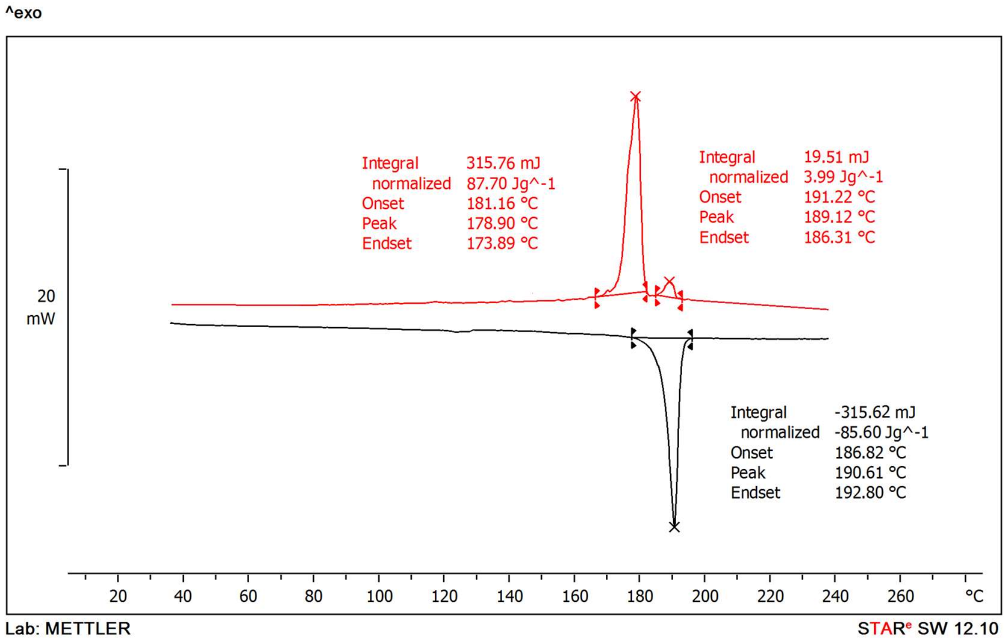

Fig. S2A.64: DSC Thermogram of *II-8*

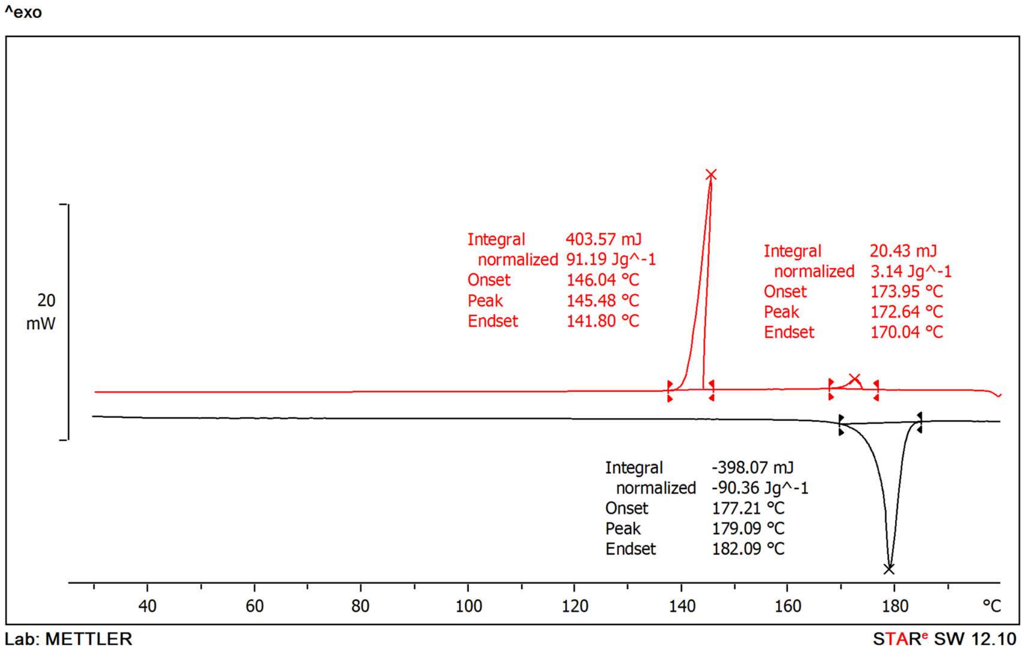

Fig. S2A.65 DSC Thermogram of *II-10*

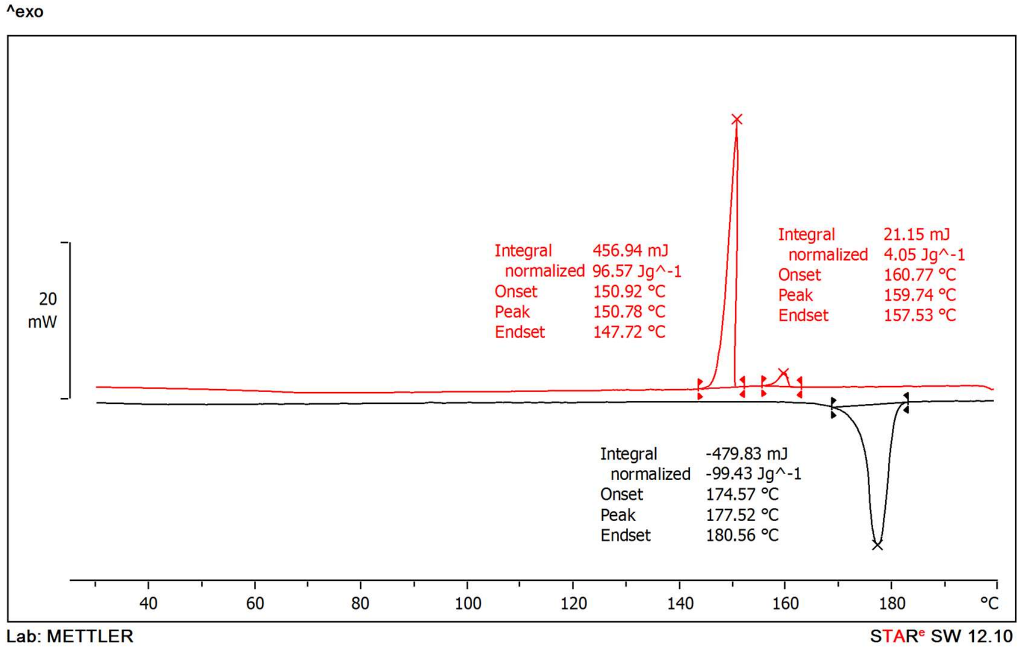

Fig. S2A.66: DSC Thermogram of *II-12*

2A.8 References

1 A. K. Prajapati, H. M. Pandya and N. L. Bonde, *J. Chem. Sci.*, 2004, **116**, 227–233.

2 H. N. Patel and A. K. Prajapati, *Mol. Cryst. Liq. Cryst.*, 2017, **643**, 106–115.

3 H. A. Ahmed and M. A. El-Atawy, *Liq. Cryst.*, 2021, **48**, 1940–1952.

4 C. T. Imrie, ed. D. M. P. Mingos, Springer Berlin Heidelberg, Berlin, Heidelberg, 1999, pp. 149–192.

5 C. T. Imrie and P. A. Henderson, *Chem. Soc. Rev.*, 2007, **36**, 2096–2124.

6 M. Alaasar and C. Tschierske, *Liq. Cryst.*, 2017, **44**, 387–393.

7 A. T. M. Marcelis, A. Koudijs, Z. Karczmarzyk1 and E. J. R. Sudhölter, *Liq. Cryst.*, 2003, **30**, 1357–1364.

8 M. Rabari, Y. Parmar and A. K. Prajapati, *Liq. Cryst.*, 2023, **50**, 2552-2570.

9 M. Rabari, C. Koli and A. K. Prajapati, *Soft Mater., 2024,* **22,** 1-12.

10 Y. Arakawa, K. Komatsu, J. Feng, C. Zhu and H. Tsuji, *Mater. Adv.*, 2021, **2**, 261–272.

11 P. A. Henderson, O. Niemeyer and C. T. Imrie, *Liq. Cryst.*, 2001, **28**, 463–472.

12 Y. Arakawa, K. Komatsu, Y. Ishida, K. Igawa and H. Tsuji, *Tetrahedron*, 2021, **81**, 131870.

13 Y. Arakawa, K. Komatsu, S. Inui and H. Tsuji, *J. Mol. Struct.*, 2020, **1199**, 126913.

14 Z. Fang and C. Wu, *Liq. Cryst.*, 2020, **47**, 1086–1099.

15 M. M. Antonijevic and M. B. Petrović, *Int. J. Electrochem. Sci.,* 2008, **3**, 1-28.

16 X. Chen, L. Wang, C. Li, J. Xiao, H. Ding, X. Liu, X. Zhang, W. He and H. Yang, *Chem. Commun.*, 2013, **49**, 10097–10099.

17 A. R. Yuvaraj, G. S. Mei, A. D. Kulkarni, M. Y. Mashitah and G. Hegde, *RSC Adv.*, 2014, **4**, 50811–50818.

18 A. Zep, K. Sitkowska, D. Pociecha and E. Gorecka, *J. Mater. Chem. C*, 2014, **2**, 2323–2327.

19 G.-Y. Yeap, S. Balamurugan and S. Rakesh, *Liq. Cryst.*, 2013, **40**, 555–563.

20 Y. Arakawa, K. Komatsu, Y. Ishida and H. Tsuji, *Liq. Cryst.*, 2021, **48**, 641-652.

21 M. M., A. Roy and V. Prasad, *New J. Chem.*, 2017, **41**, 11576–11583.

22 M. Horčic, J. Svoboda, V. Novotná, D. Pociecha and E. Gorecka, *RSC Adv.*, 2018, **8**, 22974–22985.

23 A. K. Prajapati, M. C. Varia and S. P. Sahoo, *Liq. Cryst.*, 2011, **38**, 861–869.

24 A. K. Prajapati, M. C. Varia and S. P. Sahoo, *Phase Transitions*, 2011, **84**, 325–342.

25 M. C. Varia, S. Kumar and A. K. Prajapati, *Liq. Cryst.*, 2012, **39**, 365–371.

26 A. K. Prajapati and M. C. Varia, *Liq. Cryst.*, 2013, **40**, 1151–1158.

27 S. M. Gan, A. R. Yuvaraj, M. R. Lutfor, M. Y. Mashitah and H. Gurumurthy, *RSC Adv.*, 2015, **5**, 6279–6285.

28 M. Vijay Srinivasan and P. Kannan, *J. Mater. Sci.*, 2011, **46**, 5029–5043.

29 G. Hegde, R. A. Alla, A. Matharu and L. Komitov, *J. Mater. Chem. C*, 2013, **1**, 3600–3605.

30 C. V. Yelamaggad, M. Mathews, U. S. Hiremath, G. G. Nair, D. S. Shankar Rao and S. Krishna Prasad, *Liq. Cryst.*, 2003, **30**, 899–908.

31 A. Iwan, P. Bilski, H. Janeczek, B. Jarzabek, M. Domanski, P. Rannou, A. Sikora, D. Pociecha and B. Kaczmarczyk, *J. Mol. Struct.*, 2010, **963**, 175–182.

32 P. K. Bhowmik, H. Han, A. K. Nedeltchev, H. D. Mandal, J. A. Jimenez-Hernandez, P. M. McGannon, L. Lopez, S.-W. Kang and S. Kumar, *Liq. Cryst.*, 2009, **36**, 1389–1399.

33 L. Marin, A. Zabulica and M. Sava, *Liq. Cryst.*, 2011, **38**, 433–440.

34 E. Perju and L. Marin, *Molecules*, 2021, **8,** 2183

35 E. Cruickshank, R. Walker, G. J. Strachan, C. H. F. Goode, M. M. Majewska, D. Pociecha, E. Gorecka, J. M. D. Storey and C. T. Imrie, *J. Mol. Liq.*, 2023, **391**, 123226.

36 E. Forsyth, D. A. Paterson, E. Cruickshank, G. J. Strachan, E. Gorecka, R. Walker, J. M. D. Storey and C. T. Imrie, *J. Mol. Liq.*, 2020, **320**, 114391.

37 Y. Arakawa, Y. Ishida, K. Komatsu, Y. Arai and H. Tsuji, *Tetrahedron*, 2021, **95**, 132351.

38 K.-L. Foo, S.-T. Ha, C.-M. Lin, H.-C. Lin, S.-L. Lee, G.-Y. Yeap and S. S. Sastry, *Karbala Int. J. Mod. Sci.*, 2015, **1**, 152–158.

39 R. W. Date, C. T. Imrie, G. R. Luckhurst and J. M. Seddon, *Liq. Cryst.*, 1992, **12**, 203–238.

40 G. S. Attard and C. T. Imrie, *Liq. Cryst.*, 1992, **11**, 785–789.

41 G. S. Attard, C. T. Imrie and F. E. Karasz, *Chem. Mater.*, 1992, **4**, 1246–1253.

42 R. Walker, M. Majewska, D. Pociecha, A. Makal, J. M. D. Storey, E. Gorecka and C. T. Imrie, *ChemPhysChem*, 2021, **22**, 461–470.

43 T. Donaldson, H. Staesche, Z. B. Lu, P. A. Henderson, M. F. Achard and C. T. Imrie, *Liq. Cryst.*, 2010, **37**, 1097–1110.

44 M. Rabari, R. S. Kumar CH and A. K. Prajapati, *J. Mol. Struct.*, 2023, **1293**, 136252.

45 P. Govindasamy, S. Gunasekaran and S. Srinivasan, *Spectrochim. Acta. A. Mol. Biomol. Spectrosc.*, 2014, **130**, 329–336.

46 D. Bhattacharjee, T. K. Devi, R. Dabrowski and A. Bhattacharjee, *J. Mol. Liq.*, 2018, **272**, 239–252.

CHAPTER 2 (B)

NAPHTHYL DERIVATIVES WITH BROMOALKOXY TAIL: SYNTHESIS, CHARACTERIZATION AND ITS MESOMORPHIC PROPERTIES

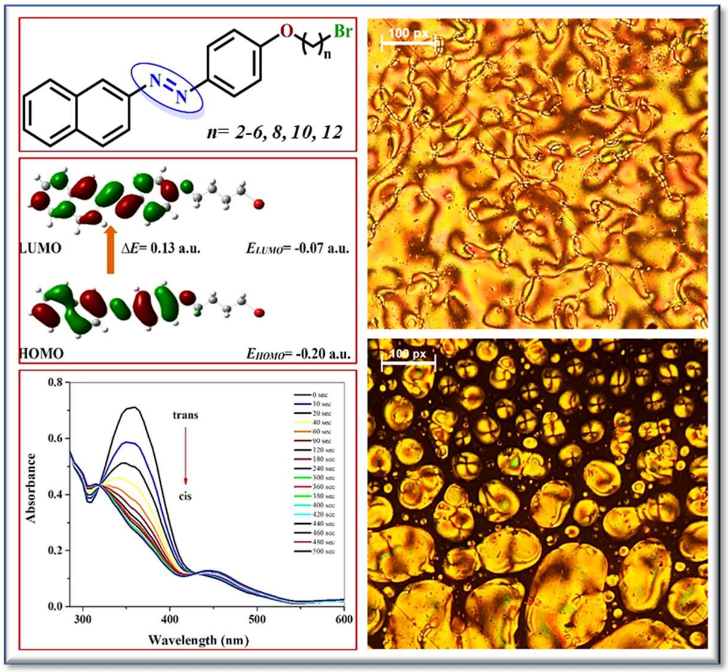

2B.1 Introduction

The mesogenic behaviour of a compound depends primarily on its molecular geometry, and studies have shown that even little changes to a material's molecular architecture can result in significant changes to its mesomorphic features.[1,2] To create a novel geometry for LCs that might produce compounds with varying mesomorphic characteristics and other technological uses, the azo (-N=N-) group is regarded as a worthy connecting group[3,4]. Azo linkage containing LCs are advantageous for thermo-stable mechanisms due to their high thermal stability.[5,6] Azo linkages keep the molecular geometry stiff and linear, supporting the stability of the mesomorphic features of LCs.[7,8] Because of their photochromic and photothermal properties, compounds based on azobenzene have a variety of uses, including photonics, optical storage devices etc.[9,10] Additionally, it is known that liquid crystals containing azo benzene exhibit a reversible *trans-cis* photo isomerization process when exposed to alternating UV-vis light.[11]

The mesogenic characteristics may be diminished when the molecules' width rises.[12] Derivatives of naphthalene, however, may show rich mesomorphism provided the molecule is made with care and precision. As naphthalene derivatives display rich mesomorphism, a significant number of liquid crystalline naphthyl derivatives are documented in the literature.[13] Mesogenic compounds possessing naphthalene moiety are depicted in **Fig. 2B.1.**

In 1954 Wiegand reported many LC Schiff bases of 1,4-, 2,6-, and 1,5-diaminonaphthalenes.[14] Different alkoxy naphthoic acids were examined for mesomorphic characteristics by Gray and Jones[15]. Dave et al. investigated a range of mesogenic naphthalene derivatives, including cholesterol esters and alkoxy benzoates of 1,4- and 1,5-dihydroxynaphthalene[16]. Recent publications on the synthesis and mesomorphic features of liquid crystalline 2,3- and 2,6-dihydroxynaphthalene compounds as well as a few reports of the synthesis of banana-shaped 2,7-dihydroxyxanthone derivatives[17–20]. Ahmed et al. recently described a naphthalene derivative with good mesomorphic characteristics that has two proportionated terminal alkoxy groups.[21] Recently, some naphthalene imidazolium-based ionic liquid crystals that show luminescence were discovered.[22] Earlier our group synthesized the homologous series of unsubstituted Schiff's base esters of naphthalene, Schiff base ester with a lateral thiol group on position-1 of naphthalene moiety [23] and bulky lateral methoxy group on central phenyl moiety[24] to study the effect of lateral thiol and methoxy group on mesomorphism.

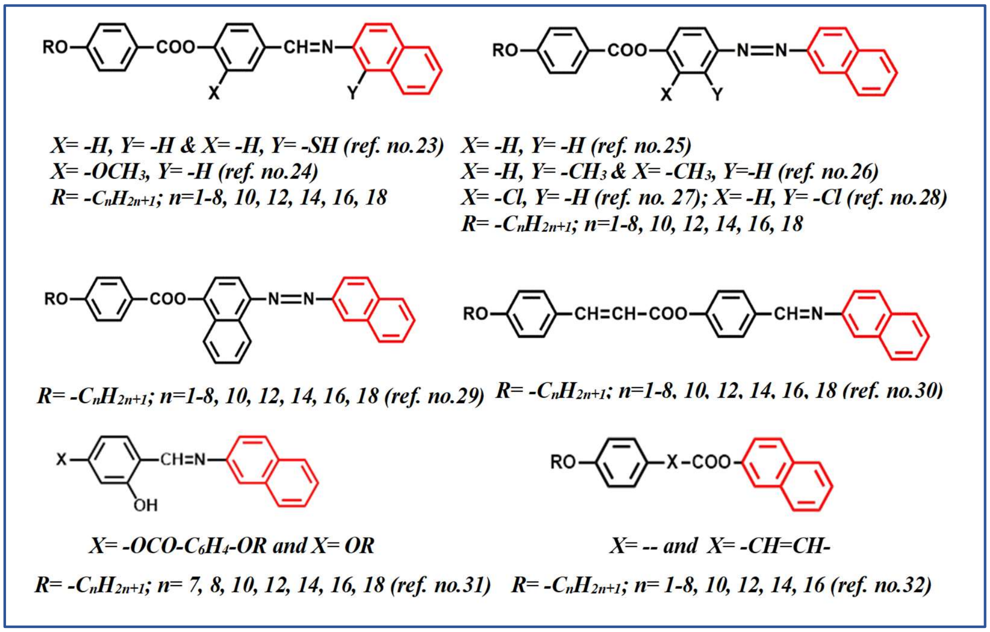

Fig. 2B.1: Mesogenic compounds possessing naphthalene moiety

Our group has reported various compounds of naphthalene containing azo mesogens with and without lateral substituents and investigated the effect of various lateral substituents on mesogenic properties.[25–28] A new liquid crystalline homologous series in which two naphthalene units are connected to each other by azo linkage also reported by us.[29] Homologous series containing cinnamoyl linkages also has been reported and the mesomorphic properties and structure-property relationship between naphthalene moiety and various linking groups investigated.[30] Two liquid crystalline homologous series of salicylaldimines and their mesogenic Cu(II) complexes containing naphthalene moiety and the effects of different chain lengths on their mesogenic properties were investigated by studying the physical parameters.[31] Recent reports on two mesogenic series of naphthyl derivatives, viz. 2-Naphthyl-4-*n*-alkoxybenzoate and *trans*-2-Naphthyl-4-*n*-alkoxycinnamates.[32]

2B.2 Objectives

The rigid core of naphthalene is attached to linking unit azobenzene leads to stability of less ordered mesophases. The presence of terminal chain with polar bromine (Br) atom in the structure gives flexibility to the molecule. The objective of the current work is to synthesize bromine-terminated naphthyl azomesogens (**NpAzOnBr**) and examine their mesomorphism, as well as their optical properties and thermal properties. The effect of the number of flexible methylene spacers (n = 2,3,4,5,6,8,10,12) on transition temperatures and their thermal stability were studied. Density functional theory (DFT) calculations were used to study various theoretical parameters.

2B.3 Results and Discussion

2B.3.1 Synthesis

The synthesis of *(E)*-4-(naphthalen-2-yldiazenyl) phenol **NpAzOH** involved the conversion of naphthalene-2-amine to the desired product via diazotization and subsequent coupling with phenol in alkaline conditions. This was achieved by initially treating naphthalene-2-amine with concentrated HCl and sodium nitrite followed by addition to a mixture of phenol and sodium hydroxide. The resulting crude product was then recrystallized with absolute alcohol to yield an orange solid. Subsequently, the synthesis of **NpAzOnBr** *(E)*-1(4-(ω-bromoalkoxy)phenyl)-2-(naphthalen-2-yl)diazene was accomplished by refluxing *(E)*-4-(naphthalen-2-yldiazenyl) phenol with excess of α, ω-dibromoalkanes in the presence of anhydrous K_2CO_3 in acetone. The reaction mixture was monitored by TLC and after completion, the product was isolated by filtration, washed, and purified via column chromatography. Synthesis scheme for the NpAzOnBr is given in **Scheme 2B.1.**

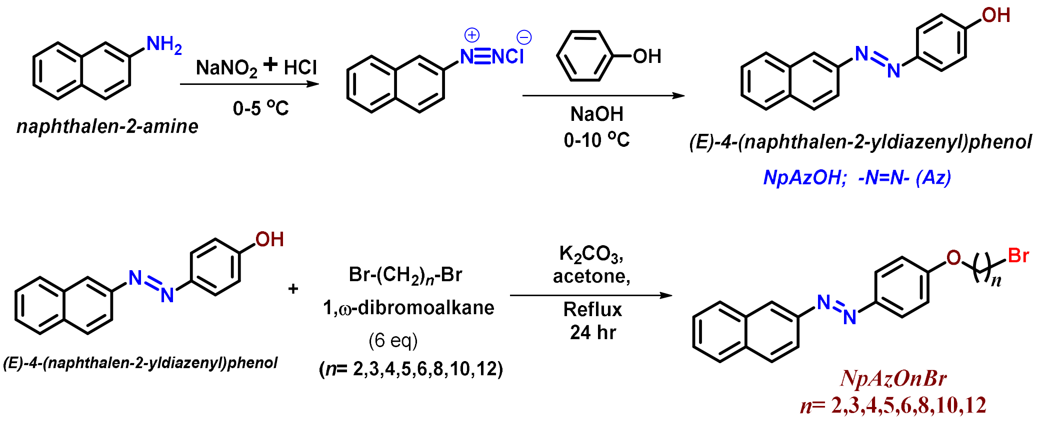

Scheme 2B.1: Synthesis scheme for the naphthyl derivatives

2B.3.2 Chemistry:

Through the use of various analytical methods, including FT-IR, ^{1}H NMR, ^{13}C NMR, mass spectrometry and ESI-Mass, the correct structures were verified. **NpAzOnBr** showed three peaks in their **FT-IR** spectra for the alkyl chain between 3095 and 2840 cm^{-1}, while the azo group's -N=N- stretching frequency was found between 1595 and

1600 cm^{-1}. The ether group experienced -C-O-C- stretching between 1200 and 1250 cm^{-1}, and the lack of a broad peak in the region of 3400-3450 cm^{-1} indicates that there is no free -OH group. Methylene protons ($-CH_2-CH_2-$) in the chain were seen as a multiplet at δ 1.2-2.0 in the **^{1}H-NMR** spectra of various substances. When methylene protons are connected to oxygen, triplets are seen in around δ 4.06-4.39 ppm, whereas when they are attached to -Br, triplets are present around δ 3.43-3.70 ppm. It is important to note that methylene protons attached to oxygen have a slightly lower value of chemical shift (more shielded region) than those attached to -Br. This suggests that the environment around the methylene protons is slightly more electron-rich when connected to oxygen than when connected to -Br. The aromatic protons of the naphthalene ring and phenyl ring had a chemical shift range of δ 6.5-8.0 ppm. Alkyl carbon peaks were found in the range of 15 to 30 ppm in the **^{13}C-NMR** spectra of **NpAzOnBr**, while peaks for methylene carbons which is directly connected to oxygen ($-\underline{O}-\mathbf{C}-$) were found at 68 ppm and methylene carbons next to bromine ($-\underline{\mathbf{C}}-Br$) were found at 32 ppm δ value. **ESI-MS** of **NpAzOnBr** shows $[M]^+$ peak corresponding to their molecular weight and $[M+2]^+$ isotopic peak corresponding to loss of -Br.

2B.3.3 Mesomorphic Behaviour

DSC curves and POM measurements allowed for the identification of distinct transition temperatures and textures for each compound, and they were all in good agreement throughout the various heating/cooling cycles.

2B.3.3.1 Differential scanning calorimetry study (DSC)

The thermograms were calculated utilising DSC (DSC-822, Mettler Toledo having Stare software). During both heating and cooling cycles, all phase transitions of the compounds were monitored at a rate of 10 ºC min^{-1}.

Without any mesogenic property, **NpAzOnBr** with a number of methylene units n = 2, 3, 8, 10, and 12 showed one endotherm on heating for crystalline to isotropic liquid phase (Cr-Iso) and one exotherm on cooling for isotropic liquid phase to crystallisation (Iso-Cr), whereas **NpAzOnBr** with a number of methylene units n = 4, 5, 6 showed one endotherm on heating for crystalline to isotropic liquid phase (Cr-Iso). The endotherm was found to occur at different temperatures depending on the length of the alkyl chain, suggesting a greater degree of mobility in compounds with longer chains.

Tble 2B. 1: Transition temperatures (in °C) and associated enthalpy of transition (ΔH) in (kJ mol^{-1}) of NpAzOnBr

Compound	n	Transition Temperatures (°C) and ΔH (kJmol^{-1})	
		Heating	Cooling
NpAzO2Br	2	Cr 134 (24.81) Iso	Iso 75 (-24.79) Cr
NpAzO3Br	3	Cr 108 (76.53) Iso	Iso 57 (-19.88) Cr
NpAzO4Br	4	Cr 113 (40.9) Iso	Iso 110 (-0.94) N 98 (-36.24) Cr
NpAzO5Br	5	Cr 109 (141.7) Iso	Iso 54 (-2.13) N 45 (-8.81) Cr
NpAzO6Br	6	Cr 126 (24.03) Iso	Iso 92 (-0.82) N 82 (-10.8) Cr
NpAzO8Br	8	Cr 112 (178.7) Iso	Iso 92 (-181.56) Cr
NpAzO10Br	10	Cr 106 (71.8) Iso	Iso 91 (-144.2) Cr
NpAzO12Br	12	Cr 111 (46.8) Iso	Iso 101 (-32.3) Cr

N, Nematic; Iso, Isotropic liquid; Cr, Crystalline solid

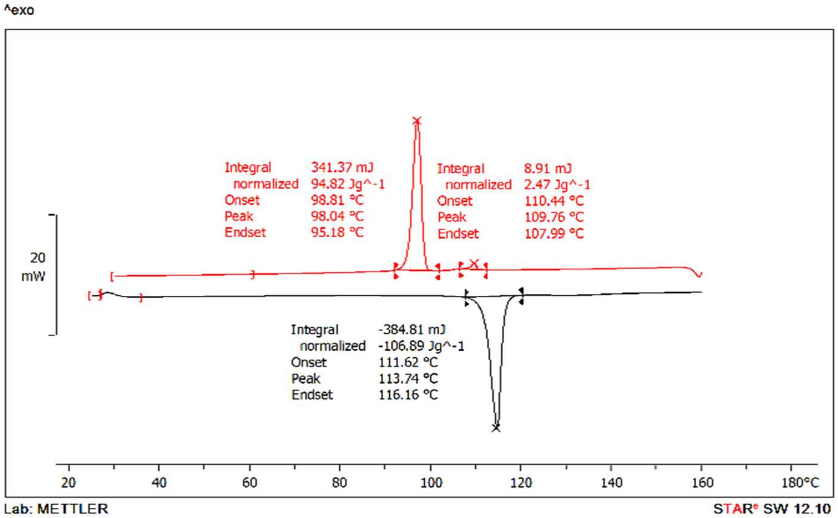

Fig. 2B.2: DSC Plot of compound NpAzO4Br

Two exotherms are seen as a result of the cooling, and they correspond to the transitions from the isotropic liquid phase to the nematic phase (Iso-N) and from the nematic phase to the crystalline solid state (N-Cr), respectively. Corresponding transition and mesogenic temperatures with the associated enthalpy of transition of the synthesized bromoalkoxy terminated azo naphthalene compounds mentioned in **Table 2B.1**. **Fig. 2B.2** represents the DSC thermogram of representative member **NpAzO4Br** which showed one endotherm on heating at 113.74 ºC for Cr-Iso transition and two exotherms are seen at 109.76 ºC and 98.04 ºC for Iso-N and N-Cr transitions, respectively.

2B.3.3.2 Polarising optical microscopy (POM)

The mesogenic properties of the compounds were observed using polarized light microscopy Leica DM2500P with phase contrast was used to observe the mesogenic characteristics, and the Leica DFC295 camera was used to capture the details of each compound. Lower members of series with ethyl (**NpAzO2Br**) and propyl (**NpAzO3Br**) chains, as well as higher members of series with octyl (**NpAzO8Br**), decyl (**NpAzO10Br**) and dodecyl (**NpAzO12Br**) chain, did not show any mesomorphic properties. Compounds having butyl (**NpAzO4Br**), pentyl (**NpAzO5Br**) and hexyl (**NpAzO6Br**) chains showed monotropic nematic phase. The photomicrographs (**Fig. 2B.3**) showed a clear transition from an isotropic liquid phase to a nematic phase as the temperature decreased. The nematic droplets remained stable until the transition temperature was reached, after which they began to merge and coalesce until the schlieren texture of the nematic phase was established. This schlieren texture eventually disappeared upon cooling further, which corresponded with the onset of crystallisation.

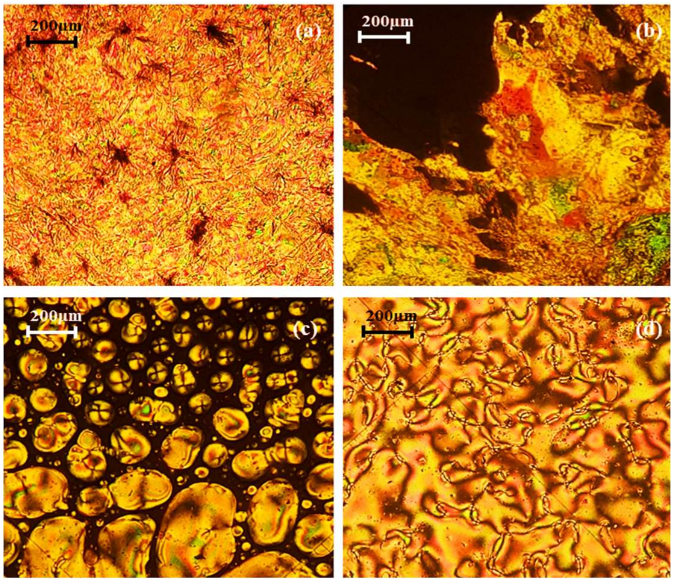

Fig. 2B.3: Optical photomicrographs of NpAzO4Br (a) Crystalline state (b) Cr-Iso at 113 °C (c) nematic droplets of Iso-N transition at 110 °C (d) schlieren texture at 108 °C

The compound **NpAzO2Br and NpAzO3Br** melt into isotropic liquid without a mesophase and on cooling from isotropic liquid, crystallized directly without exhibiting any liquid crystalline properties. On heating, from crystalline solid (**Fig. 2B.3a**) in an ordinary slide, **NpAzO4Br** directly melts into an isotropic liquid at 113 °C (**Fig.**

2B.3b). On cooling from isotropic liquid, **NpAzO4Br** showed nematic droplets at 110 °C (**Fig. 2B.3c**) which coalesces to a classical thread like schlieren texture (**Fig. 2B.3d**). On further cooling it starts crystallizing around 99 °C. The compounds **NpAzO5Br** and **NpAzO6Br** also show the thread-like schlieren texture of nematic mesophase on cooling from an isotropic liquid.

2B.3.3.3 Structural dependence on mesomorphism:

The graph of phase-transition temperatures against the number of carbons in the bromo-alkoxy tail enabled the identification of the effects of the terminal chain on the LC properties.

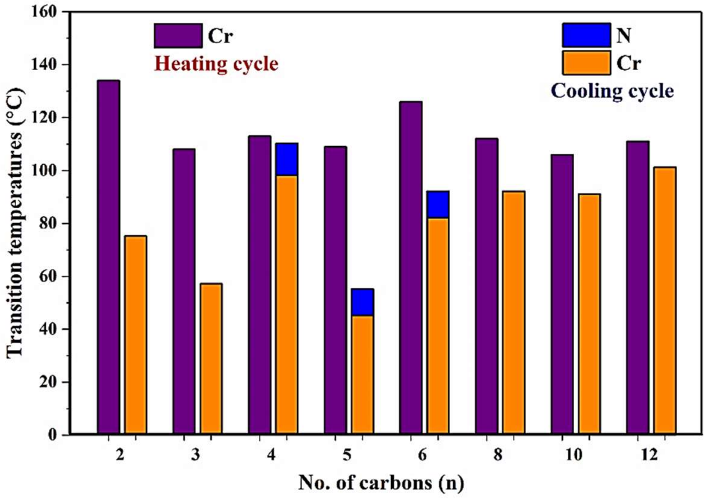

Fig. 2B.4: Bar graph of transition temperatures against no. of carbon of NpAzOnBr showing thermal stability of the mesophase in heating and cooling cycle

The plot (**Fig. 2B.4**) was used to establish the relationship. Lower members' isotropic liquid does not supercool sufficiently to produce a monotropic nematic mesophase. Lower members of the series aren't mesomorphic; this lack of mesophase development may be partially attributed to their high melting points. When a suitable substance is heated above the temperature at which the crystal lattice is stable, mesophases are most frequently seen.

All of the compounds in the current series are made up of long, thin, linear molecules that include dipolar groups, which should provide potent intermolecular forces. For the Iso-N transition temperatures, middle members had a declining tendency and a clear odd-even effect. This discovery implies that the decrease in Iso-N transition temperatures with increasing chain length is caused not only by stronger cohesive forces but also by the steric effect of larger molecules, which exacerbates the strength of these forces. However, the observed intermolecular interactions were not as strong as previously thought, and when other factors such as chain length, steric effect, and ordering of the hydrocarbon chains are taken into account, it is clear that these forces may not be entirely responsible for the decreased Iso-N transition temperatures. The two main factors to consider when predicting whether or not a compound will exhibit liquid crystalline properties are the nature and likely strength of the intermolecular attraction, as well as the geometric aspect of the molecule. Geometrically, the molecules of higher homologous naphthalene derivatives are suitable for mesophase formation, but the intermolecular attraction is not strong enough to produce a liquid crystalline phase. As the chain length increases, there are two opposing tendencies at work - one, the decrease in residual terminal attractions and two, the increased polarizability of molecules and resistance to interlayer sliding. The octyl, decyl, and dodecyl derivatives of the series, as well as ethyl and propyl, are unable to withstand the thermal vibrations that are applied to them. As a result, they sharply melt at their melting point without making the transition into a successive state known as the liquid crystal state. The non-mesomorphic behaviour of homologues is thus due to their very short phase length and crystallising tendency, which dis-aligns molecules on the surface and causes them to be randomly oriented in a floating state with no regularity or ordered molecular arrangement. Because of this, the current series lacks any smectic characteristics and is primarily non-mesogenic and partially nematogenic.

Table 2B. 2: Transition temperatures (°C) of series *I*-n and NpAzOnBr

No. of C in chain (n)	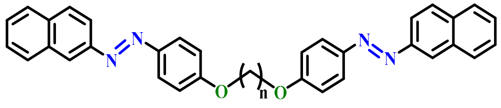 **Series *I-n***		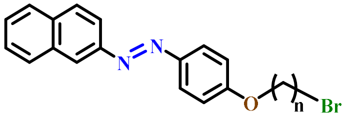 **NpAzOnBr**	
	Transition Temperatures (°C)			
	T_{Iso-N}	T_{N-Cr}	T_{Iso-N}	T_{N-Cr}
4	225.38	199.01	110.44	98.04
6	197.78	186.28	92.96	82.78

N, Nematic; Iso, Isotropic liquid; Cr, Crystalline solid

Table 2B.2 presents an outline of transition temperatures (in °C) of series **I-n** and **NpAzOnBr**. Monomers featuring a flexible bromoalkoxy tail and an azonaphthalene moiety, **NpAzOnBr**, essentially constituting the monomeric units of the ***I-n*** series were described in our earlier work[44]. While the individual monomers containing the naphthyl moiety tend to lack enantiotropic mesogenic properties, an interesting phenomenon emerges when these monomers form the resulting dimers and exhibit enantiotropic mesogenic behaviour.

2B.3.4 Optical properties

Ellipsometry model Alpha-SE J. A. Woollam Inc. USA that operates over 180 wavelengths with four different angles of incidence 65,70 and 75 and straight 90 is a special method that enables the interaction of Quartz tungsten halogen light in a specified direction with a molecule to visualize optical response corresponding to a thickness of the film. The optical response includes the determination of the refractive index, absorption coefficient and dielectric constant of a compound. The real part of dielectric constant $\mathcal{E}_1$ and imaginary dielectric constant $\mathcal{E}_2$ are visualized as corresponding to a wavelength of light. Organic compounds in a powdered form dissolved in a suitable solvent were transformed into a film of uniform thickness and placed in the path of polarized light to determine optical properties. The films are formed using the drop-casting technique where the powder samples of 1mg are dissolved in 2 mL of ethyl acetate and spread over the glass slide and further dried out to get the film. Optical properties are determined by illumination of light incident at 75 degrees with the spectroscopic ellipsometer on the film of uniform thickness on the glass substrate. Studies were performed with B Spline Model a basis set for polynomial splines. Fitting of SE data is performed with the Complete EASE package available with an ellipsometer [33] that determines the dielectric constant, refractive index and extinction coefficient. By utilizing this model, the dielectric function of thin film material can be calculated without any predetermined assumptions about the functional form of light-matter interaction. After parameterizing the material's imaginary dielectric spectra with a B-spline curve, the real dielectric spectra can be calculated analytically using the KK causality relationships. Thus, this model provides a straightforward and efficient approach for determining the real dielectric function of materials based on their imaginary dielectric spectra.

Table 2B. 3: Refractive index and dielectric constant of NpAzO6Br by Ellipsometry technique

Refractive Index (n)	**1.3717**
Real part of dielectric constant, $\mathcal{E}_{1,}$ (e_1)	**1.8704**
Imaginary dielectric constant, $\mathcal{E}_{2,}$ (e_2)	**0.2894**
Dielectric constant, $\mathcal{E} = \sqrt{e_1^2 + e_2^2}$	**1.8927**

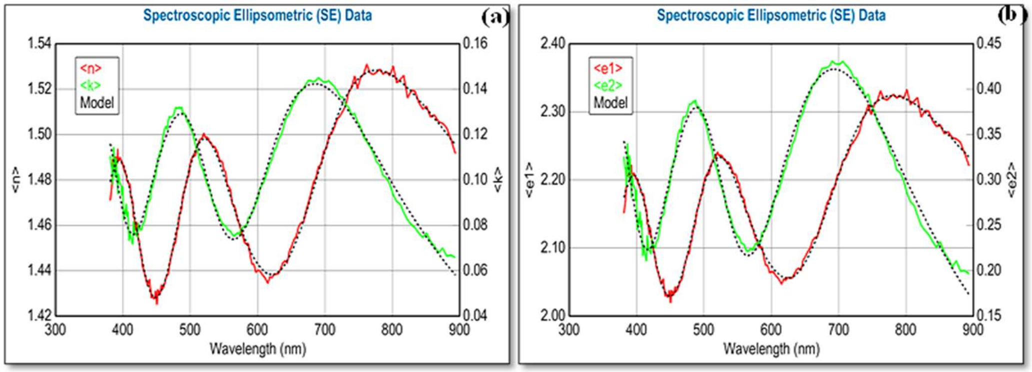

Fig. 2B.5: (a) SE data of Wavelength vs. Refractive index (n) and extinction coefficient (k), and (b) Wavelength vs. Real ($\mathcal{E}_1$) and imaginary ($\mathcal{E}_2$) part of dielectric constant for the NpAzO6Br

By parameterizing the imaginary dielectric spectra of material using B-splines and then applying the Kramers–Kronig consistent basis functions to obtain the real dielectric spectra, this model provides an effective approach for studying the optical and dielectric properties of materials without the need for any additional fitting or measurement procedures. The response of the extinction coefficient, refractive index and dielectric coefficient is illustrated in **Fig. 2B.5** and values are shown in **Table 2B.3**. The optical properties like refractive index and dielectric constant of the **NpAzO6Br** were determined to be 1.3717 and 1.8927 respectively.

2B.3.5 Thermogravimetric analysis

The compounds **NpAzO4Br** and **NpAzO6Br** were subjected to TGA measurements in a nitrogen atmosphere at temperatures ranging from 50 to 550 °C.

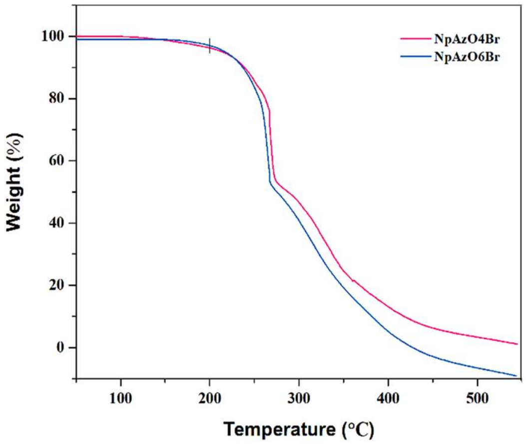

Fig. 2B.6: TGA plot for the compounds NpAzO4Br and NpAzO6Br

Fig. 2B.6 presents the TG curves for both compounds. Because there is no mass loss up to 200°C and a steady loss of mass between 200 and 500°C, which may be attributed to the compound's thermal decomposition, the TG curves demonstrate the thermal stability of the synthesised compounds.

2B.3.6. Computational Studies

Electronic properties of compounds are visualized in terms of Frontier Molecular Orbital (FMO) contours determined with quantum mechanical descriptors and Electrostatic potential contours locating potential during the formation of compounds using Gaussian 09 software with B3LYP, basis set 6-31G (d, p) in the gas phase.

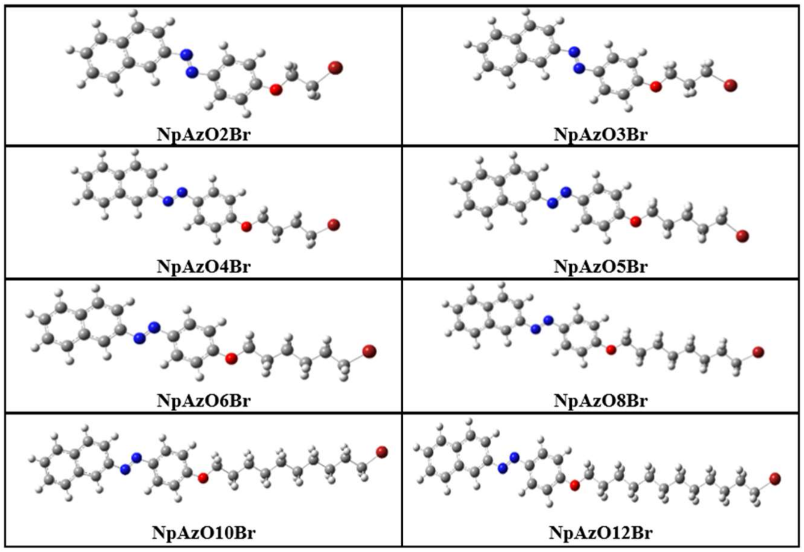
NpAzO2Br
NpAzO3Br
NpAzO4Br
NpAzO5Br
NpAzO6Br
NpAzO8Br
NpAzO10Br
NpAzO12Br

Fig. 2B.7: Optimized Molecular Structures of Compounds NpAzOnBr

Optimized molecular geometry of all the synthesized compounds of the series was determined with Gaussian 09 software with B3LYP, basis set 6-31G (d, p) in the gas phase. The molecular structures are represented in a ball and stick model with atoms of Carbon in grey colour, nitrogen in blue, oxygen in red, bromine in brown and hydrogen in white representing the chemical element (atoms) in the sphere (balls) and connected to each other with sigma and pi bonds(sticks) providing a three-dimensional structure of the molecule. All the optimized molecular structures are shown in **Fig. 2B.7**.

2B.3.6.1. Frontier Molecular Orbital Contours and Descriptors studies

Quantum mechanical descriptors[34] are the Ionization potential, Electron affinity and electrophilicity index with changes in electronic densities during the formation of compounds. Ionization potential corresponds to Highest Occupied Molecular Orbital (HOMO) as electron donating sites with the Lowest Unoccupied Molecular Orbital (LUMO) the electron affinity as the electron accepting sites with energies in electron volts (eV) with the difference in energy the energy gap **ΔE** a significant parameter of the molecule to be polarized that is suitable for electronic industry. Quantum mechanical descriptors (**Table 2B.4**) provide visualization of changes in electron density in terms of Frontier Molecular Orbital (FMO) Contours illustrated in **Fig. 2B.8**.

Table 2B.4: Quantum mechanical descriptors of compounds NpAzOnBr

Name of Compound	***Energy Minima (Hartree)***	***I* (eV)**	***A* (eV)**	***ΔE* (eV)**	***η***	***δ=1/η***	***χ***	***ω***
NpAzO2Br	-3451.37	5.64	2.10	3.54	1.77	0.56	3.87	4.23
NpAzO3Br	-3490.69	5.62	2.08	3.54	1.77	0.56	3.85	4.18
NpAzO4Br	-3530.01	5.59	2.05	3.54	1.77	0.56	3.82	4.12
NpAzO5Br	-3569.38	5.58	2.04	3.54	1.77	0.56	3.81	4.10
NpAzO6Br	-3608.64	5.56	2.02	3.54	1.77	0.56	3.79	4.05
NpAzO8Br	-3687.27	5.54	2.00	3.54	1.77	0.56	3.77	4.01
NpAzO10Br	-3765.91	5.53	1.99	3.54	1.77	0.56	3.76	3.99
NpAzO12Br	-3844.54	5.52	1.98	3.54	1.77	0.56	3.75	3.97

I, Ionization Potential; *A*, Electron Affinity; *ΔE*, Energy gap; *η*, Global hardness; *δ*, Global softness; *χ*, Chemical reactivity; *ω*, Electrophilicity index

A change in electron density refers to the bonding mechanism in terms of the weak bond and strong bond influencing the reactivity and polarity of the molecule. These bonds change the resistance to oppose the flow of electrons interpreted in terms of hardness, its reciprocal as softness, and the electrophilicity index[35] of the compounds listed in **Table 2B.4**.

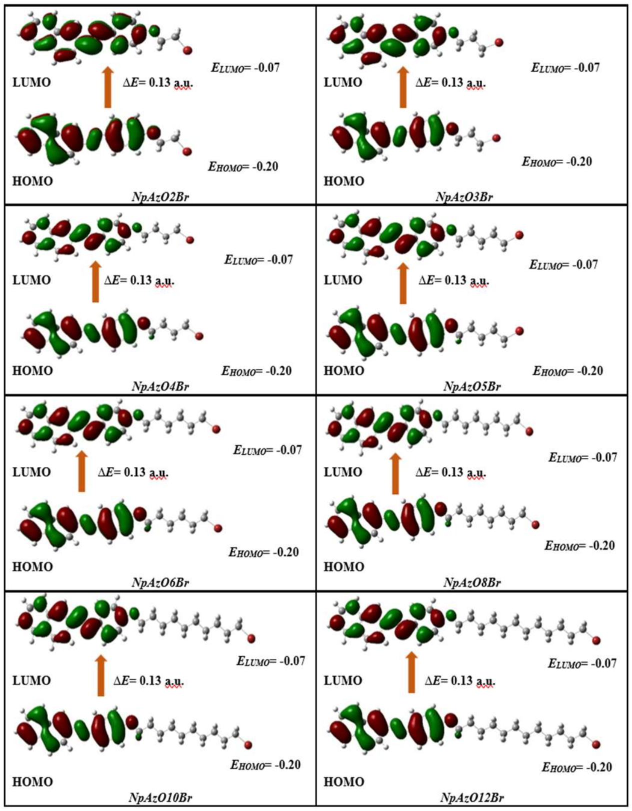

Fig. 2B.8: FMO Contours of Compounds NpAzOnBr

The energies specified in **Fig. 2B.8** are corresponding to HOMO (***E_{HOMO}***), LUMO (***E_{LUMO}***) and change in energy (Δ***E***) are in atomic units (a.u.), where, 1 atomic units = 27.2114 eV). For example, (Δ***E***= 0.13 a.u. = 0.13 * 27.2114 eV = 3.54 eV). Observation of these contours reveals the same spatial arrangement with inverse positive and negative surfaces. Among all the compounds studied, **NpAzO6Br** stands out as the most reactive compound. It demonstrates several favourable characteristics, including the development of a uniform thermal span, a good aspect ratio, and an energy gap of 3.54 eV (0.13 a.u.), indicating its semiconducting nature. Its exceptional optical properties, including the refractive index and dielectric constant, further support its suitability for optoelectronic applications[36].

2B.3.6.2. Calculated optical properties

It is observed that electronic properties are similar in compounds but changes in electron density with an energy gap of 3.5 eV are influenced in different directions with different energies along the molecular axes. Changes in electron density contribute to optical properties listed in **Table 2B.5** as a consequence of intermolecular interactions resulting in altered charge transfer, the orientation of the molecule, double bonds of carbon in the molecule and polarity of the molecule.

Table 2B.5: Optical properties of compounds NpAzOnBr

Name of Compound	Dipole Moment μ (debye)	Polarizability α (a.u.)	Anisotropy of polarizability $\Delta\alpha$	1st order Hyperpolarizability β
NpAzO2Br	0.566	288.21	17.23	165.24
NpAzO3Br	1.653	301.50	21.43	73.65
NpAzO4Br	0.531	313.93	15.55	17.30
NpAzO5Br	1.696	324.67	21.83	35.89
NpAzO6Br	0.479	338.05	24.72	170.15
NpAzO8Br	0.465	361.61	33.80	353.85
NpAzO10Br	0.462	384.83	46.03	552.52
NpAzO12Br	0.461	407.89	57.77	760.62

Odd-membered compounds (**NpAzO3Br** and **NpAzO5Br**) have a higher dipole moment than compounds with an even number of carbons (**NpAzOnBr**, **n=2,4,6,8,10,12**). This phenomenon is known as the “odd-even effect” and can be attributed to the difference in molecular symmetry between even and odd-numbered carbon chains. In the isotropic state, these molecules are in random orientation and in the anisotropic state they have specified directions as a consequence of the polarizability of the molecule. Symmetry of molecules with constraints is a consequence of first-order hyperpolarizability with 10 components independent of symmetry among 27 components. Studies of all the principal components of tensors corresponding to polarizability and first-order hyperpolarizability values are positive and negative. There is significant behaviour in **NpAzO4Br, NpAzO5Br** and **NpAzO6Br** as they have negative polarizability components along the principal diagonal and have positive polarizability components along the off-diagonal elements. The elements of first order hyperpolarizability matrix reveal responses in different directions with principal elements lowered than off-diagonal elements indicating large changes in electron cloud due to domination of dispersive forces. Studies of first-order hyperpolarizability in **NpAzO4Br** and **NpAzO5Br** there is a dominance of dispersive forces in comparison to other molecules. In **NpAzOnBr** with flexible spacers with n= 4, 5, 6, there is an approximate uniform thermal span, same width and reduced disorder responsible for schlieren nematic texture as listed in **Table 2B.6.**

Table 2B.6: Thermal parameters and dimensional parameters of the prepared compounds NpAzOnBr

Parameter/ Compounds	**NpAzO4Br**	**NpAzO5Br**	**NpAzO6Br**
$T_{N\text{-}Cr}$, Nematic	98.06	45.68	82.78
Entropy	0.02	0.05	0.02
Mesomorphic range, ΔT	11.70	8.93	10.18
Mesomorphic stability, T_C	109.76	54.61	92.96

Dimensions/(n)	**2**	**3**	**4**	**5**	**6**	**8**	**10**	**12**
Length (L)	17.5	18.9	19.4	21.5	22.6	25.2	27.8	30.3
Width (D)	6.1	5.8	5.5	5.5	5.5	5.4	5.7	5.6
Aspect ratio (L/D)	2.8	3.2	3.4	3.9	4.0	4.6	4.8	5.3

2B.3.6.3. Electrostatic potential Contours

Change in the electron density influenced the electrophilicity index, mesogenic nature, and increase in bond lengths altering the nature of molecule is due to *pi-pi* transitions in compounds of **NpAzO4Br, NpAzO5Br** and **NpAzO6Br** while the other compounds are completely ionized thereby affecting reactivity of compound i.e., **NpAzO2Br, NpAzO3Br, NpAzO8Br, NpAzO10Br** and **NpAzO12Br** as it associates sigma transitions. Changes in electron density are best visualized with electrostatic potential contours with illustration as the distribution of charges with a gradient of colours indicates the regions of responsible attractive and repulsive forces due to its interactions. An increase in wavelength is a consequence of inverse variation in electrostatic potential (ESP) from isodensity values of -2.662e-2 to 2.662e-2 eV as illustrated in **Fig. 2B.9.** Regions of wavelengths are inversely proportional to potential sequentially with colour accordingly as blue > green > yellow > red. Regions of blue are reactive regions highly polarized regions due to electron deficiency while the red regions are less reactive, with high electron densities and less polarized a consequence of bond formation within the molecule can be observed with changes in blue regions extensively with an increase in its atomic sites and green regions are neutral regions.

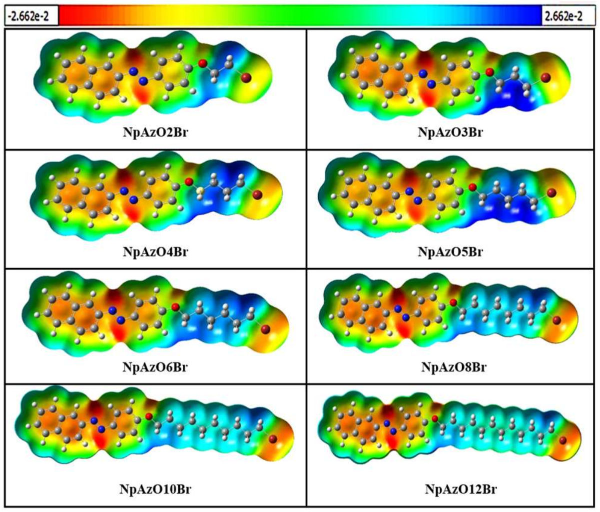

Fig. 2B.9: ESP contours of Compounds NpAzOnBr

In particular, there are enhanced blue regions observed in atomic sites corresponding to 4, 5 and 6 with greater participation with the schlieren nematic texture. Studies of these transitions between the orbital's associate population of changes in the electronic charge of molecule corresponding to atom in terms of either overlap of deviation from its distribution are attributed to mulliken charges. The geometry of molecules is vital in which atomic charges are calculated in terms of electrophilicity index with its origin from quantum mechanical descriptors providing accepting and donor powers of the molecule.

2B.3.6.4 Vibrational studies

Fig. 2B.10 shows a comparison between the experimental FT-IR spectrum of solid **NpAzO6Br** and the corresponding predicted spectrum in the gas phase using the B3LYP/6-31G method. The stretching modes of C-H of the aromatic ring (sp^2) and aliphatic chain (sp^3) are present in the region of 2800-3100 cm^{-1}. Furthermore, the presence of the N=N stretching frequency between 1550-1580 cm^{-1} indicates the presence of the azo group in the compound. The -C-O-C- stretching between 1240-1250 cm^{-1} is characteristic of the ether group, which is present in all **NpAzOnBr**. The C-C and C-N stretching modes and as well as some deformations of the naphthyl and benzyl rings of **NpAzO6Br**, are features of the region between 1600-1000 cm^{-1}. Meanwhile, the region 1000-400 cm^{-1} can provide information on the stretching and rocking modes of the CH and CH_2 groups, various deformations and torsion modes. The peak at 621 cm^{-1}, corresponding to the C-Br stretching. However, it is important to note that the experimental spectrum was obtained in the solid state, where the molecule is subject to intermolecular interactions and crystal packing effects. This means that the experimental spectrum is influenced by factors such as molecular symmetry, lattice vibrations, and hydrogen bonding interactions, which are not taken into account in the gas phase calculations. Therefore, it is expected that there will be some differences between the experimental and theoretical spectra, particularly in the low frequency region where lattice vibrations are more pronounced. Examining wave numbers reveal that (i) there are no negative wave numbers signifying that there are no intermediate transitions (ii) bonding is spontaneous favouring the formation of synthesized compound (iii) wave numbers in the assigned region in accordance with literature in functional and fingerprint region. Computed wave numbers are in agreement with experimental spectra for all the compounds in the proposed work.

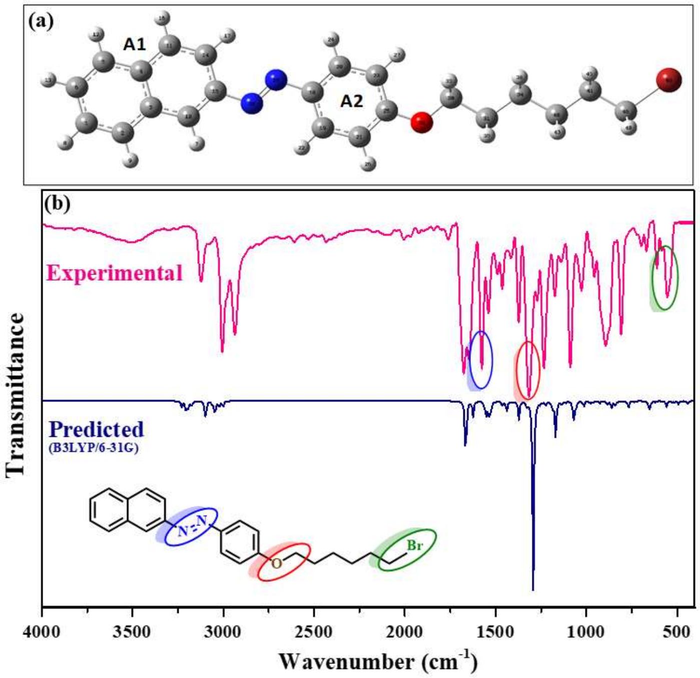

Fig. 2B.10: (a) Theoretical molecular structure of NpAzO6Br, atoms labelling and identification of their rings (b) Experimental infrared spectrum of NpAzO6Br compared with the corresponding predicted for the free base by using B3LYP/6-31G level of theory

2B.3.7 Photophysical properties

Azobenzene molecules are particularly appealing for storage devices and molecular switches because they can be switched back and forth between their two isomers with relatively small changes in the physical environment such as temperature, light, and electric fields. The normalised UV-Visible absorption spectrum of **NpAzO6Br** shows three absorption bands: the medium intensity band around 252 nm is for the σ-σ* transition, the stronger 360 nm band is associated with the π-π* transition, and the weaker band at 440 nm is for the n-π* transitions.

Photoisomerization is generally triggered by the π-π* transition and results in interconversion between *cis (Z)* and *trans (E)* isomers and because of this property, azobenzene is regarded as a dynamic substance. To use azobenzene as an optical data storage medium, the thermal back relaxation time should be as long as possible because this gives more time for information to be processed and stored. The photoisomerization in **NpAzO6Br** studies was done using a dual beam spectrophotometer with a 1 cm quartz cuvette with a 365 nm filter. The experiments conducted were able to demonstrate a clear correlation between the UV-visible spectra of *trans(E)* and *cis(Z)* isomers of **NpAzO6Br**, indicating that the strong peak present in the UV region corresponds to π-π* transition for *trans (E)*- and n-π* transition for *cis (Z)*- isomers. **Fig. 2B.11(a)** shows the UV-visible spectra for **NpAzO6Br** with various UV exposure times. The UV illumination of 0 sec is equivalent to no UV and illumination uses a 5 mW cm^{-2} intensity It shows a decrease of the absorption maxima, which is at 360 nm, and it is followed by a slight increase in the absorbance at the long wavelength (450 nm) and short wavelength (305 nm).

The photo conversion efficiency (CE) of the *E-Z* photoisomerization process was determined using the equation $[\boldsymbol{CE}= (\boldsymbol{A_{t_0}} - \boldsymbol{A_{t_\infty}}/\boldsymbol{A_{t_0}})\boldsymbol{*100\%}]$, and it was found that ~6 minutes was needed to reach a photo stationary state which is due to the photo isomeric equilibrium of the *E-Z* form of the compound [37,38]. Where absorbance after UV is $\boldsymbol{A_{t_\infty}}$ and absorbance before UV is $\boldsymbol{A_{t_0}}$. The photo conversion efficiency (CE) of **NpAzO6Br** was calculated to be 63.4% which is fairly high and that the *Z* isomer is thermodynamically unstable as this is sterically crowded and prone to thermal back relaxation to its *E* isomer after attaining photo saturation state. The thermal back relaxation process is shown in **Fig. 2B.11(b).**

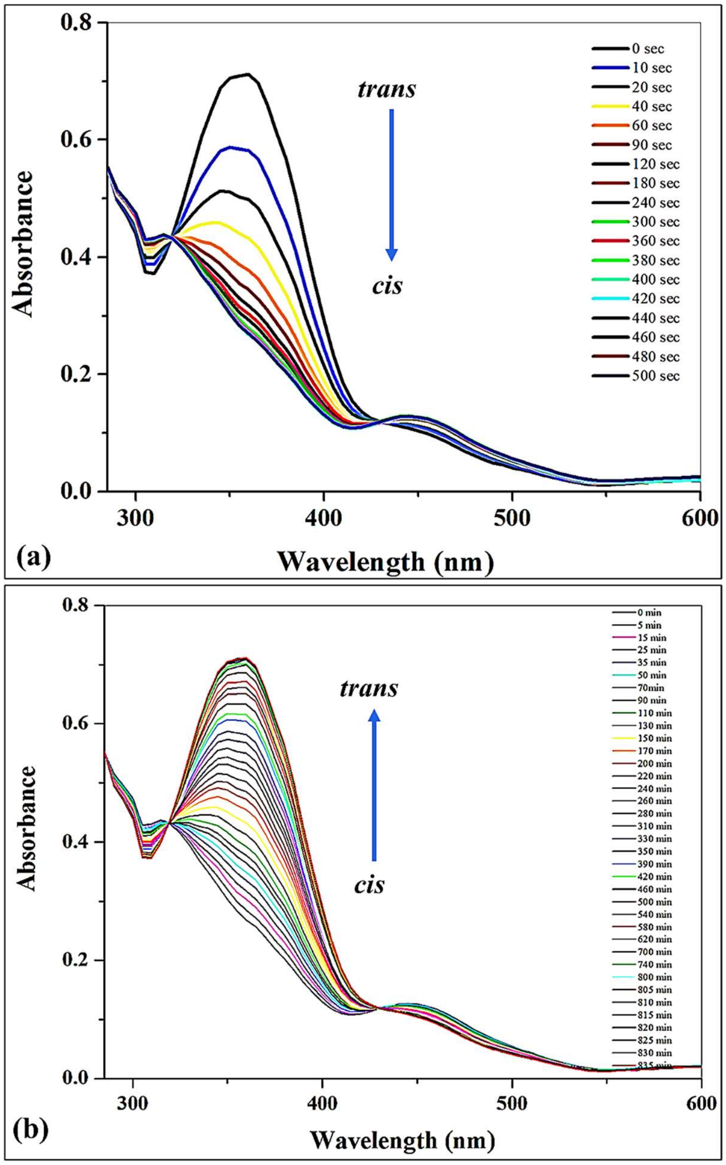

Fig. 2B.11: Absorption spectra for NpAzO6Br (a) with various UV exposure times and a 365 nm filter (b)Thermal back relaxation process

Once the compound attained a photo stationary state, it was kept in the dark, without any external energy and then absorbance was measured till its complete conversion to the *E* form. Two isosbestic points show the absence of any side reaction. In the photo stationary state, a dynamic equilibrium is established between the *E* and *Z* isomers, where the rates of photoisomerization from *E-Z* and from *Z-E* are balanced. This equilibrium is influenced by factors such as the wavelength and intensity of light, temperature, and the specific molecular structure of the azo compound.

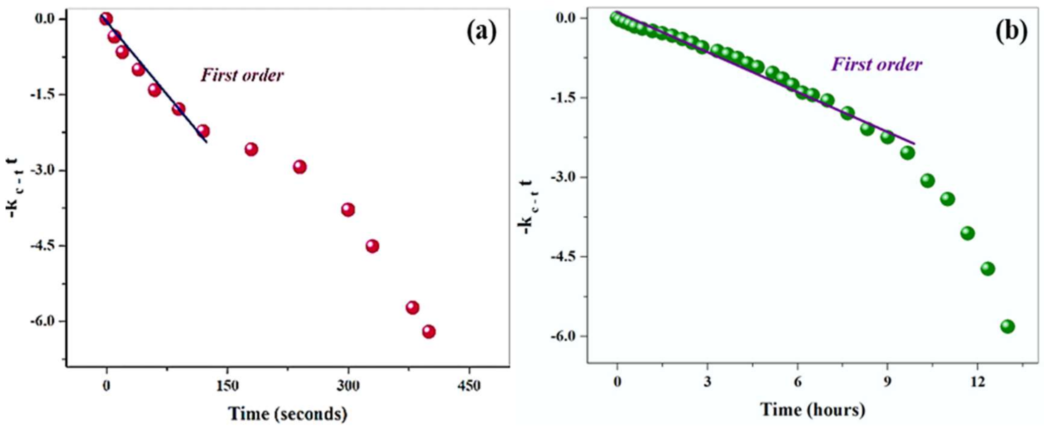

Fig. 2B.12: (a) First-order plots for *E-Z* and (b) *Z–E* photoisomerization

Fig. 2B.12 (a and b) depicts the first-order plot for photoisomerization, which was obtained by fitting the experimental data to equation $[-\boldsymbol{k_{c-t}t} = \mathbf{ln}(\boldsymbol{A_\infty - A_t})/(\boldsymbol{A_\infty - A_0})]$[39] at 25 °C. where $\mathbf{A_0}$, $\mathbf{A_t}$ and $\mathbf{A_\infty}$ are the absorbances at peak wavelength at time zero, time t, and infinite time, respectively. In the indicated time period, the reaction was a first-order reaction. However, the reaction departed from the first order at a later stage. Because this experiment was conducted in solution, the experimental temperature conditions may have been influenced by the extended thermal back relaxation. The reverse isomerisation process of **NpAzO6Br** as a function of recovery time is as shown in **Fig. 2B.13**, it took about 13.5 hours to convert back to stable *E* configuration.

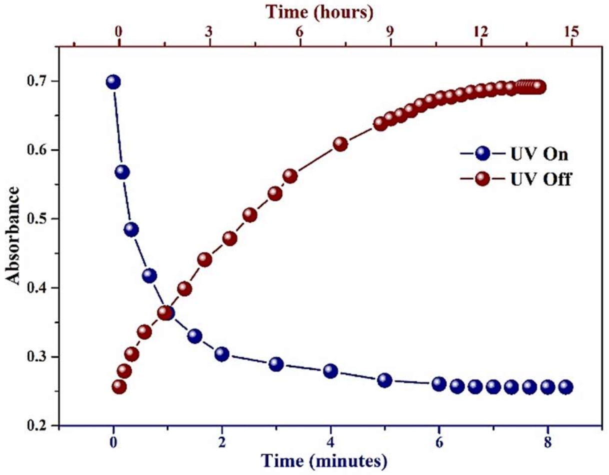

Fig. 2B.13: Plot of NpAzO6Br as a function of time during UV illumination (*E-Z*) and during thermal back relaxation from photo stationary state (*Z-E*)

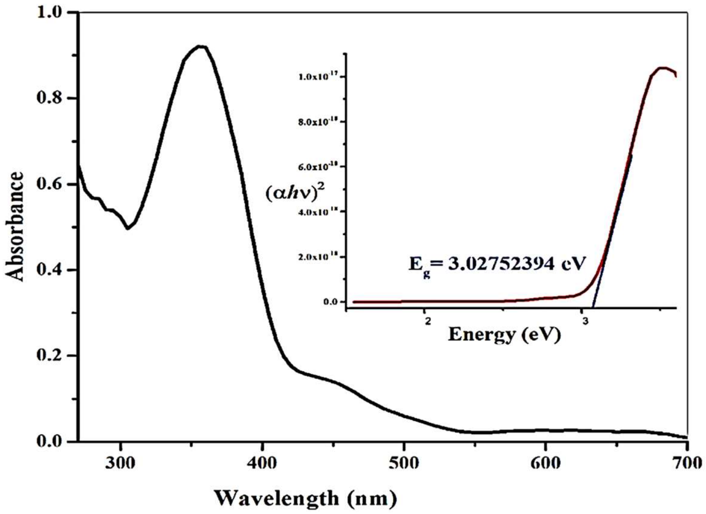

Fig. 2B.14: Experimental energy gap obtained from Tauc plot for NpAzO6Br

Electronic studies of UV-Visible spectroscopy provide absorption wavelengths related to electronic transitions, further ascribed with FMOs, which is important for the electro-optical properties. Absorption maxima at 360 nm corresponds to energy gap is **3.027eV** confirms the corresponding transitions are unique and intermolecular in nature with energy gap obtained from the Tauc plot illustrated in **Fig. 2B.14** is convinced with the computed energy gap (see **Table 2B.4**, Computational studies).

2B.4 Conclusion

The studies significantly aided in the design of synthesis, characterization, mesomorphic properties of naphthyl derivatives, and the investigation of the structure-mesomorphic property relationship. **NpAzO6Br** undergoes significant photoisomerization, where the energy gap is 3.027 eV, which was highly reversible, with recovery times of approximately 13.5 hours indicating that the compound could remain in a stable form without requiring any external energy or side reactions. As a result, we can consider this compound for the development of optoelectronic devices. Mesogenic molecules are responsible for the refractive index and dielectric constant; they have a lower extinction coefficient, which is characteristic of low anisotropic materials with first-order hyperpolarizability suitable for linear optical materials. With a thin film of mesogenic material of 10nm thickness interacting with polarized light escorted to be used as light guiding material with a refractive index of 1.35 for optical applications. Additionally, the detailed analysis of theoretical models that predict the parameters associated with mesophase transitions provided a better understanding of the relationship between molecular structure with excellent mesogenic dielectric material suitable for electronic and industrial applications. Quantum mechanical descriptors are provided to visualize changes in electron density with a suitable energy gap of 3.54 eV an excellent mesogenic material suitable for electronic applications.

2B.5 Experimental Section

2B.5.1 Materials

Naphthalene-2-amine, phenol, α,ω-dibromoalkanes, sodium nitrite ($NaNO_2$), potassium carbonate (K_2CO_3), sodium hydroxide (NaOH) and hydrochloric acid (HCl) were purchased from (S.R.L. Chemicals) and used without further purification. Solvents like acetone, ethyl acetate and petroleum ether (60-80) were de-moisturized and purified before use.

2B.5.2 Measurements

The instruments used are the same as in section **2A.5.2.** Spectroscopic Ellipsometric analysis was done on Alpha- SE J. A. Woollam Inc. USA that operates over 180 wavelengths with four different angles of incidence 65, 70 and 75 and straight 90.

2B.5.3 Synthesis and Characterization

2B.5.3.1 Synthesis of (E)-4-(naphthalen-2-yldiazenyl) phenol (NpAzOH)

The synthesis of *(E)*-4-(naphthalen-2-yldiazenyl)phenol (NpAzOH) is described in Chapter 2, Section 2A.5.1.

2B.5.3.2 Synthesis of (E)-1(4-(ω-bromoalkoxy)phenyl)-2-(naphthalen-2-yl)diazene (NpAzOnBr)

In a round bottom flask with a reflux system and stirring for 15 minutes, (*E*)-4-(naphthalen-2-yldiazenyl) phenol (**3**) (0.12 g, 0.5 mmol) and anhydrous K_2CO_3 (2.17 g, 15.7 mmol) were dissolved in acetone. Dropwise additions of, α, ω -dibromoalkanes (3.5 mmol) were made to the reaction mixture, and the system was refluxed for about 48 h (monitored by TLC). The hot solution was filtered and washed with acetone after the reaction was finished. The filtrate was then collected and evaporated in a rotary evaporator. Cold petroleum ether was added to the concentrated extracts, and the resulting precipitate was filtered and washed two times with this same solvent. Column chromatography is used to purify the resulting compound. (99:1 pet ether: ethyl acetate)

2B.5.3.3 Characterization data of NpAzOnBr

(E)-1-(4-(2-bromoethoxy)phenyl)-2-(naphthalen-2-yl)diazene (NpAzO2Br):

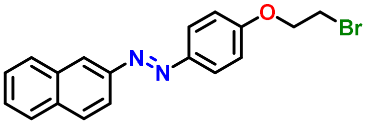

(*E*)-1-(4-(2-bromoethoxy)phenyl)-2-(naphthalen-2-yl)diazene

Orange crystals, Yield: 61%; **IR** ν_{max}/cm^{-1}: 2942.87 (C_{sp3}-H), 1603.04 (-N=N-), 1248.40 (C-O), 1163.29 (C-N), 858.92; **^{1}H NMR (400 MHz, $CDCl_3$): δ (In ppm)**: 8.44 (s, 1H, Naph.-H), 8.09 (d, *J* = 2 Hz, 1H, Naph.-H), 8.07 (d, *J* = 2 Hz, 1H, Naph.-H), 8.02 (d, 1H, *J* = 8.8 Hz, Naph.-H), 7.99 (d, *J* = 8.5 Hz, 1H, Naph.-H), 7.93 (d, *J* = 8.8 Hz, 2H, Ar-H), 7.58 (d, *J* = 9.4 Hz, 2H, Naph.-H), 7.07 (d, *J* = 9.2 Hz, 2H, Ar-H), 4.39 (t, *J* = 6 Hz, 2H, -O-CH_2-), 3.70 (t, *J* = 6.4 Hz, 2H, -CH_2-Br); **^{13}C NMR (400MHz, $CDCl_3$): δ (In ppm):**160.46 (Ar C-O-), 150.2 (Napthyl C-N-),147.5 (Ar C-N-), 134.62, 133.60, 129.29, 127.9, 127.2, 126.7, 124.8, 117.2, 114.95, 68.01 (Ar-O-C-), 38.04 (-C-Br); **ESI-MS: *m/z*** calculated for **$C_{18}H_{15}BrN_2O$:** $[M]^+$ 354.04, $[M+2]^+$ 356.03, found $[M]^+$ 354.05, $[M+2]^+$ 356.16; **Elemental Analysis**: $C_{18}H_{15}BrN_2O$:(cal): C, 60.86; H, 4.26; N, 7.89; O, 4.50; found C, 60.81; H, 4.22; N, 7.82; O, 4.43; %;

(E)-1-(4-(3-bromopropoxy)phenyl)-2-(naphthalen-2-yl)diazene (NpAzO3Br):

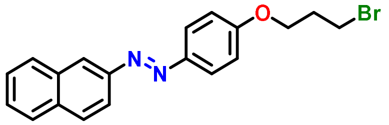

(*E*)-1-(4-(3-bromopropoxy)phenyl)-2-(naphthalen-2-yl)diazene

Orange crystals, Yield: 61%; **IR** ν_{max}/cm^{-1}: 2884.90 (C_{sp3}-H), 1607.29 (-N=N-), 1255.40 (C-O), 1169.03 (C-N), 858.92; **^{1}H NMR (400 MHz, $CDCl_3$): δ (In ppm)**: 8.43 (s, 1H, Naph.-H), 8.09 (d, *J* = 2 Hz, 1H, Naph.-H), 8.07 (d, *J* = 2 Hz, 1H, Naph.-H), 8.01 (d, 1H, *J* = 8.8 Hz, Naph.-H), 7.99 (d, *J* = 8.4 Hz, 1H, Naph.-H), 7.93 (d, *J* = 8.8 Hz, 2H, Ar-H), 7.57 (d, *J* = 9.4 Hz, 2H, Naph.-H), 7.07 (d, *J* = 9.2 Hz, 2H, Ar-H), 4.22 (t, *J* = 6 Hz, 2H, -O-CH_2-), 3.66 (t, *J* = 6.4 Hz, 2H, -CH_2-Br), 2.39 (m, 2H, -H_2C-C-Br); **^{13}C NMR (400MHz, $CDCl_3$): δ (In ppm):**161.35 (Ar C-O-), 150.3 ((Napthyl C-N-), 147.2 (Ar C-N-), 134.5, 133.6, 129.27, 127.9, 127.2, 126.6, 124.8, 117.2, 114.7, 65.6 (Ar-O-C-), 32.26 (-C-Br), 29.9 (-C-C-Br); **ESI-MS: *m/z*** calculated for **$C_{19}H_{17}BrN_2O$:** $[M]^+$ 368.05, $[M+2]^+$ 370.04, found $[M]^+$ 368.13, $[M+2]^+$ 370.14;

Elemental Analysis: $C_{19}H_{17}BrN_2O$ (cal): C, 61.80; H, 4.64; N, 7.59; O, 4.33; found C, 61.74; H, 4.63; N, 7.53; O, 4.29; %;

(E)-1-(4-(4-bromobutoxy)phenyl)-2-(naphthalen-2-yl)diazene (NpAzO4Br):

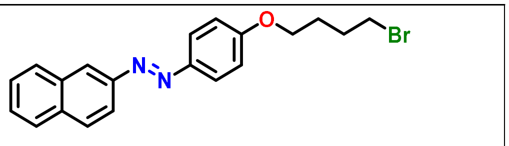

(*E*)-1-(4-(4-bromobutoxy)phenyl)-2-(naphthalen-2-yl)diazene

Orange crystals, Yield: 62%; **IR** ν_{max}/cm^{-1}: 2877.35 (C_{sp3}-H), 1607.48 (-N=N-), 1252.09 (C-O), 1170.75 (C-N), 822.48; **^{1}H NMR (400 MHz, $CDCl_3$): δ (In ppm)**: 8.43 (s, 1H, Naph.-H), 8.1 (d, *J* = 2 Hz, 1H, Naph.-H), 8.07 (d, *J* = 2 Hz, 1H, Naph.-H), 8.0 (d, 1H, *J* = 8.8 Hz, Naph.-H), 7.99 (d, *J* = 8.4 Hz, 1H, Naph.-H), 7.93 (d, *J* = 8.8 Hz, 2H, Ar-H), 7.58 (d, *J* = 9.4 Hz, 2H, Naph.-H), 7.04 (d, *J* = 9.2 Hz, 2H, Ar-H), 4.10 (t, *J* = 6 Hz, 2H, -O-CH_2-), 3.54 (t, *J* = 6.4 Hz, 2H, -CH_2-Br), 2.10 (m, 2H, -O-C-H_2C-), 2.02 (m, 2H, -H_2C-C-Br); **^{13}C NMR (400MHz, $CDCl_3$): δ (In ppm):** 161.37 (Ar C-O-), 150.3 (Napthyl C-N-), 147.1 (Ar C-N-), 134.5, 133.6, 129.27, 127.9, 127.2, 126.6, 124.8, 117.2, 114.7, 67.19 (Ar-O-C-), 33.48 (-C-Br), 29.4 (-C-C-Br), 27.85 (-O-C-C-); **ESI-MS:** ***m/z*** calculated for **$C_{20}H_{19}BrN_2O$:** $[M]^+$ 382.07, $[M+2]^+$ 384.07, found $[M]^+$ 381.96, $[M+2]^+$ 384.21; **Elemental Analysis**: $C_{20}H_{19}BrN_2O$: (cal) C, 62.67; H, 5.00; N, 7.31; O, 4.17; found C, 62.58; H, 4.92; N, 7.38; O, 4.11; %;

(E)-1-(4-((5-bromopentyl)oxy)phenyl)-2-(naphthalen-2-yl)diazene (NpAzO5Br):

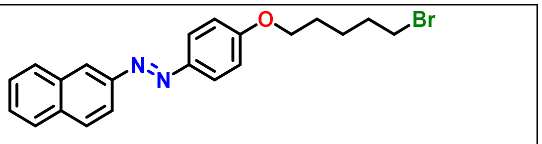

(*E*)-1-(4-((5-bromopentyl)oxy)phenyl)-2-(naphthalen-2-yl)diazene

Orange crystals, Yield: 64%; **IR** ν_{max}/cm^{-1}: 2864.25 (C_{sp3}-H), 1602.93 (-N=N-), 1250.50 (C-O), 1169.06 (C-N), 835.73**; ^{1}H NMR (400 MHz, $CDCl_3$): δ (In ppm)**: 8.42 (s, 1H, Naph.-H), 8.09 (d, *J* = 2 Hz, 1H, Naph.-H), 8.06 (d, *J* = 2 Hz, 1H, Naph.-H), 8.01 (d, 1H, *J* = 8.8 Hz, Naph.-H), 7.99 (d, *J* = 8.4 Hz, 1H, Naph.-H), 7.92 (d, *J* = 8.8 Hz, 2H, Ar-H), 7.58 (d, *J* = 9.4 Hz, 2H, Naph.-H), 7.04 (d, *J* = 9.2 Hz, 2H, Ar-H), 4.09 (t, *J* = 6 Hz, 2H, -O-CH_2-), 3.48 (t, *J* = 6.4 Hz, 2H, -CH_2-Br), 1.98 (m, 2H -O-C-H_2C-), 1.89 (m, 2H, -H_2C-C-Br), 1.70 (m, 2H, -CH_2-C-C-Br); **^{13}C NMR (400MHz, $CDCl_3$): δ (In ppm):**161.51 (Ar C-O), 150.3 (Napthyl C-N), 147.0 (Ar C-N), 134.5, 133.6, 129.27, 127.9, 127.2, 126.6, 124.8, 117.3, 114.7, 67.9 (Ar-O-C-), 33.64 (-C-Br), 32.47 (-C-C-Br), 28.40 (-O-C-C-), 24.83 (-O-C-C-C-); **ESI-MS:** ***m/z*** calculated for **$C_{21}H_{21}BrN_2O$:** $[M]^+$ 396.08, $[M+2]^+$ 398.08, found $[M]^+$ 396.03, $[M+2]^+$ 398.26; **Elemental Analysis**: $C_{21}H_{21}BrN_2O$: (cal) C, 63.48; H, 5.33; N, 7.05; O, 4.03; found C, 62.88; H, 5.07; N, 7.20; O, 4.02; %;

(E)-1-(4-((6-bromohexyl)oxy)phenyl)-2-(naphthalen-2-yl)diazene (NpAzO6Br):

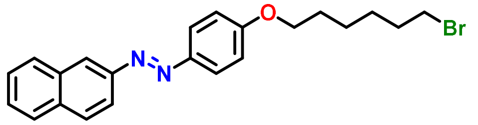

(*E*)-1-(4-((6-bromohexyl)oxy)phenyl)-2-(naphthalen-2-yl)diazene

Orange crystals, Yield: 63%; **IR** ν_{max}/cm^{-1}: 2858.07 (C_{sp3}-H), 1607.76 (-N=N-), 1250.20 (C-O), 1166.88 (C-N), 820.36 ; **^{1}H NMR (400 MHz, $CDCl_3$): δ (In ppm)**: 8.4 (s, 1H, Naph.-H), 8.09 (d, *J* = 2 Hz, 1H, Naph.-H), 8.06 (d, *J* = 2 Hz, 1H, Naph.-H), 8.02 (d, 1H, *J* = 8.8 Hz, Naph.-H), 7.99 (d, *J* = 8.4 Hz, 1H, Naph.-H), 7.93 (d, *J* = 8.8 Hz, 2H, Ar-H), 7.58 (d, *J* = 9.4 Hz, 2H, Naph.-H), 7.07 (d, *J* = 9.2 Hz, 2H, Ar-H), 4.11 (t, *J* = 6 Hz, 2H, -O-CH_2-), 3.54 (t, *J* = 6.4 Hz, 2H, -CH_2-Br), 2.14 (m, 2H, -O-C-H_2C-), 1.89 (m, 2H, -H_2C-C-Br), 1.63 (m, 2H, -H_2C-C-C-Br), 1.27 (m, 2H, -O-C-C-CH_2-); **^{13}C NMR (400MHz, $CDCl_3$): δ (In ppm):** 161.36 (Ar C-O), 150.3 (Napthyl C-N), 147.1 (Ar C-N), 134.5, 133.6, 129.1, 127.9, 127.1, 126.6, 124.7, 117.2, 114.7, 67.19 (Ar-O-C), 33.46 (-C-Br), 32.11 (-C-C-Br), 29.4 (-O-C-C-), 25.4 (-C-C-C-Br), 24.83 (-O-C-C-C-); **ESI-MS:** ***m/z*** calculated for **$C_{22}H_{23}BrN_2O$:** $[M]^+$ 410.10, $[M+2]^+$ 412.10, found $[M]^+$ 410.01, $[M+2]^+$ 412.21; **Elemental Analysis**: $C_{22}H_{23}BrN_2O$: (cal) C, 64.24; H, 5.64; N, 6.81; O, 3.89; found C, 64.29; H, 5.52; N, 6.75; O, 3.82; %;

(E)-1-(4-((8-bromooctyl)oxy)phenyl)-2-(naphthalen-2-yl)diazene (NpAzO8Br):

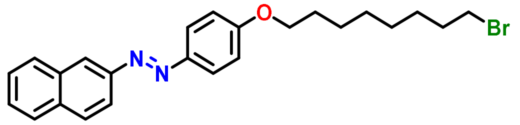

(*E*)-1-(4-((8-bromooctyl)oxy)phenyl)-2-(naphthalen-2-yl)diazene

Orange crystals, Yield: 63%; **IR** ν_{max}/cm^{-1}: 2868.74 (C_{sp3}-H), 1607.88 (-N=N-), 1249.39 (C-O), 1166.77 (C-N), 826.22 ; ; **^{1}H NMR (400 MHz, $CDCl_3$): δ (In ppm)**: 8.43 (s, 1H, Naph.-H), 8.09 (d, *J* = 2 Hz, 1H, Naph.-H), 8.07 (d, *J* = 2 Hz, 1H, Naph.-H), 8.01 (d, 1H, *J* = 8.8 Hz, Naph.-H), 7.99 (d, *J* = 8.4 Hz, 1H, Naph.-H), 7.93 (d, *J* = 8.8 Hz, 2H, Ar-H), 7.58 (d, *J* = 9.4 Hz, 2H, Naph.-H), 7.06 (d, *J* = 9.2 Hz, 2H, Ar-H), 4.06 (t, *J* = 6 Hz, 2H, -O-CH_2-), 3.57 (t, *J* = 6.4 Hz, 2H, -CH_2-Br), 2.19 (m, 2H, -O-C-H_2C-), 1.83 (m, 2H, -H_2C-C-Br), 1.51 (m, 2H, -O-C-C-CH_2-), 1.48 (m, 6H, methylene protons -(CH_2)$_3$); **^{13}C NMR (400MHz, CDCl$_3$): δ (In ppm):** 161.69 (Ar C-O), 150.3 (Napthyl C-N), 146.9 (Ar C-N), 134.5, 133.6, 129.1, 127.9, 127.1, 126.6, 124.7, 117.2, 114.7, 68.28 (Ar-O-C-), 34.11 (-C-Br), 32.79 (-C-C-Br), 29.23 (-O-C-C-), 29.18 (-C-C-C-Br), 28.72 (O-C-C-C-), 28.12, 25.97; **ESI-MS: *m/z*** calculated for **$C_{24}H_{27}BrN_2O$:** $[M]^+$ 438.13, $[M+2]^+$ 440.13, found $[M]^+$ 437.96, $[M+2]^+$ 439.32; **Elemental Analysis**: $C_{24}H_{27}BrN_2O$: (cal) C, 65.60; H, 6.19; N, 6.38; O, 3.64; found C, 65.69; H, 6.14; N, 6.28; O, 3.59; %;

(E)-1-(4-((10-bromodecyl)oxy)phenyl)-2-(naphthalen-2-yl)diazene (NpAzO10Br):

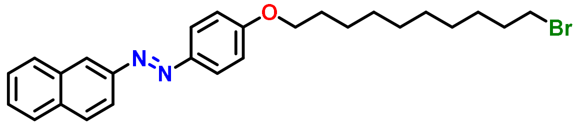

(*E*)-1-(4-((10-bromodecyl)oxy)phenyl)-2-(naphthalen-2-yl)diazene

Orange crystals, Yield: 64%; **IR** ν_{max}/cm^{-1}: 2851.02 (C_{sp3}-H), 1608.09 (-N=N-), 1251.50 (C-O), 1167 (C-N), 820.28; **^{1}H NMR (400 MHz, CDCl$_3$): δ (In ppm)**: 8.4 (s, 1H, Naph.-H), 8.09 (d, *J* = 2 Hz, 1H, Naph.-H), 8.07 (d, *J* = 2 Hz, 1H, Naph.-H), 8.02 (d, 1H, *J* = 8.8 Hz, Naph.-H), 7.99 (d, *J* = 8.4 Hz, 1H, Naph.-H), 7.93 (d, *J* = 8.8 Hz, 2H, Ar-H), 7.58 (d, *J* = 9.4 Hz, 2H, Naph.-H), 7.07 (d, *J* = 9.2 Hz, 2H, Ar-H), 4.07 (t, *J* = 6 Hz, 2H, -O-CH_2-), 3.44 (t, *J* = 6.4 Hz, 2H, -CH_2-Br), 1.86 (m, 2H, -O-C-CH_2-), 1.82 (m, 2H, -H_2C-C-Br), 1.62 (m, 2H, -O-C-C-CH_2-), 1.34 (m, 10H, methylene protons -(CH_2)$_5$); **^{13}C NMR (400MHz, CDCl$_3$): δ (In ppm):** 161.72 (Ar C-O), 150.3 (Napthyl C-N), 146.9 (Ar C-N), 134.5, 133.6, 129.1, 127.9, 127.1, 126.6, 124.7, 117.2, 114.7, 68.35 (Ar-O-C), 34.15 (-C-Br), 32.83 (-C-C-Br), 29.7 (-O-C-C-), 29.2 (-C-C-C-Br), 28.77 (-O-C-C-C-), 28.18, 26.02; **ESI-MS: *m/z*** calculated for **$C_{26}H_{31}BrN_2O$:** $[M]^+$ 466.16, $[M+2]^+$ 468.16, found $[M]^+$ 466.32, $[M+2]^+$ 468.28; **Elemental Analysis**: $C_{26}H_{31}BrN_2O$: (cal) C, 66.81; H, 6.68; N, 5.99; O, 3.42; found C, 66.73; H, 6.73; N, 5.91; O, 3.38; %;

(E)-1-(4-((12-bromododecyl)oxy)phenyl)-2-(naphthalen-2-yl)diazene (NpAzO12Br):

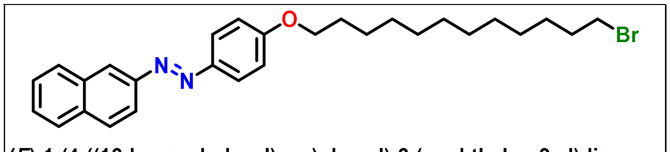

(*E*)-1-(4-((12-bromododecyl)oxy)phenyl)-2-(naphthalen-2-yl)diazene

Orange crystals, Yield: 61%; **IR** ν_{max}/cm^{-1}: 2858.02 (C_{sp3}-H), 1607.60 (-N=N-), 1247.85 (C-O), 1164.70 (C-N), 822.61; **^{1}H NMR (400 MHz, $CDCl_3$): δ (In ppm):** 8.4 (s, 1H, Naph.-H), 8.09 (d, *J* = 2 Hz, 1H, Naph.-H), 8.07 (d, *J* = 2 Hz, 1H, Naph.-H), 8.02 (d, 1H, *J* = 8.8 Hz, Naph.-H), 7.99 (d, *J* = 8.4 Hz, 1H, Naph.-H), 7.93 (d, *J* = 8.8 Hz, 2H, Ar-H), 7.58 (d, *J* = 9.4 Hz, 2H, Naph.-H), 7.06 (d, *J* = 9.2 Hz, 2H, Ar-H), 4.06 (t, *J* = 6 Hz, 2H, -O-C$\underline{H}_2$-), 3.43 (t, *J* = 6.4 Hz, 2H, -C$\underline{H}_2$-Br), 1.87 (m, 2H, -O-C-C$\underline{H}_2$-), 1.81 (m, 2H, -$\underline{H}_2$C-C-Br), 1.63 (m, 2H, -O-C-C-C$\underline{H}_2$-), 1.32 (m, 14H, methylene protons -(C$\underline{H}_2$)$_7$); **^{13}C NMR (400MHz, $CDCl_3$): δ (In ppm)**: 161.73 (Ar $\underline{C}$-O), 150.3 (Napthyl $\underline{C}$-N), 146.9 (Ar $\underline{C}$-N), 134.5, 133.6, 129.1, 127.9, 127.1, 126.6, 124.7, 117.2, 114.7, 68.38 (Ar-O-$\underline{C}$), 34.1 (-$\underline{C}$-Br), 32.85 (-$\underline{C}$-C-Br), 29.4 (-O-C-C-), 29.22 (-$\underline{C}$-C-C-Br), 28.8 (-O-C-C-$\underline{C}$-), 28.2, 26.04; **ESI-MS:** ***m/z*** calculated for **$C_{28}H_{35}BrN_2O$:** $[M]^+$ 494.19, $[M+2]^+$ 496.19, found $[M]^+$ 494.26, $[M+2]^+$ 496.36; **Elemental Analysis**: $C_{28}H_{35}BrN_2O$: (cal.) C, 67.87; H, 7.12; N, 5.65; O, 3.23; C, 67.79; H, 7.18; N, 5.61; O, 3.19 found ; %;

2B.6 Spectras

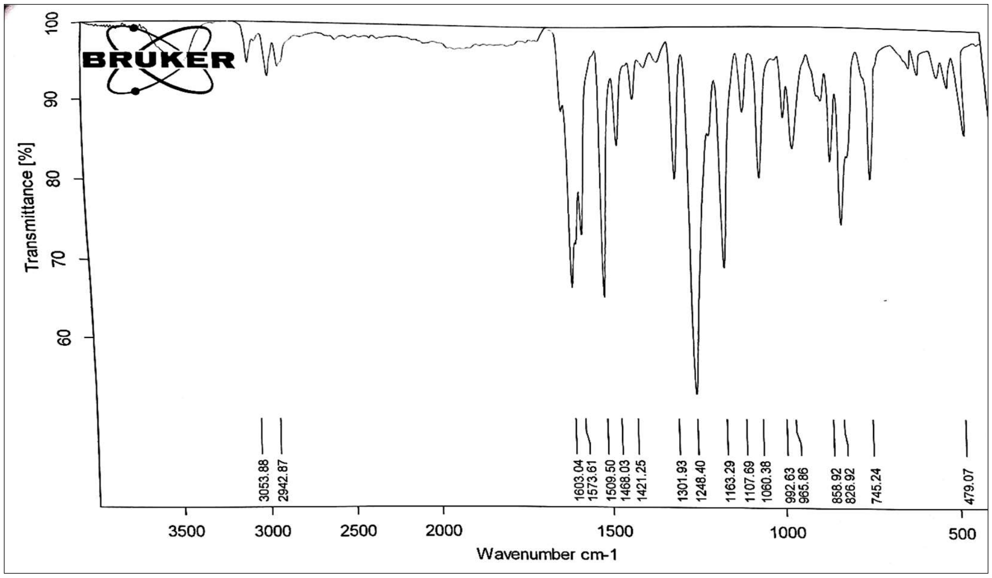

Fig. S2B.1: FT-IR Spectra of NpAzO2Br

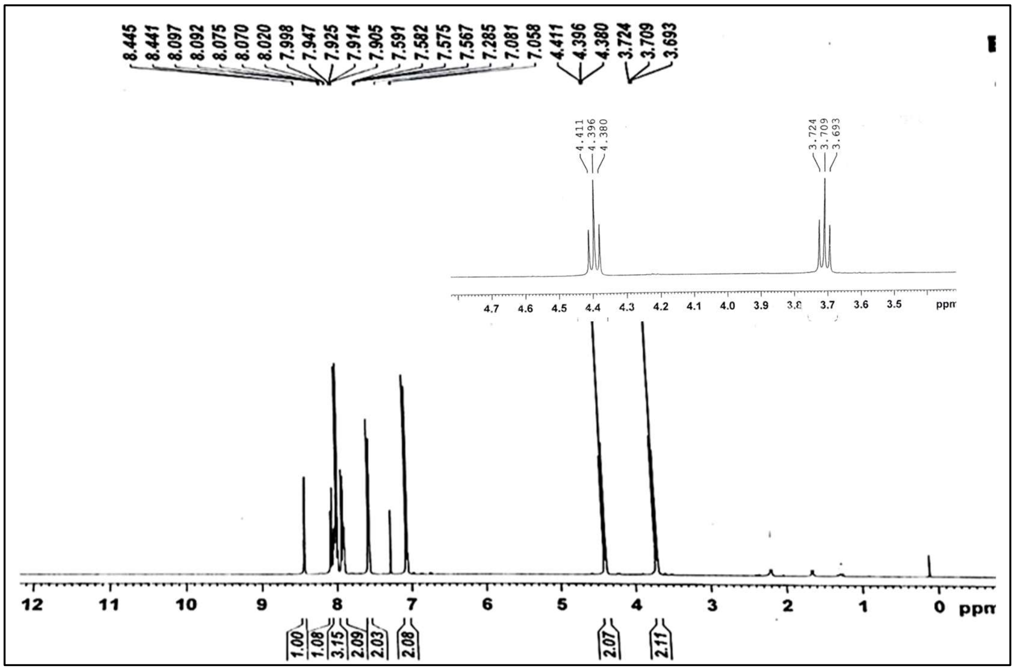

Fig. S2B.2: ^{1}H-NMR Spectra of NpAzO2Br

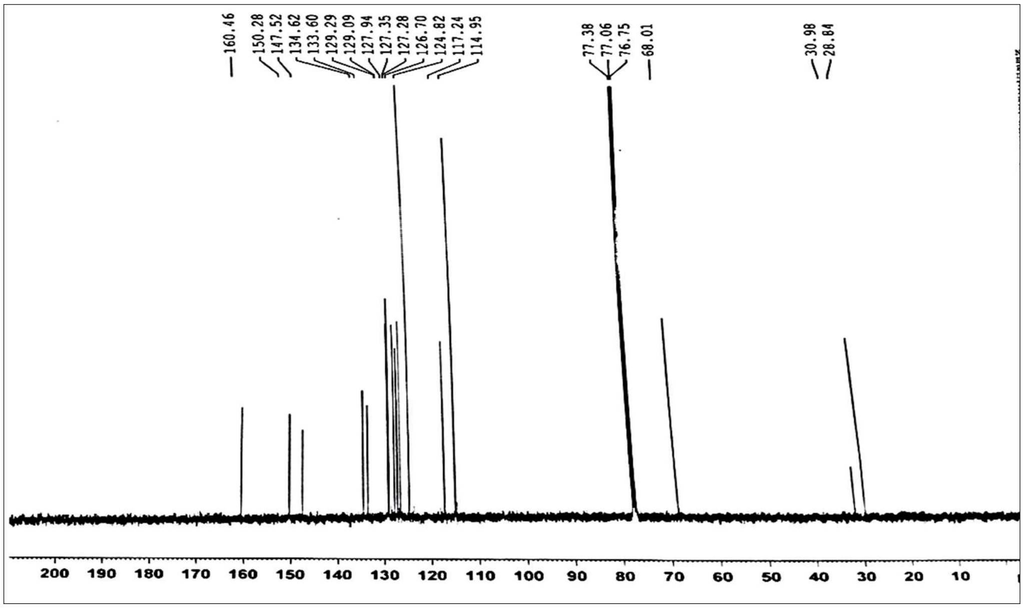

Fig. S2B.3: ^{13}C-NMR Spectra of NpAzO2Br

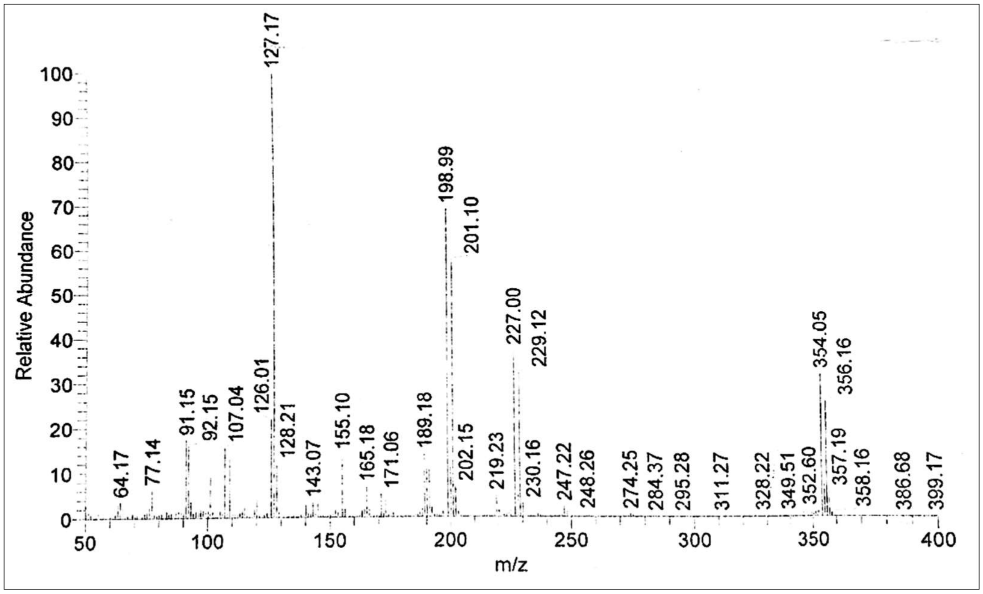

Fig. S2B.4: Mass Spectra of NpAzO2Br

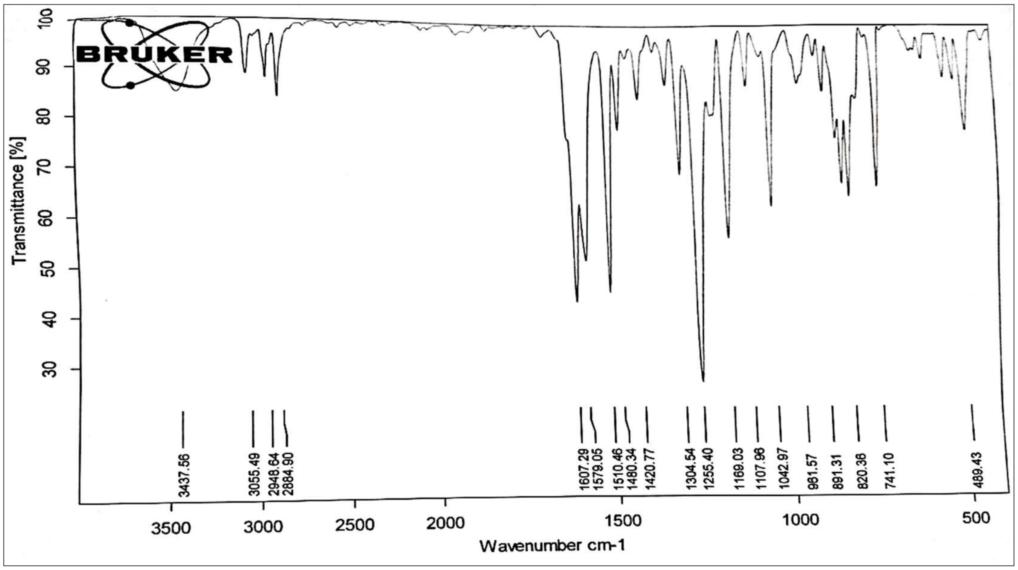

Fig. S2B.5: FT-IR Spectra of NpAzO3Br

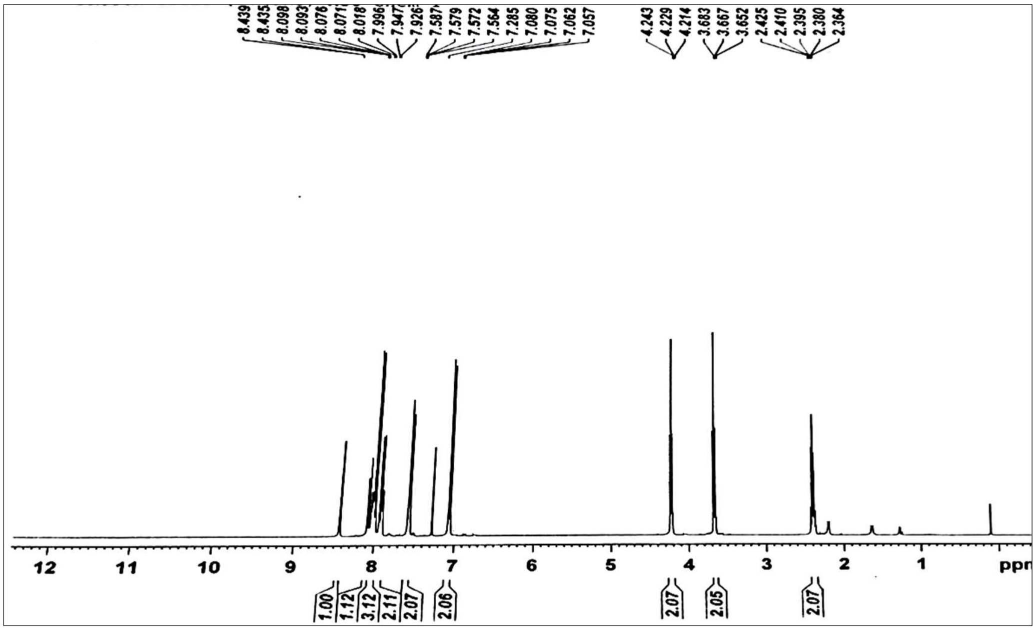

Fig. S2B.6: ^{1}H-NMR Spectra of NpAzO3Br

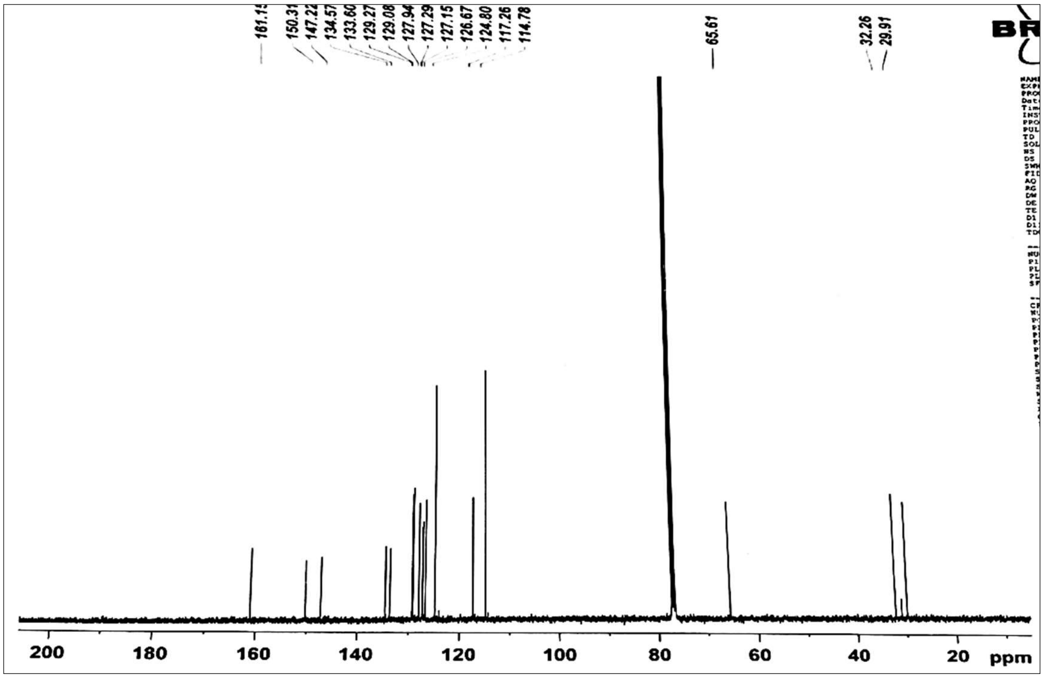

Fig. S2B.7: ^{13}C-NMR Spectra of NpAzO3Br

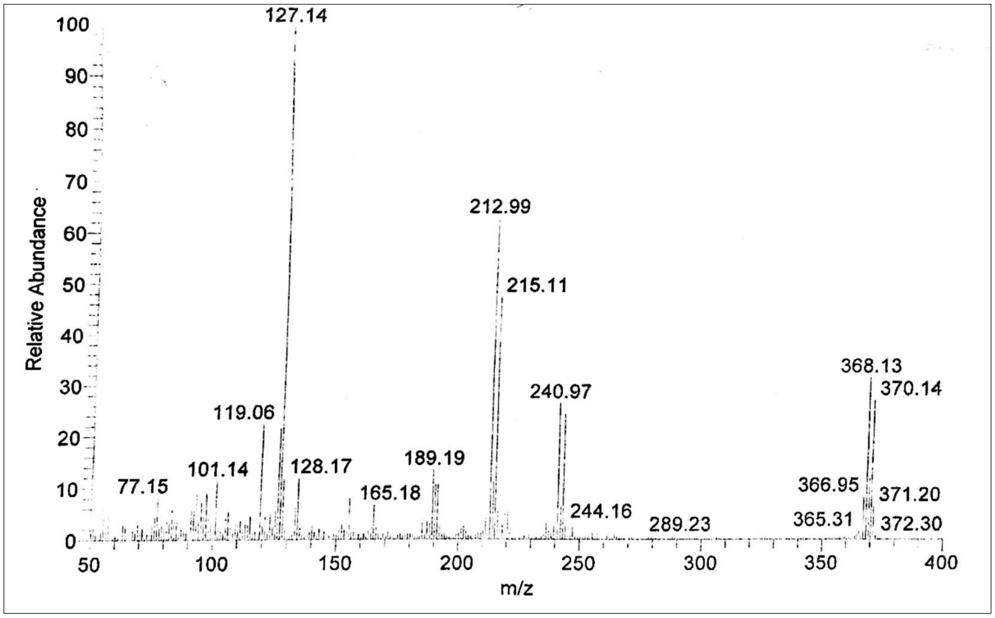

Fig. S2B.8: Mass Spectra of NpAzO3Br

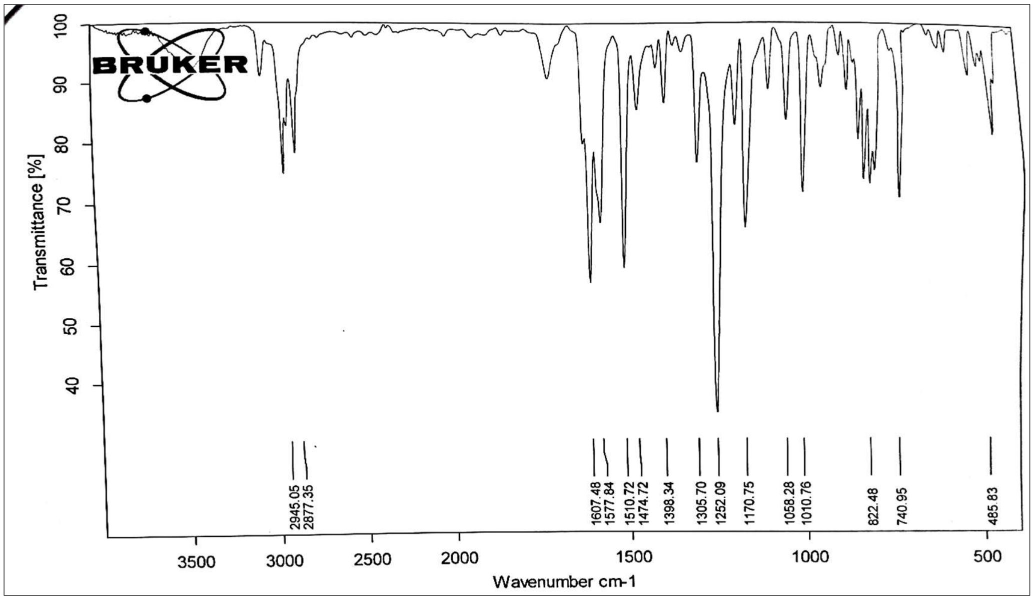

Fig. S2B.9: FT-IR Spectra of NpAzO4Br

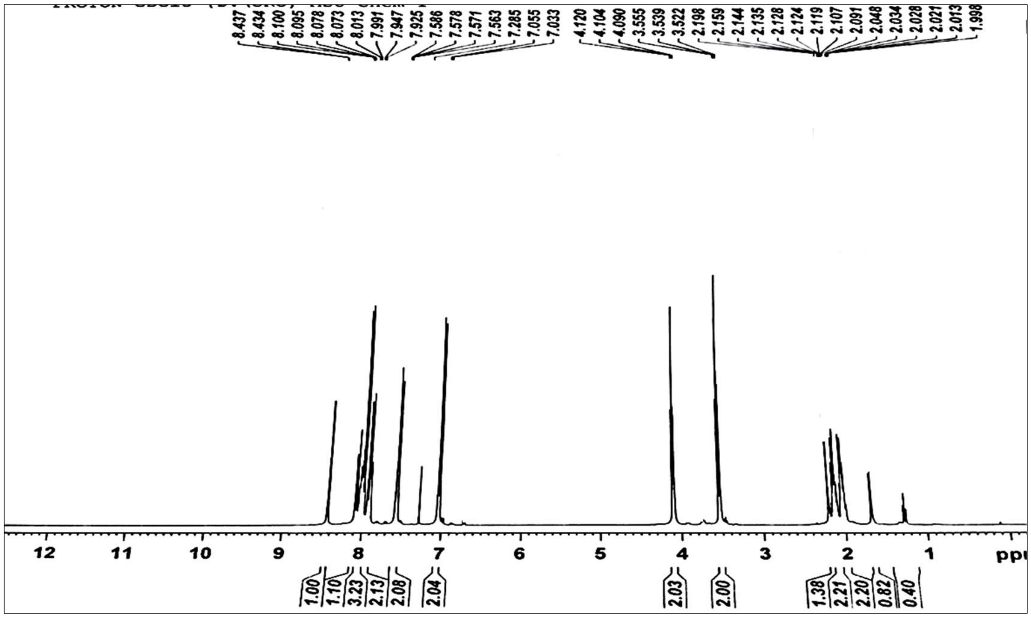

Fig. S2B.10: ^{1}H-NMR Spectra of NpAzO4Br

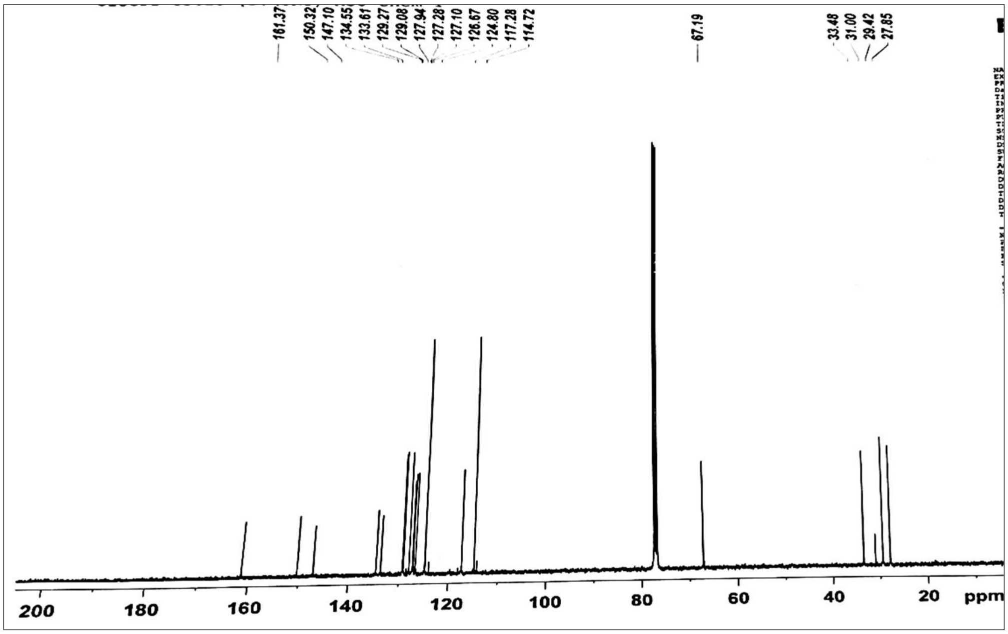

Fig. S2B.11: ^{13}C-NMR Spectra of NpAzO4Br

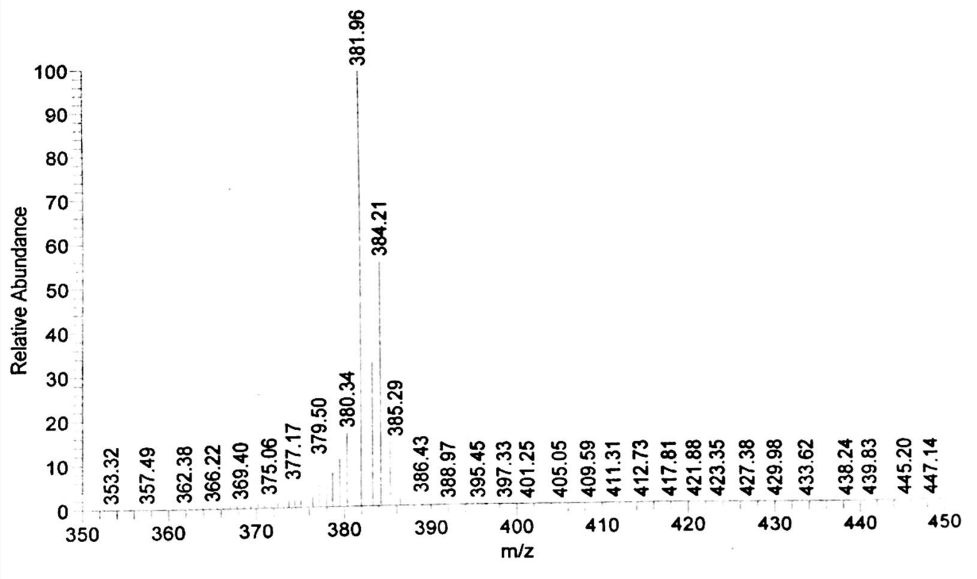

Fig. S2B.12: Mass Spectra of NpAzO4Br

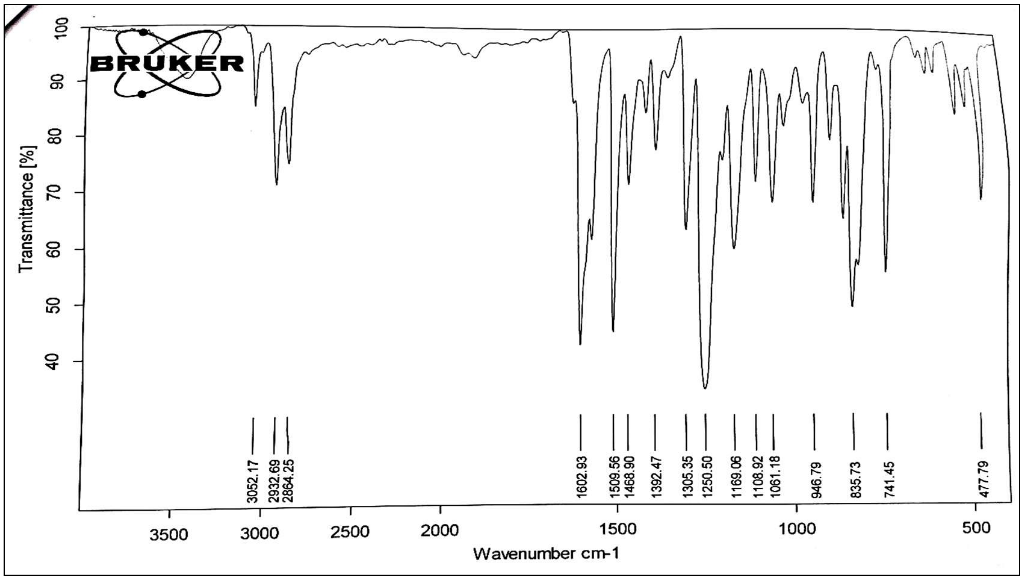

Fig. S2B.13 FT-IR Spectra of NpAzO5Br

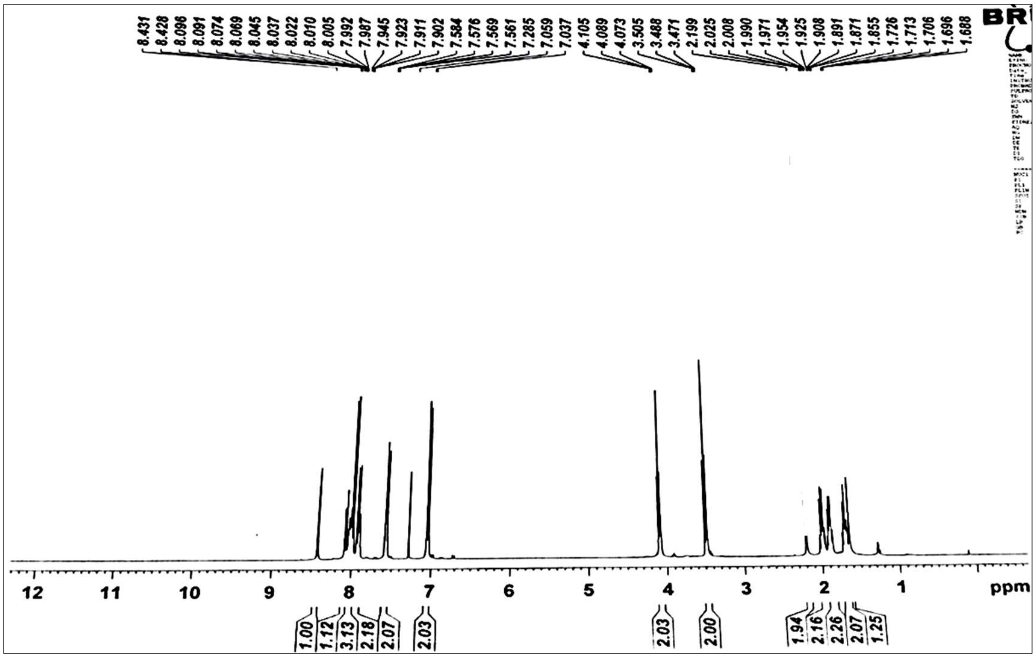

Fig. S2B.14: ^{1}H-NMR Spectra of NpAzO5Br

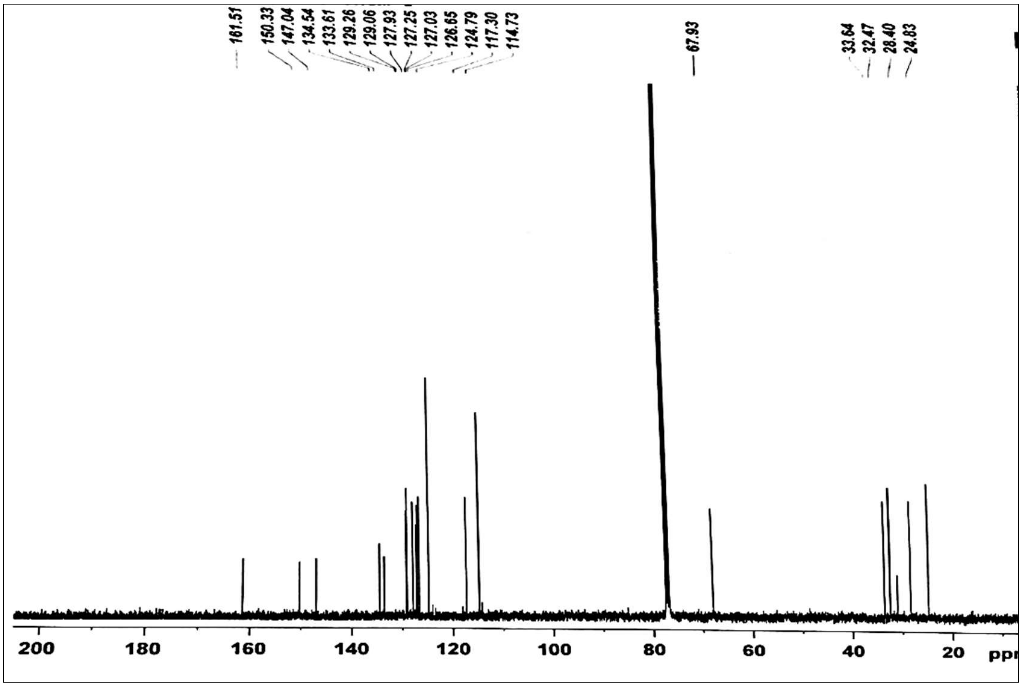

Fig. S2B.15: ^{13}C-NMR Spectra of NpAzO5Br

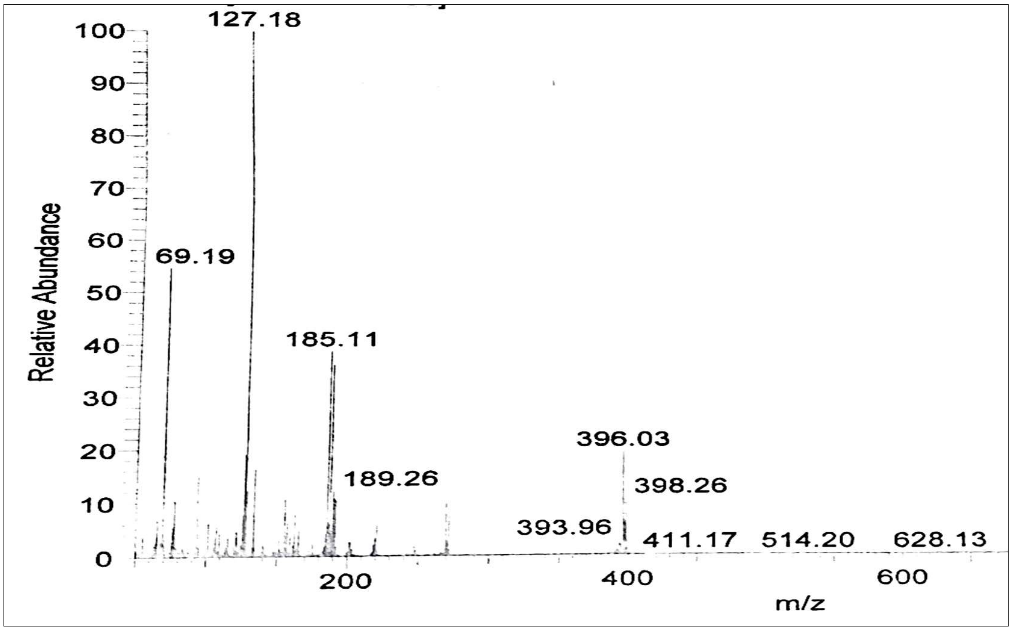

Fig. S2B.16: Mass Spectra of NpAzO5Br

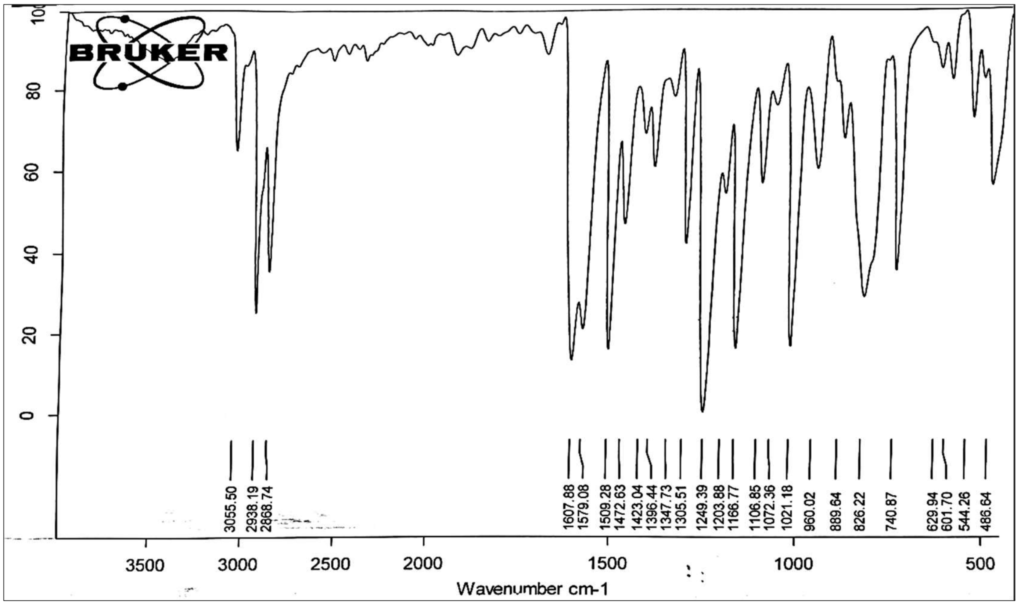

Fig. S2B.17: FT-IR Spectra of NpAzO6Br

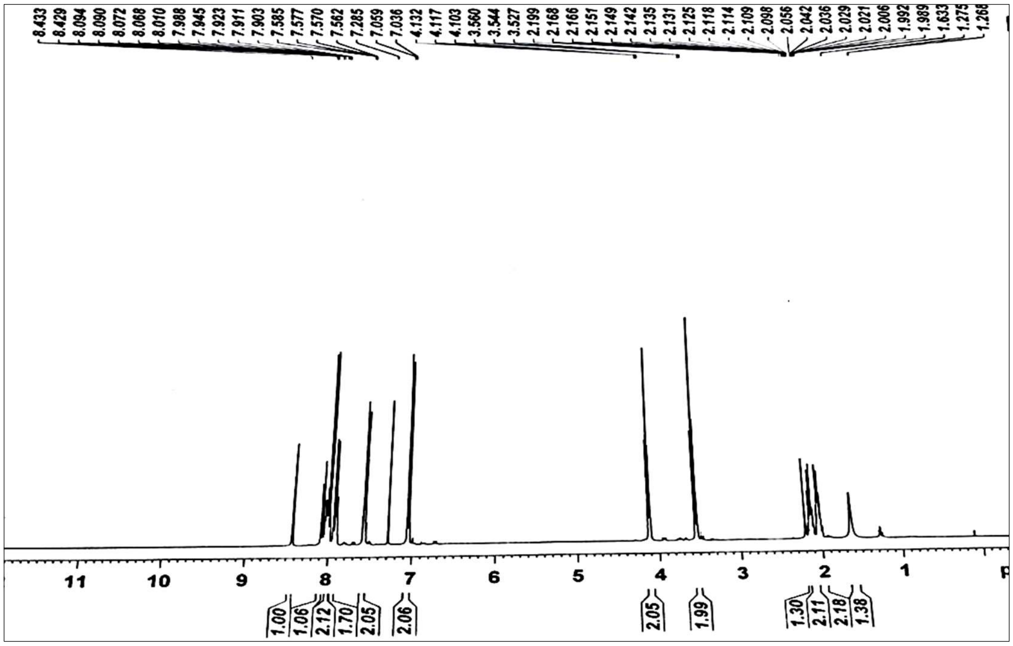

Fig. S2B.18: ^{1}H-NMR Spectra of NpAzO6Br

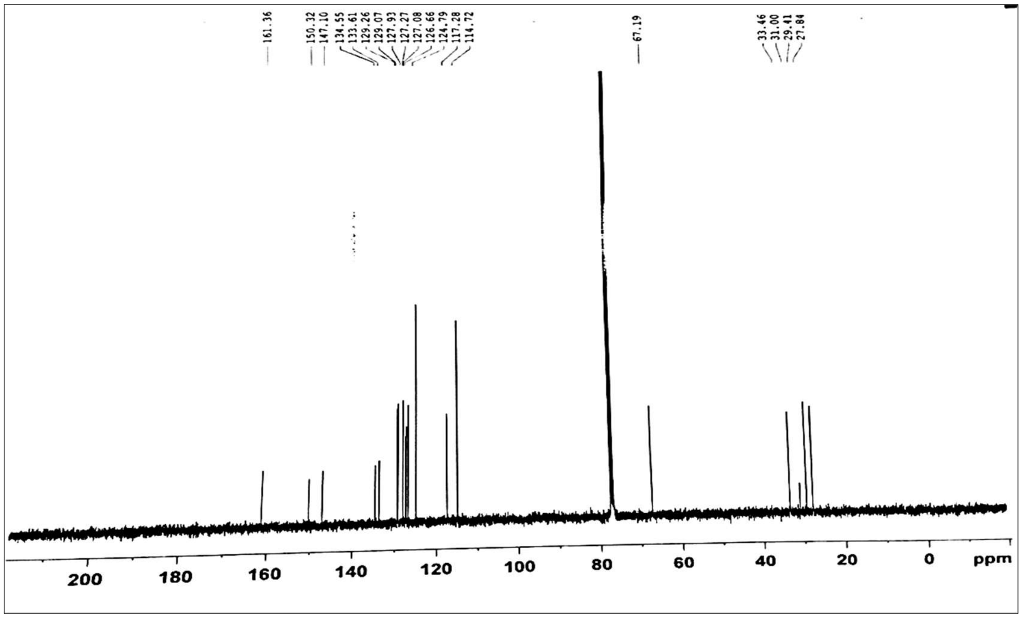

Fig. S2B.19: ^{13}C-NMR Spectra of NpAzO6Br

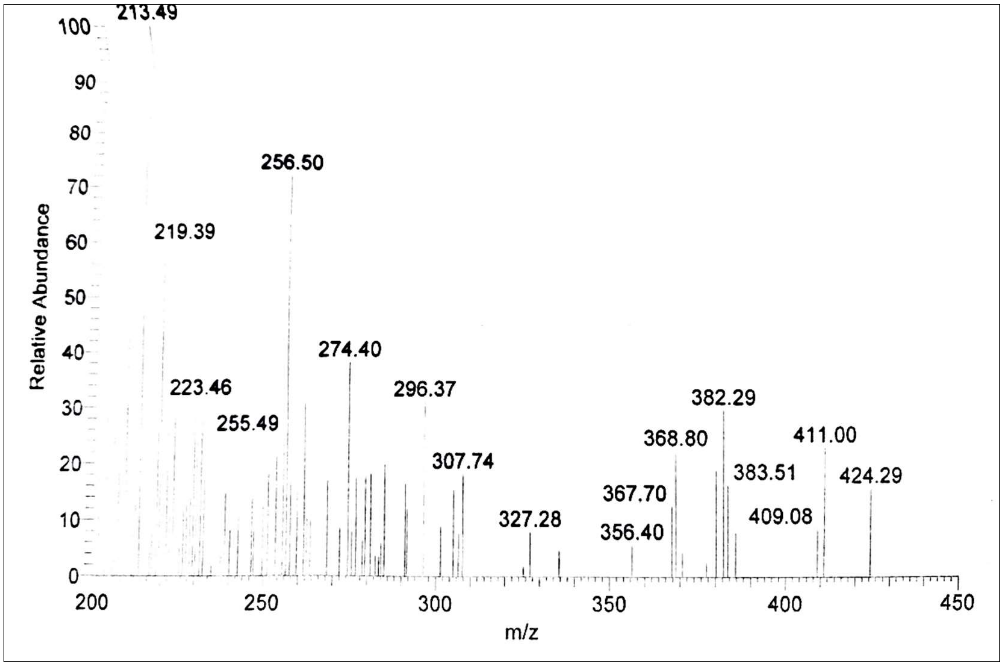

Fig. S2B.20: Mass Spectra of NpAzO6Br

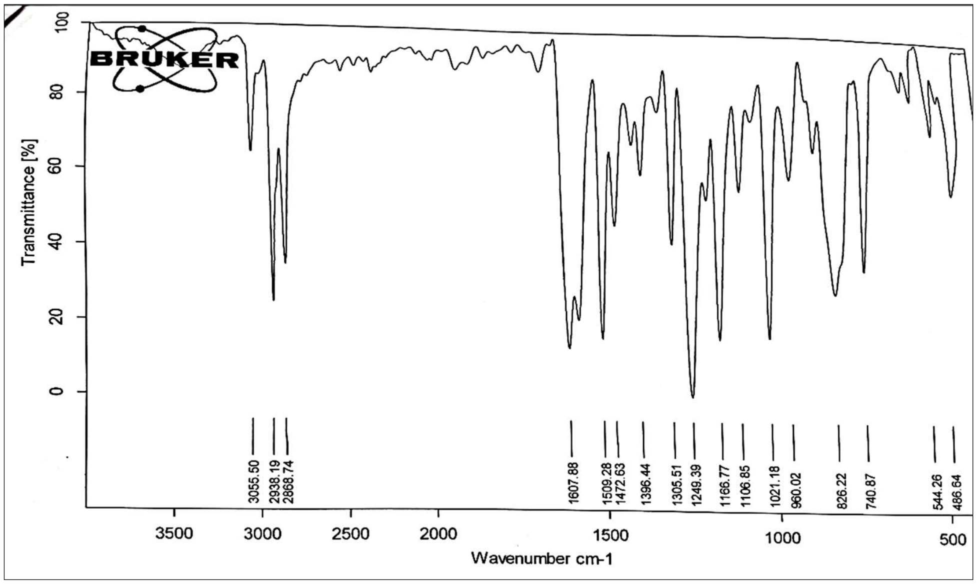

Fig. S2B.21: FT-IR Spectra of NpAzO8Br

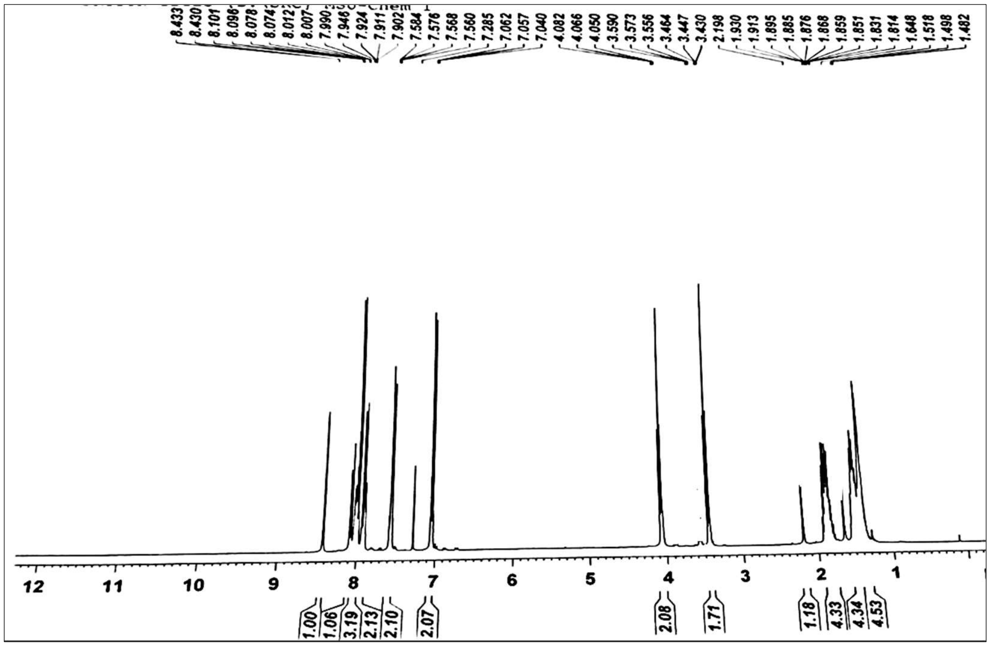

Fig. S2B.22: ^{1}H-NMR Spectra of NpAzO8Br

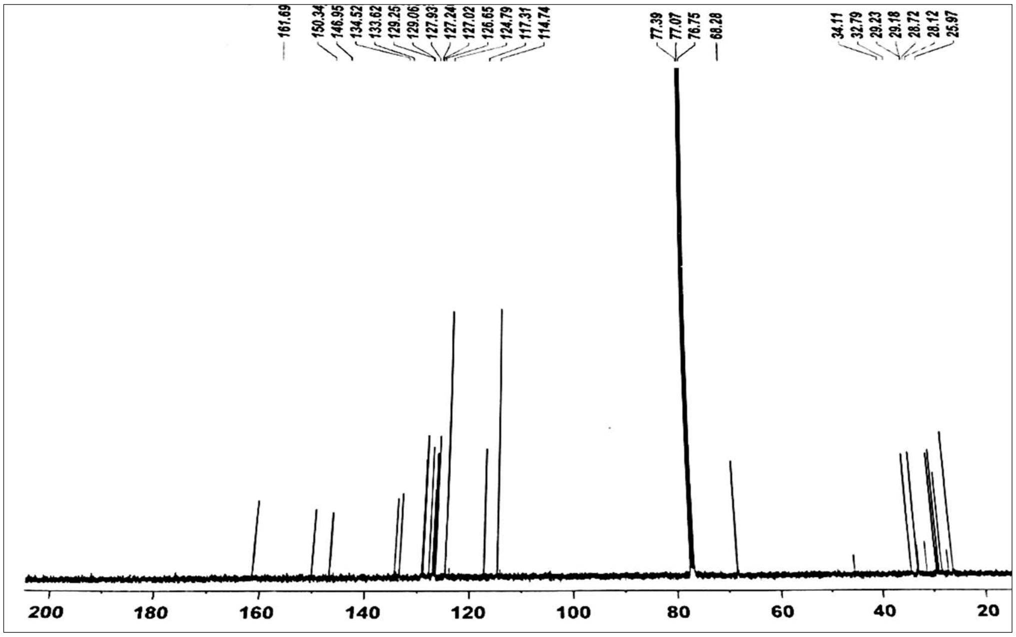

Fig. S2B.23: ^{13}C-NMR Spectra of NpAzO8Br

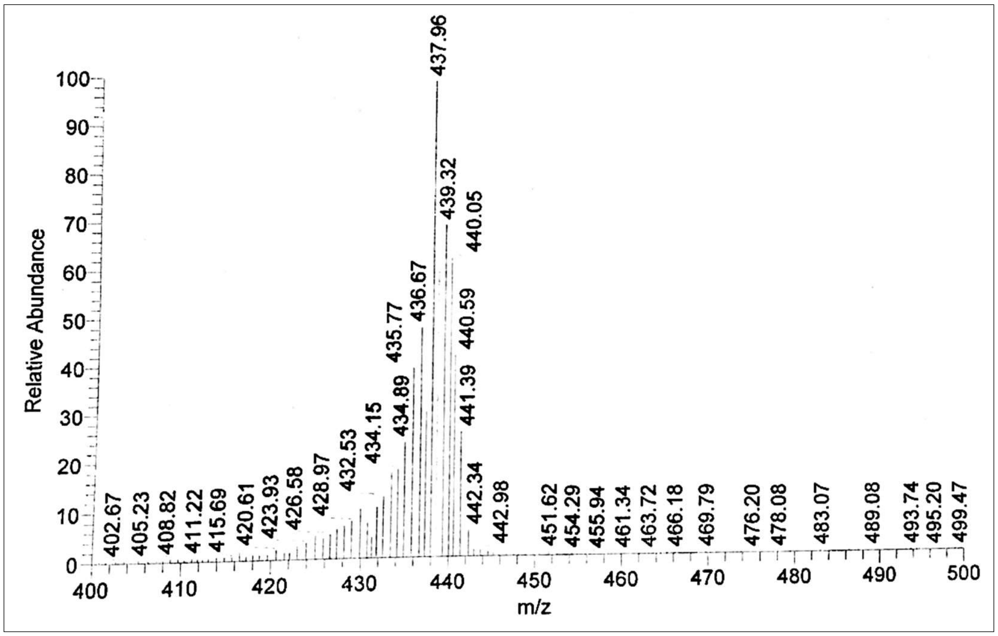

Fig. S2B.24: Mass Spectra of NpAzO8Br

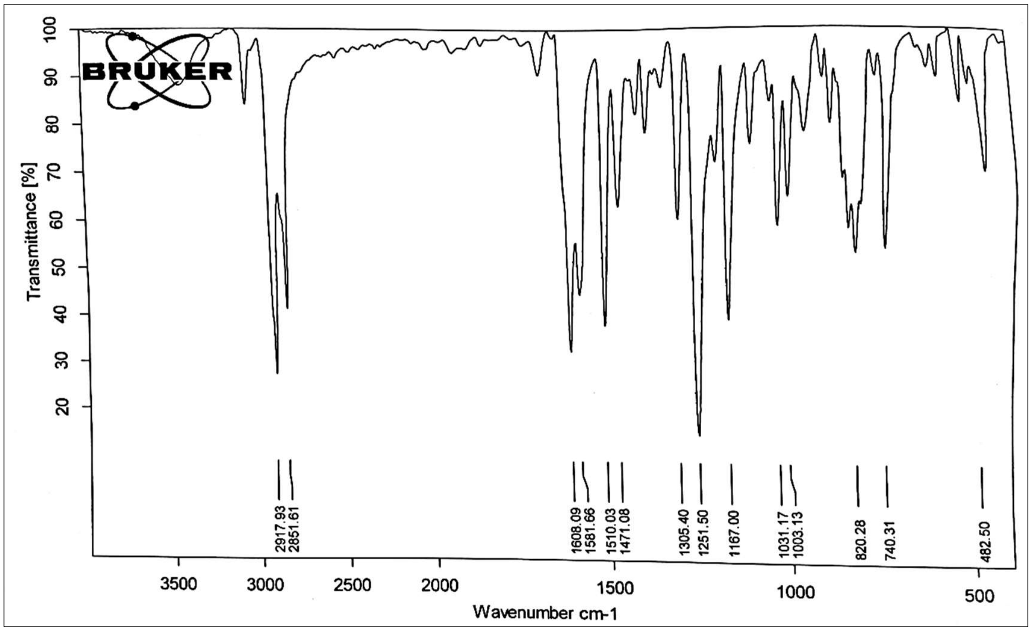

Fig. S2B.25: FT-IR Spectra of NpAzO10Br

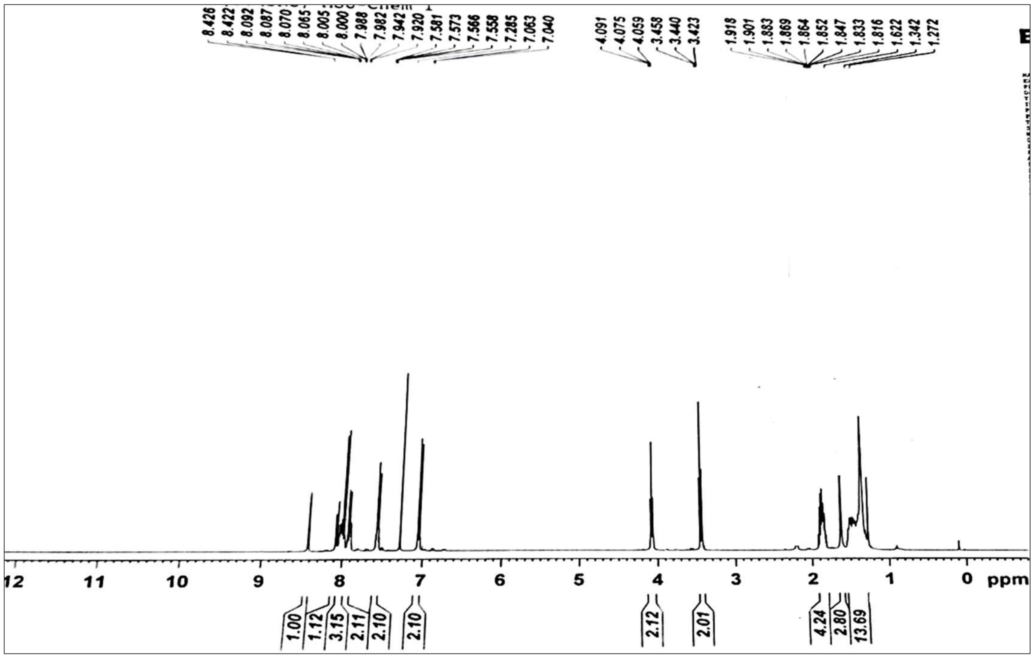

Fig. S2B.26: ^{1}H-NMR Spectra of NpAzO10Br

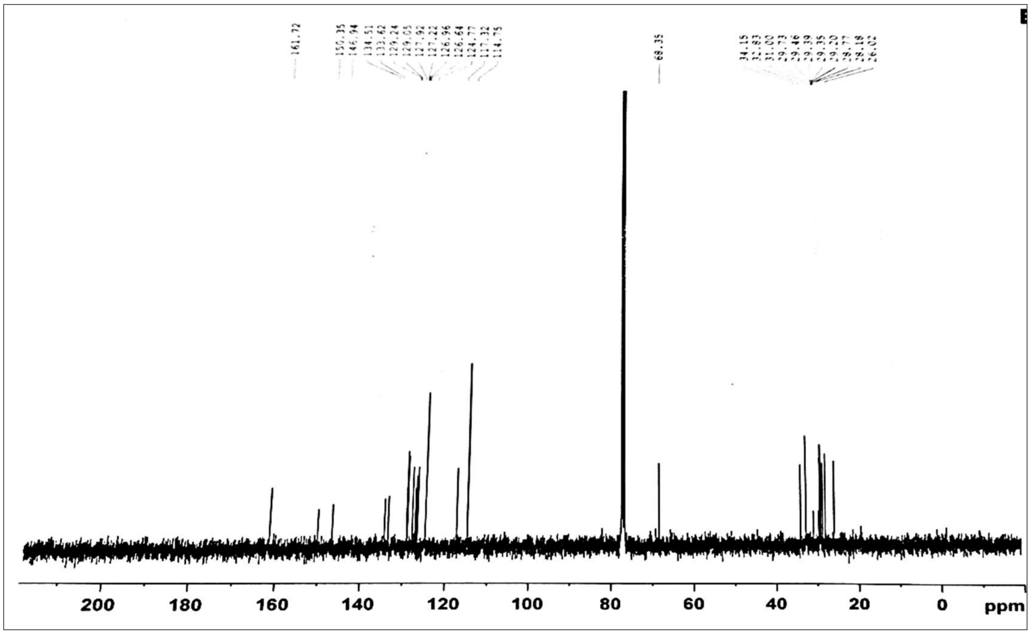

Fig. S2B.27: ^{13}C-NMR Spectra of NpAzO10Br

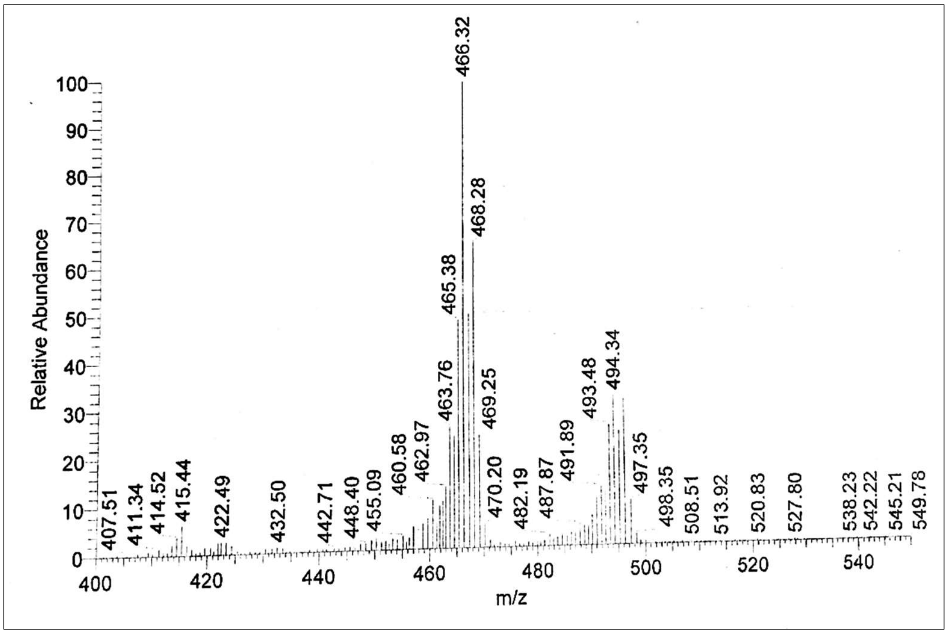

Fig. S2B.28: Mass Spectra of NpAzO10Br

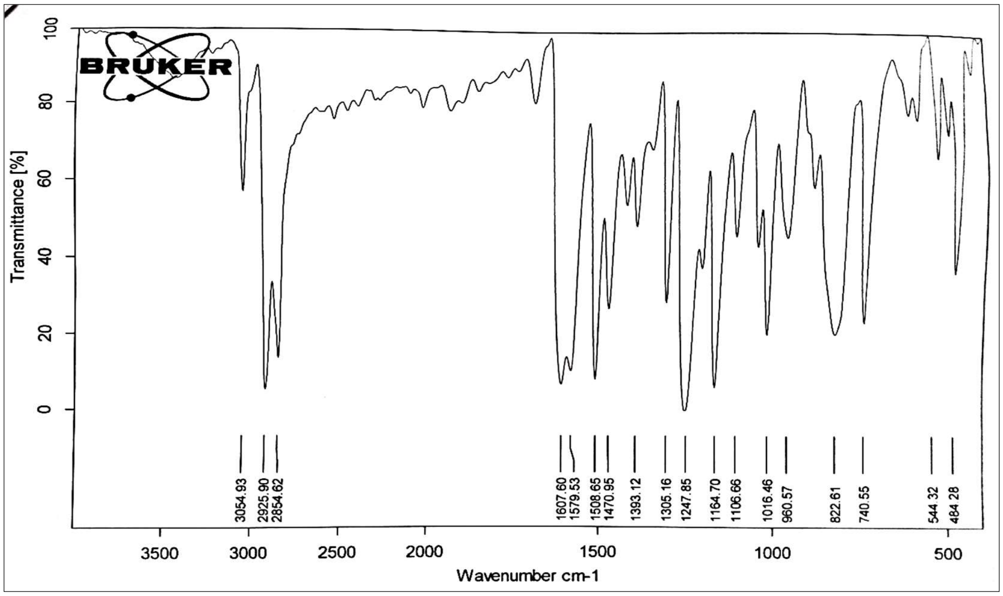

Fig. S2B.29: FT-IR Spectra of NpAzO12Br

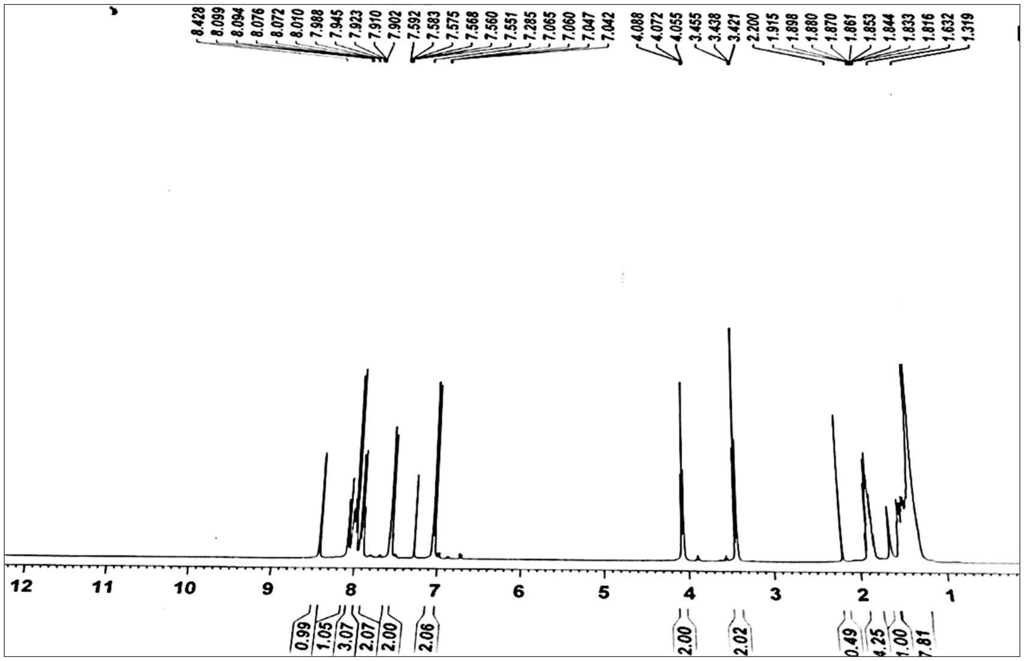

Fig. S2B.30: ^{1}H-NMR Spectra of NpAzO12Br

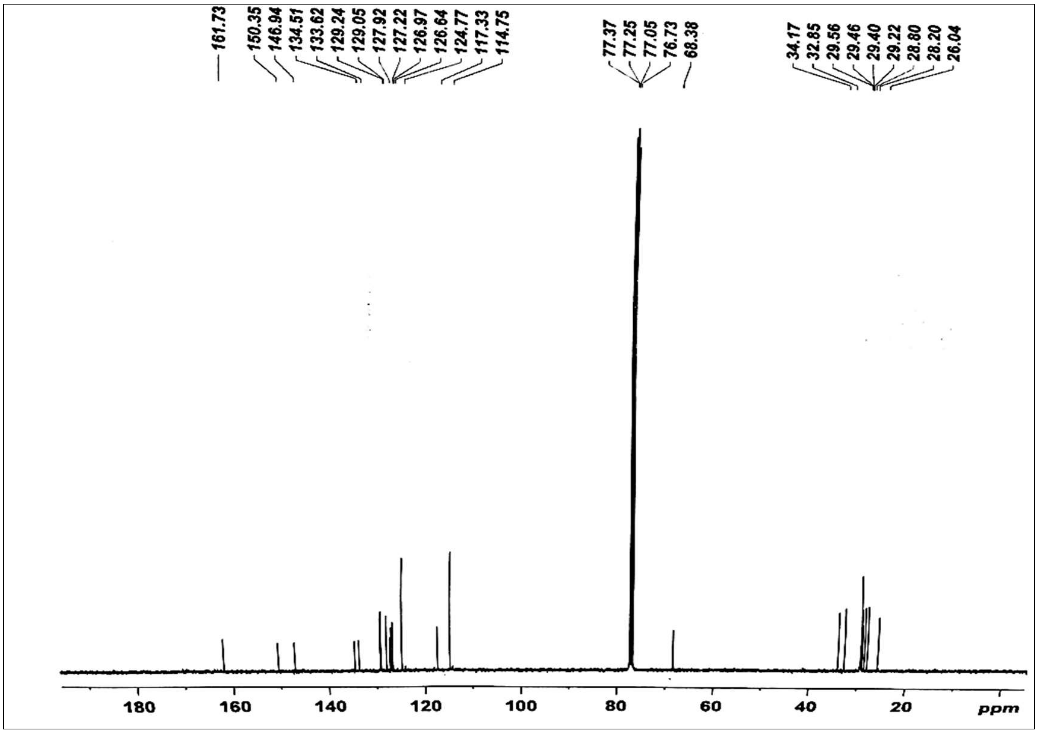

Fig. S2B.31: ^{13}C-NMR Spectra of NpAzO12Br

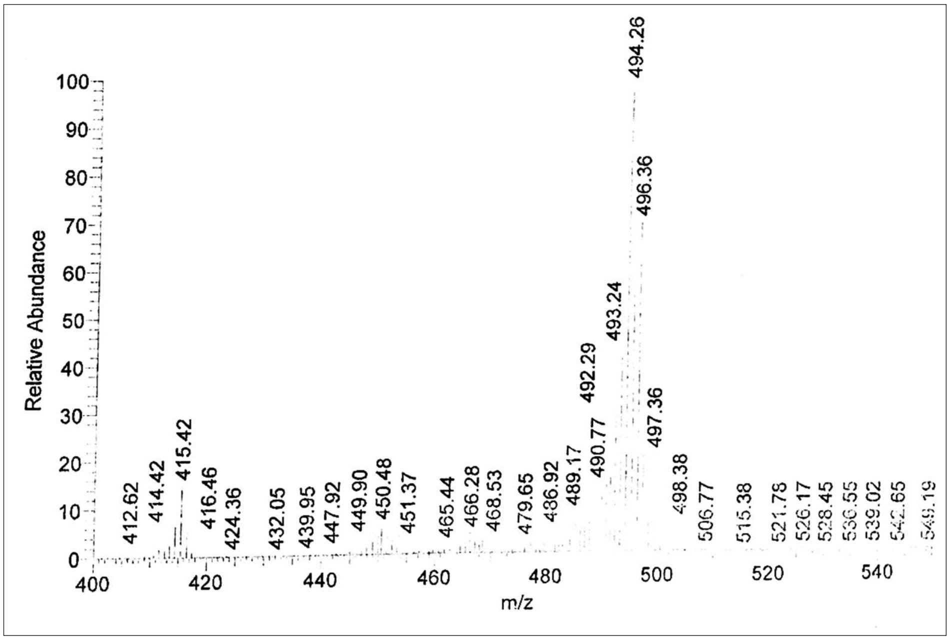

Fig. S2B.32: Mass Spectra of NpAzO12Br

2B.7 References

1 G. W. Gray, *Mol. Phys. Liq. Cryst.*, 1979, 263–284.

2 G. W. Gray, *Mol. Phys. Liq. Cryst.*, 1979, 1–29.

3 M. Rabari, C. Koli and A. K. Prajapati, *Soft Mater.*, 2024, **22**, 1–12.

4 H. Mali, V. S. Sharma, J. Panchal, S. Kher and H. R. Prajapati, *Mol. Cryst. Liq. Cryst.*, 2022, **745**, 40–59.

5 M. R. Karim, M. R. K. Sheikh, N. M. Salleh, R. Yahya, A. Hassan and M. A. Hoque, *Mater. Chem. Phys.*, 2013, **140**, 543–552.

6 Y. Yu and T. Ikeda, in *Smart Light-Responsive Materials*, 2009, pp. 95–144.

7 A. R. Abbasi, Z. Rezvani and K. Nejati, *Dye. Pigment.*, 2006, **70**, 71–75.

8 R. S. Hegde, B. N. Sunil, G. Hegde and V. Prasad, *J. Mol. Liq.*, 2020, **309**, 113091.

9 K. Goda, M. Omori and K. Takatoh, *Liq. Cryst.*, 2018, **45**, 485–490.

10 Y. Kim and N. Tamaoki, *ACS Appl. Mater. Interfaces*, 2016, **8**, 4918–4926.

11 D. Pirone, N. A. G. Bandeira, B. Tylkowski, E. Boswell, R. Labeque, R. G. Valls and M. Giamberini, *Polymers*, 2020, **5**, 12.

12 P. Wei, H. Lou, J. Yan, L. Li, Y. Zhang, Y. Xia, Y. Wang and Y. Wang, *Polymer (Guildf).*, 2022, **240**, 124472.

13 H. T. Srinivasa, B. S. Palakshamurthy, H. C. Devarajegowda and S. Hariprasad, *J. Mol. Struct.*, 2018, **1173**, 620–626.

14 C. Wiegand, *Zeitschrift fur Naturforsch. - Sect. B J. Chem. Sci.*, 1954, **9**, 516–518.

15 G. W. Gray and B. Jones, *J. Chem. Soc.*, 1954, 678–683.

16 G. Kurian and J. S. Dave, *Mol. Cryst. Liq. Cryst.*, 1977, **42**, 193–201.

17 L. G. Derkach, N. S. Novikova and E. Gorecka, *Russ. J. Gen. Chem.*, 2015, **85**, 577–583.

18 V. Kozmík, M. Kuchař, J. Svoboda, V. Novotná, M. Glogarová, U. Baumeister, S. Diele and G. Pelzl, *Liq. Cryst.*, 2005, **32**, 1151–1160.

19 B. T. Thaker, N. J. Chothani, Y. T. Dhimmar, B. S. Patel, D. B. Solanki, N. B. Patel, J. B. Kanojiya and R. S. Tandel, *Liq. Cryst.*, 2012, **39**, 551–569.

20 W. L. Tasi, S. W. Yeh, M. J. Hsie and H. C. Lee, *Liq. Cryst.*, 2002, **29**, 251–253.

21 H. A. Ahmed and M. A. El-Atawy, *Liq. Cryst.*, 2021, **48**, 1940–1952.

22 N. del Giudice, M. L'Her, E. Scrafton, Y. Atoini, G. Gentile, B. Heinrich, R. Berthiot, A. Aliprandi and L. Douce, *European J. Org. Chem.*, 2021, **2021**, 2091–2098.

23 R. A. Vora and A. K. Prajapati, *Liq. Cryst.*, 1998, **25**, 567–572.

24 A. K. Prajapati, *Mol. Cryst. Liq. Cryst. Sci. Technol. Sect. A Mol. Cryst. Liq. Cryst.*, 2000, **348**, 65–72.

25 A. K. Prajapati, *Liq. Cryst.*, 2000, **27**, 1017–1020.

26 A. K. Prajapati, H. M. Pandya and N. L. Bonde, *J. Chem. Sci.*, 2004, **116**, 227–233.

27 A. K. Prajapati and H. M. Pandya, *Mol. Cryst. Liq. Cryst.*, 2003, **393**, 31–39.

28 A. K. Prajapati, H. M. Pandya and N. L. Bonde, *J. Chem. Sci.*, 2004, **116**, 227–233.

29 N. D. Jadav, B. A. Prajapati and A. K. Prajapati, *Mol. Cryst. Liq. Cryst.*, 2003, **399**, 53–60.

30 A. K. Prajapati, V. Thakkar and N. Bonde, *Mol. Cryst. Liq. Cryst.*, 2003, **393**, 41–48.

31 A. K. Prajapati and N. Bonde, *Liq. Cryst.*, 2006, **33**, 1189–1197.

32 H. N. Patel and A. K. Prajapati, *Mol. Cryst. Liq. Cryst.*, 2017, **643**, 106–115.

33 P. Nestler and C. A. Helm, *Opt. Express*, 2017, **25**, 27077–27085.

34 S. R. Pilli, T. Banerjee and K. Mohanty, *J. Mol. Liq.*, 2015, **207**, 112–124.

35 L. R. Domingo, M. Ríos-Gutiérrez and P. Pérez, *Molecules*, 2016,**7,** 21.

36 B. Manoj, in *Woodhead Publishing Series in Composites Science and Engineering*, eds. A. Khan, M. Jawaid, Inamuddin and A. M. B. T.-N. and its C. Asiri, Woodhead Publishing, 2019, pp. 589–600.

37 H. M. D. Bandara and S. C. Burdette, *Chem. Soc. Rev.*, 2012, **41**, 1809–1825.

38 T. Sasaki, T. Ikeda and K. Ichimura, *Macromolecules*, 1993, **26**, 151–154.

39 S. M. Gan, A. R. Yuvaraj, M. R. Lutfor, M. Y. Mashitah and H. Gurumurthy, *RSC Adv.*, 2015, **5**, 6279–6285.